Investigation into the Friction Stir Welding of Thick Section Aluminium Alloys

George Henry Brooks

In Collaboration with The Welding Institute (TWI Ltd) and National Structural Integrity Research Centre (NSIRC)

A thesis submitted in partial fulfilment of the requirements of Sheffield Hallam University
for the degree of Doctor of Philosophy

December 2021

Candidate Declaration

I hereby declare that:

1. I have not been enrolled for another award of the University, or other academic or professional organisation, whilst undertaking my research degree.

2. None of the material contained in the thesis has been used in any other submission for an academic award.

3. I am aware of and understand the University's policy on plagiarism and certify that this thesis is my own work. The use of all published or other sources of material consulted have been properly and fully acknowledged.

4. The work undertaken towards the thesis has been conducted in accordance with the SHU Principles of Integrity in Research and the SHU Research Ethics Policy.

5. The word count of the thesis is 46,001

Name	George Henry Brooks
Award	Doctor of Philosophy
Date of Submission	December 2021
Faculty	Materials Engineering Research Institute (MERI)
Director(s) of Studies	Dr Stephen Magowan

Table of Contents

Acknowledgements

Firstly, I would like to thank my supervisory team; Dr Stephen Magowan and Stephen Cater and formerly Prof Alan Smith. This project would not have been possible without the guidance and support you have given over the last three years.

Further thanks are necessary for the technical support I have received; Chris Stanhope, Joe Sykes and Alun Davies helped make everything possible with their support in manufacturing, preparing, and analysing the material. The rest of the SYF team not mentioned; Jonathan, Jeroen and Sam. I've learned and developed a lot from the environment you created. I'd also like to thank the administrators of both MERI and NSIRC for their support particularly with regards to leave for surgery and the difficulties of Covid-19. I am also grateful to Dr Oliver Lewis for leading me to FSW for my BEng dissertation. Without this, I would've never heard of FSW and this chapter of my career may never have happened.

Finally, my family and friends. Helen, Steve, and I took on this journey together and I am very grateful to have had friends like you going through each challenge together. My family, you have helped me, sometimes dragging me, through so much the last three years. You kept me sane during the lockdowns and kept me at my best when I needed it most and I am eternally grateful. And to Abi, you've been a part of this journey from step one, and I cannot put into words how grateful I am that you have been. No one has supported me through every high and low and distracted me when I needed to step back better than you. Thank you.

Abstract

Friction stir welding (FSW) is a solid-state joining technology with a growing range of applications, many of them in safety critical service. These include aircraft wing spars and fusion reactor components, where the heat input associated with thick section components and long-term service performance are becoming increasingly important. However, there is a limited pool of published knowledge relating to FSW of thick section materials due to the previous industrial demand surrounding thin section welding.

The primary aim of this research project was to investigate the influence of FSW using three different techniques joining 50 mm thick aluminium alloys AA5083-H111, AA6082-T651 and AA7050-T6451. These techniques, namely Weld-Flip-Weld (WFW), Simultaneous Double Sided (SDS) and Supported Stationary Shoulder (SSS) each have a different thermo-mechanical weld input and effect on the weld zone which have yet to be extensively investigated and quantified.

The stir zone experienced large deformation and recrystallization resulting in an equiaxed and refined grain structure. Grain size was influenced by energy input with a greater input resulting in a larger grain structure. In each weld, constituent particles were identified with common elements of iron and aluminium being observed in all cases. Further particles of Mg_2Si were found in AA5083 and AA6082 welds while Silica was recorded welds of AA7050.

Simultaneous Double Sided FSW was shown to be an effective process and arguably the most appropriate for a wide range of industrial uses. In non-heat treatable AA5083 the process not only used less energy but also retained higher strength (298 MPa) than Weld-Flip-Weld (277 MPa). The retention of strength in the SDS weld in heat-treatable alloy AA7050 (352 MPa) and was not as high as that in the WFW weld (419 MPa),

however, coupled with the other benefits, such as faster production time and lower energy input, can be considered the most industrially suitable variant for AA7050-T7451.

List of Figures

List of Tables

Nomenclature

AS	Advancing side
e	Efficiency factor of Power Stir machine
FS	Friction stir
FSW	Friction Stir Welding
FSWed	Friction Stir Welded
GMAW	Gas metal arc welding
GP	Guinier-Preston
HAZ	Heat affected zone
HV	Vickers Hardness
IFM	Infinite focus microscope
MIG	Metal inert gas welding
NZ	Nugget zone
PM	Parent Material
r	Spindle rotation – measured in Rev/min
RS	Retreating side
SDS	Simultaneous double sided
SSB	Supported stationary bobbin
SSS	Supported stationary shoulder
SZ	Stir zone
T	Spindle torque – measured in Nm
TIG	Tungsten inert gas welding
TMAZ	Thermo-mechanically affected zone
TWI	The Welding Institute
UTS	Ultimate tensile strength – measured in MPa
v	Traverse speed – measured in mm/min
WFW	Weld flip weld
σ	Stress – measured in MPa

1 Introduction

1.1 Outline

The joining of two or more components can be achieved by welding, a fabrication process that has surged in use since the turn of the 20th century. Since this time welding processes such as fusion welding have been common practice for joining in a wide range of industries such as transportation, energy and construction (TWI Ltd (2021)c). Fusion welding, the process of melting and fusing material together has many variants such as Gas Metal Arc Welding (GMAW), Gas Tungsten Arc Welding (GTAW) and Submerged Arc Welding (SAW) (TWI Ltd (2021)b). While fusion welding has several benefits including the ability to join more than two components easily as well as the ability to join components despite large spaces between them by using a filler wire, there are also disadvantages. Difficulty joining dissimilar metals, the need for a shielding gas, the potential of porosity within the weld and large amounts of distortion and residual stress are all factors to consider. Further to this, increasing material thickness leads to lengthy manufacturing times slowing the progress of the components manufacture. These disadvantages can be tackled through the use of other welding techniques such as friction welding.

Friction welding is the process of joining materials by generating mechanical frictional heat between a moving and stationary component while applying what is called an ‘upset’ or lateral force that displaces and fuses the material together. Friction welding is conducted in a linear or rotary motion, demonstrated in Figure 1, although the principle remains the same. Typically the process is used for manufacturing rollers, tubes and shafts and has the advantage of not requiring filler metal, shielding gas or edge preparation as well as achieving welds in ‘non-weldable’ aluminium alloys due to the solid-state nature of the process (TWI Ltd (2021)a). However, like fusion welding there are disadvantages that limit the application of the process. Drawbacks such as large flash generation and the limited geometry prevent the process going further and provides scope for further variation on the process in the form of Friction Stir Welding (FSW).

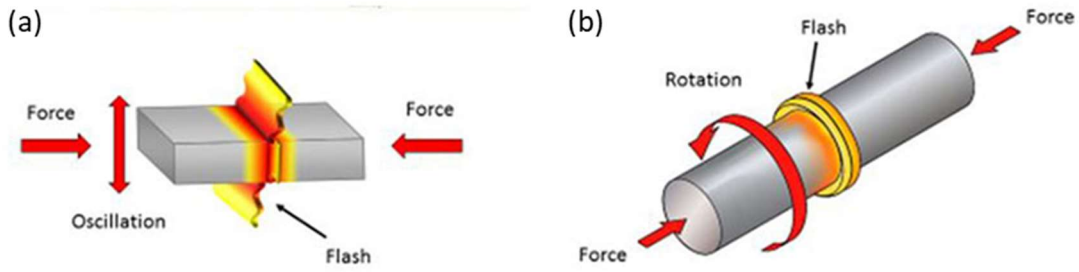

Figure 1 - Process schematics for friction welding variants a) linear and b) rotary (TWI Ltd (2021)a).

Friction Stir Welding (FSW) is a solid-state joining process that combines elements of the thermal and working techniques to join an array of materials. In its simplest form the process uses a non-consumable tool with a specially designed shoulder and probe to stir material softened by frictional heating to form a joint. Since its invention at TWI in 1991, FSW has been widely adopted for welding aluminium in sectors such as automotive, aerospace, rail, and shipbuilding where high integrity, light-weight fatigue resistant fabrications are required (V. M. Magalhães, Leitão, and Rodrigues (2018)). These applications are primarily in thin structures, varying from sheet and extrusions of just a few millimetres in thickness up to beams and plates of around 20 mm (Cater and Brooks (2020)). The process, however, has a far wider application than aluminium having been shown to be successful in a wide range of metals and polymers. There are also several types of FSW, which further expand its applications, such as Friction Stir Spot Welding (FSSW) and channeling. FSSW uses the principle of FSW without any traversing, generating a solid-state weld in a single location whereas channeling uses a specially designed tool to generate a sub-surface cavity, typically used to aid thermal management, by expelling material through the tool whilst maintaining a sealed upper surface.

Applications of FSW in thicknesses in excess of 20 mm are much rarer due to a limited corpus of research in this area, which is due to numerous reasons including technology requirements as well as previous industrial demand focused on thin section. In order to manufacture welds in >20 mm thick material, the technology must be capable of

operating under sustained high forces such as torque and bending stresses. This limits the range of FSW machines capable of achieving such welds and therefore subsequently limits the organisations able to conduct research. Previous research (V. M. Magalhães, Leitão, and Rodrigues (2018)) also indicated that the automotive industry accounted for approximately 30% of all applications for FSW. This is an industry that requires thin section joining and has previously driven the direction of research in this field. However, a growing demand for thick section FSW is driving the requirement for more research surrounding this topic. Both marine and aerospace sectors have shown interest in developing thick section FSW for applications including superstructures and wing spars. In this project, the term 'thick section' is defined as material that is greater than 20 mm thick although the project looks solely at 50 mm thick aluminium alloys.

1.2 Research aim

The aim of this study was to investigate the influence of friction stir welding techniques Weld-Flip-Weld (WFW), Simultaneous Double Sided (SDS) and Supported Stationary Shoulder (SSS) on the microstructure and mechanical properties of 50 mm thick aluminium alloys AA5083-H111, AA6082-T651 and AA7050-T7451 using pre-selected welding parameters.

1.3 Research objectives

In order to accomplish the research aim, a series of objectives were established.

1. Characterise the parent materials.
2. Produce samples using the techniques and alloys identified.
3. Undertake microstructural analysis on the welds.
4. Undertake mechanical testing including tensile testing, macro- and micro-hardness testing.
5. Calculate the energy input and swept volume of material for each of the welds investigated.

6. Appraise the performance of four supported stationary shoulder tools used to produce welds in AA6082-T651.
7. Compare the influence of the applied FSW techniques on the properties of each sample material.
8. Evaluate the influence of natural ageing on the mechanical properties of friction stir welded AA7050-T7451.

2 Literature review

2.1 Metals

2.1.1 Engineering metals

Metals, which are commonly found in the earth's crust, and their alloys have a wide and varying range of engineering applications from structural components to the expansive transportation sector. Through alloying with other elements, the range of applications possible is further enhanced. Metals such as iron, aluminium and copper are extracted in huge quantities every year. Table 1 shows continual growth in the quantity of aluminium extracted over a nine year period from 40.8 million tonnes to 63.66 million tonnes per year ('Mineral Commodity Summaries 2012' (2012); 'Mineral Commodity Summaries 2021' (2021)). Iron ore, used to also form steel, is extracted in vastly greater quantities than any other metal (2.45 billion metric tonnes in 2019 ('Mineral Commodity Summaries 2021' (2021))).

Metal - Thousands of tonnes (metric)		2010[1]	2015[2]	2019[3]
Iron ore	Fe	2 590 000	2 280 000	2 450 000
Aluminium	Al	40 800	57 500	63 657
Copper	Cu	15 900	19 100	20 400
Zin	Zn	12 000	12 800	12 700
Nickel	Ni	1590	2280	2610

Table 1 – Production in thousands of metric tonnes of five commonly extracted metals between 2010-2019. ([1]'Mineral Commodity Summaries 2012' (2012); [2]'Mineral Commodity Summaries 2017' (2017); [3]'Mineral Commodity Summaries 2021' (2021)).

2.1.2 Crystalline structure of metals

In their solid state, metallic atoms arrange themselves into configurations called crystals with the arrangement the atoms take within the crystal being known as a crystalline structure (Kalpakjian and Schmid (2001)). Broadly, there are three main unit cell structures that metals take; Body-Centre Cubic (BCC), Face-Centre Cubic (FCC) and Hexagonal Close Packed (HCP) as illustrated in Figure 2. Metals form these different structures to minimize the energy required to fit together in a regular pattern. To this end, aluminium, for example, forms an FCC structure while zinc forms an HCP structure for the same reason. However, at different temperatures the same metal can take different crystalline structures because the minimal energy required at that temperature can vary. This is a phenomenon called polymorphism.

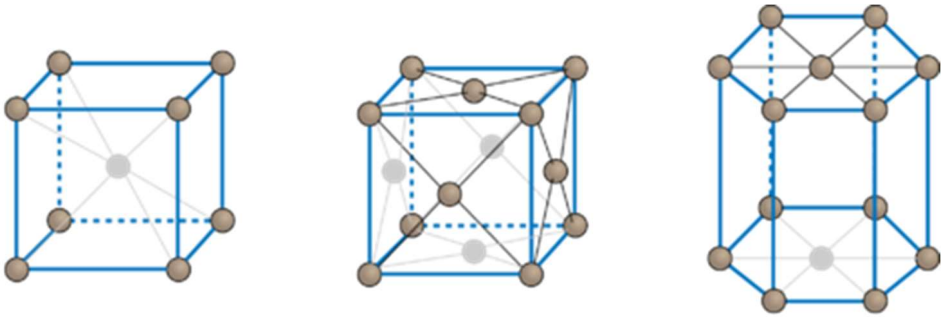

a) Body-centre cubic (BCC) b) Face-centre cubic (FCC) c) Hexagonal close packed (HCP)

Figure 2 - Crystalline structures of metallic materials ('Crystal Structures of Metals | Chemistry for Non-Majors' (n.d.))

A crystal structure is formed, according to Rohrer (2001), when identical copies of a basis (a set of one or more atoms that share the stoichiometry of the material) are located at each point of a Bravais lattice. In three-dimensional space there are 14 Bravais lattices which can be obtained by combining one of the seven lattice systems, shown in Figure 3 below, with one of the centring structures: Primitive, Base-centred, Body-centred, or Face-centred.

Crystal family	Lattice system	Schönflies	14 Bravais lattices			
			Primitive (P)	Base-centered (C)	Body-centered (I)	Face-centered (F)
Triclinic		C_i	 aP			
Monoclinic		C_{2h}	 mP	 mS		
Orthorhombic		D_{2h}	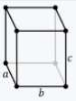 oP	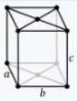 oS	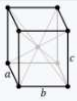 oI	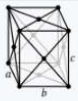 oF
Tetragonal		D_{4h}	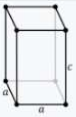 tP		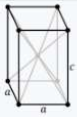 tI	
Hexagonal	Rhombohedral	D_{3d}	 hR			
	Hexagonal	D_{6h}	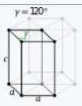 hP			
Cubic		O_h	 cP		 cI	 cF

Figure 3 – Bravais lattices are formed from the combination of one of seven lattice systems with a centring structure (Th. Hahn (2006)).

2.1.3 Deformation of crystals

The crystal structure, when exposed to an external force, initially undergoes elastic deformation where the structure returns to its original shape after the force is removed. As the force is increased significantly the structure undergoes plastic deformation where it will no longer return to its original shape and is permanently distorted. Plastic deformation, the macroscopic deformation of a material, is a consequence of large numbers of dislocations moving and multiplying (Callister and Rethwisch (2014)).

2.1.3.1 Dislocations

Dislocation, a linear crystallographic defect within a metal, controls plastic deformation (Princeton University, (n.d.)) and occurs when stress is applied to a metal. Dislocations allow for a plane of atoms to be translated over an adjacent plane when subjected to shear stress. There are two types of mobile dislocations, edge and screw, which can be visualized in different manners. Firstly, edge dislocations can be considered as being caused by the termination of a plane of atoms midway through a crystal (Madhu (2018)). This is visualized by Kalpakjian and Schmid (2001) as an earthworm, 'which moves forward by means of a hump that starts at the tail and moves to the head'. In this instance the surrounding planes are not straight but rather bend to the edge of the terminating plane such that the crystal structure is perfectly ordered. When stress is applied with such a defect present, the dislocation moves parallel to the direction of stress. The other dislocation type, screw, is considered as a plane of atoms in the crystal lattice travelling helically around the dislocation line. Conversely to edge dislocations, screw moves perpendicular to the direction of stress.

The movement of dislocations, when a material is plastically deformed, is unwavering unless stopped by an inhibitor within the crystalline lattice. One of the most effective inhibitors is another dislocation. Dislocations cannot pass through one another and therefore two dislocations running on different planes that intersect will halt the progress of the other. This can cause a build-up of dislocations leading to entanglement which prevents any further permanent deformation of the grain, without the use of significantly greater energy (Brush Wellman Inc (2010)).

Dislocations can also be hindered by grain refinement. Dislocations require greater energy to change direction and move to adjacent grains. By refining the grain structure, the number of grain boundaries is increased and the lattice structure of the grains differs in orientation, thus meaning that the dislocation requires more energy to move and is therefore inhibited (Callister (2005)). A further inhibitor of dislocation is 'pinning'. Pinning points, such as alloying elements, can introduce stress fields that ultimately strengthen the material by requiring a higher applied stress to overcome

the pinning stress and continue dislocation motion. This stress is called the 'Orowan stress' – the stress required to push a dislocation between particles (Smilauerova, (n.d.)). Pinning also shortens the dislocation as residual dislocation loops remain, encircling the second phase material, as demonstrated in Figure 4. It is possible, however, for the pinning point to become obsolete. This is possible if the incoherent precipitates and space between them exceed a threshold above which dislocations bow and pass the precipitates, such as in the 'over-ageing' process. This results in a reduced strength and hardness of the material.

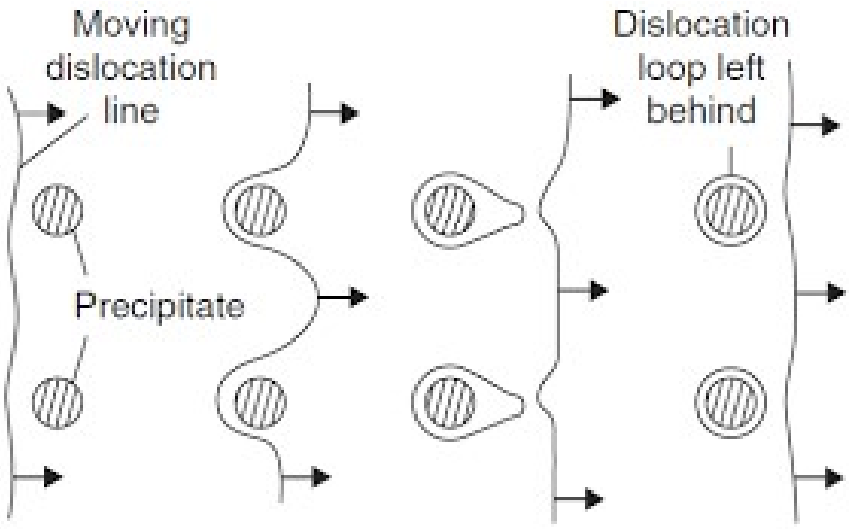

Figure 4 - Schematic of the pinning of dislocations using second phase material (Smilauerova, (n.d.)).

The influence of dislocation movement on mechanical properties such as yield strength and hardness is detrimental. Where dislocations are left unchecked and move freely through a material it is observed that the material is typically weaker and malleable. However, as mentioned previously, dislocations can be used to inhibit their own movement and improve strength. This is the case in work hardening which uses dislocation interaction and entanglement to inhibit motion (Soboyejo (2003)).

2.1.3.2 Mechanisms of plastic deformation

Where plastic deformation takes place, according to Kalpakjian and Schmid (2001), there are two basic mechanisms; slip and twinning. Twinning, shown in Figure 5b, is a

mechanism commonly found to occur in HCP structures, in which a portion of a crystal will abruptly form a mirror image of itself across the plane of twinning.

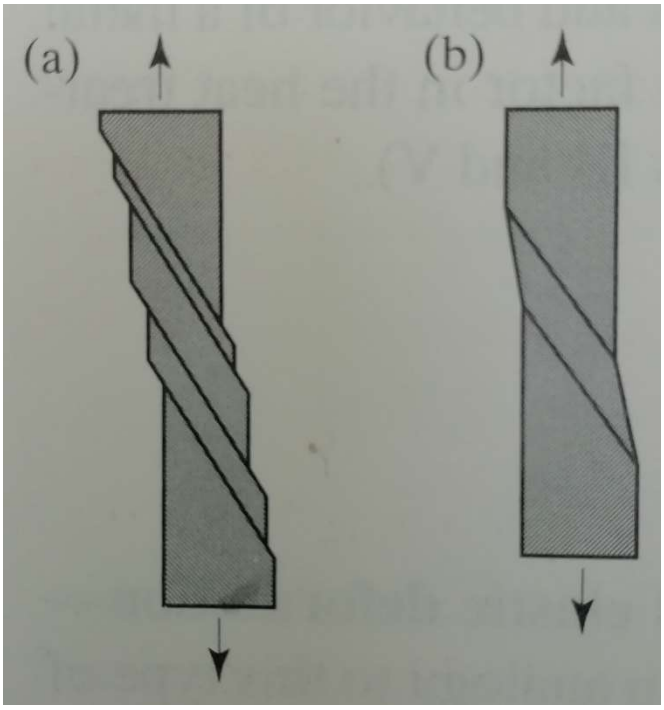

Figure 5 – a) Plastic deformation as a result of a tensile load. b) Twinning in a single crystal as a result of tension. Kalpakjian and Schmid (2001).

The other mechanism for plastic deformation, slip (Figure 5a), is the movement of dislocations, causing translation of one plane of atoms over an adjacent plane when subjected to shear stress. The shear stress applied is directly proportional to the ratio *b/a* where *a* is the spacing of the atomic planes and *b* is inversely proportional to atomic density. Therefore, it can be stated that slip occurs in planes of maximum atomic density (or slip occurs in closely packed planes and in closely packed directions).

Slip systems, the combination of the slip plane and direction, help to determine the ductility of a metal. In general, metals with five or more slip systems are ductile in nature (tec-science (2018)) while those with fewer than five slip systems are brittle. Metals with BCC crystalline structures have good strength properties and moderate

ductility. These body-centre cubic (BCC) crystals have 48 possible slip systems (6 planes of type {110} each with 2 directions and 24 {123} and 12 {112} slip planes each with a single slip direction) and therefore have a high probability that an external shear stress would operate within one of these systems. However, as the ratio of *b/a* is relatively high, a larger shear stress is required for the slip to occur.

Face-centre cubic (FCC) crystals have 12 slip systems (4 slip planes and 3 slip directions) which results in a moderate probability of slip occurring with a shear stress that is lower than that required in BCC as the ratio of atomic spacing and atomic density is low. These structures have moderate strength properties and good ductility. Finally, Hexagonal close-packed (HCP) crystalline structures have 3 slip systems (1 slip plane and 3 slip directions) and therefore a low probability of slip occurring within the structure. However, as the temperature at which the metal is stressed increases, more slip systems become active, as is the case in the other two structures also. As such at room temperature, when the HCP structure has 3 slip systems, the material is brittle as ductility requires a minimum of 5 slip systems, however, at elevated temperatures in which more slip systems become active it is possible for HCP structures to be more ductile.

2.1.4 Recovery and recrystallisation in metals

When metals have been plastically deformed it is possible that recovery, recrystallisation and grain growth can occur. Each is a stage of annealing and can be considered beneficial or detrimental depending on the desired application of the material. Recovery is a phenomenon in which stored energy within deformed grains is reduced through the removal/rearrangement of defects within the crystalline structure (Callister (2007)). Sub grains are formed and subsequently coarsen, reducing the stored energy through reduction in the total area of the grain boundaries. This has no appreciable impact on the mechanical properties such as hardness or strength according to Kalpakjian and Schmid (2001). Recovery only occurs at certain temperatures below the recrystallisation temperature range.

Recrystallisation is the formation of new equiaxed, strain free grains in the place of older, coarser grains. This process only occurs within a certain temperature range which can be considered as $0.3T_m$ to $0.5T_m$, where T_m is the melting temperature of the metal. Typically, recrystallisation is accompanied with a reduction in strength, dislocation density and a rise in ductility. The process is a function of time as it involves diffusion or the movement and exchange of atoms across grain boundaries. However, recrystallisation is also dependent on the extent of cold working prior to reaching the certain temperature. If cold working has been done in abundance prior to heating, then the process will occur at a lower temperature. This is because an increase in cold working results in an increase in dislocations and stored energy. This stored energy is required for recrystallisation to occur.

2.1.5 Alloying of metals

Alloying has the benefit of improving the properties of metal in order to improve its performance in application. Alloying is the combining of two or more elements together by one of two primary methods. The first of these is substitutional solid solution. This alloying technique is the process of an atom exchange between the solvent and the solute atoms, shown in Figure 6b. If the solute atom is of similar size to the solvent, then it can replace the atom and form a substitutional solid solution twinning (Kalpakjian and Schmid (2001)). Two conditions (known as the Hume-Rothery rules after W. Hume-Rothery) are generally required to form a complete substitutional solid solution, these are;

- Two metals must have similar crystal structures.
- Difference in atomic radii should be less than 15%.

Failure to meet these conditions results in a limited solid solution. Brass is an example of this alloying method as some copper atoms are substituted with zinc. The properties of brass can be altered by controlling the amount of zinc.

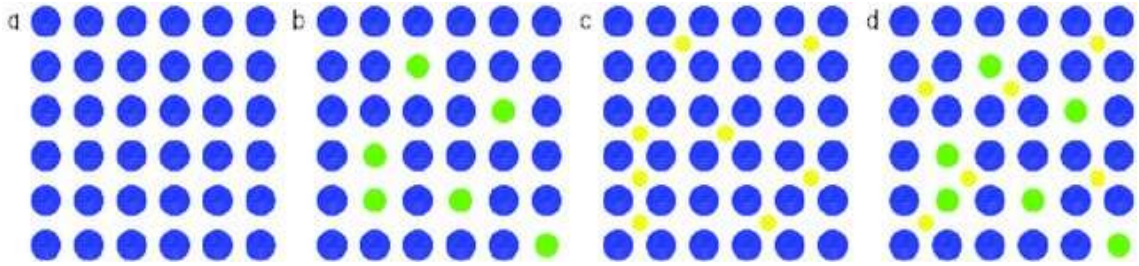

Figure 6 – (a) pure metal; (b) substitutional alloy; (c) interstitial alloy; (d) substitutional/interstitial alloy (Maślak and Skiba (2015)).

The other primary alloying technique is interstitial alloying, shown in Figure 6c. This occurs when atoms of significantly different sizes are alloyed together. In this situation, the smaller solute atoms are too small to replace solvent atoms and become trapped in the spaces within the solvent crystal matrix, called interstices. In this process conditions must also be met to ensure a fully solid solution is formed;

- The solvent atom must have more than one valence.
- Atomic radii of the solute atom must be less than 59% of the atomic radii for the atom.

Steel is an important family of interstitial alloys. An alloy of iron and carbon, where carbon atoms are present in interstitial positions between the iron atoms. The atomic radius of carbon is 0.071nm which is less than 59% of the 0.124nm radius of iron atoms.

2.2 Aluminium alloys

Aluminium is a soft, ductile and durable material which is readily available in the earth's crust. It adopts a face-centre cubic (FCC) crystal structure, see Figure 7, resulting in high amounts of ductility, but low strength and hardness.

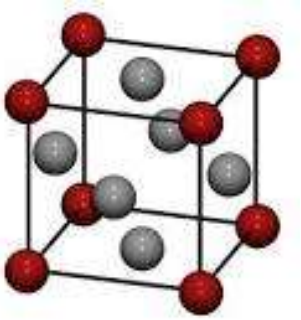

Figure 7 - Face-centre cubic lattice structure ‘Opinions on Cubic Crystal System’ (n.d.)

However, through alloying with other elements aluminium’s strength and hardness can be improved. Table 2 shows the primary alloying elements used per series of wrought aluminium alloy. Wrought alloys can be broadly separated into heat treatable and non-heat treatable alloys and are further classified into a number of families based on a numerical system (nxxx) which identifies their principle alloying content. These alloys, similarly, to pure aluminium, can also be highly corrosion resistant as a result of a layer of aluminium oxide (Al_2O_3) film which forms through interaction with oxygen. Each series of aluminium alloy has been tailored towards improving a specific property or collection of properties making each alloy series useful for different applications. For example, due to 5xxx alloys low density and high corrosion resistance in marine environments as well as aluminium’s better ductility versus steel at low temperatures, the 5xxx series is widely used within the marine industry, in thick and thin section, for applications such as decking, hull fabrication and super structures (Sanders and Staley (2019); Sielski (2008)). An example of this use is the SS United States which was built solely from aluminium and gave a dead weight of 45 400 long tons compared to the 77 000 long tons of the similar sized Cunard Queens (‘Save the SS United States | PropTalk’ (n.d.)). Demonstrating that the use of aluminium alloys in this type of application will increase the efficiency of the vessel and enhance its performance using equivalent propulsion systems.

2.2.1 Effect of primary alloying elements

Each alloy series of aluminium has a different primary alloying element or elements, as shown in Table 2, in order to produce a material with the properties for a specific function. The effect of alloying different elements with aluminium is various however the objective remains similar; improve the stability of the microstructure without hindering the mechanical properties.

Wrought grades	Primary alloying element (s)	Wt. %
1xxx	Aluminium	>99.0%
2xxx	Copper	0.8-6.8
3xxx	Manganese	0.05-1.8
4xxx	Silicon	0.8-13.5
5xxx	Magnesium	0.2-5.6
6xxx	Magnesium and silicon	(0.05-1.5) + (0.2-1.8)
7xxx	Zinc	0.8-8.7
8xxx	Other elements	Varies

Table 2 - Wrought grades and primary alloying elements of aluminium alloys (Hatch, Aluminum Association, and American Society for Metals (1984)).

2.2.1.1 Copper

Adding copper, Cu, to aluminium forms the basic basis of the 2xxx series. Figure 8 shows the aluminium end of the Al-Cu phase diagram, showing the range of copper wt% that forms 2xxx alloys. In most commercial 2xxx series alloys, copper combines with aluminium and iron impurities present to form Al_2Cu (see Figure 9), Al_7Cu_2Fe or α-(Al,Cu,Fe) constituent particles during solidification. Al_2Cu forms rounded and well dispersed particles which are predominantly copper based (52.5-53.9 wt% Cu content) however the inclusion of iron or magnesium results in the formation of the phase Al_7Cu_2(Fe, Mn), where iron or magnesium replace up to 16.2 wt% of the copper. This phase is identifiable due to the thin needle morphology (Mondolfo (1976); Hatch,

Aluminium Association, and American Society for Metals (1984)), illustrated in Figure 10.

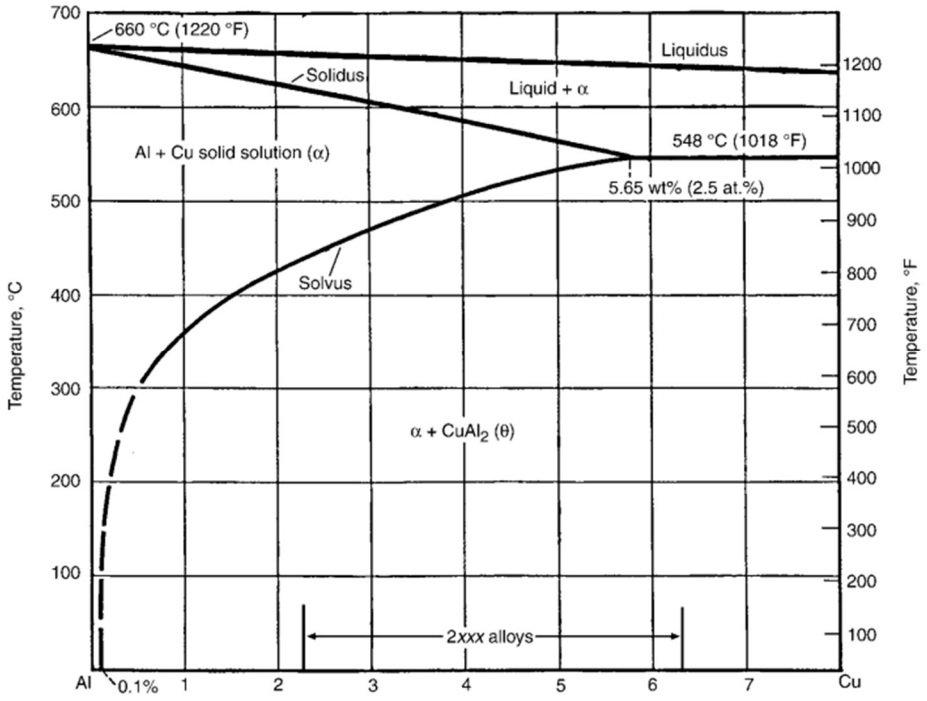

Figure 8 - Aluminium end of the Al-Cu phase diagram Vander Voort (2004).

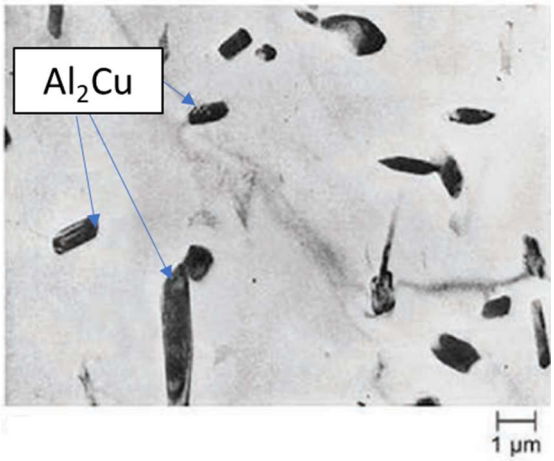

Figure 9 - Al_2Cu phase in an Al-Cu alloy (Porter and Easterling (1997)) .

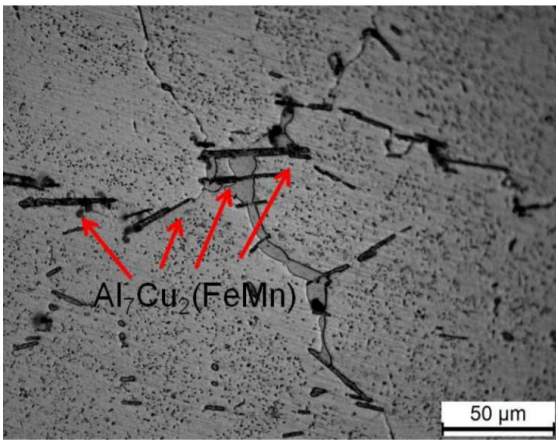

Figure 10 – Al7Cu2(Fe, Mn) intermetallics in AA2219 (Xu et al. (2021)).

The Al-Cu system forms the basic basis of 2xxx alloys; however, the Al-Cu-Mg system is more often used in wrought alloys. Adding magnesium, silicon and manganese to the alloy expands the range of hardening phases possible. Previous studies of 2xxx series alloys found phases including Al_2CuMg, $Al_5Cu_2Mg_8Si_6$, $Al_{20}Cu_2Mn_3$ and Al_6MnFe.

Al_2CuMg is distinguishable from the other phases within these alloys as it can adopt a lath morphology (Radmilovic et al. (1999)), shown in Figure 11. Both $Al_5Cu_2Mg_8Si_6$ and $Al_{20}Cu_2Mn_3$ are 'irregular' particles identified as round and rod like respectively, see Figure 12 and Figure 13.

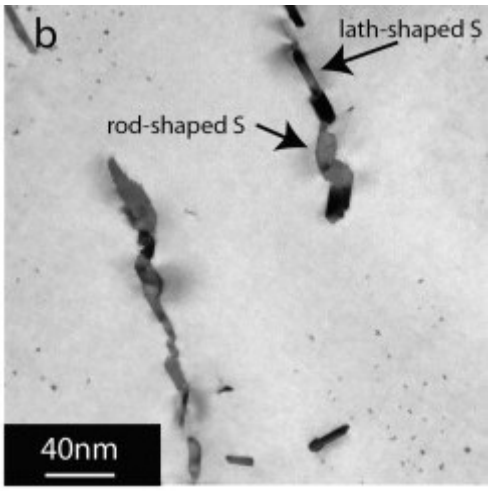

Figure 11 – S phase (Al_2CuMg) present as lath and rod-shaped particles in Al–2.5Cu–1.5Mg (wt%) after 9 hours ageing at 200°C (Styles et al. (2012)).

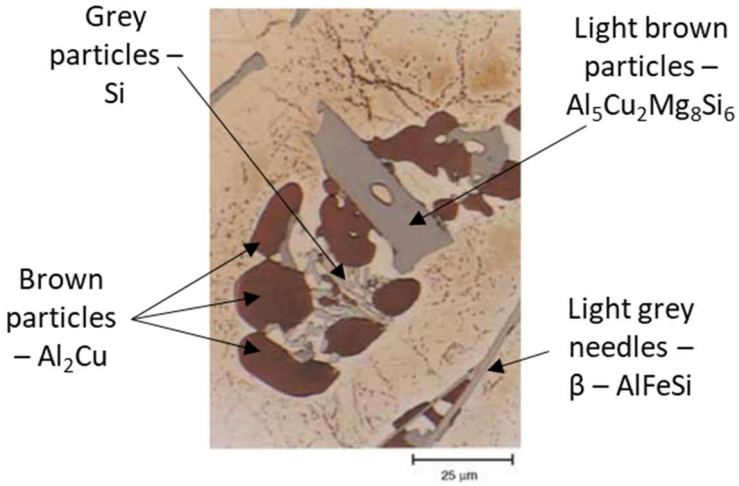

Figure 12 – Alloy 319.0 showing the phases present. Etched in 1 g NaOH and 100 mL distilled H_2O. (Vander Voort (2004)).

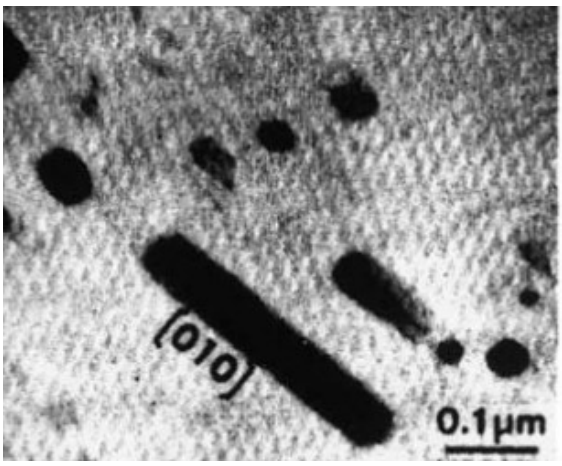

Figure 13 - $Al_{20}Cu_2Mn_3$ rod like phase present in AA2024 (Wang and Starink (2005)).

2.2.1.2 Manganese

Manganese, Mn, is a valuable element whether it is forming the basis of 3xxx series alloys or acting as a transition element. 3xxx series aluminium's are most commonly used due to their formability and corrosion resistance properties. Here, manganese is added in quantities up to 1.8 wt% to increase the material strength with no detrimental impact to the corrosion resistance. Figure 14 shows the aluminium end of the Al-Mn phase diagram. During solidification Mn initially forms parallelograms of $Al_6(MnFe)$ before forming $Al_{15}(FeMn)_3Si_2$ (Alexander and Greer † (2004)). The remaining Mn stays in solution and is precipitated out during pre-heating to form dispersoids of α-Al(FeMnSi), discernible by the Chinese script morphology, or Al_6(Mn, Fe). These phases control grain size of recrystallised grains as well as strengthening the material (Alexander and Greer † (2004)).

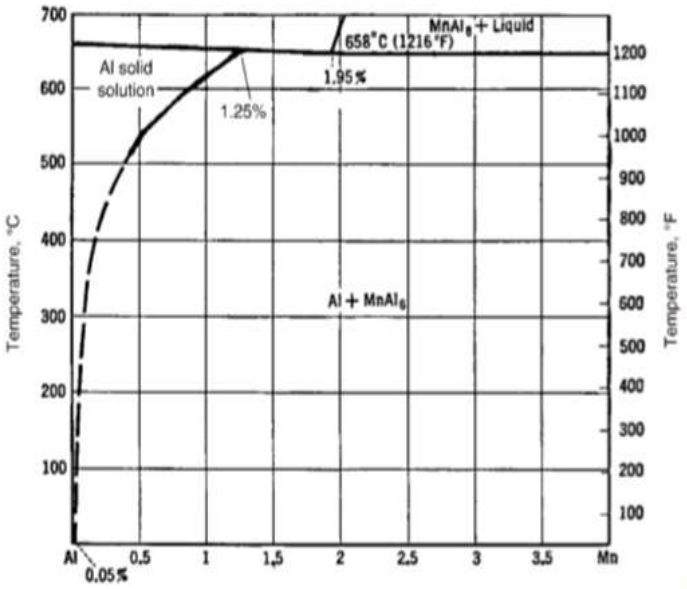

Figure 14 - Aluminium corner of the Al-Mn phase diagram. Adapted from Okamoto (2002).

2.2.1.3 Silicon

In most aluminium series (excluding 4xxx and 6xxx alloys) silicon, Si, is, with iron, a common impurity. Cáceres, Svensson, and Taylor (2003) state that in low silicon contents, iron forms the needle like, monoclinic Al_3Fe phase, however, as silicon content increases two additional phases are formed; α-(Al_8Fe_2Si) and β-(Al_5FeSi) (see Figure 15) – Chinese script and platelet in nature respectively. Cáceres, Svensson, and Taylor (2003) do not give specific values for how low the silicon content was, nor the value silicon rises to. However, in 4xxx series alloys silicon is the primary alloying element in contents of 0.8-13.5 wt% to form materials with good corrosion resistance. Figure 16 shows the binary phase diagram of Al-Si, where it is presented that the eutectic point does not occur until Si content reaches 12.6 wt% at 577 °C. Here, as the silicon content is higher, the β-(AlFeSi) phase is present in the form of precipitates with needle morphology (Hatch, Aluminum Association, and American Society for Metals (1984); Mondolfo (1976)).

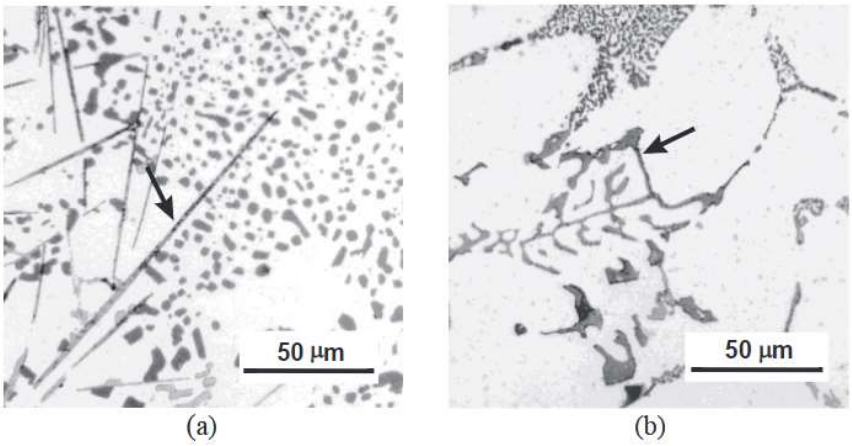

Figure 15 - Phases present in Al-5Si-1Cu-0.5Mg-(Fe) alloy. a) β-(Al_5FeSi) platelets b) α-(Al_8Fe_2Si) script. (Taylor (2012)).

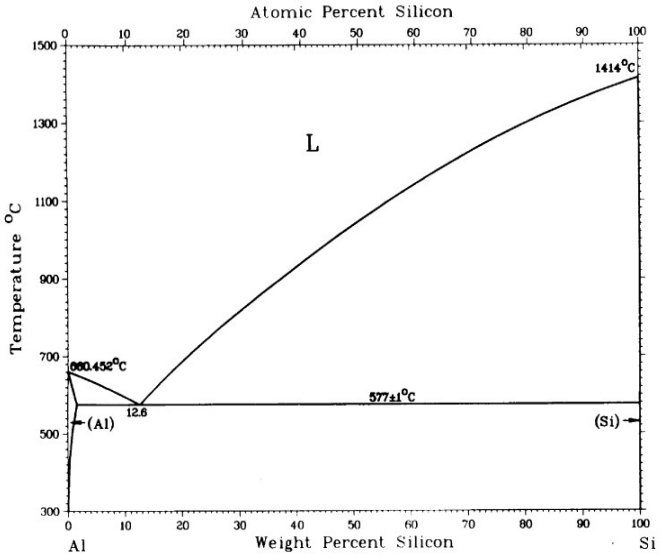

Figure 16 - Al-Si phase diagram (Okamoto, Schlesinger, and Mueller (2016)).

2.2.1.4 Magnesium

The addition of magnesium as a lone primary alloying element forms the basis of the non-heat treatable 5xxx series. The phase diagram, seen in Figure 17, shows that Al_3Mg_2 is formed below the solvus temperature. 5xxx series alloys contain between 0.8-5.6Wt% Mg. The phase diagram therefore suggests that the upper limit before the material becomes an aluminium solid solution is ~300 °C for the highest Mg content of

5xxx however for lower contents a change of phase occurs at a much lower temperature.

The phase Al_3Mg_2 is typically found outlining grains and is round and compact in morphology. Like the aluminium matrix, the phase follows an FCC crystalline structure. This phase forms the β-phase of the alloy AA5083 and is covered in greater detail in section 2.2.3.

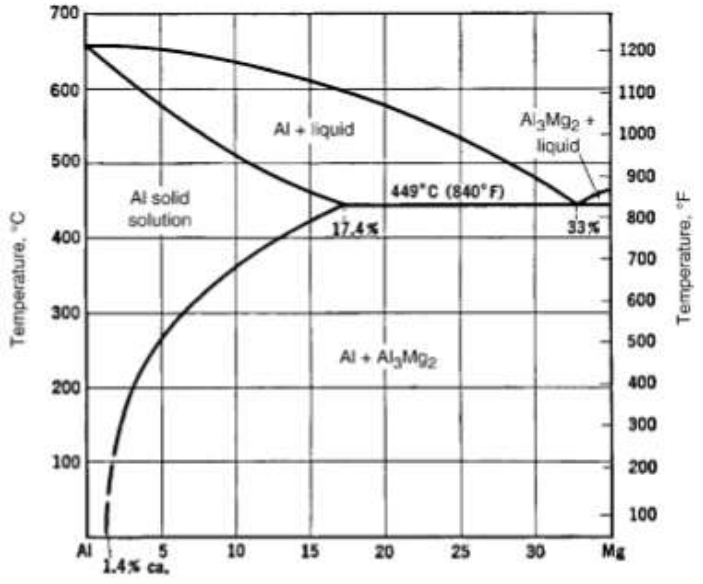

Figure 17 - Aluminium end of the Al-Mg phase diagram. Adapted from Massalski, Okamoto, and ASM International (1990).

2.2.1.5 Magnesium and silicon

Magnesium and silicon are both present individually as primary alloying elements in some aluminium alloy series as well as being present as second phase constituents or impurities in other series, for example silicon's presence in AA5083 (an Al-Mg alloy). However, the two are primary particles in the formation of the heat treatable 6xxx series. Al-Mg-Si alloys are strengthened through the precipitation of Mg_2Si. In alloys with low magnesium content, silicon is commonly a secondary phase in addition to small amounts of Mg_2Si constituents. As magnesium is increased less silicon particles

are present until enough magnesium is added to form Mg_2Si constituents only. This phase, comprising of 63.2 wt% magnesium and 36.8 wt% silicon, looks Chinese script like in nature and follows the FCC crystal structure, aluminium. Figure 19 shows that when viewed under an optical light microscope this phase can be differentiated from other Chinese script phases present such as $Al_8FeMg_3Si_6$ due to the blue colour that it adopts.

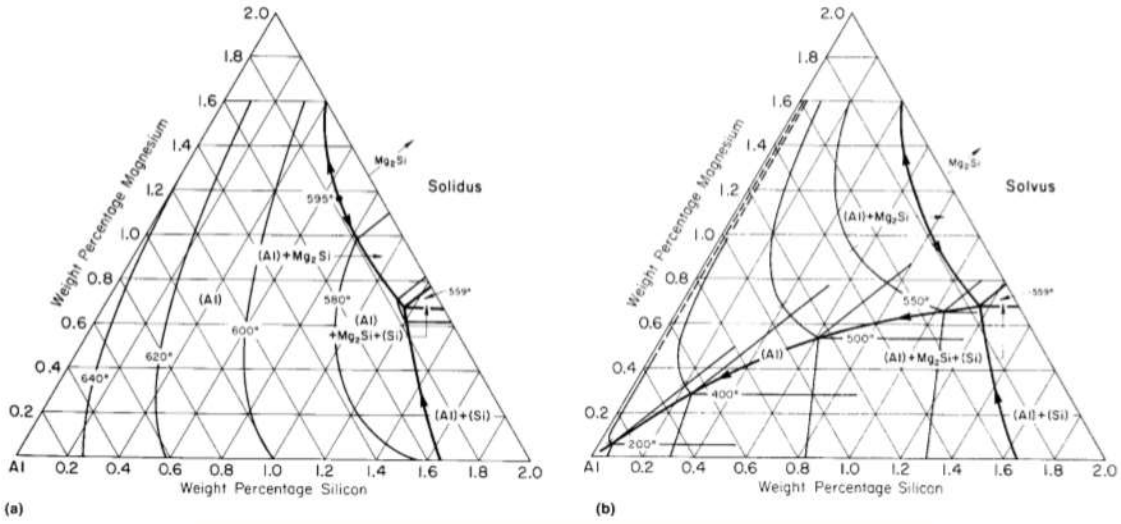

Figure 18 - Al-Mg-Si ternary phase diagram. a) Solidus projection. b) Solvus projection (Lyman (1973)).

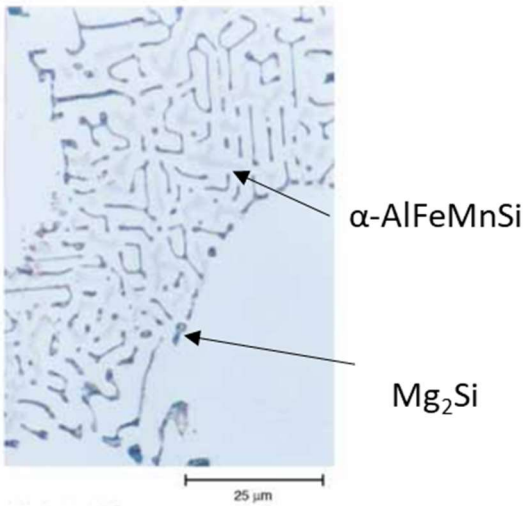

Figure 19 - Mg_2Si (Blue) + α-AlFeMnSi (Grey) phases present in AA5083 (Vander Voort (2004)). Etched in 0.5 mL HF (40%) and 100 mL H_2O for 5 seconds.

2.2.1.6 Magnesium and zinc

On its own zinc, Zn, offers little benefit, conferring inconsequential solid solution strengthening or work hardening. However, by adding either or both of copper and magnesium it is possible to form heat treatable alloys discernible by high strength (~400-600 MPa (Anderson, Weritz, and Kaufman (2019a))). When just magnesium is added, two phases are present: $MgZn_2$ and $Al_2Mg_3Zn_3$. $MgZn_2$ are round in morphology and J.-T. Liu et al. (2016) states that the phase forms a lamellar structure within the aluminium matrix. Figure 21 shows MgZn2 within AA7056. The addition of copper to the Al-Zn-Mg matrix substitutes aluminium and copper for zinc in the $MgZn_2$ phase, forming $Mg(Zn, Cu, Al)_2$.

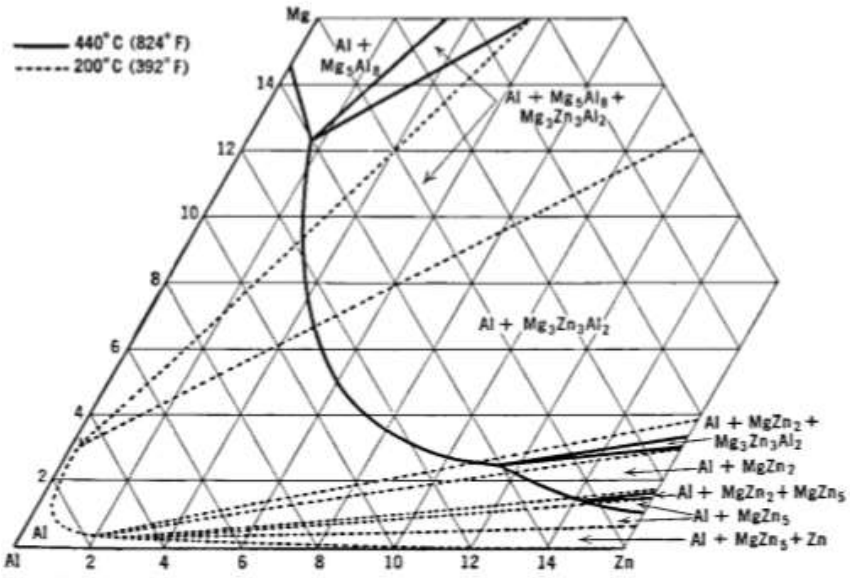

Figure 20 - Aluminium corner of the Al-Mg-Zn ternary phase diagram detailing solid solubilities of various phases (Mondolfo (1943)).

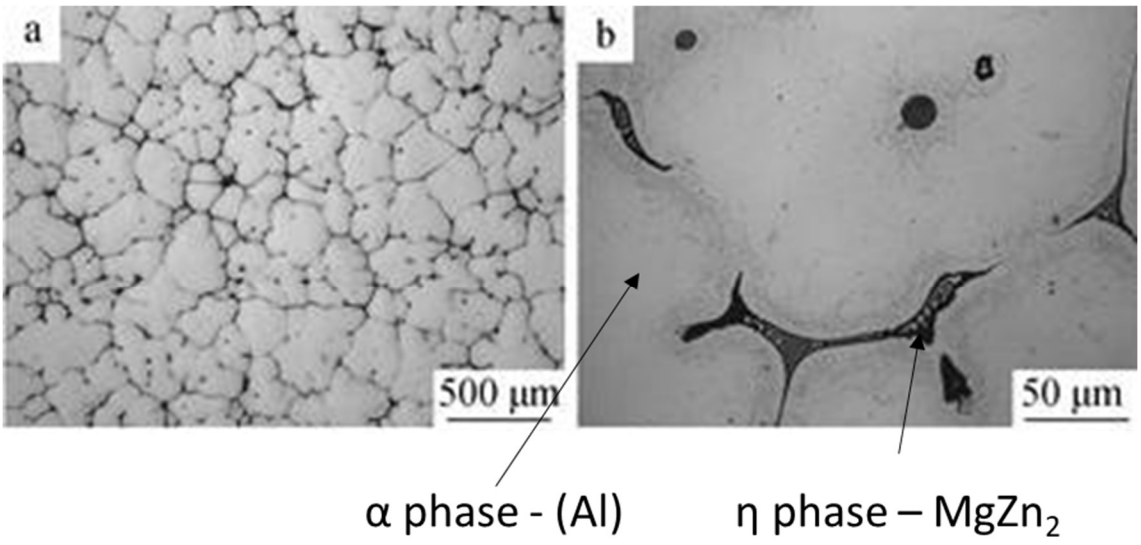

Figure 21 - Optical images of as-cast alloy 7056 with different magnifications (J.-T. Liu et al. (2016)).

2.2.2 Second-phase Structure

Second-phase particles are divided into four classes based upon their mode of formation and their ability to be dissolved (Vander Voort (2004)). These are primary particles, constituents, dispersoids and precipitates. Primary particles are the solid phase which separates first from melted material while constituents, which are widely considered not to be beneficial, are described by Vander Voort (2004) as either intermetallic compounds or metal crystals that form during solidification of hypoeutectic alloys. Their size can range from several micrometres to tens of micrometres.

Dispersoids, such as manganese, zirconium or chromium, form in solid-state precipitation during ingot preheating or thermal heat treatment and tend to have a limited solubility (1.25 wt%, 0.28 wt% and 0.77 wt% respectively) in solid aluminium. Dispersoids play an important role in providing dispersion strengthening, however, this is not the only significant role they have. Ou, Yang, and Wei (2007) state that the size of dispersoids in wrought alloys also help to control the degree of recrystallisation, recrystallised grain size and crystallographic texture in addition to offering significantly more dispersion strengthening in non-heat treatable alloys, such as 3xxx and 5xxx, than in heat treatable alloys (Vander Voort (2004)). In more modern 7xxx series alloys

zirconium is present which forms the dispersoid Al_3Zr while previously the phase $Al_{12}Mg_2Cr$ would be present. This dispersoid exhibited incoherent interfaces, which nucleate to form $MgZn_2$ during quenching thus losing potential to develop into high strength alloys after slow quenching.

The final second-phase particle are precipitates. These can be formed during any thermal operation under the solvus temperature (The temperature under which a solid solution is homogenous instead of multi phased stated by Callister and Rethwisch (2008)). Precipitates should dissolve fully in a properly solution heat treated environment however can reform depending on the quench rate and alloy composition at grain boundaries. Coarse precipitates do not contribute to the age hardening and can negatively impact properties such as ductility and fracture toughness.

2.2.3 Non-heat treatable alloys

Aluminium alloy grades: 1xxx, 3xxx, 5xxx and most 4xxx grade alloys are not heat treatable and are instead strengthened from solid solution formation, strain hardening, grain size control and second-phase microstructural constituents such as dispersoids. These grades of alloy contain elements such as manganese, magnesium, or silicon as the main functional elements.

The 5xxx series adheres to an Al-Mg system consisting primarily of aluminium and anywhere between 0.8-5.6 wt% of magnesium. The magnesium is alloyed with the aluminium through solid solution, the process of alloying additional elements with a metal matrix to cause a variation in the shear modulus and can be further strengthened by work hardening. Transition elements, such as chromium or manganese, are also often added along with magnesium to contribute to strengthening the material as these elements, according to Anderson, Weritz, and Kaufman (2018b), allow the formation of complex precipitates, $Al_{18}Mg_3Cr_2$ and Al_6Mn, that retard grain growth during re-heating and assist in grain refinement during rolling.

Retardation of grain growth involves rapid solidification and cooling during casting of ingots such that a solid solution state is formed with concentrations of Mn and/or Cr that greatly exceeds their equilibrium solubility. During reheating for the processing of the material, the supersaturated metastable solid solution is designed to cause solid-state precipitation of complex phases. This is designed to produce finely dispersed particles that inhibit recrystallization and grain growth. The smaller grains that subsequently occur, with their increased number of different directional grain boundaries, improve the strength by reducing the ease with which slip can occur across the structure.

Iron and silicon impurities are frequently present in the form of intermetallic particles, to such an extent that Scamans, Holroyd, and Tuck (1987) and Lucadamo et al. (2006) claim that iron-rich particles are one of the main types of intermetallic particles present in AA5083. The presence of iron reduces the strengthening effect of the transition elements, manganese and chromium, as it readily forms insoluble, more brittle compounds that are prone to cracking during future processing as discussed by Anderson, Weritz, and Kaufman (2018b). The presence of silicon also has a negative effect as it will form Mg_2Si which subsequently reduces the plasticity of the metal. This is because there is an excess of magnesium over the required amount to form the phase which sharply reduces the solid solubility of the compound (Anderson, Weritz, and Kaufman (2018)).

The precipitation sequence of AA5083 is detailed by Yan and Hodge (2017) as being:

$$\alpha_{SS} \rightarrow GP\ zones \rightarrow \beta'' \rightarrow \beta' \rightarrow \beta$$

The precipitation of the β phase (Al_3Mg_2) nucleates from β', a semi-coherent phase which itself nucleates from β'' (Al_3Mg). β phase consists of between 34.8-37.1 wt% magnesium and is the equilibrium phase of the sequence, pictured in Figure 22 (Goswami et al. (2010)). The arrows present in Figure 22a identify Mg-rich (β phase) precipitates forming on pre-existing Mn-rich precipitates.

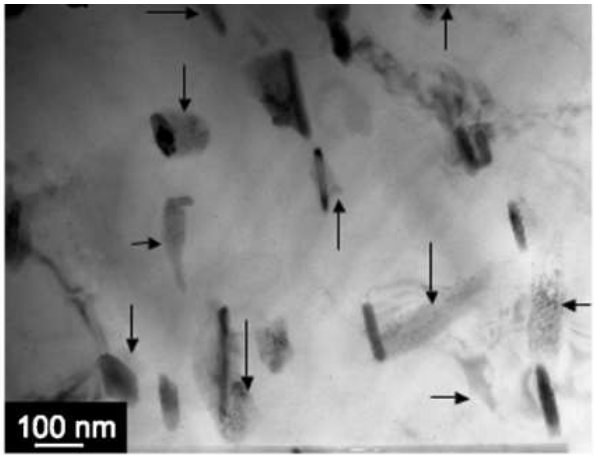

a) β phase present on an existing Mn-rich particle.

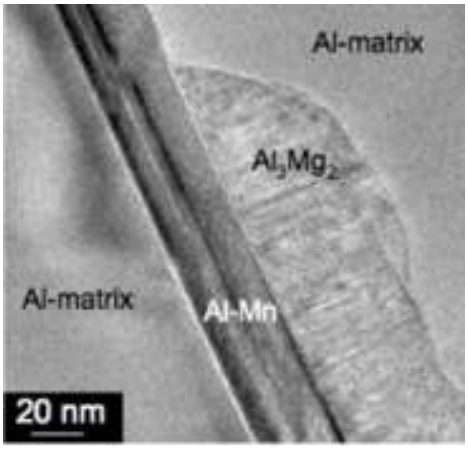

b) β phase formed on rod-like Al-Mn particle.

Figure 22 – β phase present in an Al-Mg alloy (Goswami et al. (2010)).

Vander Voort (2004) describe the phase as compact and round outlining grain boundaries, however Yan and Hodge (2017) showed that the β phase can also form on dispersoids. The β phase was identified on dispersoids of Al_6Mn and near to Al_6(Mn, Fe) dispersoids connected by dislocations which assisted in the nucleation and growth of the β phase by reducing the free energy barrier to nucleation through a reduction in the total strain energy. Yan and Hodge (2017) also showed that the β phase formed on grain boundaries, shown in Figure 23. However, it was observed that the β phase only formed on grain boundaries with high angles and that the driving force of precipitation at these sites was proportional to the reduction in the Gibbs free energy (Murr et al. (2009)).

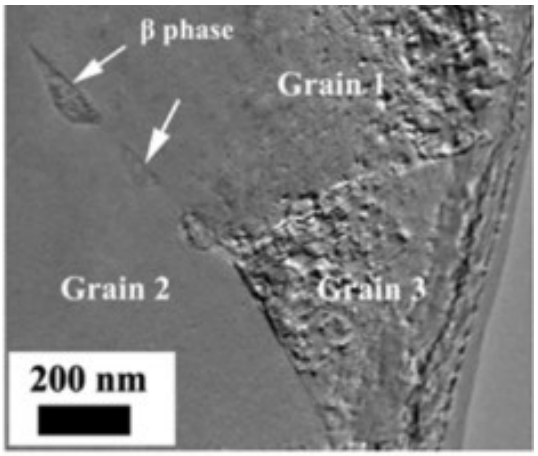

Figure 23 – β phase present at grain boundaries in AA5083 (Yan and Hodge (2017)).

2.2.4 Heat treatable alloys

In contrast, aluminium alloy grades; 2xxx, 6xxx, 7xxx as well as many 8xxx grade alloys are heat treatable. These grades of alloy contain elements such as; copper, magnesium, silicon and/or zinc as the main functional elements (Anderson, Weritz, and Kaufman (2018)). Chromium is a common addition to the primary elements within many alloys both non-heat treatable and heat treatable, including 6xxx and 7xxx series grades. In non-heat treatable grades chromium dispersoids contribute to strength while in heat treatable alloys it can control grain size and the degree of recrystallization.

In the heat treatable 6xxx series, which follows an Al-Mg-Si system, strengthening occurs from the formation of magnesium silicide (Mg_2Si), contrary to the effects of this phase in 5xxx series alloys. This compound forms a quasi-binary eutectic with the aluminium in solid solution. At the eutectic temperature, Mg_2Si has a solubility of 1.85% however this reduces to 0.1% at room temperature (20 °C). The ratio of Mg:Si is critical to the ageing process. Although according to Kerins, (n.d.) the maximum strength levels of ageing are achieved at a ratio closer to 1:1 rather than 2.0 for 'dilute 6xxx alloys', in solute-rich alloys, such as 6082, the maximum strengthening effect of the phase is achieved at a ratio of 1.73 (Benedyk, (n.d.)). Other phases that have been identified in 6xxx series alloys contain the impurity, iron. α-Al(FeSi) and β-AlFeSi both commonly form in 6xxx series alloys. Figure 24 shows the morphology of both phases, suggesting that the alpha phase is 'Chinese script' while the monoclinic beta phase is described as sharp needles.

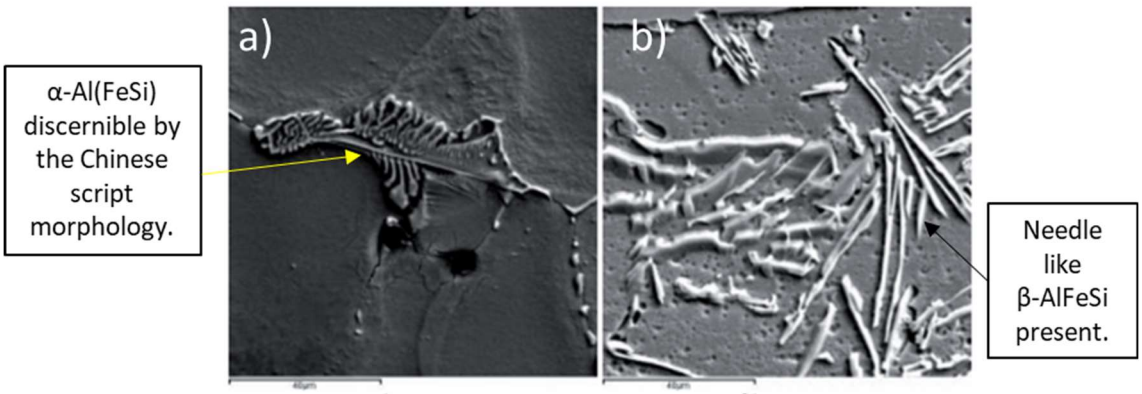

Figure 24 - a) α-Al(FeSi) phase, discernible by the Chinese script morphology. b) β-AlFeSi phase identified by the needle like morphology (Rosefort et al., (n.d.)).

The precipitation sequence for 6xxx series alloys is detailed below;

$$\alpha_{SS} \rightarrow (Mg) + (Si) + (Si, Mg) \rightarrow GP\ zones\ \rightarrow\ \beta'' \rightarrow \beta' \rightarrow \beta(Mg_2Si)$$

At ~70-90 °C early GP zones of Mg and Si are formed. Independent clusters of silicon and magnesium begin to form as well as clusters of both silicon and magnesium together as the temperature and time increase to 150-200 °C and 2 hours. The clusters tend to be platelets or spherical in shape (Totten (2016)). This is followed by the formation of GP zones, descendible by the short needles of no more than 6nm that make these zones up. GP zones form after short periods of artificial ageing (~150-200 °C), usually up to 20 minutes in duration.

Longer exposure to artificial ageing, between 2-30 hours, results in the β'' phase, which is the main strengthening phase of 6xxx series alloys, forming from the GP zones. It was thought that β'' consisted of Mg and Si in a ratio of 5:6 (Andersen et al. (1998)), however, work conducted in the early 21st century has proven that Si is partially replaced by Al (Ninive et al. (2014); Hasting et al. (2009)). This leads to a phase that can be any of the following compositions: Mg_5Si_6, $Mg_5Al_2Si_4$ and $Mg_4Al_3Si_4$.

By continuing the ageing process for a longer period or by elevating the temperature further to above 250 °C, over aging and coarsening of precipitates will occur. The β'' phase evolves into the β' phase which has a composition of $Mg_{1.8}Si$ and forms rod like precipitates of up to 500 nm long. Where the alloy has an excess of Si – a trait very common within engineering alloys – the precipitation sequence is modified so that an additional three precipitate types are formed before equilibrium can be reached (Totten (2016a)). These are identified as A, B and C or U1, U2 and B' depending on the source reviewed (Totten (2016a); Matsuda et al. (2000)). Sigmund J. Andersen et al. (2010) showed that these precipitates share a common silicon rich structure. The semi coherent, orthorhombic phase U2, $Al_4Mg_4Si_4$, precipitates first. As this phase is orthorhombic, meaning the lattice has resulted from stretching the cubic lattice along two of its orthogonal pairs by different factors, it forms rods a few micrometres in length. Following U2 comes U1, a hexagonal crystalline structured phase that forms rods of 50-500 nm in length, consisting of Al_2MgSi_2. The final metastable precipitate to form in silicon rich Al-Mg-Si alloys is B'. This phase also has a hexagonal crystalline structure and rod-like morphology. B' commonly forms as $Al_3Mg_9Si_7$.

In the instance of a silicon rich Al-Mg-Si alloy, the β' section of precipitation sequence above can be modified as below;

$$\dots \rightarrow \beta' \rightarrow U2 \rightarrow U1 \rightarrow B' \rightarrow \beta$$

The final stage of the precipitation sequence is the equilibrium phase, β. With a composition of Mg_2Si and platelet morphology, this phase only forms when the material has been annealed, typically at ~400 °C (Totten (2016b)) and is associated with low strength. Where the alloys are silicon-rich, it has also been observed that silicon only precipitates can form during this stage of the sequence.

In 7xxx Al-Zn-Mg-Cu alloys, several phases have been identified that occur in Al-Zn-Mg-Cu alloys as a function of precipitation sequences.

Four precipitation sequences have been identified and are described in the following paragraph:

$$\alpha_{SS} \rightarrow S$$

$$\alpha_{SS} \rightarrow T' \rightarrow T$$

$$\alpha_{SS} \rightarrow Vacancy - rich\ cluster\ \rightarrow GP\ zone \rightarrow \eta' \rightarrow \eta$$

$$\alpha_{SS} \rightarrow \eta$$

In the first precipitation sequence, the S phase, Al_2CuMg (shown in Figure 25), is precipitated directly from the supersaturated solid solution. This phase is a coarse intermetallic that is insoluble in typical Al-Zn-Mg-Cu alloys at 465 °C. In the second precipitation sequence, an intermediate, semi-coherent phase T' occurs in the decomposition of the supersaturated solid solution Al-Mg-Zn-Cu, when artificially ageing at 115-130 °C. This will precipitate in place of η when the alloy is high in Mg (Bigot et al. (1997)). Further in the second precipitation sequence at temperatures above 200 °C, the incoherent, equilibrium T phase forms which can increase hardness (Bergman, Waugh, and Pauling (1957)). In general, the T' and T phases are not too different compositionally – the phase T has been identified as a low quantity phase of $Mg_{32}(Al, Zn)_{49}$ even though commercial heat treatments up to 150 °C lay in the Al + $MgZn_2$ + $Mg_{32}(Al, Zn)_{49}$ phase field.

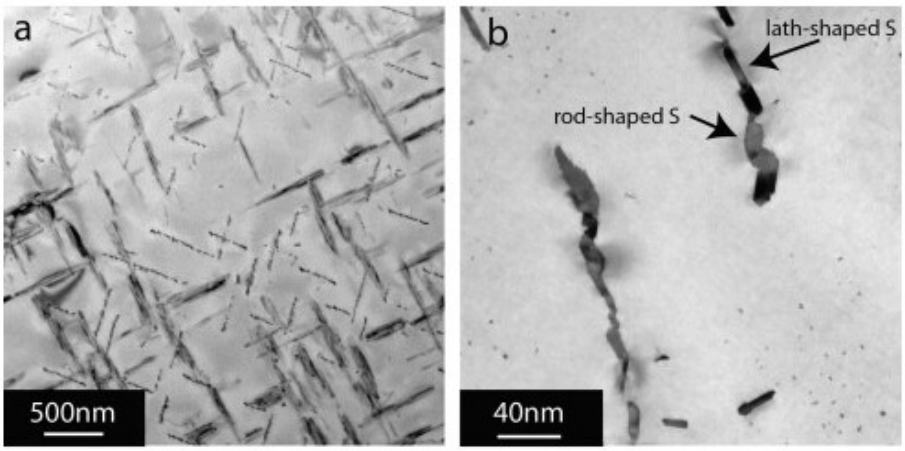

Figure 25 - Al_2CuMg phase present in A7050 (Styles et al. (2012)).

In the third precipitation sequence, the supersaturated solid solution decomposes into coherent, cigar shaped clusters and early-stage GP zones, GP zone I, as the ageing temperature reaches 120 °C. As the clusters grow their composition, which had previously consisted of Al, Cu and large amounts of Mg, changes to 'equiatomic' (Sha and Cerezo (2004)). This stage of the sequence dominates for about 60 minutes (at 120 °C) of the artificial ageing, the peak density of this stage occurring after 30 minutes. In this sequence GP zone II is not observed, instead elongated and larger zinc rich GP zone I are formed for up to 24 hrs.

The main strengthening phase for this precipitation sequence is the metastable η'. This phase is found after just a few hours of artificial ageing at 120 °C, identifiable by the platelet like morphology. Typically, η' is composed of $Zn_{1.3}Mg$ and is semi-coherent to the FCC structure of the aluminium. After a further 24 hrs the first indications of the equilibrium stage, η, are visible. This stage contributes little hardening effect, forms on or from η' and is discernible by a thick plate (up to 8 nm thick) like morphology. In the last sequence, under very slow cooling, the equilibrium precipitate $Mg(Zn, Cu, Al)_2$ is formed on grain boundaries and in the interior of the grains and sub grains (Anderson, Weritz, and Kaufman (2018)).

2.2.5 Heat treating process

Only through age hardening can heat treatable aluminium alloys be made useful in applications where high loads will be experienced. Age hardening is a strengthening process where the formation of precipitates is used to restrict dislocation slip. Precipitates of a different phase from the matrix provide strong obstacles against dislocation motion. However, the continued growth of precipitates at an elevated temperature can have a detrimental impact on the properties of the material. This process is called 'over aging'. The increased precipitate size and spacing results in the dislocations bypassing them to progress through the material, consequently the material is weaker.

The process of precipitation hardening occurs in three steps, as shown in Figure 26:

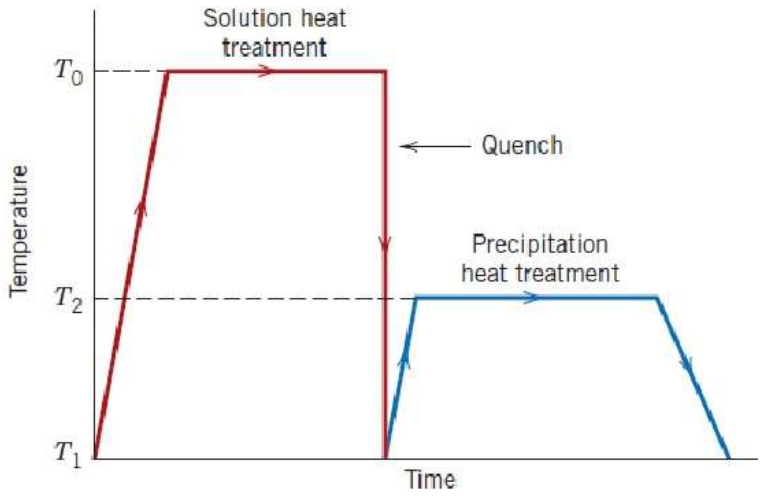

Figure 26 – Schematic of temperature vs time for precipitation hardening Callister and Rethwisch (2014).

1. **Solution treatment**: The metal is heated to a high temperature (typically 465-565 °C) within a single-phase region to dissolve & disperse the alloying elements in the matrix.

2. **Quenching**: The aluminium alloy is rapidly cooled using water or oil to take the temperature to a two-phase region (i.e. from solution temperature to room). This is done to preserve a supersaturated solid solution of alloying elements in the host

metal (Totten and MacKenzie (2016)). The rate of quench is important in controlling precipitation growth. By cooling too slowly the temperature is allowed to remain elevated for longer and the nucleation rate is low which means that precipitates are well spaced (see Figure 27a) – allowing dislocations to pass through easier resulting in a soft metal (Callister and Rethwisch (2014)). By cooling quickly the precipitate distribution is much finer as the temperature is forced down resulting in a high nucleation rate and small closely packed precipitates which prevent dislocation slip resulting in a harder metal, as illustrated by Figure 27b.

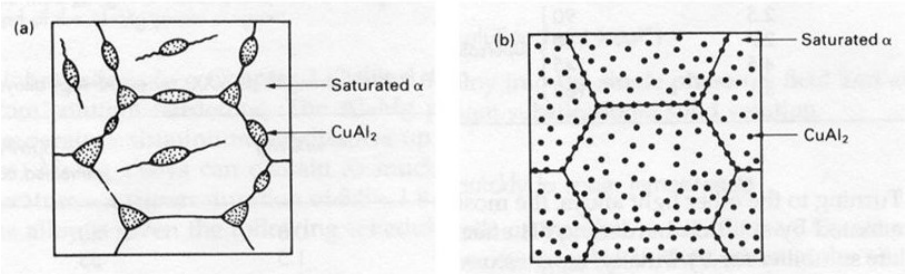

Figure 27 - Precipitate structure following a) slow cooling b) rapid cooling - Callister and Rethwisch (2014).

3. **Age-hardening**: The material is reheated to an intermediate temperature or left at room temperature, for naturally ageing, to convert the supersaturated solution to finely dispersed precipitate particles.

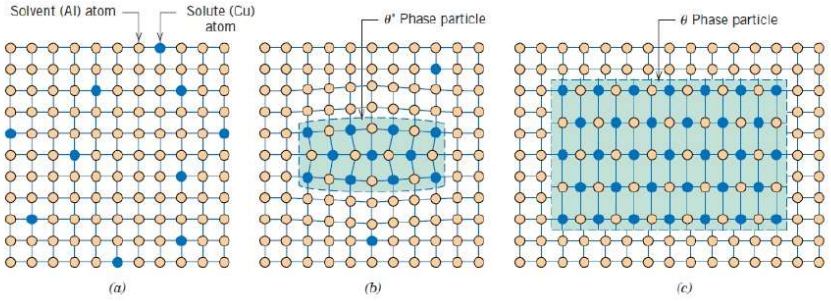

Figure 28 - Schematic depiction of several stages in the formation of the equilibrium phase. a) Supersaturated α solid solution. b) A transition, θ, precipitate phase. c) The equilibrium θ phase, within the α-matrix phase. (Callister and Rethwisch (2014)).

During the ageing process, the solid solution decomposes into multiple phases as dissolved atoms start to diffuse within the aluminium matrix. The first stage of this results in clusters of solute atoms which maintain coherence with the face-centre cubic (FCC) crystallographic structure of the aluminium, however, due to the volumetric difference of the atoms a strain is put on the lattice structure which hinders the movement of dislocations and consequently improves the strength of the material (Mondolfo (1976); Totten (2016)). As the ageing process continues solute clusters continue to evolve into other precipitates, the crystallographic structures of which may differ too much from the aluminium matrix and therefore become semi- or incoherent. At this point the maximum strength is reached (Mouritz (2012)). Eventually, if age-hardening is maintained at an elevated temperature, then over-ageing is a risk. This mechanism is when the incoherent precipitates and space between them exceed a threshold above which dislocations bow and pass the precipitates reducing the strength and hardness of the material.

The heat treatment process is identified in material certificates by the designation – 'T'. This means the material has been thermally treated with or without additional strain hardening to produce a stable temper. The 'T' is always followed by digits to further identify the heat treatment process as per ISO 2107:2007, as detailed in Table 3.

Temper	Description
T1	Cooled from elevated temperature shaping process and naturally aged.
T2	Cooled from elevated temperature shaping process, cold worked and naturally aged.
T3	Solution heat treated, cold worked and naturally aged.
T4	Solution heat treated and naturally aged.
T5	Cooled from elevated temperature shaping process and artificially aged.
T6	Solution heat treated and artificially aged.
T651	Solution heat treated, stress relieved by stretching a controlled amount and artificially aged. The products receive no further straightening after stretching.
T7	Solution heat treated and stabilized.
T74	Solution heat treated and artificially overaged (between T73 and T76).
T7451	Solution heat treated (3 to 6 hours at 120 °C followed by 24 to 30 hours at 165 °C), stress relieved by stretching a controlled amount and artificially overaged (between T73 and T76). The products receive no further strengthening after stretching.
T8	Solution heat treated, cold worked, and artificially aged.
T9	Solution heat treated, artificially aged, and cold worked.

Table 3 - Temper designations for heat treatment ('Understanding the Aluminum Alloy Designation System' (n.d.)).

2.2.6 Natural ageing

Natural ageing is the ageing process in which the material sees changes to the microstructure as a result of being exposed to ambient temperature. This only affects aluminium alloys susceptible to heat treatment. Generally, the properties obtained by natural ageing are of such inferior quality to those obtained by artificial ageing (AA) that the process is of little industrial importance on its own. However, natural ageing is also almost unavoidable after quenching which does impact the subsequent AA. On several occasions, clusters of tens of atoms have been observed in Al-Mg-Si alloys, during and after quenching. These clusters have been identified as Mg, Si and (Mg+Si)

(Murayama et al. (1998)), however no consistent picture can be drawn regarding clusters of only Mg or Si and Serizawa, Sato, and Poole (2010) suggest that after quenching either no clusters or co-clusters of (Mg+Si) are detected but no single element clusters.

In Al-Mg-Zn-Cu alloys the effect of natural ageing is very pronounced. Sha and Cerezo (2004) stated that 90 minutes after quenching AA7050 exhibited signs of clusters of 30 atoms, comprising of $Zn_{0.85}Mg$, and that the natural ageing process can continue for years in these alloys. Sha et al (2004) suggest the clusters are shapeless, coherent and nucleate homogenously. It was shown that as natural ageing continued spherical GP zones formed where the ratio Zn:Mg ~1.0 resulting in higher electrical resistivity and hardness which increased proportionally with the volume fraction of the GP zone.

The influence of natural ageing in 7xxx series alloys is limited. Regardless of the duration of natural ageing, the strengthening phase η' will never precipitate below 70 °C and therefore any improvements to the strength will be capped. The η' phase can be formed from naturally aged material if it is subsequently heated above 100 °C, above this temperature the natural aged precipitates dissolve in the matrix – this process is called reversion (Ungar et al. (1979)).

2.2.7 Mechanical behaviour of Aluminium alloys

The mechanical properties are a fundamental factor in the choice of any material for a given application. For example, in the aerospace industry properties such as tensile strength, fracture toughness, fatigue resistance and corrosion resistance are all safety critical for structural components. These mechanical properties are governed by principle microstructural features, as discussed by Polmear et al. (2017), such as;

1. Coarse intermetallic compounds
2. Smaller submicron particles formed during homogenization
3. Fine precipitates
4. Grain size & shape
5. Dislocation substructure
6. Crystallographic textures

2.2.7.1 Tensile properties.

Broadly, aluminium alloys range in tensile strength from 70 to 550 MPa depending on the grade and condition. High strength aluminium alloys, such as 2xxx and 7xxx, balance strength and weight to provide materials highly sort after in sectors such as the aerospace industry. These alloys offer strength greater than some Steels but at a significantly reduced weight. Tensile properties, notably ductility, are greatest in the longitudinal direction & least in the transverse direction in which stressing is normal to the stringers or intermetallics. Tensile strength is an important property to consider in the design of a component; however, it should not be the sole parameter for material selection. Other factors such as fatigue life and susceptibility to corrosion are also critical in the selection of the correct material for a given application.

In aluminium alloys yield and tensile properties are improved through the dispersion of fine precipitates which are 'dominant' in inhibiting dislocation motion (Polmear et al. (2017)). Whereas the microstructural feature ‘coarse intermetallic compounds’ is ineffectual with regards to both yield and tensile strength. Although this feature can have a marked loss on ductility which is noticeable in both wrought and cast alloys. Ductility and strength are often traded off, though a combination of the two is often desired in structural components (Anderson, Weritz, and Kaufman (2019)). Particles may crack at small plastic strains forming internal voids which can, under the action of further plastic strain, coalesce leading to premature fracture.

2.2.7.2 Fracture toughness

Fracture toughness, defined as a materials ability to resist fracture, is in many design applications a fundamental property. Toughness is measured in units of energy and therefore it can be argued that a brittle material does not absorb much energy, while a ductile material requires a large amount of energy during the fracture process (Hertzberg (1996)). High toughness is achieved through optimising high strength and ductility, either property alone (i.e. just high strength or excellent ductility) does not produce a material with a large fracture energy absorption (Hertzberg (1996)).

Coarse intermetallic compounds, typically containing impurities like iron and silicon, form preferential crack paths reducing the fracture toughness of the material (Hahn and Rosenfield (1975)). As such, a common approach to improve toughness in high strength alloys is to reduce the iron and silicon content and thus reduce the volume of compounds such as Al_6(Mn, Fe) and Al(FeMnSi). An example of where this has been implemented is the introduction of AA7475, a higher purity alloy based on the pre-existing alloy AA7075. Compared to its predecessor (which contained Fe<=0.50 wt%, Si<= 0.40 wt% ('Aluminum 7075-T6; 7075-T651' (n.d.))), AA7475 contains approximately 75% less Fe and Si (Fe<=0.12 wt%, Si<=0.10wt% ('Aluminum 7475-T7351', (n.d.))) and improves the fracture toughness by maintaining a high strength to density ratio (Gao (2011); Kim (2013)).

Fine precipitates and dispersoids also have an influence on the fracture toughness. J. Wang (2020) suggests that for 'superior toughness' the number of dispersoid-forming elements, such as chromium, zirconium and manganese, should be limited to the minimum required for control of grains and resistance stress-corrosion cracking. Figure 29 shows the detrimental effect of increasing chromium content on the toughness of a 7xxx series alloy. Fine precipitates have the primary function to strengthen the material but changes to the composition of these, in particular the quantity of magnesium, can produce significant effects on toughness. As discussed in section 2.2.4, the phases of 7xxx series alloys are; S (Al_2CuMg), T ($Mg_{32}(Al, Zn)_{49}$) and η ($Mg(Zn, Cu, Al)_2$). If these phases are not fully dissolved into solution, Wang (2020) intimates

the initiation of crack propagation can be enhanced and thus reducing the toughness of the material.

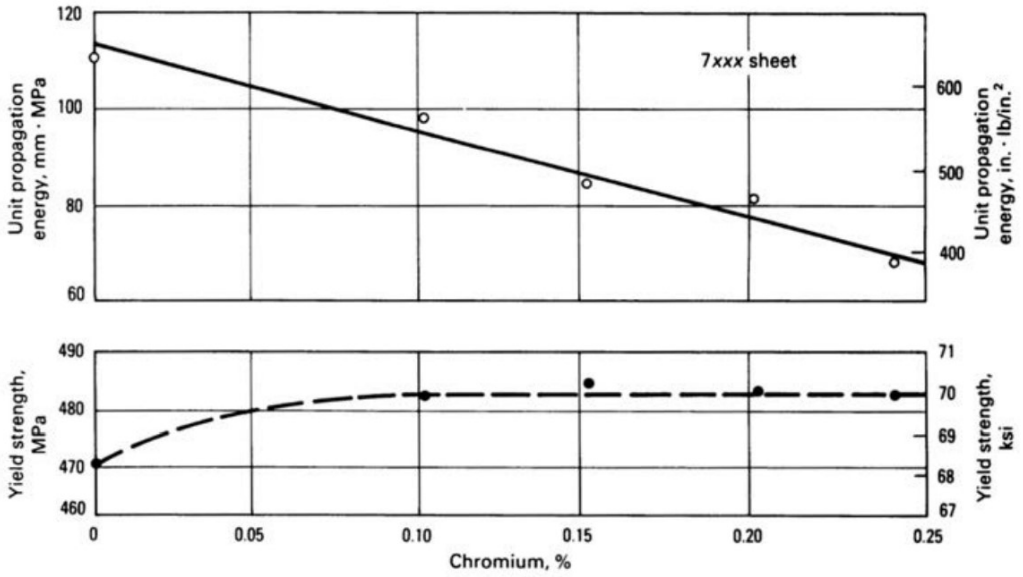

Figure 29 – Effect of chromium on fracture toughness in a Al-Zn-Mg-Cu alloy (J. Wang (2020)).

Bucci (1979) presented data on the fracture toughness of a range of heat-treatable materials with various tempers, shown in Figure 30. From their work it is clear that different heat tempers had a significant impact on the toughness of the material which is supported by the information mentioned in section 2.2.5 regarding precipitates growth at elevated temperatures.

Product	Alloy	Temper	Yield strength(a)		Plane-strain fracture toughness, K_{Ic}					
					L-T		T-L		S-L	
			MPa	ksi	MPa$\sqrt{m}$	ksi$\sqrt{in.}$	MPa$\sqrt{m}$	ksi$\sqrt{in.}$	MPa$\sqrt{m}$	ksi$\sqrt{in.}$
Plate	2014	T651	440	64	24	22	22	20	19	17
	2024	T351	325	47	36	33	33	30	26	24
	2024	T851	455	66	24	22	23	21	18	16
	2124	T851	440	64	32	29	25	23	24	22
	2219	T851	435	63	39	35	36	33	...	...
	7050	T73651	455	66	35	32	30	27	29	26
	7075	T651	505	73	29	26	25	23	20	18
	7075	T7651	470	68	30	27	24	22	20	18
	7075	T7351	435	63	32	29	29	26	21	19
	7475	T651	495	72	43	39	37	34	32	29
	7475	T7651	460	67	47	43	39	35	31	28
	7475	T7351	430	62	53	48	42	38	35	32

Figure 30 - Typical room-temperature yield strength and fracture toughness values for various high strength aluminium alloys (Bucci (1979)).

2.2.7.3 Fatigue

Fatigue failure is the effect caused by alternating or cyclic loading at a load lower than the ultimate tensile strength - by applying a cyclic load a crack can be grown which will eventually lead to failure. As a result of fatigue, it has been shown that the initiation of cracks normally occurs on the surface of the material. At these sites the strain becomes localized due to the presence of pre-existing stress concentrations such as corrosion pits, coarse slip bands or relatively soft zones such as precipitate free regions adjacent to the grain boundaries (Polmear et al. (2017)). Stress concentrations can also result from deliberate features such as a fillet weld or a rivet hole.

Fatigue, like all mechanical properties, is influenced by microstructural features. One in particular is the dispersion of precipitates within the alloy. If the precipitates are round, small and evenly distributed then fatigue life is increased with precipitation hardening. However, not all features improve fatigue life. Potential differences between the base (aluminium) and second-phase particles can create corrosion cells which can accelerate fatigue (Chan (2010); Kamp et al. (2007)).

In age-hardened aluminium alloys the fatigue properties are considered generally disappointing stemming from the metastable nature of the metallurgical structure under cyclic loading. Strain is then localized in this area which is particularly harmful because the precipitates may be removed from important slip bands which can cause softening and lead to a further concentration of stress and acceleration of crack growth. Consequently, the fatigue behaviour of age-hardened aluminium alloys is disappointing and should be improved in order for the fatigue deformation to be more uniformly distributed.

2.2.7.4 Corrosion fatigue

Corrosion fatigue occurs from the simultaneous corrosion and cyclic loading of a material. Under these conditions the reduction in strength is greater than the cumulative effect of these processes occurring separately. Although protection from

corrosion can often be formed by a surface film, this can be easily broken up or disrupted by cyclic loading. Cyclic loading, if rapid, can also accentuate corrosion fatigue as the movement of the corrosion medium can 'wash away' the protective layers (Polmear et al. (2017)).

Localized corrosive attacks such as pitting will generate stress concentrations which in turn greatly reduce the fatigue life, as mentioned in section 2.2.7.3. This reduction in fatigue life is dependent on the materials resistance to the corrosive medium. If the materials resistance to the medium is good, then the fatigue resistance is not as significantly reduced as when the materials resistance to the medium is poor. Importantly, under conditions of corrosive fatigue, all types of aluminium alloy exhibit the same percentage loss in strength when compared to fatigue strength in air. For example, Polmear et al (2017) found that under freshwater, the fatigue strength at 10^8 cycles is ~60% of that in air whereas in NaCl solution it is normally between ~25-35% of air. Therefore, the corrosive fatigue of a particular aluminium alloy is virtually independent of its metallurgical condition but rather dependent on the resistance to the corrosive medium and the damage caused by cyclic loading to the surface film formed.

2.2.8 Joining of high strength aluminium alloys

High strength aluminium alloys are commonly joined by adhesive bonding, riveting or solid-state welding. Adhesive bonding and riveting are both regularly used joining methods, with riveting being seen as the traditional method for joining components such as fuselages and wing structures (both produced from high strength aluminium alloys) in the aerospace sector. However, riveting increases the weight of an aircraft making it less fuel efficient and causes stress concentrations which can lead to fatigue crack initiation (Dursun and Soutis (2014)). Adhesive bonding is a direct competitor to riveting however due to safety limits on critical components stronger joining methods are preferred. Instead adhesive bonding is used in other applications for the joining of medical equipment and automotive structures.

High strength aluminium alloys, such as 2xxx and 7xxx series aluminium alloys, are difficult to produce industry standard welds in using fusion welding techniques due to concerns regarding hot cracking, residual stress levels and stress concentrations (Cater and TWI Ltd (2018)). In addition, a significant problem arises from volatility of many of the alloying elements in these grades of aluminium alloy. For example, the lithium present in AA2195 (Used in the light weight external fuel tank of the NASA shuttle STS-91 named 'discovery' National Aeronautics and Space Administration (2005)) is easily oxidised, and in some instances burned off, during fusion welding which results in a weld zone of a different grade of aluminium alloy as the parent material. As such, these high strength alloys are deemed 'unweldable' by fusion welding, see Figure 31, by Dursun and Soutis (2014).

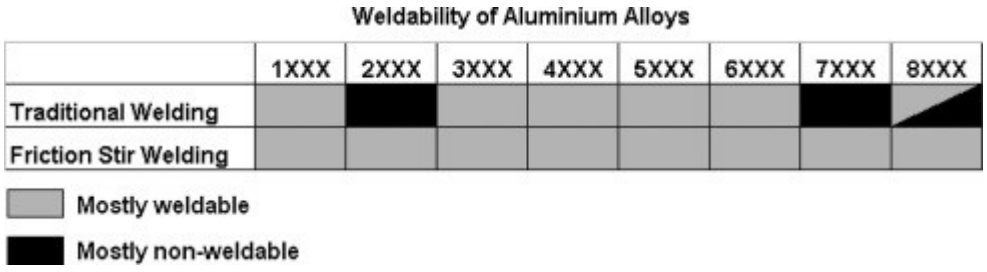

Figure 31 - Weldability of various aluminium alloys Dursun and Soutis (2014).

Another issue with fusion welding high strength aluminium alloys arises when the aluminium oxide layer which protects the alloy from corrosion is coupled with characteristics commonly associated with high strength aluminium alloys, such as low melting point and high conductivity which can make the material difficult to weld by fusion techniques such as tungsten inert gas (TIG) welding (Cater and TWI Ltd (2018)). The oxide layer that forms is more troublesome in fusion welding than solid-state welding due to the solubility of hydrogen. Hydrogen has high solubility in aluminium alloys in the liquid state however it has very low solubility after solidification leading to gas porosity (Monteiro and Monteiro (2014); Dursun and Soutis (2014)). This is less of an issue in solid-state welding as the process does not raise the metals temperature to the liquid state and therefore gas porosity is less likely to occur.

However, Friction Stir Welding (FSW) is a solid-state process therefore these issues do not arise and all grades of aluminium alloy have been found to be weldable by this technique without such a loss in properties as to render the process detrimental – making this a viable joining method for industrial sectors such as aerospace, automotive and marine.

2.3 Friction Stir Welding - The process

Friction Stir Welding (FSW), a process invented by The Welding Institute (TWI) in 1991, is a solid-state joining process combining elements of both the traditional thermal and working techniques used for joining aluminium alloys in a single process (Mishra and Ma (2005)). In its simplest form, FSW uses a non-consumable tool with a specially designed shoulder and probe to stir softened material forming the joint, such as demonstrated in Figure 32.

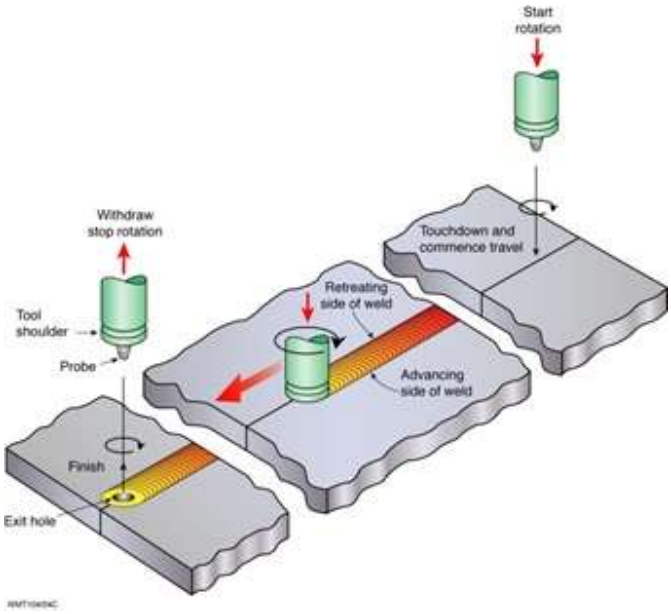

Figure 32 - Schematic of the FSW process (Cater, Andrews, and TWI Ltd 2014).

The rotating probe is inserted into the abutting edge of the two work pieces. In thin section welds this is done directly into the material however in thicker material a pre-

drilled pilot hole is used. The pilot hole is an important additional step to thick section FSW as it reduces the amount material the probe needs to displace and keeps initial stresses on the probe low (Thomas (1998)). The hole is nominally 60-70% the volume of the probe. This is an important factor to consider in the drilling of the pilot hole as too large and there will be very little friction generated between material and probe resulting in high lateral forces occurring once the probe starts to traverse. In thin section a pilot hole is not a considered requirement as the heat generated does not have far to propagate to soften the material surrounding the probe. Once inserted, the probe is left to dwell for a period of time to allow the shoulder and probe to generate friction (Frigaard, Grong, and Midling (2001)) which heats the work pieces to a temperature below the melting point but high enough to allow plasticised flow. Once the pre-determined parameters are met, the probe is traversed along the join line while its rotation pulls material from one work piece, called the advancing side, to the other named the retreating side. This is best represented in Figure 33 - Figure 34 which show the flow of the material in the three planes.

In vertical plane (Figure 33), the material is visibly drawn towards the centre of the weld from top and bottom surfaces by the profile of the probes thread. This is done to consolidate the weld and prevent void production (Cater and TWI Ltd (2018)) in the centre thickness of the material. When looking at the effect of the probes motion on the lateral plane (Figure 34) a partial penetration weld (that is to say the material is not completely welded through its thickness) is used. A partial weld is used so that the joint line is still visible at the base of the plates so this can be used as a marker for where the joint originates. As is seen, the copper and brass are mixed together with both present on each side of the joint line. This occurs from the rotation of the probe drawing material from the advancing side, across the front face of the probe to the retreating side and drawing material from the retreating side along the rear of the probe to the advancing side (Cater and TWI Ltd (2018)). The third plane is the longitudinal plane. As the tool is traversed along the length of the joint a cyclic stirring of the material occurs, as shown in Figure 35. As the front of the probe moves from the front to the rear back to the front in a single rotation, a cyclic motion is generated as the material is moved around the tool.

Figure 33 - Copper and brass FS weld showing material flow in the vertical plane (Cater and TWI Ltd (2018)).

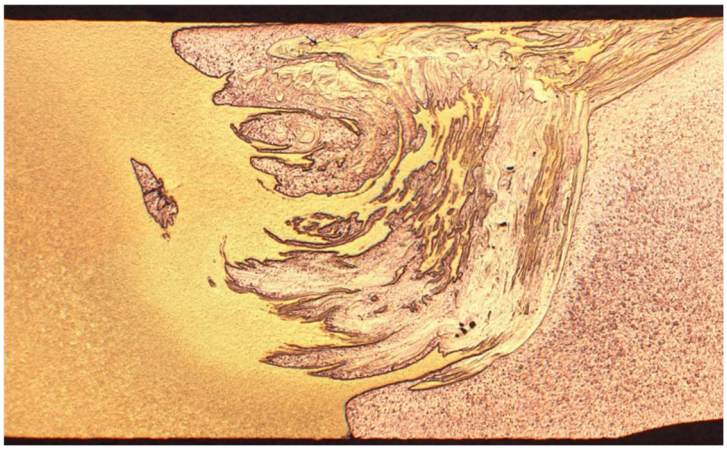

Figure 34 - Copper and brass FS weld showing the material flow in the lateral plane (Cater and TWI Ltd (2018)).

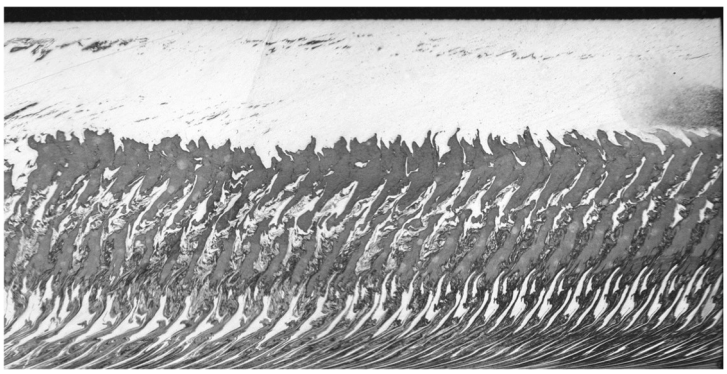

Figure 35 - Copper and Silver FS weld in the longitudinal plane showing the cyclic nature of mixing along the weld (Cater and TWI Ltd (2018)).

As the process has become better understood and therefore able to tackle a wider variety of materials and geometries so has the demand for FSW of thick section components increased. To do so efficiently with reduced loss to the mechanical properties, several process variants can be used;

- Conventional single probe full penetration
- Weld-Flip-Weld (WFW-FSW) (Figure 36a)
- Simultaneous Double Sided (SDS-FSW) (Figure 36b)
- Stationary Supported Bobbin (SSB-FSW) (Figure 36c)
- Stationary Supported Shoulder (SSS-FSW) (Figure 36d)

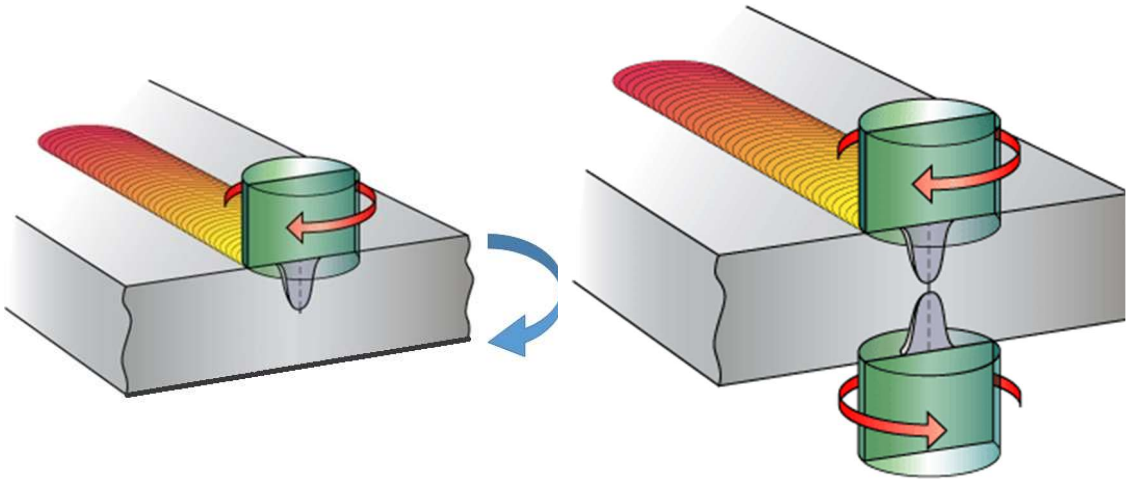

a) Weld-flip-weld FSW (Thomas et al., (n.d.))

b) Simultaneous double sided FSW (Thomas et al., (n.d.))

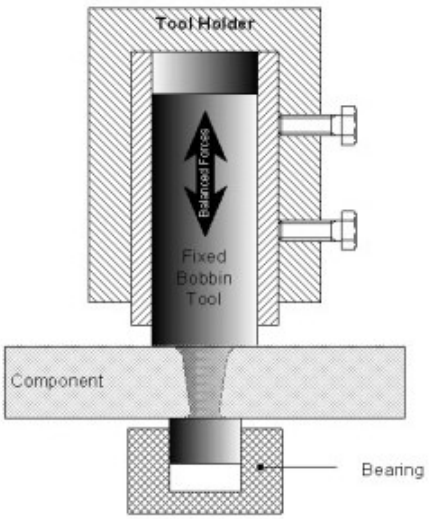

c) Supported bobbin FSW (Cater, Andrews, and TWI Ltd (2014))

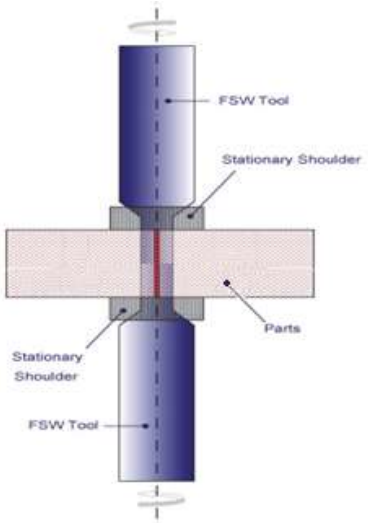

d) Stationary shoulder FSW (Martin (2017))

Figure 36 - Process variants used for thick section Al alloys.

2.3.1 Weld-Flip-Weld

The Weld-Flip-Weld technique (WFW-FSW) as the name suggests requires the work piece to be welded using a probe of nominally half the thickness of the material then flipped over and the process repeated. The cycle time of the process is considerably greater than that of Simultaneous Double Sided FSW (SDS-FSW) as the necessity to machine the first welded surface flat before turning the part over and re-clamping it to the bench is time consuming (Cater and TWI Ltd (2018)). WFW-FSW is beneficial, however, where time constraints are not critical but good surface finish is. As the process requires the top surface to be machined before the part is turned over, the surface is flat with no flash present. The surface finish of the second weld can also be improved as the parameters can be adjusted between the two welds to accommodate for any issues experienced in the first weld, such as large quantities of flash build up or the tool being too deep within the material. An additional benefit comes from using the nominally half thickness probes. As the probe is shorter, there is less bending stress experienced by the tool versus SSB-FSW thus improving tool life and reducing the chances of tool failure within the component (Cater (2020)).

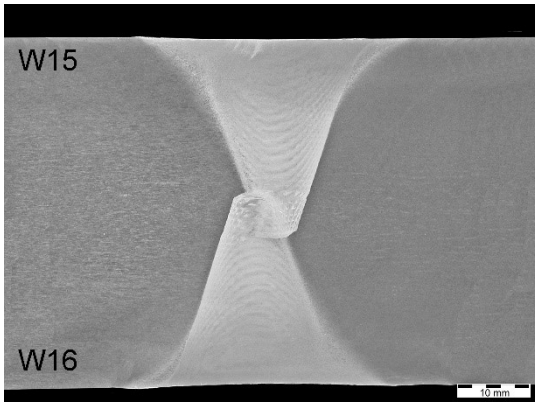

Figure 37 - Macrograph of weld-flip-weld process in 50 mm thick AA5083 showing the skewed nature of the stir zone (Cater (2020)).

A noticeable feature that can occur in the WFW-FSW process, in thick section material, is the skewed stir zone, as demonstrated in Figure 37, which results from the bending stresses acting on the probes (Cater (2020)). If the tool is traversing at the upper limit

of its workable parameter envelope, then the bending stresses acting on the probe cause it to be pushed 'off-centre'. The direction of probe rotation is a contributing factor to the skew direction. As the probe rotates, the material flow is more prominent down the retreating side of the tool resulting in more material being pushed towards the advancing side. The magnitude of the deflection is dependent on the tools traverse speed. When traversed at high speeds, the tool is moving through colder, and thus stronger, metal which results in a higher bending stress present on the probe. In extreme situations the two passes will be deflected in opposite directions by such a magnitude as to generate an unwelded region between the probe paths. This is very uncommon and can be prevented by using traverse speeds that do not produce the bending stress magnitudes associated with such a phenomenon.

2.3.2 Simultaneous Double Sided

The Simultaneous Double Sided (SDS-FSW) technique uses two probes which are run simultaneously to join the work pieces together in a considerably quicker time than the WFW-FSW process, as illustrated by Figure 38. The time taken to remove and reload the material is negated by this process making it far faster from loading to completion than WFW-FSW (Cater, Andrews, and TWI Ltd (2014)). This technique also benefits from good tool life as well as reducing manufacturing time, however, the complexity of machinery increases significantly adding to the start-up costs.

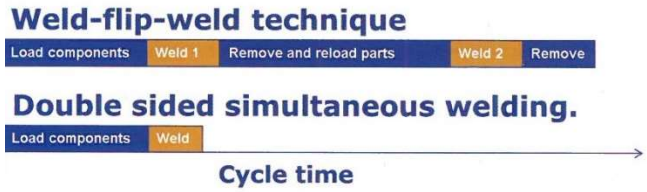

Figure 38 - Time frame for double pass welding (Cater, Andrews, and TWI Ltd (2014)).

The two probes can be configured either directly opposed to each other and each just shorter than half the materials thickness (Staines and Watts (2005)), or as two off set probes each slightly longer than half the thickness of the work piece, as demonstrated

in Figure 39. By using two directly opposing tools a central region of the weld (circled in Figure 39a) is not physically passed through, however due to the plasticised flow of the material it is still welded. This phenomenon is called ‘under stir’. Whereas, off set overlapping probes have the advantage of ensuring the whole joint is welded, as shown in Figure 39b. This variation of SDS-FSW results in a double processed centreline region (Martin (2017)). Passing through the central region twice typically produces a significantly refined grain structure, resulting in more grain boundaries reducing dislocation slip. Habitually, this has the effect of improving the retention of strength in the weld.

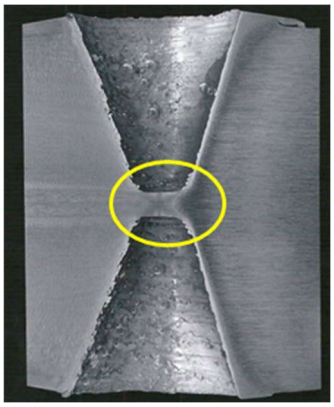

a) Double sided FSW using shortened probes (Longitudinal weld section). Area circled shows region where ‘under stir’ occurs.

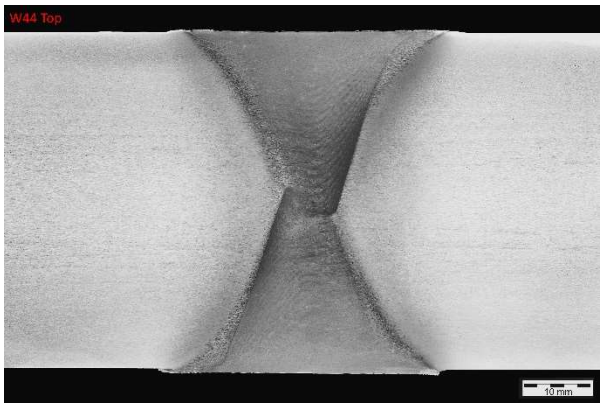

b) Macrograph of a double-sided weld using two longer, off set probes.

Figure 39 - Variations of simultaneous double sided FSW (Cater, Andrews, and TWI Ltd (2014)).

The SDS-FSW technique, like the WFW technique before it, produces an hourglass shaped heat input due to the conical shape of the two tools used. At the shoulder of the probes the heat affected zone (HAZ) is much wider than at the probe tip (in the centre of the weld). Therefore, the mechanical performance and microstructure of the weld vary through the thickness.

2.3.3 Supported Stationary Bobbin

Bobbin welding is an adaptation of the conventional FSW technique which uses a full-length cylindrical probe to pass through the joint line's complete thickness (G.-Q. Wang, Zhao, and Tang (2020)). As such it is limited in the thickness it can weld by the bending stresses experienced by the tool and awareness of these bending stresses must be maintained to prevent damage. To tackle this, a support bearing is added to the lower shoulder to prevent 'out of plane movement' and allow for higher bending stresses which results in practical faster traverse rates.

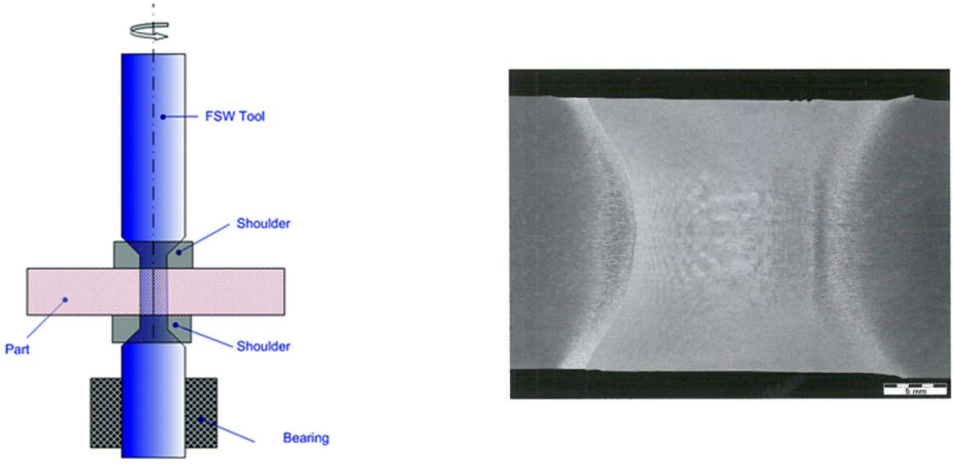

a) Stationary supported bobbin schematic (Martin 2017)

b) Stationary supported bobbin macrograph. (Cater, Andrews, and TWI Ltd 2014)

Figure 40 - Supported bobbin schematic and macrograph.

Supported Stationary Bobbin Friction Stir Welding (SSB-FSW) uses a simple design which is easily implemented to produce single pass, full penetration welds. Full penetration results in a lack of weld root, thus removing potential root defects. As well as this, the SSB-FSW technique produces a more linear heat input, as demonstrated by Figure 40b, than techniques where a conventional conical tool is used (W. F. Xu, Luo, and Fu (2018)). From this figure it can be seen that the hourglass shape of the stir zone, seen in SDS-FSW and WFW-FSW, is not as prominent with the central region

being broader than in these techniques. This means that the weld properties are not as varied through the thickness of the material, a beneficial feature of the process. The SSB-FSW technique has been used to make a limited number of welds in thick section aluminium alloys and therefore benefits of the process are still only perceived and requiring validation (TWI Ltd (2018)).

2.3.4 Supported Stationary Shoulder

The Supported Stationary Shoulder technique (SSS-FSW) was originally used for welding Titanium alloys of up to 10 mm in thickness. Titanium alloys are challenging to weld by conventional friction stir techniques as they have high softening temperatures and low thermal conductivity. This results in difficultly maintaining sufficient heat to soften the material without causing localised overheating (Cater and TWI Ltd (2018)). Titanium alloys, typically of hexagonal close packed crystalline structure, are considered weldable by fusion techniques however high residual stresses, distortion due to low thermal conductivity and solidification defects detract from the attractiveness of this process (H. Liu and Fujii (2018)).

SSS-FSW uses a rotating probe which protrudes through the shoulder component which does not rotate. For thick section material a second shoulder is fitted to the probe, much like the bearing used in SSB-FSW, to reduce the bending stresses acting on the probe (Cater and TWI Ltd (2018)). The shoulders add no heat to the surface, so all heat is provided by the probe resulting in a lower and essentially linear heat input through the materials thickness, as indicated in Figure 41. This figure also shows that there is a distinct, sharp transition between the fine grain structure of the weld nugget and the parent material microstructure of the advancing side (right). In contrast, the transition from weld nugget to parent material on the retreating side (left) is far more gradual as denoted by the slightly more blurred transition (Hovanski et al. (2017)). SSS-FSW may be very beneficial for welding heat treatable aluminium alloys, such as 2xxx and 7xxx grades, as they obtain their strength by solution heat treatment and ageing, and this process ensures less thermal damage is done.

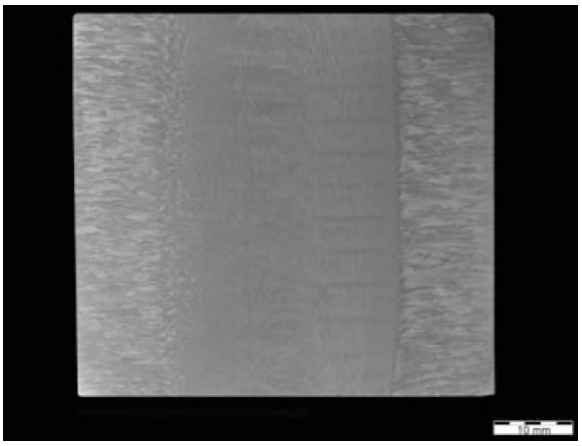

Figure 41 – A stationary shoulder FS weld in 50 mm thickness AA6082-T6 (Hovanski et al. (2017))**.**

The Supported Stationary Shoulder technique has been used to make a limited number of welds in large thickness plates however it is expected that the process, similar to supported bobbin FSW will; increase the thickness of material possible to weld in a single pass, increase welding speeds through the use of smaller diameter shoulders and remove the lack of penetration defect by passing through the material fully (Hovanski et al. (2017)).

2.4 Tool design and material

2.4.1 Requirements of tooling

Tool design is arguably the most important aspect of FSW, as stated by TWI Ltd (2018). Correct tool design and material selection are essential for producing high quality welds. When designing a new tool, the requirements of the shoulder and probe are key. Table 4 highlights some of the most important requirements of the shoulder and probe.

Tool Component	Purpose
Shoulder	Generate heat at the surface by friction, both directly and by the internal shear of the material beneath it.
	Exert a downward force on the work piece to consolidate the weld.
	Contain the plasticised material within the weld zone.
Probe	Break up the oxide layers and contaminants at the join line.
	Generate heat by friction to soften the work piece.
	Direct material to the centre of the weld.
	Mechanically mix the two plates, uniting them to form the weld.

Table 4 - Tool component requirements.

2.4.2 Material selection

For the shoulder and probe to serve their purposes discussed in section 2.4.1 efficiently, the geometry and choice of material must take into account properties such as strength, wear, toughness and fatigue. The tool must have adequate strength and wear resistance to be able to withstand the high bending stresses and torsional forces TWI Ltd (2018), as well as both the abrasive and adhesive wear mechanisms it is subjected to during the welding process. The geometry and material are also important in producing a good quality weld as the incorrect material selection could lead to failure of the probe or poor heat transfer.

Suitable fracture toughness over a wide temperature range is an important property for the tool material (TWI Ltd, (n.d.)). During the FSW process, and depending on the work piece material, the temperature can range from 20 °C to in excess of 1250 °C (for example in Steel welding) (Cater and TWI Ltd (2018)). Therefore, it is important that the tools fracture toughness is adequate across this whole range to limit tool damage. Thermal cycling, the coupling of high temperatures with the rotational stresses of the process, is also a significant problem along with fatigue.

Further properties considered in material selection are creep resistance and reactivity. Very long welds, such as those in marine or rail construction, result in the tool being subjected to low but continuous stresses and moderate temperatures in which creep can become a prominent issue. Reactivity is also important to consider as the tool should be inert to the work piece and surrounding atmosphere so as to not contaminate the weld.

Aluminium and magnesium alloys are commonly welded using Steel tools such as AISI H13. This material is used as it is readily available and has the suitable properties mentioned for joining such alloys. The life of Steel tools depends on the parameters used during welding. Rai et al. (2011) indicated that increased rotational speeds were shown to increase the wear on the tool while a lower traverse rate was shown to improve tool life.

For higher strength grades of aluminium alloy, such as 2xxx and 7xxx series, the Cobalt-Nickel-Chrome super alloy MP159 is used. This alloy is becoming increasingly used in FSW probes due to its high strength and moderate ductility at 500 °C (the temperature at which aluminium alloys are welded). Using MP159 also eliminates the susceptibility to zinc induced corrosion cracking that tool Steels experience when interacting with 7xxx series aluminium alloys. The zinc content of this alloy series attacks the grain boundaries of tool Steels and causes intergranular micro cracks which subsequently lead to propagation under loading and fracture. MP159 is readily machined in its as-received state and is further strengthened through precipitation hardening, though a drawback of this material is the cost. Lienert et al. (2011), however, suggests that the cost of super alloy is ‘very good’ as despite the initial cost being high, this is outweighed by the value of the weld as super alloys are largely used for aerospace components or thick section welds which make using tool Steels impractical.

Other materials such as Steel and Titanium tend to use tools made of Polycrystalline Cubic Boron Nitride (pcBN). However, these tools are very costly owing to the high temperatures and pressures required to manufacture the tool Rai et al. (2011). As well as the high cost, this material has a tendency to fail during the initial plunge stage due to its low fracture toughness.

2.4.3 Probe design

As discussed, the probe's purpose is to generate heat and mechanically mix the two plates to form the weld. To achieve this across a wide variety of materials, thicknesses and speeds, an increasing array of tool and probe designs now exist (Andrews and Horrex (2013)). One such variation is the MX-Triflute™, shown in Figure 42a. This tool was designed to not have parallel flutes like its predecessor but rather have a 'frustum' shape. This allows the tool to displace up to 70% less material during welding and provide a more uniformly stressed tool (TWI Ltd, (n.d.)). The major factor in determining the high performance and popularity of the MX-Triflute™ over conventional cylindrical probes is the ratio of volume of the probe swept during rotation to the volume of the probe itself.

a) MX-Triflute™ probe b) MX-Triflat™ probe

Figure 42 – FSW probe designs (Andrews and Horrex (2013)).

Despite the advantages of the MX-Triflute™, another probe was designed for the FSW of high strength aluminium alloys. This is known as the MX-Triflat™, illustrated in Figure 42b. The flutes of the previous MX-Triflute™ were replaced with flats which generated a milder stirring motion and resulted in reduction in welding temperature (TWI Ltd, (n.d.)). The MX-Triflat™ importantly also improved the strength of the tool by

increasing the volume of core material within the probe. This probe design also has the benefit of reducing the traverse forces experienced by the tool which reduces the likelihood of probe failure when welding.

Probe shape is an important feature in determining the weld outline and consequently the variation in strength across a weld. The first probes used were cylindrical, such as that illustrated in Figure 43a. This initial design was soon replaced, however, by the now commonly used conical (or tapered) probe, shown in Figure 43b. This probe shape was designed to reduce the traverse forces experienced during welding. By reducing the tip diameter, a lower traverse force is experienced by the tool which reduces the risk of fracture and failure (Cater and TWI Ltd (2018)). This design however also introduces a variation in the size of the stir zone through the thickness of the material being welded. In simpler terms; the stir zone narrows towards the root of the weld. This has the effect of altering the width of the HAZ which impacts on the properties of the weld.

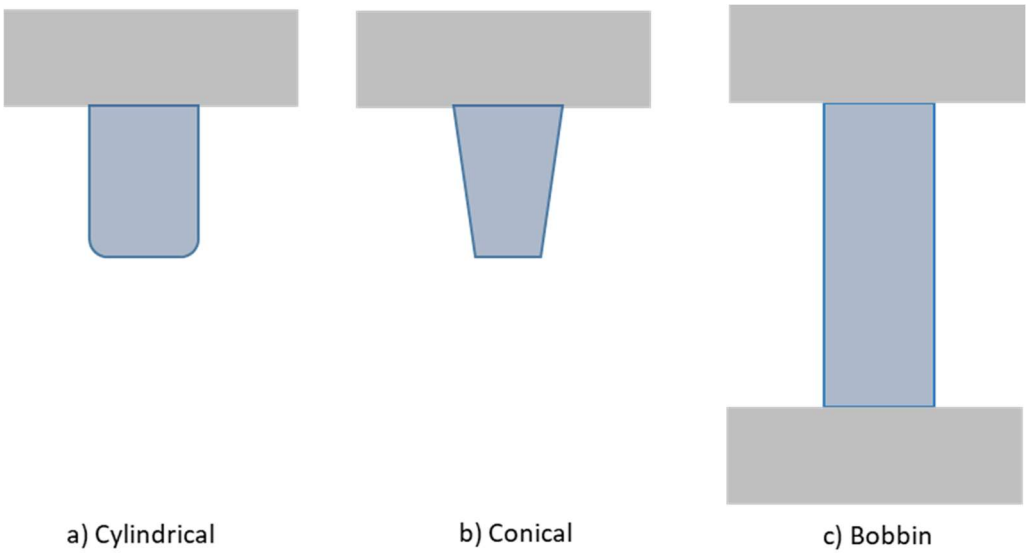

Figure 43 - Probe shape variations.

The FSW probe can be produced with a variety of profiles, examples of which are illustrated in Figure 44. The threadless probe, shown in Figure 44a, is good for welding

Titanium alloys which require a very strong probe material which makes machining a profile highly difficult. Although, probes with a threaded profile are considered better as they allow more stirring action and a larger heat input due to their increased interacting surface (Rai et al. (2011)). However, as Titanium alloys are so tough, any machined probe would wear quicker than usual thus making them not as cost effective as using a thread less probe.

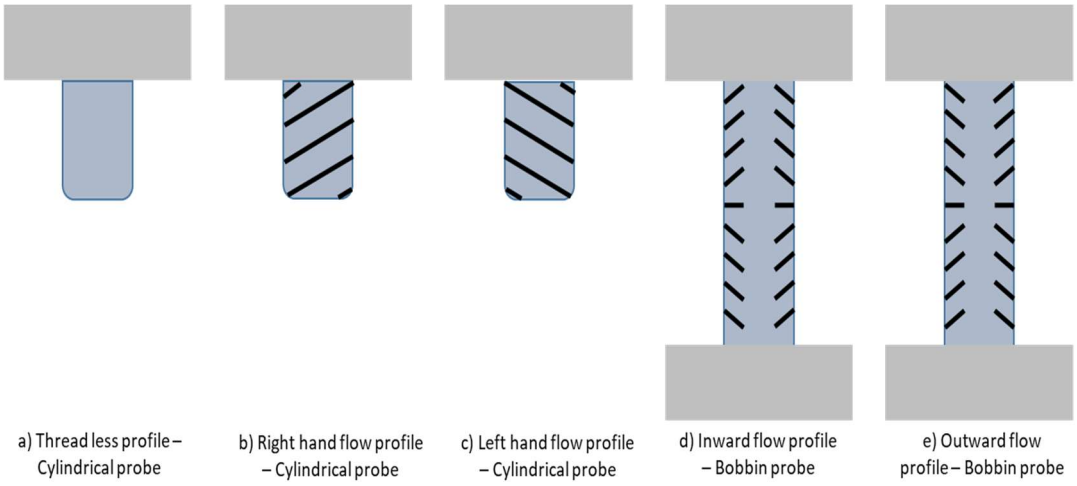

Figure 44 - Profile designs for a probe.

The probe profile exhibited in Figure 44d is designed to direct the flow of the plasticised material towards the centre of the join (Chowdhury et al. (2010)). This is a very common selection in SSB- and SSS-FSW as it has been proven through application to be effective in ensuring minimal defects and voids, when coupled with sensible process parameters such as traverse rate and spindle speed. The physical flow pattern that occurs is in practice far more complex and yet to be confidently explained. In previous welds it has been recorded that surface voids do not occur as a result of material flow towards the shoulder of the tool (Cater and TWI Ltd (2018)). It is assumed that the flow field towards the shoulder occurs as a result of too much material being directed to the centre of the weld and consequently being re-directed towards the shoulder. With bobbin tools, such as that shown in Figure 44d, the probe must be perfectly flat (that is to say no tilt angle is used) and consequently the shoulder typically used has a scrolled profile, discussed in section 2.4.4. The scroll

shape ‘scrapes’ a small amount of material from the weld surface and feeds it towards the probe, the features on which then direct it inwards towards the material centreline. This adds to the material being directed to the centre of the weld which causes a re-direction of flow away from the centre line.

In a similar fashion, the outward flow design of the profile, shown in Figure 44e, directs material towards the shoulders of the tool. This should cause void defects within the weld, however, as a result of similar interactions as the probe in Figure 44d material is re-directed towards the centre of the weld due to too much material being directed towards the shoulder and voids at the centre of the weld are not a common trait.

2.4.4 Shoulder Design

Due to their proven effectiveness, the shoulder of the FSW tool has seen less development than the probe. The primary purpose of the shoulder is to contain the deformed material within the weld zone, if the shoulder is not stationary then its secondary function is to generate friction and heat to soften the material (Hoyos and Serna (2021)). Two common designs for the shoulder are ‘concave’ and ‘scrolled’, these are shown in Figure 45.

The concave shoulder, shown in Figure 45a, is commonly used for aluminium grades 5xxx, 6xxx and some 2xxx alloys, whereas the scroll shoulder is generally used for welding high strength aluminium alloys as it has been shown to improve weld quality and mechanical properties.

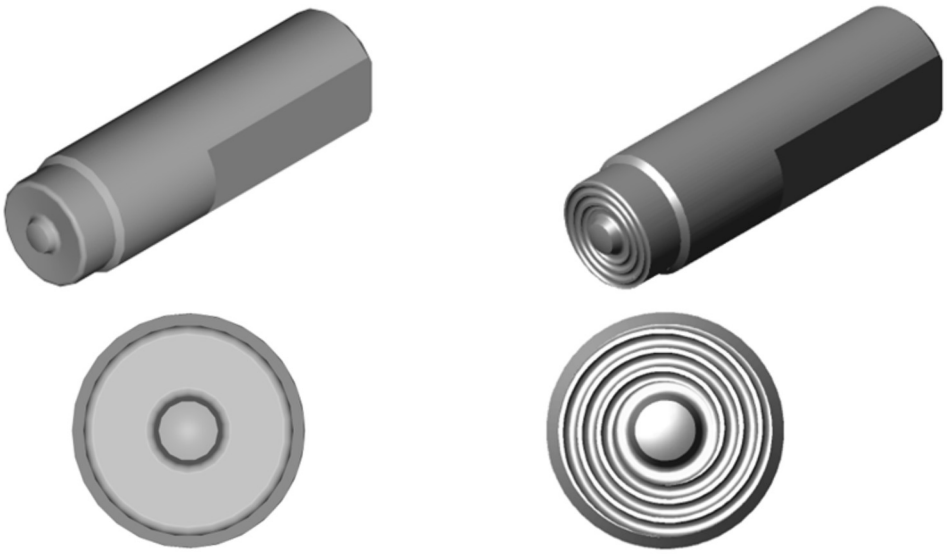

a) Concave shoulder b) Scroll shoulder

Figure 45 - Tool shoulder designs (shown with a plain probe) (Andrews and Horrex (2013)).

A concave shoulder is usually smooth and has no features, instead it uses its hollow cone shape as a reservoir for the material displaced during the plunge phase of the process (Lienert et al. (2011)) and serves to return material back towards the probe to ensure full consolidation and reduce the possibility of void defects. A tilt angle of 1-3 ° is used with concave shoulders to prevent the front of the shoulder undercutting the heated material and causing a 'bow wave' to form.

In comparison, the scroll shoulder is commonly used without a tilt angle as the profile sweeps material from the periphery and directs it to the centre of the weld where it is consolidated. This removes the complexity of requiring a tilting angle which makes the machine considerably cheaper to manufacture. Rai et al. (2011) argue that a scrolled shoulder, such as the one shown in Figure 45b, improves the FSW process by improving stability. It was argued that when a scrolled shoulder is used in constant axial force mode, any increase in plunge depth from its normal value results in greater contact area between the shoulder and work piece (Cater and TWI Ltd (2018)).

In order to further increase the range of depth possible in FSW, convex scrolled shoulders have been designed. These tools are designed such that the outer radius of the shoulder is further away from the end of the probe than the inner radius (Lienert et al. (2011)). This allows the range of thickness to be increased to roughly the same as the depth of the taper in the shoulder. Cederqvist et al. (2009); De Backer (2014) found that a convex scrolled shoulder resulted in minimum flash and no defects as opposed to concave shoulder which resulted in medium flash and some defects. Therefore, it can be argued that convex scrolled shoulders improve weld quality versus concave shoulders.

A final shoulder design is the stationary shoulder. Originally designed for use in FSW Titanium, the shoulder does not rotate like a conventional shoulder but rather is used solely to contain the material (Cater, Andrews, and TWI Ltd (2014)). This results in the tools production of friction coming exclusively from the probe. The result of this is that the TMAZ and HAZ are smaller as the heat is not coming from the width of the shoulder which is significantly larger than the probes width.

An important design feature to consider is the diameter of the shoulder. In non-stationary shoulder applications, the shoulder is used to produce friction and largely establishes the material flow field (Lienert et al. (2011)). The shoulder both sticks and slides, these each generate a different torque. Both sliding and sticking generate heat while sticking also dictates material flow (Cater and TWI Ltd (2018)). The heat generated impacts upon the microstructure and consequently the mechanical properties of the component. Therefore, the diameter of the shoulder is important to the weld quality. If the diameter is too large then the HAZ of the weld will be vast which will negatively impact the mechanical properties of the material, however, if the diameter is too small it is possible that a large amount of material will escape in the form of flash and void defects will become likely to occur (Hoyos and Serna (2021)).

2.4.5 Tool wear, deformation and failure

The probe component of the tool experiences larger wear and deformation than the shoulder and is also more commonly the point of failure. This is the consequence of several factors. For example, the probe is completely immersed within the work piece and therefore subject to greater resistance during translation along the weld line (Cater and TWI Ltd (2018)). Secondly, the shoulder generates the largest proportion of heat during welding and therefore the material is softer and flows more easily. However, if the probe has a thread profile that improves downward flow of the hotter and softer material (Reza-E-Rabby, Tang, and Reynolds (2018)) from the shoulder/work piece interface then the forces acting on the probe will decrease. Finally, the load bearing capability of the probe is much less than the shoulder due to the higher stresses resulting from torsion and bending stresses which given the probes shape suggest that failure is more likely to occur along the probe than at the shoulder (Rai et al. (2011)). These reasons result in the faster wear and failure of the probe feature of the tool than the shoulder.

2.5 Metallurgy and properties of FS welded aluminium alloys

2.5.1 Microstructure of Friction Stir Welded aluminium alloys

Three fundamental regions form the microstructure of Friction Stir (FS) welded metals; the Thermo-Mechanically Affected Zone (TMAZ), the Heat Affected Zone (HAZ) and the unaffected, Parent Material (PM). Figure 46 shows that in aluminium alloys a unique, additional region, the Nugget Zone (NZ), is also present. These four regions are dependent on a series of factors including but not limited to material composition, tool geometry and parameters such as traverse and rotation speeds.

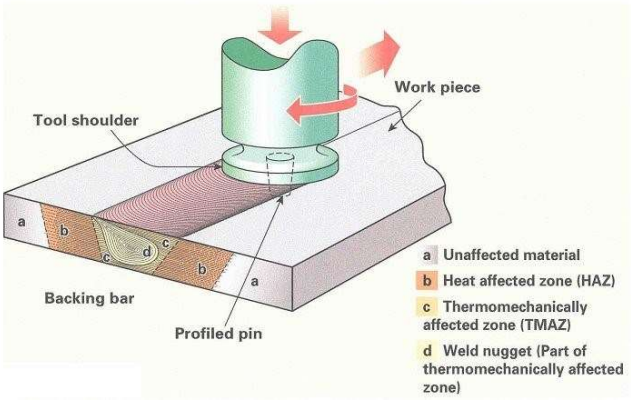

Figure 46 - Zones in a Friction Stir Welded aluminium alloy, taken from TWI Ltd (2018).

2.5.1.1 Nugget Zone

The Nugget Zone (NZ) is a region of large deformation and recrystallisation within the Thermo-Mechanically Affected Zone (TMAZ). The grain structure is frequently described as being roughly equiaxed and often an order of magnitude smaller than in the PM, a feature that aides in distinguishing the zone from the TMAZ. The NZ is only found in Friction Stir (FS) welded aluminium alloys as it is a function of the recovery and recrystallisation particular to aluminium and therefore isn't found in welds of other materials. Deformed grains, within the NZ, can reduce their stored energy by removing defects (such as dislocations), induced by the plastic deformation that occurs in Friction Stir Welding, in their crystal structure. This process is called 'recovery' and serves to reduce the dislocation density within the structure which also results in a reduction in strength and increase in ductility (Cater and TWI Ltd (2018)). The recrystallisation process competes with recovery for the stored energy within the material to replace the deformed grains with new, equiaxed ones which grow in size until they consume the original deformed grains. This process's speed and extent are dependent on several parameters such as the temperature, scale of deformation, grain size and time.

The shape of the NZ is mainly one of two types, shown in Figure 47; basin or elliptical (R. S. Mishra and Ma (2005)). The basin shape differs from the elliptical as it widens towards the shoulder of the tool. It is noted that these shapes are only the case when

the probe is tapered and change with a bobbin tool. As the NZ is a function of the recovery and recrystallisation, the extent and shape are dependent on the parameters such as temperature, scale of deformation and time.

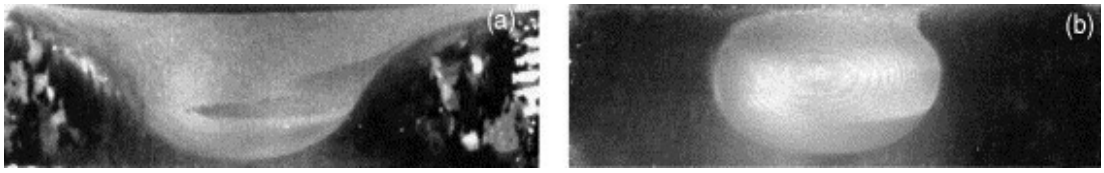

Figure 47 – 'Effect of processing parameter on nugget shape in FSP A356: (a) 300 rpm, 51 mm/min and (b) 900 rpm, 203 mm/min' (R. S. Mishra and Ma (2005)).

A further common feature in the NZ is banding, sometimes referred to as an onion-ring structure due to the layered effect associated with banding replicating the appearance of an onion (see Figure 48) (Threadgill et al. (2009)). It is considered by Cavaliere et al. (2004) and Ceschini et al. (2007) that the flow behaviour of the plasticised material and the differences in dislocation density result in the formation of the onion structure.

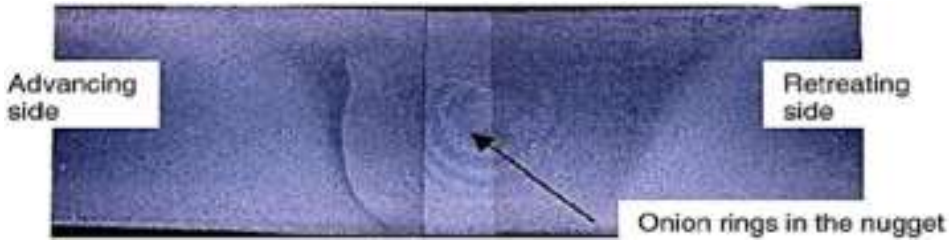

Figure 48 – Onion ring feature present in FS welded AA6061/Al_2O_3/20p (Salih et al. (2015)).

It has been widely concluded that, within the NZ, the strengthening precipitates go into solution at the elevated temperatures experienced and re-precipitate out during cooling, typically locating on dislocations (Olea et al. (2006); Threadgill et al. (2009); Sauvage et al. (2008)). The mechanical stirring from the probe deforms and rotates grains and precipitates, while the heat generated is high enough to bring the precipitates into solution. In AA7050 the temperature experienced by the NZ, typically

the highest in the weld, reaches as high as 480 °C (Fuller et al. (2010)). The precipitates in the NZ of AA7050-T7451 were found to be, low density η' type, ranging in size from 60-100 nm.

2.5.1.2 Thermo-Mechanically Affected Zone

One region that is not found in other welding processes but is in FSW is the Thermo-Mechanically Affected Zone (TMAZ). Unlike the NZ, the microstructure of the TMAZ is recognisably similar to the PM, albeit processed and rotated. There is limited evidence of recrystallisation, such as there is in the NZ, within the TMAZ in the work of Fuller et al. (2010), Su et al. (2003) or Jata, Sankaran, and Ruschau (2000). Despite experiencing plastic deformation, it is reported that there is insufficient plastic strain to cause the process to occur. The temperatures experienced (typically 400-450 °C in aluminium (Jacquin and Guillemot (2021))), although not as high as in the NZ, are still adequate to bring about a coarsening and a reduction in density of the precipitates within the region. Fonda and Bingert (2004) investigated 25mm thick AA2519-T8 and found that the temperatures in TMAZ were sufficient to, in locations, partially dissolve precipitates leading to very fine Guinier-Preston (GP) zones during cooling. These θ' precipitates were coarser than those recorded in the HAZ.

2.5.1.3 Heat Affected Zone

The Heat Affected Zone (HAZ) is present in all welding processes. The HAZ describes any region in the material that is subjected to the heat generated during welding but not mechanically processed. The HAZ is exposed to elevated temperatures (typically ~300 °C in aluminium (Svensson et al. (2000); Jacquin and Guillemot (2021))), although these temperatures are not as high as those in the TMAZ or therefore the NZ. As the material is not mechanically processed but experiences elevated temperatures the grain structure in this region is very similar to the PM, although grain and precipitate growth occurs. The rate of which varies dependant on the grains distance from the heat source, in the case of FSW – the tool.

Precipitates present in the HAZ are typically described as coarser and larger than those of the PM. Fuller et al. (2010) and Su et al. (2003), both of whom investigated FS welded AA7050, show that the HAZ was characterised by coarse η type precipitates and smaller populated GP zones. However, both also highlighted the presence of 'large' precipitate free zones, up to five times the size of those found in the PM. Jata, Sankaran, and Ruschau (2000) also supports this, stating a precipitate free zone five times the size of that of the PM was present in FS welded AA7050. Mahoney et al. (1998) also suggests the growth of precipitates in the HAZ. They report that 30-40 nm long $MgZn_2$ precipitates are present in the PM while no 50-70 nm precipitates of the same composition are recorded, however, in the HAZ the precipitates of 50-70 nm length are recorded and the 30-40 nm $MgZn_2$ are reported as being 'rare' in the HAZ. This would suggest the growth of the precipitates from 30-40 nm to 50-70 nm. Mahoney et al (1998) was written just seven years after the invention of FSW and therefore precedes the vast majority of research into the effects of FSW on the microstructure.

2.5.1.4 Parent Material

The parent material (PM) is the material outside the influence of the welding process and therefore it is neither heated nor mechanically worked. Consequently, the properties for this region are unaffected by the welding process and are as described in section 2.2.

2.5.2 Post weld properties

2.5.2.1 Tensile and hardness properties

The modifications to the microstructure that occur as a result of the FSW process, as discussed in 2.5.1, are reflected in mechanical properties such as strength, hardness and fatigue. In Friction Stir (FS) welded aluminium alloys a reduction in both the strength and hardness compared to the parent material is noticeable. Braga, da Silva, and Moreira (2014) show that this reduction is not uniform across the different zones due to the changes in grain and precipitate size and distribution. Tensile failure of any

material will typically occur in the softest region and in FSW, this is usually the HAZ of the retreating side (Nandan, Debroy, and Bhadeshia (2008)). The retention efficiency of aluminium alloys can vary between 65 to 96% (Braga, da Silva, and Moreira (2014)) depending on the parameters used to produce the weld and whether the alloy is heat-treatable or not. In non-heat-treatable alloys the retention success has been shown to be higher than in heat-treatable alloys which experience greater precipitation coarsening and grain growth than non-heat-treatable alloys such as AA5083. However, typically the joint efficiency of FSW is higher than that achieved by conventional fusion welding techniques (Biallas et al. (1999)).

According to Biallas et al. (1999), the retention of the tensile properties post weld is dependent on the thickness of the material, with thick plates retaining a lower percentage of the parent materials tensile properties than thin plates. This is a result of the increased temperatures, caused by the welding process, dissipating slower in a thicker material. The inverse correlation between heat conduction and material thickness, demonstrated by Fourier's law (‘Conductive Heat Transfer’ (n.d.)), supports this;

$$Q = (k / s) A\, dT$$

Where;

Q = Heat transfer (W)

k = Thermal conductivity of the material (W/m k)

s = Thickness of the material (mm)

A = Area of conduction (mm^2)

dT = Temperature gradient (°C)

As the thickness of the plate increases the rate of heat transfer is diminished. This results in a greater retention of heat within the material for a longer period of time.

This supports Biallas et al (1999) as prolonged raised temperatures endorse increased precipitation spacing, allowing dislocations to pass through more easily and consequently reducing the tensile properties of the material. Biallas et al is from 1999 and therefore precedes a large quantity of the research into FSW of thick section aluminium alloys.

The nature of the weld's hardness is dependent on strengthening processes of the alloy used. It is widely reported that the hardness of heat-treatable alloys, such as 2xxx and 7xxx series', assumes a 'W' shape (demonstrated in Figure 49a) – that is to say there is a reduction in the hardness within the HAZ and TMAZ however the hardness returns to near parent material levels within the stir zone. This is not the case in non-heat treatable alloys which develop a 'U' or 'V' shaped hardness plot, as demonstrated in Figure 49b. The recovery of hardness in heat-treatable alloys is a result of the peak temperatures exceeding the solvus temperature of the initial precipitates. In non-heat-treatable alloys strengthening precipitates are not temperature dependent and as such do not recover hardness like the heat-treatable alloys.

For heat-treatable alloys, the post weld tensile properties are also dependent on the heat treatment process conducted following FSW. Fuller et al. (2010) indicate that for FS welded AA7050-T7651 and AA7075-T7651 the tensile properties are improved with natural ageing, citing an increase in tensile strengths of 24 and 29% for the two materials respectively. Natural ageing improves the mechanical properties of heat-treatable alloys as precipitates are able to grow, reducing dislocation manoeuvrability. Kalemba et al. (2015) support Fuller et al (2010) results by showing the effect of natural ageing on AA7136 and AA7042. Here it was shown that natural ageing increases the tensile and hardness properties of the material, although the 'W' shape commonly found in 7xxx series alloy hardness plots was not altered. Threadgill et al. (2009) also present data showing improved tensile and hardness properties due to natural ageing in their review paper, however they do not address this directly.

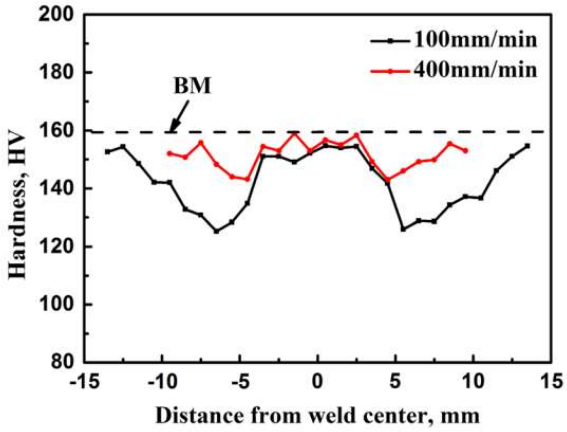

a) Mechanical properties of 5 mm thick FS welded 7050-T7451 (Zhou et al. (2016))

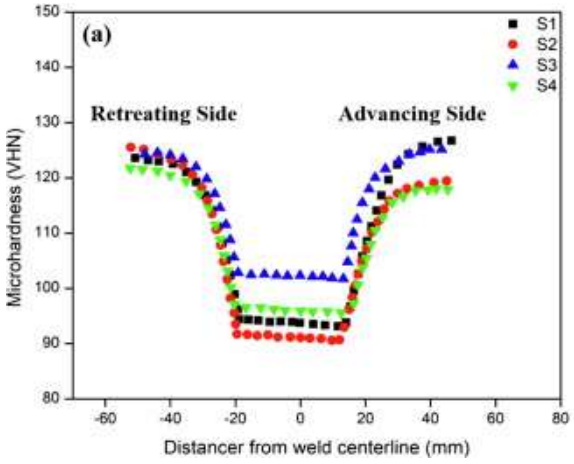

b) Hardness data for four samples of 5 mm thick AA5083-O (Sahu (2021))

Figure 49 - Hardness of FS welded alloys, depending on whether the alloy is non-/heat-treatable.

2.5.2.2 Fatigue of FS welds

Generally, FS welded components have good fatigue properties when compared with components that have been fusion welded, which tends to generate shrinkage cracking and porosity in the weld zone. FSW is largely free from such defects, which can provoke crack initiation, and therefore their absence suggests that FSW produces improved fatigue properties (TWI Ltd (2018)).

Work by Ericsson (2003) showed that AA6082 when FS welded had a higher fatigue life strength than the same material MIG or TIG welded. During testing each weld

technique was used before the material was subjected to 500,000 cycles. MIG-pulse welded samples experienced a stress-range of 60 MPa, while TIG samples showed a stress-range of 70 MPa. These were both overshadowed by the FS welded samples, which Ericsson et al suggest experienced a stress-range of 90 MPa. Ericsson et al also go on to conclude that the weld speed during FSW does not appear to impact the fatigue life of the material.

2.5.2.3 Residual stresses in FSW

Residual stress is defined as a self-equilibrating stress which exists in an elastic body even in the absence of external loads (Kumar, Mishra, and Baumann (2014)). Simply, residual stress is the stress remaining in a material after the original source of stress has been removed. Figure 50 depicts the origins of residual stress as a result of deformation, thermal history and microstructure. Kumar et al (2014) suggest that residual stress is a consequence of 'thermal and/or mechanical treatment'.

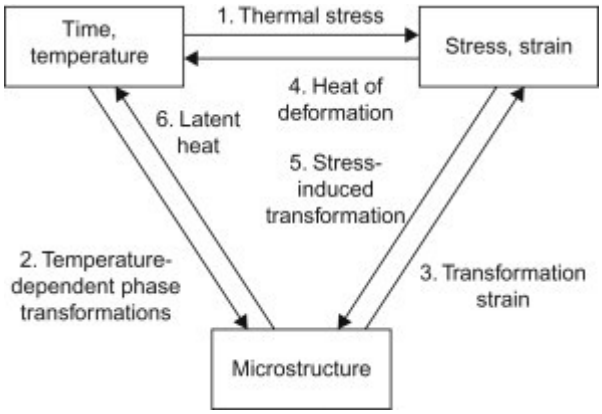

Figure 50 - Schematic of residual stress as a consequence of interactions among factors (Kumar, Mishra, and Baumann (2014)).

Depending on the type of residual stress in a component, the service life and performance can be improved or deteriorated. Typically, there are two types of residual stress: compressive and tensile. Compressive residual stresses can help improve the fatigue life of a component by retarding the rate of surface crack growth, whereas tensile residual stresses have a detrimental impact on fatigue life and crack

propagation. Compressive stresses, which are often induced by cold working are commonly induced to balance the detrimental effects of tensile residual stresses which can be a result of bending, torsion or shrinking and are the primary residual stress in which stress corrosion cracking takes place (Deveci, (n.d.)).

In FSW the residual stresses existing post weld are typically compressive, a consequence of the heavy clamping required and the force of the tool on the material. As such, Kumar et al (2014) imply that due to these residual stresses the FSW process has improved fatigue life and reduces crack propagation, though other factors including the fine grain structure and re-precipitation onto dislocations help impede crack propagation. The same author also concluded that in FS welded aluminium alloys the magnitude of the residual stress can be as high as the yield strength and therefore in 2xxx and 7xxx grade alloys, which have significantly higher yield strengths than other alloy grades, the residual stress will also be higher. A final statement drawn from this report is that tensile residual stresses are more common in the weld region suggesting that the weld region is not as fatigue resistant as the parent material.

There are several parameters in FSW that affect the magnitude and type of residual stress that occurs as a consequence of this process. Traverse speed, for example, impacts residual stress as the two are considered proportional to one another - that is to say that residual stress increases with traverse speed. At low traverse speeds the tool is in one area for longer thus increasing the heat input and correspondingly reducing the yield strength. As stated by Kumar et al (2014), the residual stress can be as high as the yield so if the yield strength is low then the residual stress will also be low. Therefore, as traverse speed is increased, resulting in a 'cooler' weld, the residual stresses in the material are increased as yield strength is not as drastically afflicted by the heat input.

Spindle rotational speed is another parameter that impacts residual stress. Lombard et al. (2009) infer that rotational speed is in 'consonant' with traverse speed. With an

increase in rotational speed, a decrease in peak tensile stress is observed. In addition, the overall longitudinal tensile stress at the weld centreline also decreases with the increase in spindle rotational speed. This phenomenon is put down to thermal relief taking place at higher rotational speeds, according to Lombard et al (2009).

A third parameter affecting residual stress is sample size. In most cases the sample size must be reduced due to machine limitations. However, this can jeopardise the integrity of the results as cutting of the sample can lead to relaxation of the residual stresses leading to an underestimation. This would be poor for design considerations.

2.5.2.4 Distortion

Distortion is a significant concern in more traditional welding techniques and can appreciably affect a component's design. FSW produces a much lower distortion in aluminium alloys as a consequence of the rigid clamping, lower heat input and ability to join the components in a solid-state. These factors allow any distortion to be managed in FSW and ensure the component does not undergo significant unwanted alteration. In doing so it has allowed companies such as Marine Aluminium in Norway to compete against larger extrusion companies. By FSW large integrally stiffened panels Marine Aluminium has been able to compete in the shipbuilding industry, where traditional arc welding techniques would have produced unusable components thus making the process unviable for this application (Anderson, Weritz, and Kaufman (2018a)). However, in thin gauge samples where asymmetry in clamping and heat sink are used, distortion can be significant (TWI Ltd (2018)).

2.5.2.5 Effect of natural ageing

Dong, Zhang, and Luan (2014) highlight the increase in GP zones as well as η' ($Zn_{1.3}Mg$) and η ($Mg(Zn, Cu, Al)_2$) phases with time within the NZ and TMAZ, stating the these 'effectively pinned the dislocations and consequently enhanced the strength of the joint'. Ungar et al. (1979) however state that η' phase cannot be precipitated below 70 °C and can only occur from natural ageing if the material is subsequently heated to

above 100 °C, above this temperature the natural aged precipitates dissolve in the matrix – this process is called reversion. Dong, Zhang, and Luan (2014) do not mention any subsequent heat treatment between natural ageing and testing so it is unclear how the presence of η' was detected.

2.6 Applications of Friction Stir Welding

Friction Stir Welding of aluminium alloys has many potential uses, primarily within the transportation industry. Aerospace, automotive, marine and rail sectors could all, and many have begun to, benefit from the application of the process due to the benefits outlined in section 2.7. As shown by Magalhães, Leitão, and Rodrigues (2018) in Figure 51, the transportation industry is responsible for over 50% of all applications of FSW – both thick and thin section – with the automotive sector responsible for around 60% of these applications.

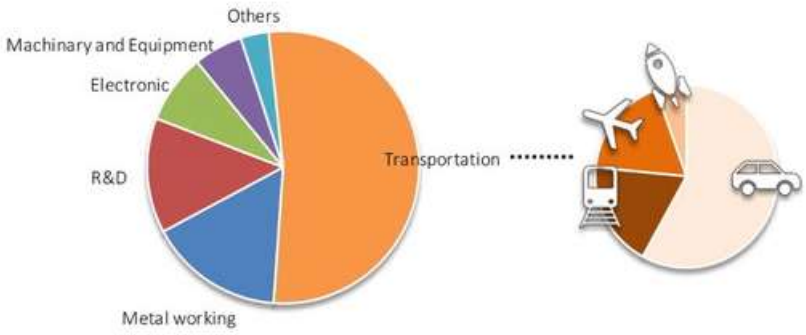

Figure 51 - Industrial sectors applying FSW (Magalhães, Leitão, and Rodrigues (2018)).

2.6.1 Aerospace

The application of FSW in the aerospace sector is possible due to its solid-state nature. This allows for welding of high strength aluminium alloys such as the AA2024 and AA7050 both of which are commonly used by other joining methods such as riveting, while also reducing the detrimental impact on the mechanical properties. The aerospace industry is attracted to FSW due to several benefits resulting from the process. Firstly, FSW has been shown to produce joints with fatigue strength greater

than that of fusion welding (Texier et al. (2018)). In addition, FS welded aluminium's have been identified as possessing excellent corrosion resistance (Anderson, Weritz, and Kaufman (2018)) and strength to weight ratios. FSW has the capacity to be used in components such as: wings, fuselages, fuel tanks, military and scientific rockets as well as in repairs of faulty fusion welds such as Metal Inert Gas (MIG) (Mazak MegaStir (n.d.)) and Tungsten Inert Gas (TIG) welds. Current applications of FSW in the aerospace sector include the Eclipse 500VLJ, the first aircraft to receive FAA certification for the use of FSW (TWI Ltd (2018)), and United Launch Alliances Delta II & IV expendable launch vehicles (G. Wang, Zhao, and Hao (2018)). Another recent application, announced by SpaceX, was the use of FSW as the sole joining method for the propellant tank onboard the Falcon 9 rocket – launched 30th May 2020 ('TWI Technology Used for Ground-Breaking SpaceX Flight' (n.d.); 'Space Exploration Technologies Corporation - Falcon 9' (2010)).

2.6.2 Automotive

The automotive industry makes up 60% of all transportation applications for FSW, as stated by Magalhães, Leitão, and Rodrigues (2018). Automotive manufacturers desire enhancement of vehicle performance as well as any incentives bestowed on them by Governments for adhering to environmental restrictions and as such look towards aluminium to lower the dead load of the vehicle. By using aluminium for a wide range of components it is possible to achieve a weight saving of between 30-40%, depending on the vehicle size (Lumley (2018)). Aluminium can be used for components such as engine cradles, body panels, chassis structure, wheel rims, fuel tanks and tail lifts on heavy goods vehicles. There is also a desire for cheaper joining processes as well as a reduction in the number of defects and the ability to join various thicknesses. These aspirations have made FSW a prominent feature in the automotive industry as the process has been well documented as being; achievable in all grades of aluminium, more environmentally friendly, defect free, cheaper to manufacture (due to the energy required and the automated of the process lowering labour costs) and having the ability to join various thicknesses (Amini, Asadi, and Zolghadr (2014)). More recently concerns regarding the weight of electric and hybrid vehicles have led many

automotive manufacturers to turn to aluminium bodies, instead of traditional steel. The increase in electric vehicles being manufactured has also increased the demand for lightweight yet stiff and heat dissipating battery trays. FSW is applicable in these situations as it has been shown to produce lighter joints than riveting and welds with fewer defects and less postproduction work required than some fusion techniques.

2.6.3 Marine

Friction Stir Welding has several applications in the marine sector. Deck panels, hull material, superstructures, masts and booms are all components that are possible to join using FSW processes (Roldo and Vulić (2019)). Due to FSW's ability to produce joints with lower distortion, thus allowing for a more accurate geometry, together with improved corrosion resistance, strength and ductility to allow rolling for transportation, the process has become widely considered for marine use. Marine applications of FSW also include joining thick section (typically 15-25 mm) 5xxx aluminium alloys used in subsea environments where temperatures range from 0-3°C ('Temperature of Ocean Water' (2001)). Before FSW existed, and certainly before it was considered a mainstream joining method, nickel-steel alloys were used in these conditions as common carbon steels did not provide the fracture toughness needed at such low temperatures. By adding small quantities of nickel to steel it is possible to enhance the fracture toughness at low temperatures (Columbia et al. (n.d.)) however nickel is an expensive material and the addition of it to steel reduces the weldability by fusion techniques. This nickel-steel alloy is however easier to fusion weld than thick section 5xxx aluminium. In recent years, as FSW has become more readily available to use, the marine industry has been able to use aluminium alloys for applications where previously the expensive nickel-steel alloys were used. This is because FSW in 5xxx, even in thick section, is readily achievable which enables the marine industry to benefit from the higher fracture toughness at sub-zero temperatures of aluminium alloys. Further marine application of FSW is the use in aluminium containers for marine cryogenic transport of compressed natural gases (LNG and CNG) as per the benefits for use in subsea conditions.

2.6.4 Rail

Rail is a fourth transportation sector that applies FSW. The rail industry was an early adaptor of FSW processes with manufacturers such as Hitachi and Nippon Sharyo using the joining process for both commuter and express trains ('Friction Stir Welding – Joining the Future of Industry | Cambridge Network' (n.d.)). Examples of how FSW can be applied to the rail industry include production of high-speed trains (such as Hitachi's 'Shinkasen' which can reach up to 320 kph), railway tankers and rolling stock for the underground systems. FSW lends itself well to the rail industry as the process is well suited to performing long linear welds while continuing to produce improved fatigue resistance, stiffness, and durability.

2.6.5 Oil and gas

An application on the horizon for FSW is the use of the process for internal repair and refurbishment of pipelines (Forth Engineering (n.d.)). The Forth Engineering led project, FSWBOT, is designed to machine away existing corroded or damaged pipeline, weld a patch over the area and inspect the weld using NDT methods all while the pipeline is still in operation. This will have a considerable impact on the oil and gas industry as the companies will no longer have to shut down pipelines in order to conduct repairs, making the process very cost effective.

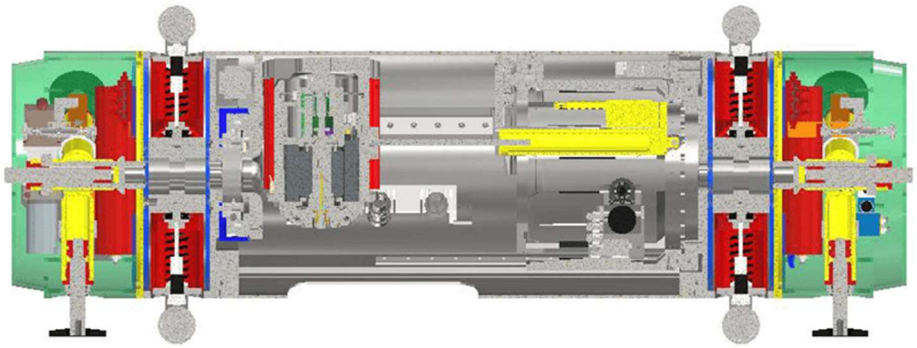

Figure 52 – Schematic of FSWBOT – an underoil Friction Stir Welding robotic crawler (Forth Engineering (n.d.)).

2.6.6 Electronics

Outside of the transportation sector, FSW is used in a variety of other applications. Electrical devices from companies such as Apple Inc. have started to incorporate FSW in manufacturing. From 2012 the 'iMac' was produced 40% thinner than previous iterations through the use of FSW (Gite, Loharkar, and Shimpi (2019)). FSW was used to join the front and back cases together to produce a 'seamless, precise' join designed to remain secure and not allow end users to access the internal components (Dilger (2013)).

2.6.7 Nuclear

Further use includes encapsulating nuclear waste in large copper vessels. Several nations, including Sweden and Finland (World Nuclear Association (2017); Gite, Loharkar, and Shimpi (2019)), encapsulate their nuclear waste in thick walled copper vessels (internally lined with cast iron or boron steel) which can survive 100 000 years. Welding any thick material is challenging but welding 50 mm thick copper is particularly challenging due to the excellent thermal and electrical conductivity the material possesses. FSW is a process weld adapted to joining thick section materials with many publications suggesting up to 70 mm is possible in a single pass. Further reason for using FSW processes is that many vessels are lined with steel, therefore, using arc welding processes can lead to enhanced residual stresses. Arc welding in steel can cause hydrogen entrapment which when exposed to the radiation being contained forms helium, He, an atom much larger than hydrogen and therefore takes up more space within the iron lattice structure, causing a strain and embrittlement which increases the residual stress. FSW does not cause hydrogen entrapment and has been shown to induce compressive residual stresses (Kumar, Mishra, and Baumann (2014)) which improve fatigue life and reduce crack propagation. In addition, regardless of how the vessel is joined an automated process is a necessity to reduce human contact with the radioactive material. FSW, an already predominantly automated process, is easier to use than a fusion welding technique modified to be automated in nature and therefore is a logical option for this purpose.

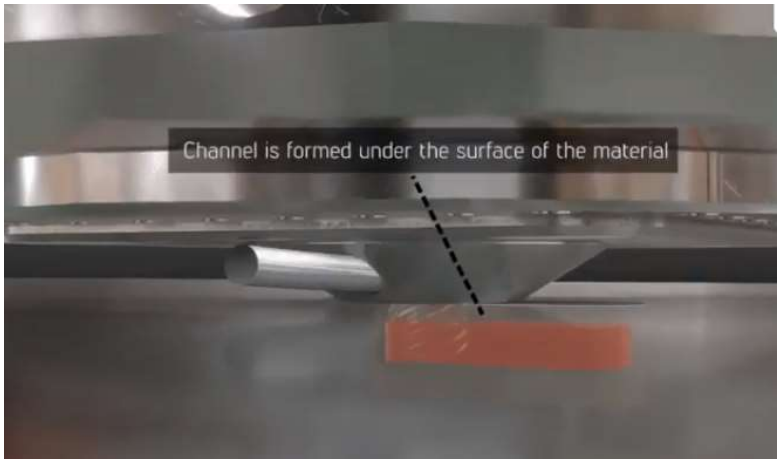

Figure 53 – CoreFlow technology launched by TWI Ltd removes plasticised material from below the surface while maintaining a leak-proof upper seal (Gandra (2020)).

A variant of FSW which is being launched which could be implemented in industry in the near future is CoreFlow. In May 2020 CoreFlow technology was launched by TWI Ltd via Webinar. This technology uses FS processes to form subsurface channels, shown in Figure 53, by ejecting plasticised material out of the top of the tool while maintaining a leak proof upper seal using the pressure applied by the shoulder of the tool (Gandra (2020)). This technology can be used in 'heat thermal management systems' in a wide variety of transportation sectors and electrical components.

2.7 Impact of Friction Stir Welding on industry

2.7.1 Economic/Commercial

When establishing the applications for FSW, the impact the process has on factors such as an industry's commercial, environmental, and social needs, wants and obligations are important to consider. One such commercial want is to reduce manufacturing time and energy consumption to benefit the user financially. Boeing illustrated how beneficial FSW can be when they reported that the FS welded specific design of both United Launch Alliances Delta II & IV expendable launch vehicles had

achieved a cost saving of 60% as well as reducing manufacturing time from 23 to 6 days (S. W. Kallee (2010)). The ability of Friction Stir Welding to make welds in single or just two passes, even in thick sections, reduces manufacturing times significantly. In Figure 54 a dual pass FS weld in 50 mm aluminium alloy is shown next to a MIG weld in the same thickness and grade of alloy. The figure shows that the MIG weld required in excess of 20 passes on both the top and bottom surfaces to form the join. In order to reduce the distortion this process generated, each side was welded alternatively which further slowed manufacturing time due to the need to cool, inspect, clean and rotate the component between welds.

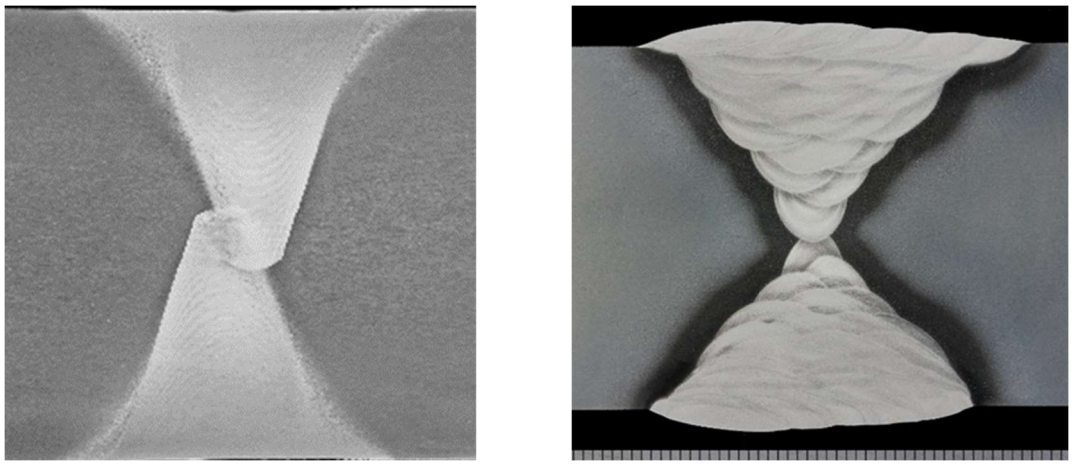

a) 50 mm section aluminium alloy FS welded using the weld-flip-weld technique (Melton (2019)).

b) MIG weld in 50 mm thick aluminium alloy (Melton (2019)).

Figure 54 - Friction Stir and Fusion welding techniques used in thick section aluminium alloys (Melton (2019)).

A further impact of FSW on the commercial needs of industry is the large reduction in post weld work required. This stems from the low distortion produced by FSW coupled with a reduction in repair work necessary. The lower distortion means less reworking of the material is required, saving both time and labour costs while the reduced need to repair welds produced by FSW impacts the costs once the component is in service. The initial start-up costs necessary to purchase bespoke tools (such as the PowerStir™ FSW machine used by TWI Ltd) can burden industrial users however as the balance of

R&D is in aluminium, as shown by Magalhães, Leitão, and Rodrigues (2018) which shows ~70% of R&D is conducted in aluminium, the cost of replacement tools (typically made of H13 steel) is lower than the recurring cost of shielding gases and filler wire used in fusion techniques. The financial benefits are improved further due to the automated nature of the process lowering health and safety costs and the training required to operate the machinery being lower than those required for fusion welding techniques.

The skill and certification required of the operator is an important consideration in selecting a process for industrial use. FSW operators are expected to be certified every two years as per the British Standard, BS EN ISO 25239-3:2011 (Institute of British Standards (2012)), however as the process is predominantly automated the level of training is not as demanding as in MIG welding. MIG welding requires a much higher maintained level of training as the process is manual however certification for the process is every three years ('Master Welders Renewal' (n.d.)). Therefore, FSW has could have a significant impact on industry as lower skilled operators can be used, providing they are certified on a more frequent basis.

2.7.2 Environmental

The environmental impact of FSW is favourable when compared to more traditional fusion welding techniques. One reason for this is that FSW does not require a gas shield to protect the weld which means the excess gases put into the air are reduced. In work conducted by Dawood, Mohammed, and Rajab (2014) it was found that the Gas Metal Arc Welding (GMAW) process released higher amounts of harmful gases such as carbon monoxide and carbon dioxide to the surroundings (2.7 ppm and 346 ppm, respectively) as opposed to 0.6 ppm and 211.6 ppm, respectively, for FSW. This shows a reduction of 450% in the production of carbon monoxide being released during the welding process which is hugely beneficial to the environment. Shrivastava, Krones, and Pfefferkorn (2015) investigated the environmental effect of GMAW and FSW in AA6061-T6. Here, FSW was found to be much more environmentally friendly, reducing the greenhouse emissions, responsible for Global Warming, by 31% with the

carbon dioxide emitted (a method used to express the effect of the processes on the climate) being 6.78 kg and 9.82 kg for FSW and GMAW respectively. Shrivastava et al (2015) also refer to the damage of FSW and GMAW on the Ozone. Measured in terms of the release of chlorofluorocarbon emissions, it was found that FSW was responsible for 1.7×10^{-7} kg CFC-11-Eq. whereas GMAW lead to 2.4×10^{-7} kg CFC-11-Eq. of Ozone depletion.

Further to this, the energy consumption during the FSW process is notably lower than that consumed in Gas Metal Arc Welding (GMAW). Shrivastava, Krones, and Pfefferkorn (2015) illustrate this in Figure 55 which indicates that the total energy used in a weld done by Friction Stir was 175 kWs, versus 303 kWs for a GMAW – a reduction of 42% in the total energy required to perform the joining process. It is worth noting that this difference in energy is exclusive to this material grade and thickness as well as the parameters such as traverse speed. Shrivastava, Krones, and Pfefferkorn (2015) are using different thickness of AA6061-T6 in order to achieve similar tensile properties for both processes, this will impact the energy required to form the joints. Shrivastava et al (2015) also conclude that the difference in energy consumption will grow as the thickness and/or length of the weld increases. It is anticipated that the pre-process work such as cutting grooves in addition to needing to make multiple GMAW passes (whereas FSW can be used in a single pass up to 75 mm thick (Imam et al. (2017); Perrett et al. (2007))) would increase the difference in energy consumed in thicker materials.

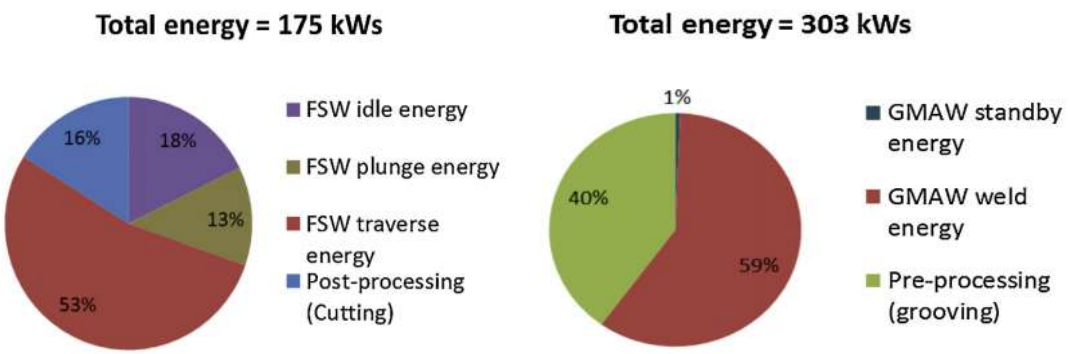

a) Energy consumption of FSW joints

b) Energy consumption of GMAW joints

Figure 55 - Comparison of energy consumption of FSW and GMAW (Shrivastava, Krones, and Pfefferkorn (2015)).

The energy consumption of the industrial sector between 2000-2017 of the EU nations (also known as the EU-28 at the time) has been widely reported on. Tsemekidi-Tzeiranaki et al. (2018) showed that the industrial sector of the EU-28 saw a continual decrease in energy consumption, see Figure 56, over a 16-year period between 2000 and 2016. The proportion of energy used by industry in 2000 was 29.43%, however, over the following 16 years this consumption reduced by 4.44% to 24.99% by 2016. The European Environment Agency (2020) reported that between 2005 and 2017, a period in which FS welding's applications have increased, the energy consumed by industry has dropped on average 1.3% per annum. This, it was stated, was a result of both industry shifting towards less-energy-intensive manufacturing techniques and a continued transition towards a service orientated economy (a sector which saw its energy consumption increase by 0.6% in the same time period). Although this is not explicitly outlining the effect of FSW on industrial energy usage it is possible to see how the need for less energy intense processes have impacted the industrial landscape.

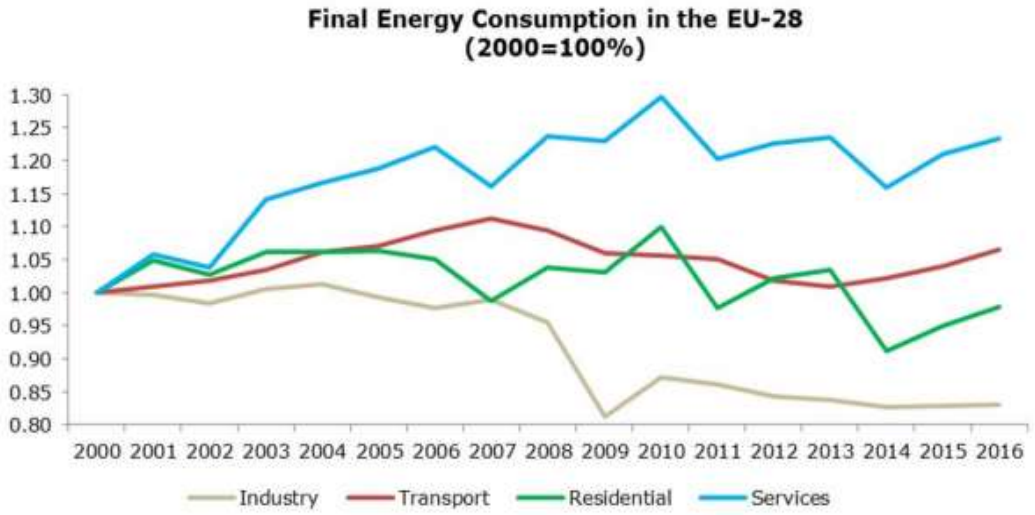

Figure 56 - Change in final energy consumption of key sectors over a 16-year period (Tsemekidi-Tzeiranaki et al. (2018)).

2.7.3 Social

Socially, there are both positive and negative impacts of FSW. As the process is mostly automated the need for labour is reduced and fewer jobs within the field exist than in fusion welding, for example. However, supplementary roles such as machine operators, metallurgists and tool manufacturers are produced generating jobs in other sectors. Furthermore, as FSW becomes more established, there is potential for the creation of work in related sectors such as aluminium extraction and alloy manufacturing. That said the development of FSW relies on the continued use of metals in transportation. Although aluminium alloys are still currently one of the most commonly used materials in aircraft, composites have been on the rise for several decades while aluminium usage has declined, as supported by Mouritz (2012) in Figure 57.

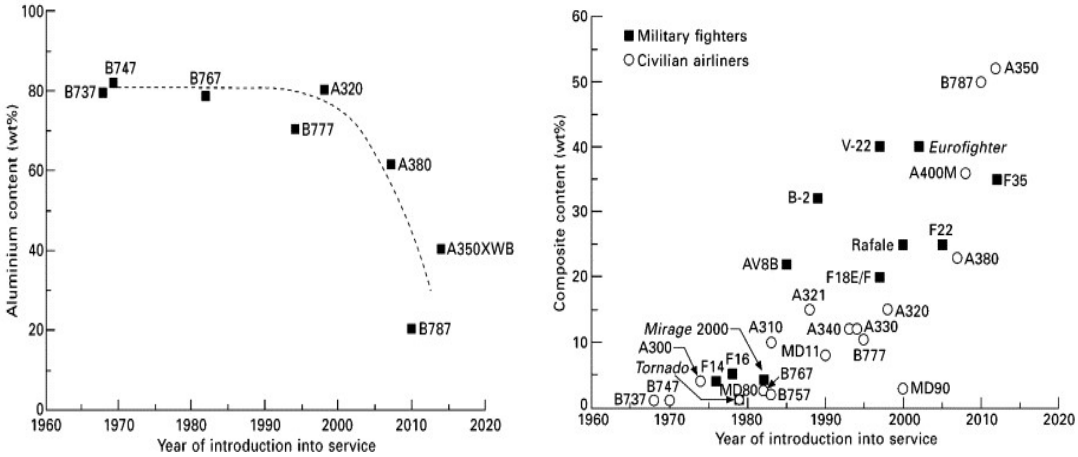

a) Plot showing the decline in aluminium content

b) Plot showing the increase in composite content

Figure 57 - Plots of aluminium and composite content against year of aircraft introduction (Mouritz (2012)).

2.7.4 Limitations to impact

There are however several limitations to FSW that restrict its capabilities and positive impact on industry. Firstly, the material must be well clamped to prevent movement during the joining process. This requires well-designed supports and can limit the complexity of the component being joined. In addition to this, high bending stresses experienced by the tool during the process is a significant limitation. Tool failure is currently one of the biggest hurdles in improving the FSW process. The high price of the components being joined makes it highly desirable to preserve tool life (i.e., ensure the tool doesn't fail within the component) however the high bending stresses experienced can lead to failure of the probe within the material being joined (Du et al. (2020)).

A further issue with FSW, particularly in thick section material, is the higher heat input at the centre of the weld than on either surface. The heat will dissipate out of the material either into the air from the top surface of the material or into the backing plate from the bottom surface. However, in thick section material, the heat is retained within the central region for longer as it cannot dissipate as easily (Yuqing et al. (2016)). This results in a microstructure which is exposed to elevated temperatures for

longer than in the rest of the material which leads to a variation in the properties of the material through the thickness. This means applications must consider the through thickness variation before using the process suitably.

2.8 Relatable papers to the thesis theme

This section identifies and reviews published articles that can be related to the work of this thesis. The published works were subdivided into three key themes from this thesis: thicknesses, FSW techniques and grades of aluminium and sequentially reviewed with regards to their similarity to these key themes.

2.8.1 Papers investigating similar thicknesses

Although there is a vast pool of literature regarding thin section FSW, there is a limited corpus of published work relating to FSW in thick section materials and the process variants that make this possible. FSW of metals, and more specifically aluminium alloys, of thicknesses up to 50 mm requires specialist equipment and is not yet fully understood, however attempts have been made to understand how the process effects the microstructural behaviour. Work that most closely resembles that of this project is that of Liang et al. (2019) which produced a double sided FS weld in 42 mm thick AA6082-T6. Liang et al (2019) is an interesting paper to consider due to the parameters used to produce the weld. It is recorded that the rotational and traverse speeds were 400 rpm and 110 mm/min respectively. This would produce a 'hot weld' and would likely be used, although not stated, to preserve tool life. Despite these parameter selections the weld retained as much as 72.8% of the tensile properties vs a standard parent material (PM) value of 310 MPa. Liang et al (2019) also consider the impact of FSW on the precipitates present. It is found that the PM contains a high density of needle shaped β'' (Mg_5Si_6) which evolves into magnesium-silicide (Mg_2Si or β-phase) at above 300 °C. This phase is coarser than β'' and Liang et al (2019) found that the double processed region, where the passes overlapped, was 62.5% coarser than the area investigated near the shoulder of the tool.

Prior to Liang et al (2019), attempts had been made to understand the effect FSW has on thick section aluminium. Canaday et al. (2013) investigated the effects of FSW 32 mm thick AA7050-T7451 although they used a conventional method in a single pass. It was observed that a variation in the properties of the weld occurred through the thickness of the material, from the crown to the root of the weld. Canaday et al (2013) suggested that a temperature decrease from crown to root caused the grain structure to vary through the thickness of the material resulting in the change in properties. Figure 58, from Canaday et al (2013), shows the grain size of as welded and post weld heat treated samples as a function of distance from the root.

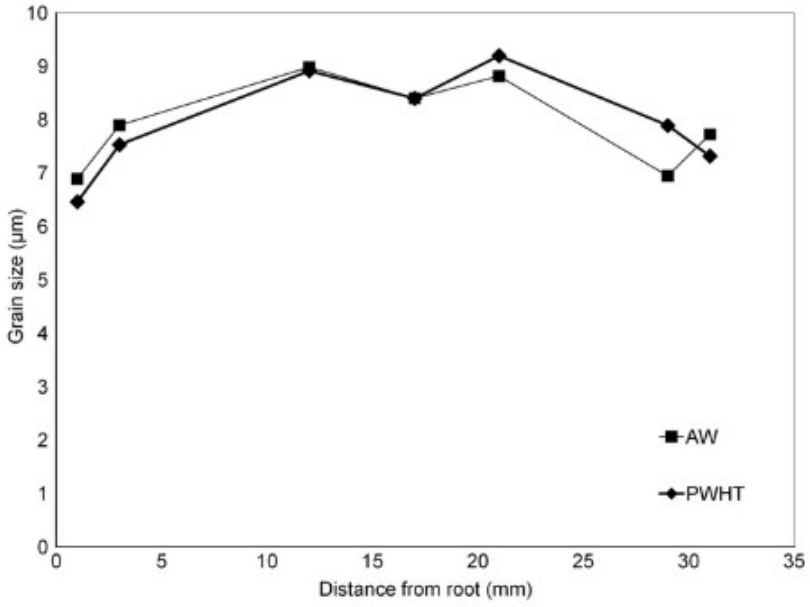

Figure 58 - Grain size as a function of distance from the root (Canaday et al. (2013)).

From this Canaday et al was also able to express that the central region of the material has the largest grain size of any part of the weld. Grains in this region were measured at around 8-9.5 µm whereas the gains near the crown and root of the weld were measured at 6-7.5 µm. This was explained as being a result of the time at which the temperature was elevated. The raised temperatures of the welding process are retained longer in centre of the material due to the conductive rate of the material. As the high temperatures linger, the grains in the region continue to grow to a larger

extent. Consequently, Canaday et al concludes that the grain growth experienced during the welding processes was a result of both the temperature the grains were subjected to and the duration of time at which they were held at the temperatures.

Thick section was defined in section 1.1 as being of thickness >20 mm. Huang and Reynolds (2018) was reviewed as they investigated the influence of FSW on the residual stresses of 25 mm thick AA7099-T7651. This investigated four variations of the welding process – stationary shoulder single and dual pass and conventional single and dual pass – using the cut compliance technique developed by Cheng and Finnie (1990), Schindler, Cheng, and Finnie (1997) and Prime (1999). As such it holds a greater similarity to the work conducted in this paper as it crosses over with section 2.8.2. From their work, it was observed that the residual stress resulting from the conventional and stationary shoulder variants showed little discrepancy although the single pass processes showed lower and more asymmetric values versus the dual pass processes. Huang et al also reported that 'critically' the power required in the single pass conventional process was <2% greater than in the stationary shoulder single pass attempt and that the temperature of the probe in the conventional process was 7 °C hotter than in the stationary shoulder weld for a single pass. Huang et al (2018), however, never state the temperature values instead only stating that the difference is 7 °C. Huang suggests that this is a small discrepancy and implies that the similarity in the power input and temperature are contributors in producing such similar residual stresses between the two shoulder variants.

It is clear that there is a limited corpus of work in FSW of 50 mm thick aluminium alloys. The majority of work that can be considered thick section (>20 mm) is typically thinner than 50 mm as shown. Liang et al. (2019), Canaday et al (2013) and Huang and Reynolds (2018) all investigated thick section aluminium material but none of these authors exceeded 42 mm.

2.8.2 Papers investigating similar techniques

One of the principle objectives of this project, set out in section 1.3, was to produce welds in three grades of aluminium using three different FSW techniques; i) Weld-Flip-Weld, ii) Simultaneous Double Sided and iii) Supported Stationary Shoulder. Studies have been conducted in these techniques previously, examples include the work of Xu et al. (2018), Rahmatian, Mirsalehi, and Dehghani (2019) and W. F. Xu, Luo, and Fu (2018). However, the majority of the work focuses on thickness <20mm and is therefore not defined as thick section. Xu et al. (2018), for example, investigated the joining of 12 mm thick AA7085-T7452 using the WFW-FSW technique at a variety of rotational rates, weld speeds and strain rates. Using rotational rates of 300 rpm, 600 rpm, 950 rpm and welding speeds of 60 mm/min, 120 mm/min and 180 mm/min respectively, Xu et al (2018) presented hardness data, as shown in Figure 59, that suggested increasing weld speed reduced the impact of FSW on the hardness. This was explained as being a result of grain growth and the precipitate strengthening effect being reduced by grain coarsening – which was stated to occur in the slower/hotter weld.

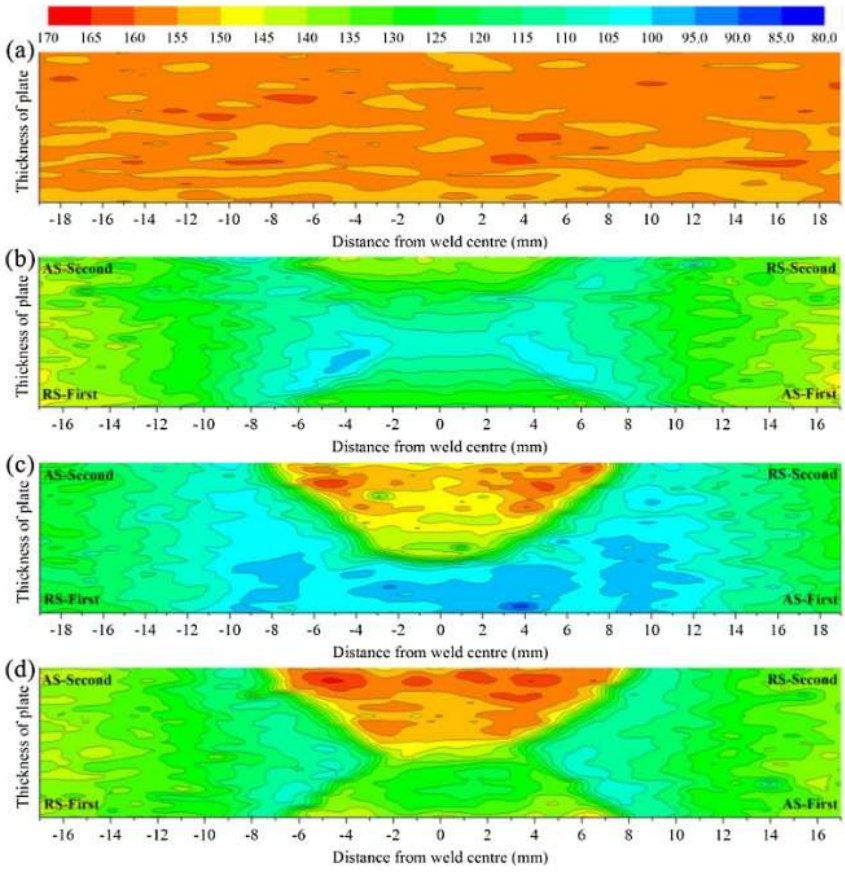

Figure 59 – Micro-hardness mapping conducted by Xu et al (2018). (a) BM, (b) 300 rpm and 60 mm/min, (c) 950 rpm and 60 mm/min, (d) 950 rpm and 180 mm/min.

Zhou et al. (2016) similarly investigated parameter selection by producing 'hot and cold' welds using traverse speeds of 100 mm/min and 400 mm/min respectively. Using 5 mm thick AA7050-T7451, Zhou et al (2016) showed that the microstructural and mechanical properties were more significantly altered during the hot weld process. Zhou recorded a parent material ultimate tensile strength (UTS) of ≈500 MPa, this was reduced in the weld to ≈400 MPa during the hot weld process - a reduction of 20% - and ≈475 MPa (5% reduction) in the cold weld process. One concern with the work of Zhou is that although the methodology is detailed and provides the parameters of the welding, there is no statement or evidence of repeatability, suggesting a lack of reliability. A further concern is no standard to which the testing was conducted has been stated and therefore it is presumed that one was not followed.

The work by Zhou et al (2016) would suggest that hotter welds are weaker, something that work by Singh et al. (2017) supports. Singh et al conducted work comparing Tungsten Inert Gas (TIG) welding with FSW in 6 mm thick AA6082-T651. It was found that joint strength versus the parent material was 85% and 65% for FSW and TIG respectively. TIG welding is a fusion technique which requires high temperatures to melt the material in order to join them. Although the hot weld conducted by Zhou does not reach such temperatures as to melt the material, comparisons with their work and the work of Singh can be drawn and show that the cooler processes in both papers produce stronger, more efficient joints. FSW is a solid-state joining process, therefore a colder process than TIG welding. Colder welds within FSW are produced by running faster traverse rates and/or lower rotation rates which result in higher mechanical working and lower thermal working. This has the effect, especially in heat treatable alloys, of reducing the solution rate and amount of precipitation growth during the welding process as well as breaking down and refining the grains to a factor of almost ten times smaller than in the parent material. This results in a material that retains a higher percentage of the parent materials properties as demonstrated by a vast number of publications in thin section FSW.

As mentioned previously, Rahmatian, Mirsalebi and Dehghani (2019) is an example of work conducted previously using a similar technique to that of this project. In this instance, ‘double-sided’ FSW in 10 mm thick AA5083 was conducted. The methodology of Rahmatian et al (2019) indicated that ‘double-sided’ FSW referred to WFW-FSW, an important note as this could have been interpreted as SDS-FSW by mistake. Investigation of the properties concluded that a significant increase occurred in the microhardness of the stir zone (SZ), in accordance with the Hall-Petch equation, due to an ‘intensive reduction in grain size’ occurring in the SZ. However, what Rahmatian et al (2019) conclude is there is little change in the hardness between the SZ and the PM. It is reasoned that in the Hall-Petch equation only high-angle grain boundaries are assumed to act as obstacles to dislocation movement. Instead, ‘severe’ plastic deformation resulting from the tools rotation leads to a fine equiaxed grain structure with high density dislocations. The result of this is dislocation tangle occurs at smaller

intervals than the grain diameter which consequently has led to a deviation from the Hall-Petch relationship.

The final example of research that investigates similar techniques to those in this project is W. F. Xu, Luo, and Fu (2018) which used both conventional single sided and bobbin FSW techniques to FS weld 12 mm thick AA7085-T7452. Parameters of 300 rpm, 60 mm/min and 2.5 ° tilt angle were used in the single sided weld while the bobbin weld was conducted using 150 rpm, 150 mm/min and 0 ° tilt. W. F. Xu, Luo, and Fu (2018) highlight the effect of FSW on grain size suggesting that maximum growth following the conventional single sided weld occurred in the middle of the stir zone. Significant grain growth was also reported in the bobbin weld which had grains of up to 42.49 µm within the HAZ. It was concluded that the average grain size was affected by frictional heat, strain rate and degree of recrystallisation – which was found to be more prominent in the welds than in the parent material.

There are numerous papers that investigate the influence of various FSW techniques including the three techniques investigated in this project, however, this work is often conducted in thin section (<20 mm) aluminium.

2.8.3 Papers investigating similar grades of aluminium

An important feature used to identify research similar to that of this project was the alloy grade. As stated in section 1.3 three grades of aluminium; AA5083-H111, 6082-T651 and 7050-T7451 were to be FS welded using the three techniques discussed. In addition to the work of Liang et al (2019), Canaday et al (2013) and Singh et al (2017), which investigated AA6082-T6, 7050-T7451 and 6082-T651 respectively, work by Silva-Magalhães et al. (2019) investigated 20 mm thick AA6082-T6. Silva-Magalhães et al. (2019) state that understanding the temperature the material is subjected to during welding is one of several pieces of data desired to help in determining the effect of the process parameters on the mechanical properties and microstructure. The temperatures experienced by the FSW tool can also provide useful information

regarding the material that is stirred during the process. To this end, Silva-Magalhães et al. (2019) presented work on the in-situ temperature measurement in FSW of 20 mm thick AA6082-T6. A tapered Triflat^{TM} tool with a probe length of 19.7 mm was used to produce the welds of 500 mm in length. It was concluded from this work that the peak temperature experienced by the tool during welding was located on the transition region between the shoulder and probe and on the retreating-trailing side, see Figure 60. The highest temperature recorded during the welding was 607 °C, which exceeded the 483 °C solution temperature of the material ('Aluminum 6082-T6' (n.d.)). It is noted that this temperature is specific to this work as the parameters such as traverse speed and rotation rate significantly influence the temperatures experienced. Silva-Magalhães et al (2019) also commented that the tip of the tool is consistently cooler than the shoulder. This is to be expected as the shoulder was of conventional design which means that it also rotated (as well as the probe) generating more frictional heat in this region and therefore further enhancing the heat input in this region.

A further article investigating AA6082 is Krasnowski, Hamilton, and Dymek (2015) who investigated the influence of tool shape and weld configuration on microstructure and mechanical properties of 8 mm (single sided conventional) and 10 mm (double sided) thick AA6082. Krasnowski et al (2015) showed similar reductions in hardness as shown in the figures provided, recording the parent material at nearly 100 HV in the 8 mm thick plates while the HAZ experienced hardness's of around 50 HV. Similarly, 10 mm thick material retained around 50% of the parent materials hardness within the HAZ. Krasnowski, Hamilton, and Dymek (2015) also highlights the difference in hardness through the thickness of the material. In the 8 mm thick single sided weld, it is shown that the hardness in the stir zone drops from ~80 HV to ~70 HV as the root of the probe is approached. However, the same is not observed in the double-sided weld in 10 mm thick material. The hardness in this instance remains consistent at ~70 HV. This would suggest that the heat input from the two separate tools effected grain growth evenly through the plate thickness.

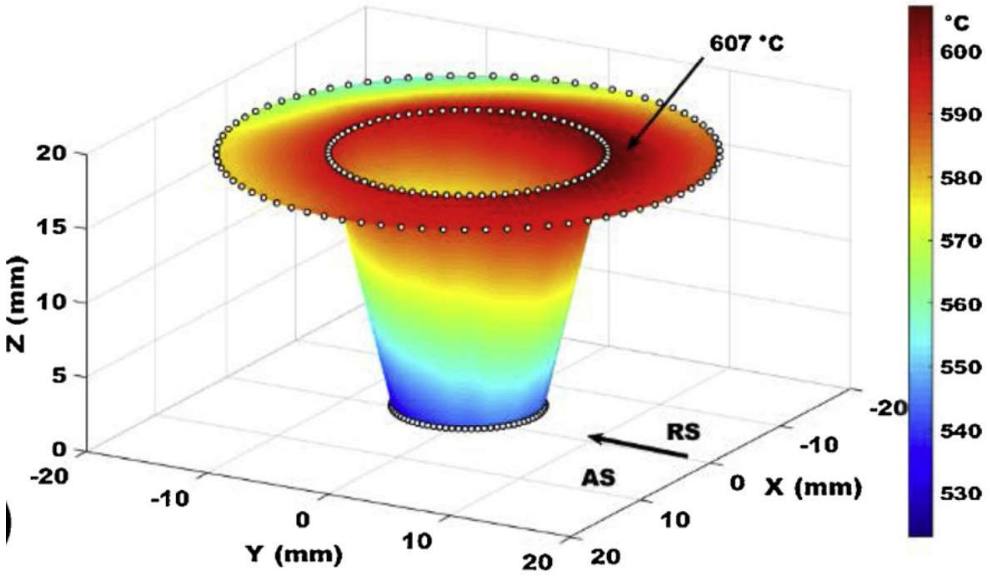

Figure 60 - Temperature measurement around the tool taken from three thermocouples each with 75 measurement points Silva-Magalhães et al. (2019).

The final alloy investigated in this project is AA5083-H111. Chen et al. (2016) investigated the same alloy with a different temper as they looked at the influence of parameter selection in FSW of 3.5 mm thick AA5083-O. They found that the hardness of the material dropped by ~20% in the HAZ but rose back to 85/90% of the parent materials value within the stir zone for a weld with 600 rpm and 360 mm/min rotation and traverse speeds respectively. Chen et al (2016) then produced a weld with a higher rotation rate but the same traverse speed (1200 rpm, 360 mm/min), thus a hotter weld. Chen et al (2016) was able to show a wider HAZ in the hotter weld with the hardness dropping as low as ~75 HV from ~100 HV. Therefore, by doubling the rotation rate, the hardness was only reduced by a further 5%. As the material is non-heat treatable, the added heat generated by the faster rotation rate is unlikely to impact the material in the same way if it were heat treatable. However, the higher rotation speed will generate a higher mechanical working which will have some influence on the work hardening of the material.

The number of papers conducted using the grades of alloy to be investigated in this project is vast. Although not all papers use similar thickness of material or FSW techniques, there are many papers that investigate conventional FSW in these alloys.

3 Methodology:

3.1 Materials

3.1.1 Aluminium alloy 5083-H111

The first of three grades of aluminium alloy used in the study was AA5083-H111. The standard composition and properties of this alloy are shown in Table 5 and Table 6. AA5083-H111 is a non-heat treatable alloy and is hardened by working. The temper designation of 'H111' indicates that the plates were partly work hardened by shaping processes (Aalco n.d.).

Component Wt. %	AA5083-H111	AA6082-T651	AA7050-T7451
Al	92.4 - 95.6	95.2-98.3	87.3 - 90.3
Cr	0.05 - 0.25	Max 0.25	Max 0.04
Cu	Max 0.1	Max 0.1	2 - 2.6
Fe	Max 0.4	Max 0.5	Max 0.15
Mg	4 - 4.9	0.6-1.2	1.9 - 2.6
Mn	0.4 - 1	0.4-1.0	Max 0.1
Other, each	Max 0.05	Max 0.05	Max 0.05
Other, total	Max 0.15	Max 0.15	Max 0.15
Si	Max 0.4	0.7-1.3	Max 0.12
Ti	Max 0.15	Max 0.1	Max 0.06
Zn	Max 0.25	Max 0.2	5.7 - 6.7
Zr	-	-	0.08 - 0.15

Table 5- Standard composition of AA5083-H111, AA6082-T651 and AA7050-T4751 (‘ASM Material Data Sheet - AA7050-T7451’ n.d.; ‘ASM Material Data Sheet - AA5083-O’ n.d.; ‘Aluminum 6082-T6’ n.d.)

Property	AA5083-H111	AA6082-T651	AA7050-T7451
UTS (MPa)	290	310	524
Yield Strength (MPa)	145	260	469
Elongation (%)	22	10	11
Vickers Hardness (HV)	87	95	162
Thermal Conductivity (W/m-K)	117	180	157
Annealing temp (°C)	413	380-420	413
Solution temp (°C)	-	483	477
Ageing temp (°C)	-	~200	121-177

Table 6 - Standard properties of AA5083-H111, AA6082-T651 and AA750-T7451 ('ASM Material Data Sheet - AA7050-T7451' n.d.; 'ASM Material Data Sheet - AA5083-O' n.d.; 'Aluminum 6082-T6' n.d.)

3.1.2 Aluminium alloy 6082-T651

The second grade of aluminium alloy used in the work was AA6082-T651. The standard composition and properties of this alloy are shown in Table 5 and Table 6. AA6082-T651 is a heat treatable alloy and is strengthened through a heat treatment process as previously described in section 2.2.5. The T651 temper suggests that the alloy was solution heat treated, stress relieved by stretching then artificially aged (El-Shennawy, Abdel-Aziz, and Omar (2017)).

3.1.3 Aluminium alloy 7050-T7451

The final material used in the study was AA7050-T7451. This material grade is an Al-Mg-Cu-Zn alloy and was the strongest alloy to be investigated, as shown by the standard composition and property values given in Table 5 and Table 6. Like the AA6082-T651 samples, the AA7050-T7451 material was heat treated. The T7451 temper indicates that the samples were heat treated as a result of being stress-relieved by controlled stretching and artificial over ageing (Alumeco n.d.).

3.1.4 Plate dimensions

Two plates of the dimensions stated in Table 7 were joined in the rolling direction by the techniques indicated to form the samples investigated. As shown, the SSS-FSW technique was conducted using shorter plates. This was done as the technique was untested in such thick section material and therefore required an investigation into tool design.

Friction Stir Welding Technique	Plate dimensions (mm)
Weld-Flip-Weld	900x130x50
Simultaneous Double Sided	900x130x50
Supported Stationary Shoulder	500x130x50

Table 7 - Dimensions of plates welded during the project.

3.2 Equipment used

3.2.1 Tooling

The probe used in the Weld-Flip-Weld (WFW-FSW) process was a tapered TriFlat™ tool made from MP159, shown in Figure 61. The tool, photographed in Appendix 2, had previously been used in 14 welds prior to this project and had a cumulative weld length of 9380 mm. A second tapered TriFlat™ tool made from MP159 was used in conjunction with the first tool to produce the Simultaneous Double Sided (SDS-FSW) samples. This tool, pictured in Appendix 3, had previously been used in 8 welds and had a cumulative weld length of 5060 mm.

For the Supported Stationary Shoulder (SSS-FSW) process a variety of bobbin tools were used. This was due to the process not being developed to the same extent as the other techniques investigated and therefore work into the effect of the tool design was required. Tool steel H13 was used in the Supported Stationary Shoulder process

for joining plates of AA6082-T651 and AA5083-H111 while a stronger tool of MP159 nickel-cobalt based super alloy was used to produce welds in AA7050-T7451 plates. The bobbin tools used were designed with three or four flat sides and different thread pitches to investigate their performance during the process. These tools, shown in Figure 62 - Figure 66 were all new and consequently had been used in 0 welds prior.

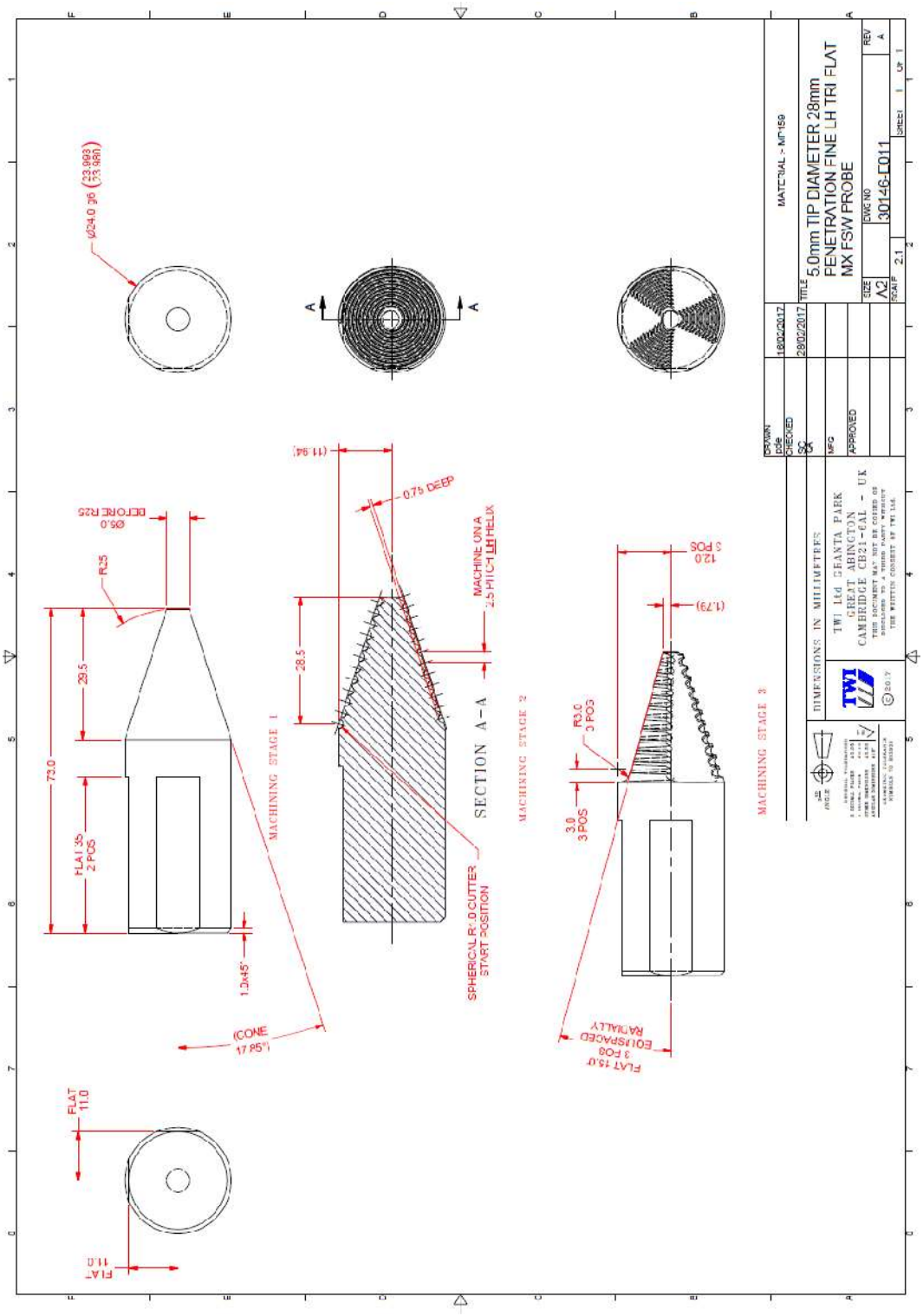

Figure 61 - Drawing of TriflatTM tool 30146-E011, used during WFW and SDS FSW.

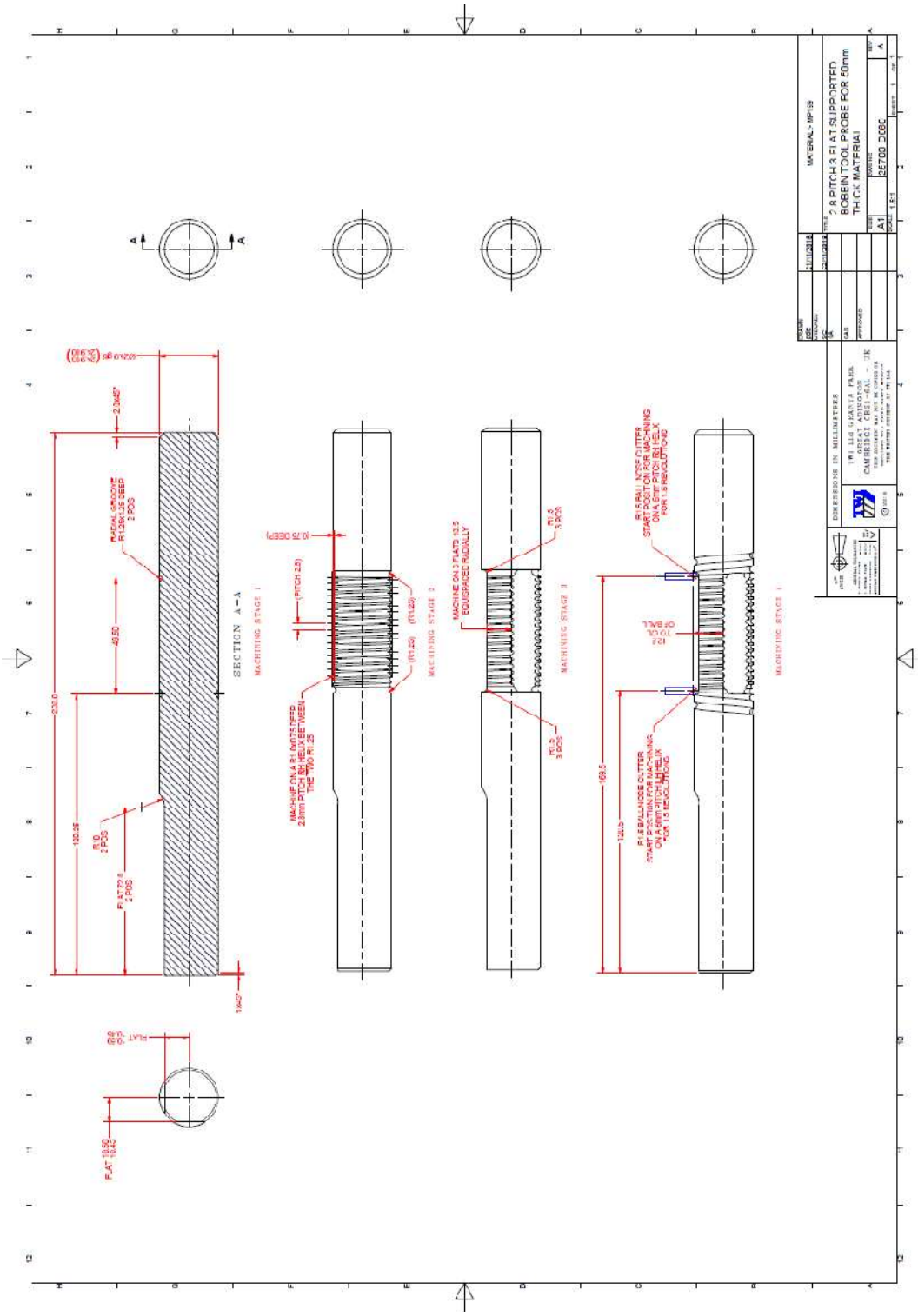

Figure 62 - Tool D060, using 3 flats and fine thread pitch to weld using SSS-FSW technique.

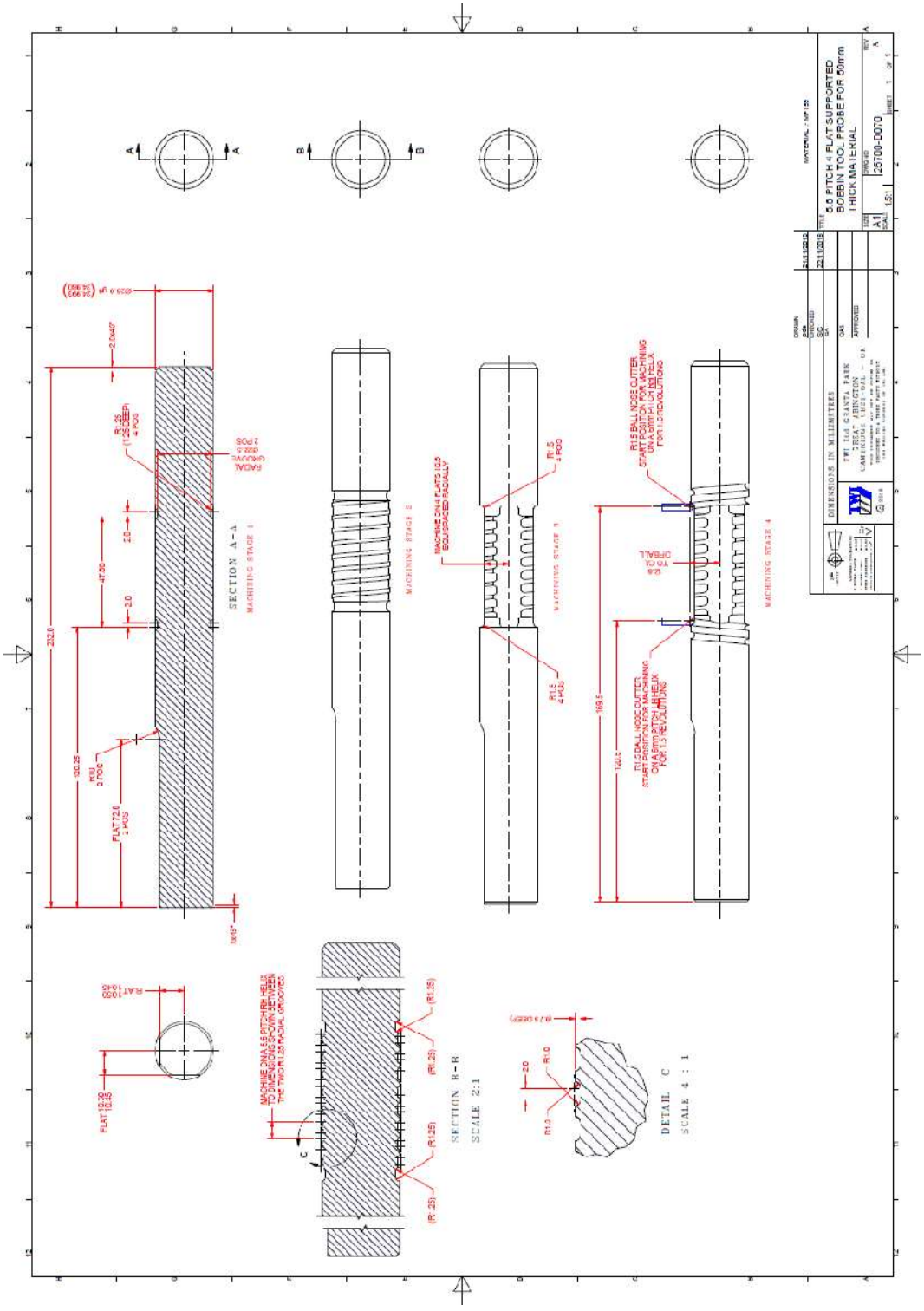

Figure 63 - Tool D070, using 4 flats and coarse thread pitch to weld using SSS-FSW technique.

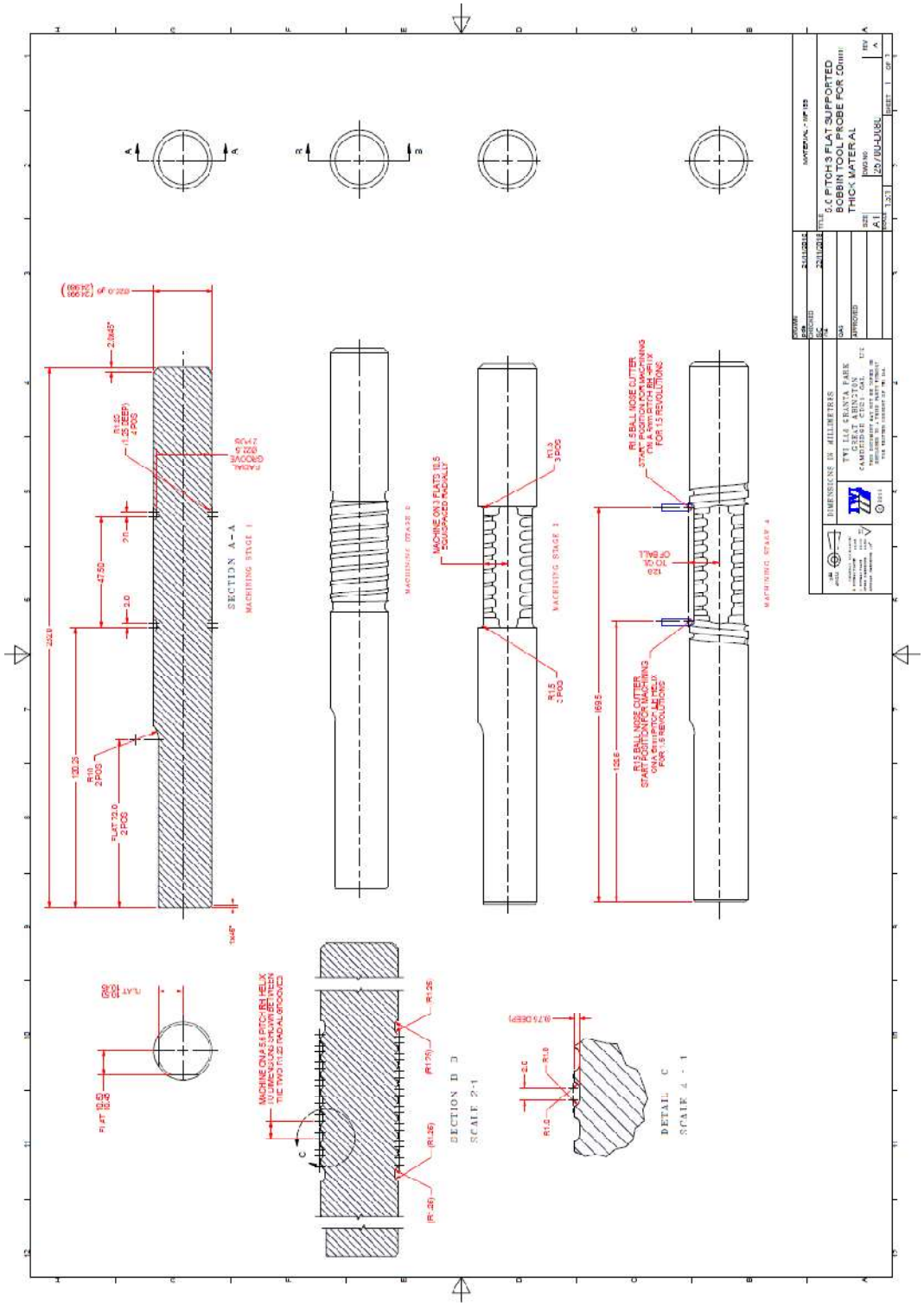

Figure 64 - Tool D080, using 3 flats and coarse thread pitch to weld using SSS-FSW technique.

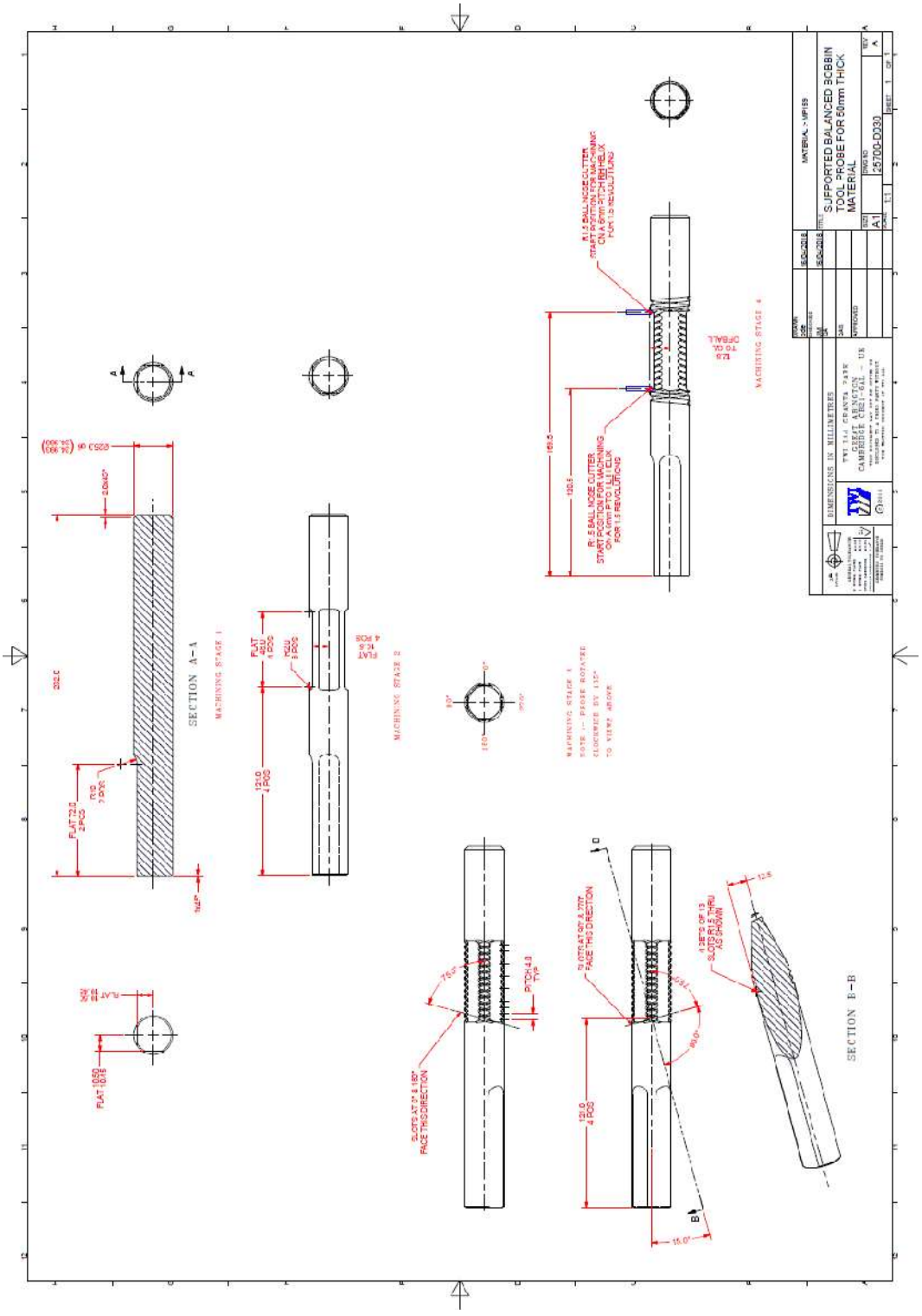

Figure 65 - Tool D030, using 4 flats and fine thread pitch to weld using SSS-FSW technique.

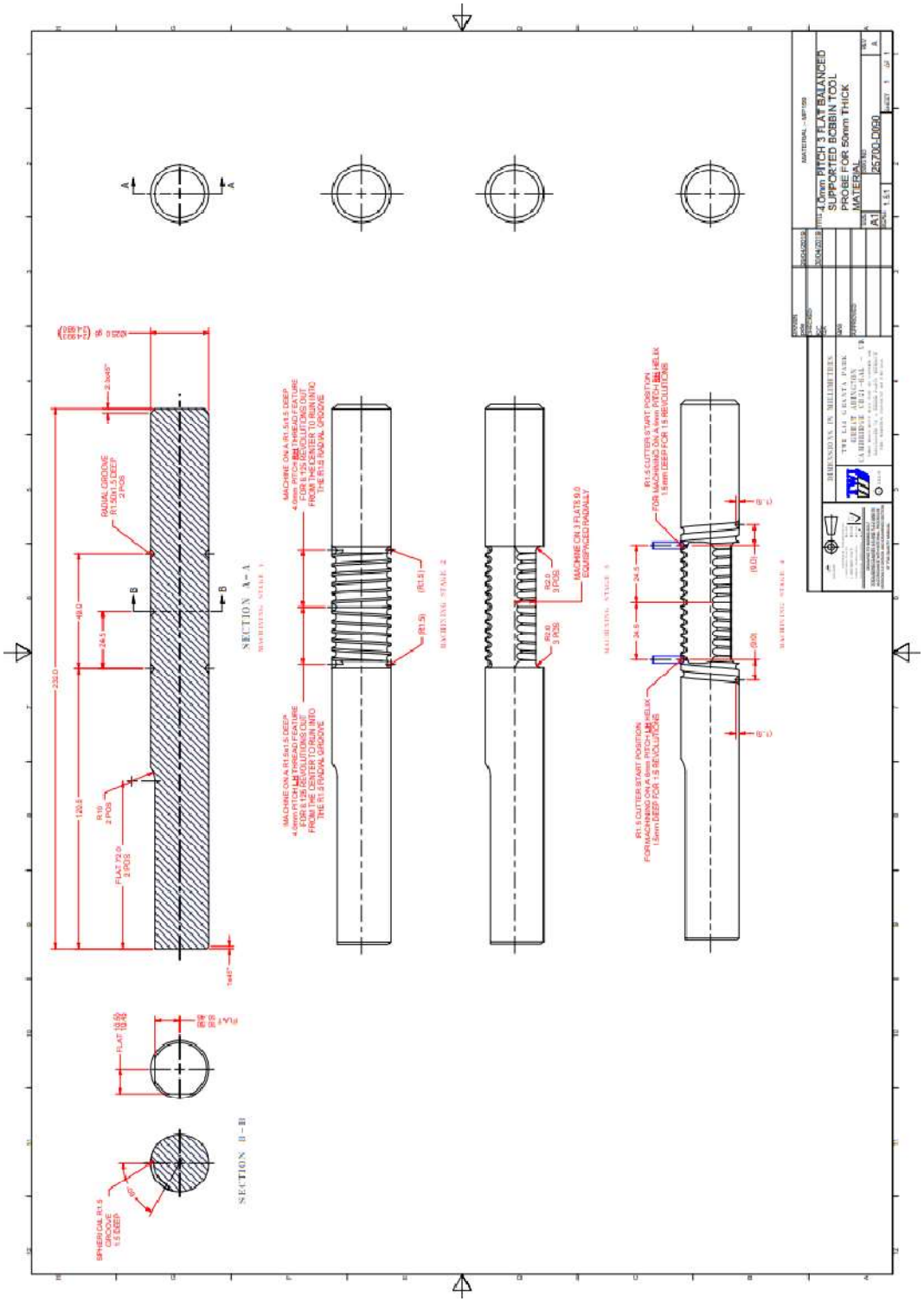

Figure 66 - Tool D090, using 3 flats and 4mm thread pitch to weld using SSS-FSW technique.

3.2.2 Friction Stir Welding machine specifications

All welds for this project were produced at TWI Ltd using the PowerStir™ FSW machine, pictured in Figure 67.

Figure 67 – PowerStirTM FSW machine at TWI South Yorkshire.

The specifications of the two heads of this machine are given in Table 8:

	Upper head	Lower head
No of Axes	8	4
Spindle Power	132 kW	60 kW
Spindle Speed Continuous	0-1000 rpm	0-1000 rpm
Axes Traverse Rate	0-3000 mm/min	0-3000 mm/min
Max. Spindle Torque	2480 Nm @ 500 rpm	1130 Nm @ 500 rpm
Z Force	0-150 kN	0-100 kN
Force on X and Y axes	0-100 kN	0-100 kN
A&B Axis Tilt	± 15 °	± 10 °

Table 8 - Specifications of the TWI PowerStir™ FSW

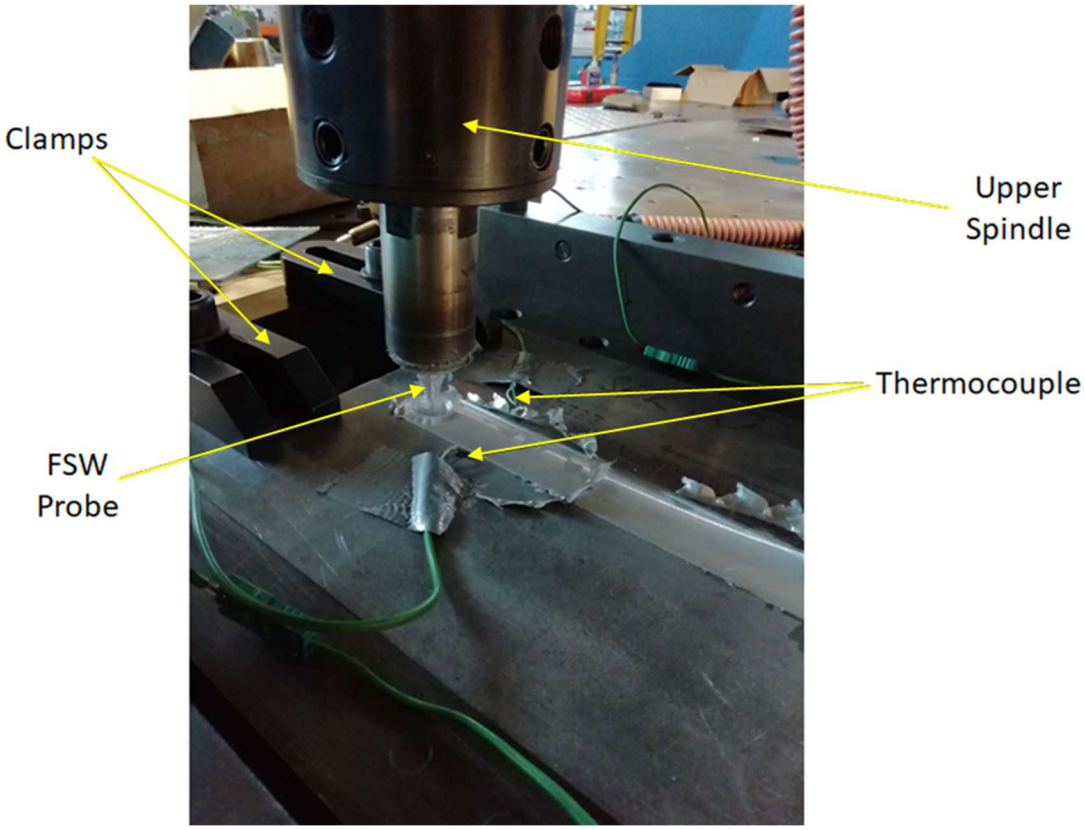

Figure 68 - Diagram of tooling and clamping.

The diagram in Figure 68 identifies key components of the weld set-up such as the thermocouples, spindle, and clamps. The location of the clamping was not predetermined by a standard but instead to ensure that the workpiece did not move. Similarly, the torque to which each clamp was tightened was not pre-set but was tightened to a level that the clamp was secure. This was the approach recommended by TWI.

3.3 Weld parameters

The parameters of each weld were selected based on previous work by TWI Ltd (TWI Ltd (2018b)) which provided insight into parameters that produced good quality welds. A good quality weld was judged based on appearance, energy input and UTS. Each of Weld-flip-weld (WFW), Simultaneous Double Sided (SDS) and Supported Stationary Shoulder (SSS) were used to produce a weld in each of the three aluminium alloys, although in AA6082-T651 four welds were produced using the SSS process to account for the four tool designs. Due to the desire to preserve tool life, welds using the SSS process were 'hotter' than those using WFW or SDS-FSW to reduce the weld forces such as torque and Z-force. These were monitored using the data logger installed as part of the PowerStir^{TM} machine.

Unsheathed K-type thermocouples were used to monitor surface temperatures; these were positioned as per the asterisks in the schematic shown in Figure 69. Surface temperatures were recorded for both passes of WFW welds in AA5083 and AA7050 as well as the upper surfaces of the SDS welds in the same grades. Thermal monitoring equipment was not available for the welds created using AA6082 material.

Each weld was assigned an identification number, GXX. The identification number and key parameters for each weld used are shown in Table 9. The weld data extracted from the PowerStir^{TM} is presented in section 4. Weld forces and parameters such as traverse speed and spindle rotation were recorded during each weld and plotted against the distance travelled.

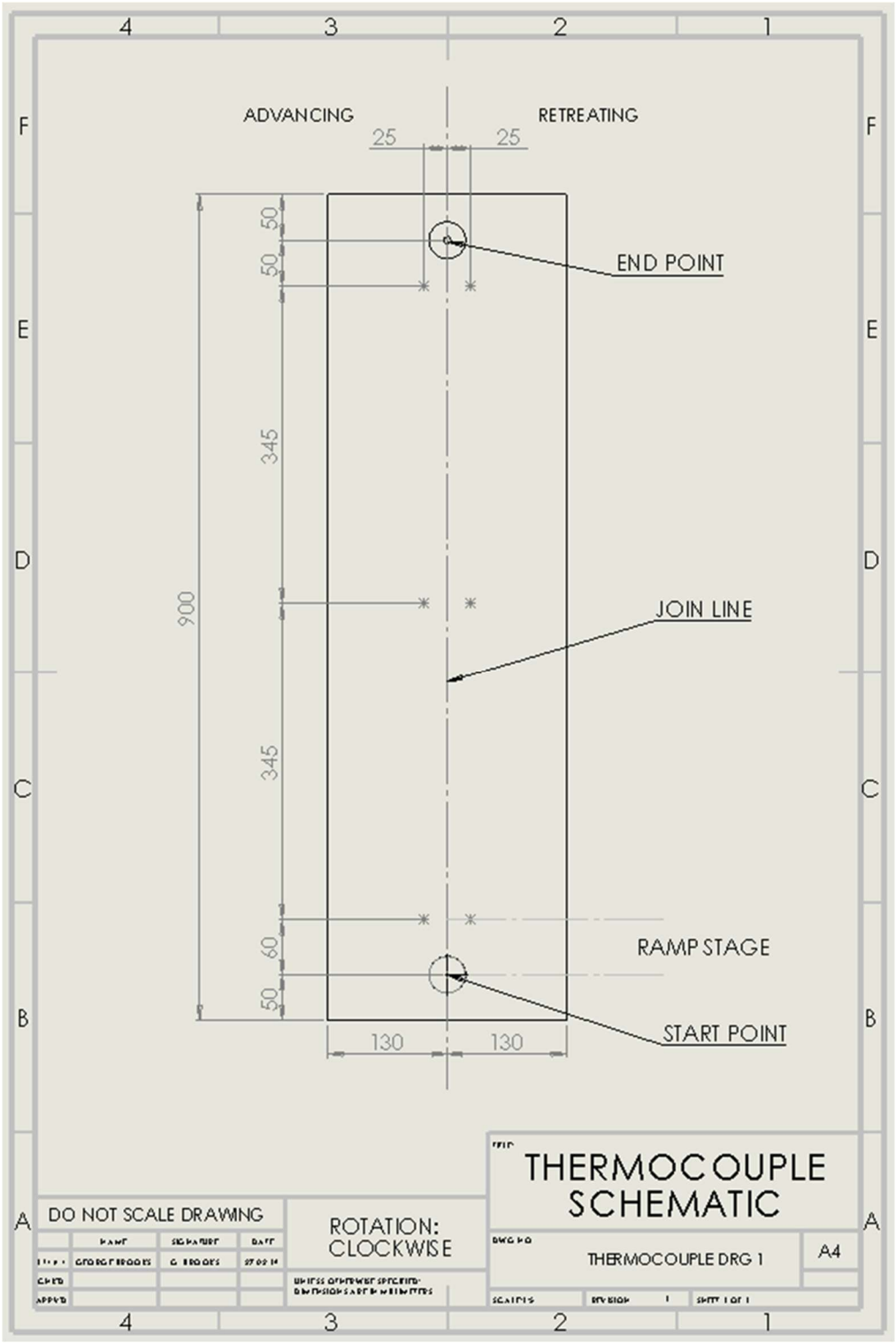

Figure 69 - Schematic detailing the location of the thermocouples used to measure surface temperature during welding. (* denote thermocouple positions.)

Material	Weld ID	Weld Type	Tool used	Weld Pass	Traverse Speed	Spindle Rotation	Tilt Angle
					mm/min	rpm	°
AA5083	G07/08	WFW	30146-E011	1st pass	130	129.70	2
				2nd pass	130	129.50	2
	G13	SDS	30146-E011	Upper	130	109.49	2
				Lower	130	109.85	2
	G34	SSS	D090	Single Pass	60	182.00	0
AA6082	G20/21	WFW	30146-E011	1st pass	150	130	2
				2nd pass	150	130	2
	G22	SDS	30146-E011	Upper	252	129	2
				Lower	252	129	2
	G14	SSS	D060	Single Pass	245	199.00	0
	G16		D070	Single Pass	245	199.00	0
	G17		D030	Single Pass	245	199.00	0
	G19		D080	Single Pass	245	199.00	0
AA7050	G03/04	WFW	30146-E011	1st pass	130	129.64	2
				2nd pass	130	129.47	2
	G12	SDS	30146-E011	Upper	130	109.57	2
				Lower	130	109.91	2
	G18	SSS	D090	Single Pass	59	122.00	0

Table 9 - Weld identification and key parameters.

Further 'back-up' material was produced where possible to provide excess material to that needed to complete the body of work, however due to demand for the machinery required this was sporadic and did not necessarily cover the materials and techniques investigated wholly. The ‘back-up’ welds are detailed in Table 10.

Material	Weld ID	Weld Type	Tool used	Weld Pass	Traverse Speed	Spindle Rotation	Tilt Angle
					mm/min	rpm	°
AA5083	G05/06	WFW	30146-E011	1st pass	130	130	2
				2nd pass	130	130	2
AA6082	G15	SSS	D060	Single Pass	245	200	0
AA7050	G09/10	WFW	30146-E011	1st pass	130	130	2
				2nd pass	130	130	2
	G11	SDS	30146-E011	Upper	130	110	2
				Lower	130	110	2

Table 10 – Weld identification and key parameters of ‘Back-up’ welds.

3.4 Post weld ageing treatment

Once welded, all plates were sectioned using a bandsaw to produce a micro hardness sample, a macro sample and 3 tensile samples, as indicated in Figure 70. These consisted of 10 mm, 10 mm and 60 mm of traverse distance respectively, therefore totalling 80 mm per set of samples. The heat treatable AA7050-T7451 plates were divided into 4 sets, as shown in Table 11, to enable natural ageing for different time periods to occur. These time periods are shown in the table.

Ageing period	Traverse length required for analysis (mm)
	AA7050-T7451
0 months	80
6 months	80
12 months	80
18 months	80

Table 11 - Sample sets required per weld for natural ageing of heat treatable alloys.

The 0-age time was typically a day due to the required time to section, transport and test these samples. The 6-month intervals were selected to provide information on how significant time periods of natural ageing were impacting the properties of the welds. These time periods are also evenly spaced out which was designed to allow the work on the previous set of samples to be carried out in the 6-month time frame. As the end date for each ageing cycle was approached, sample sets were placed in freezers, set to -18 °C, to stop the ageing process while testing equipment was made available. Once equipment was available the ageing cycle was allowed to finish, and mechanical testing/microstructural analysis was conducted. Similar to the unaged samples, in reality the time of ageing varied by 24/48 hours.

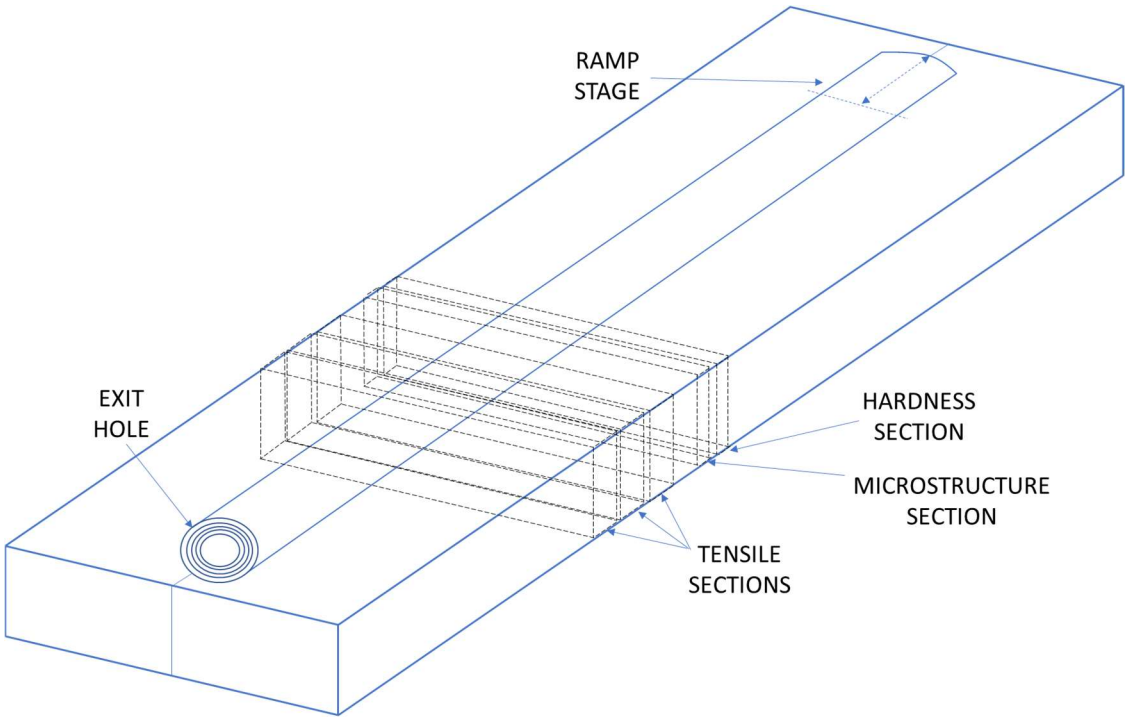

Figure 70 - Diagram showing sample sections in relation to the welded sample.

3.5 Weld data analysis

3.5.1 Energy input during welding

Energy input for each of the welds was calculated using Equation 1.

$$Energy\ Input,\ EI = \frac{2\pi rTe}{1000v} \quad (\frac{kJ}{mm}) \qquad \text{Equation 1}$$

Where;

r – Spindle rotation speed (rpm)

T – Torque (Nm)

e – Efficiency factor, nominally 98% as used by TWI Ltd.

v – Traverse speed (mm/min)

3.5.2 Swept volume per revolution

The volume of material swept per revolution by the probe was calculated using Equation 2.

$$Volume_{Swept}\left(\frac{mm^3}{rev}\right) = NG_{Area} \times \frac{V}{W} = \left(\left(\frac{r_t + r_b}{2}\right) \times t\right) \times \frac{V}{W} \qquad \text{Equation 2}$$

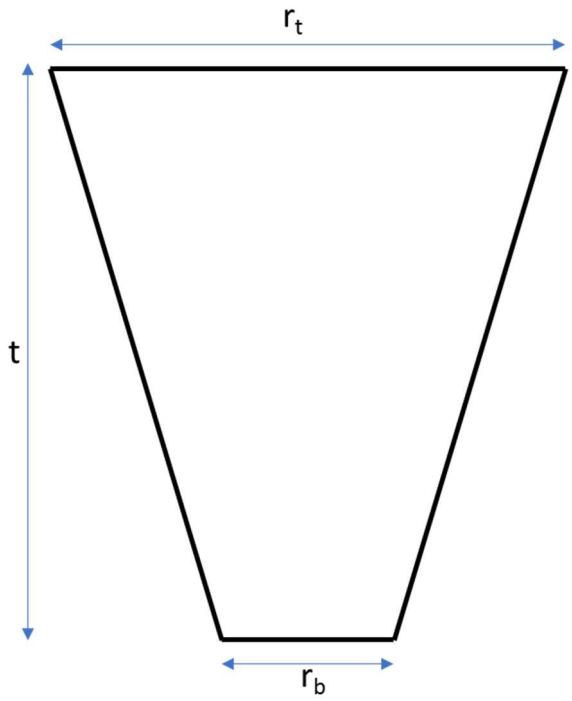

Figure 71 - Dimensions of the probe used to calculate the swept volume of material per revolution.

3.6 Weld analysis

As stated in section 3.4, a micro hardness sample (totalling 10 mm of the traverse direction), a macro sample (totalling 10 mm) and 3 tensile samples (20 mm each) were taken from each plate, totalling 80 mm of weld traverse length. The samples were taken from the 'steady state' stage of the weld – the period in which the temperature distribution is stabilised (Colligan (2010)) – and a minimum of 50 mm away from the exit hole, as demonstrated by the diagram in Figure 70.

3.6.1 Testing equipment

Testing was done using the below equipment to analyse the microstructural and mechanical properties. The below list of the equipment was used within SHU and TWI laboratories:

- Alicona infinite focus microscope (see Figure 72a)
- ESH tensile testing machine (see Figure 72b)
- Philips X'Pert Modular Powder Diffractometer (see Figure 72c)
- Quanta 650 Scanning Electron Microscope (see Figure 72d)
- SpectroMaxx Optical Emission Spectrometer (see Figure 72e)
- Wilsons VH3300 Vickers Hardness machine (see Figure 72f)
- Optical Light Microscope (see Figure 72g).

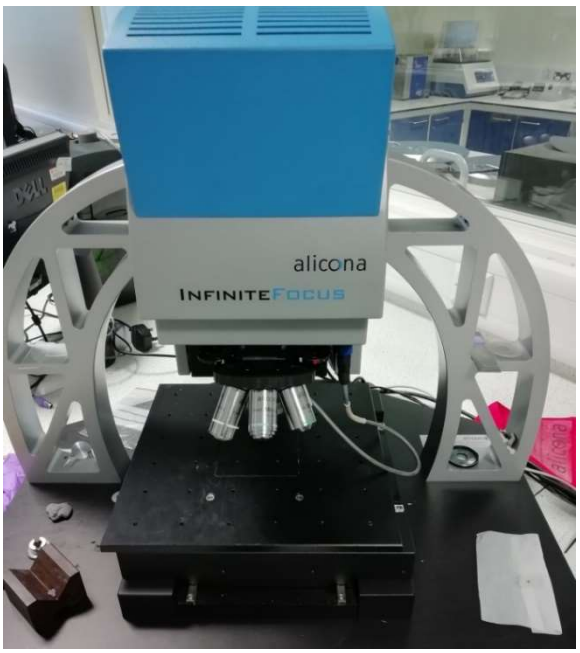

a) Alicona Infinite Focus Microscope.

b) ESH Tensile Tester

c) Philips X'Pert Modular Powder Diffractometer

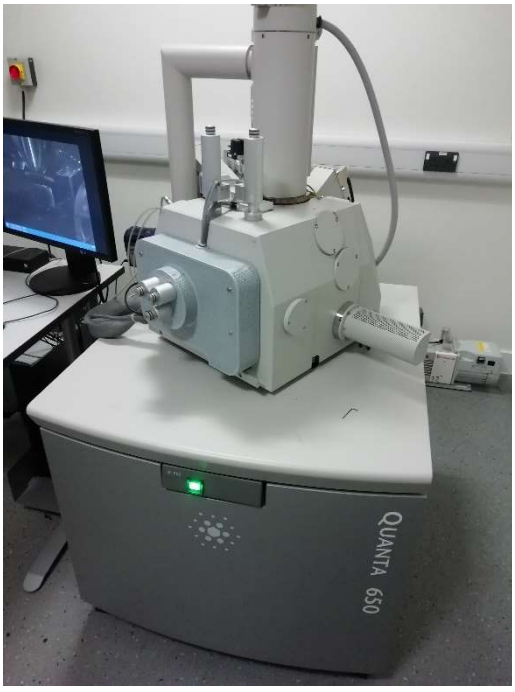

d) Scanning Electron Microscope

Figure 72 – Testing equipment used

e) SpectroMaxx Optical Emission Spectrometer

f) Wilsons VH3300 Vickers Hardness machine.

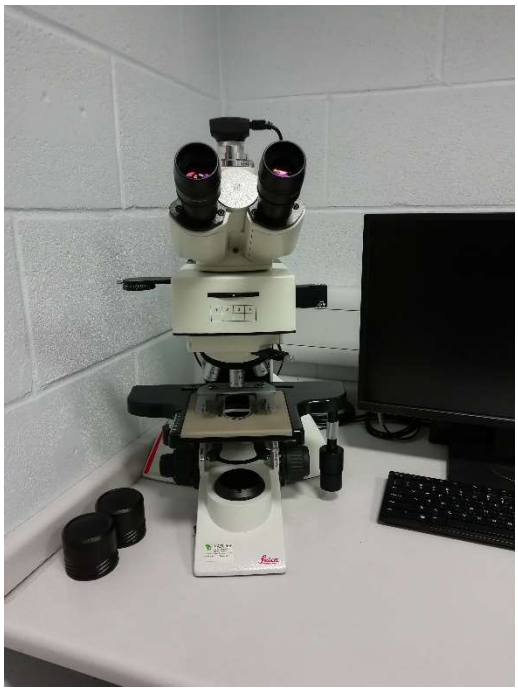

g) Optical Light Microscope

Figure 72 continued – Testing equipment used.

3.6.2 Mechanical testing

3.6.2.1 Tensile testing

Tensile testing was conducted to standard BS EN ISO 6892-1:2016. Initially testing was to be conducted at SHU within the MERI laboratories and the 'dog bones' were designed following the standard, although the constraints of the machine available meant a non-proportional approach was taken, see Figure 73. The machine used was an ESH tensile test machine, photographed in Figure 72b. The load rate of the ESH tensile tester, used at SHU, was kept constant as a control variable for each test. The rate was kept constant at 0.012(kN/min)/mm^2. This machine was used for the first three welds tested, namely G16, G17 and G19. The remaining tensile samples were tested at a separate test house. The geometry of the samples was maintained, however two strain rate ranges (Range 2 and 4 of the standard BS EN ISO 6892-1:2016) were used to determine proof stress and UTS respectively. Ranges 2 and 4 used rates of 0.00025s^{-1} and 0.0067s^{-1} respectively.

Due to limitations in the material available, it was not possible to test unwelded 50mm thick AA6082-T651. As such, material of this grade at 20 mm thickness was used to investigate the parent material tensile properties. This was again done to the standard; BS EN ISO 6892-1: 2016. The geometry of the dog bone used is shown in Appendix 1.

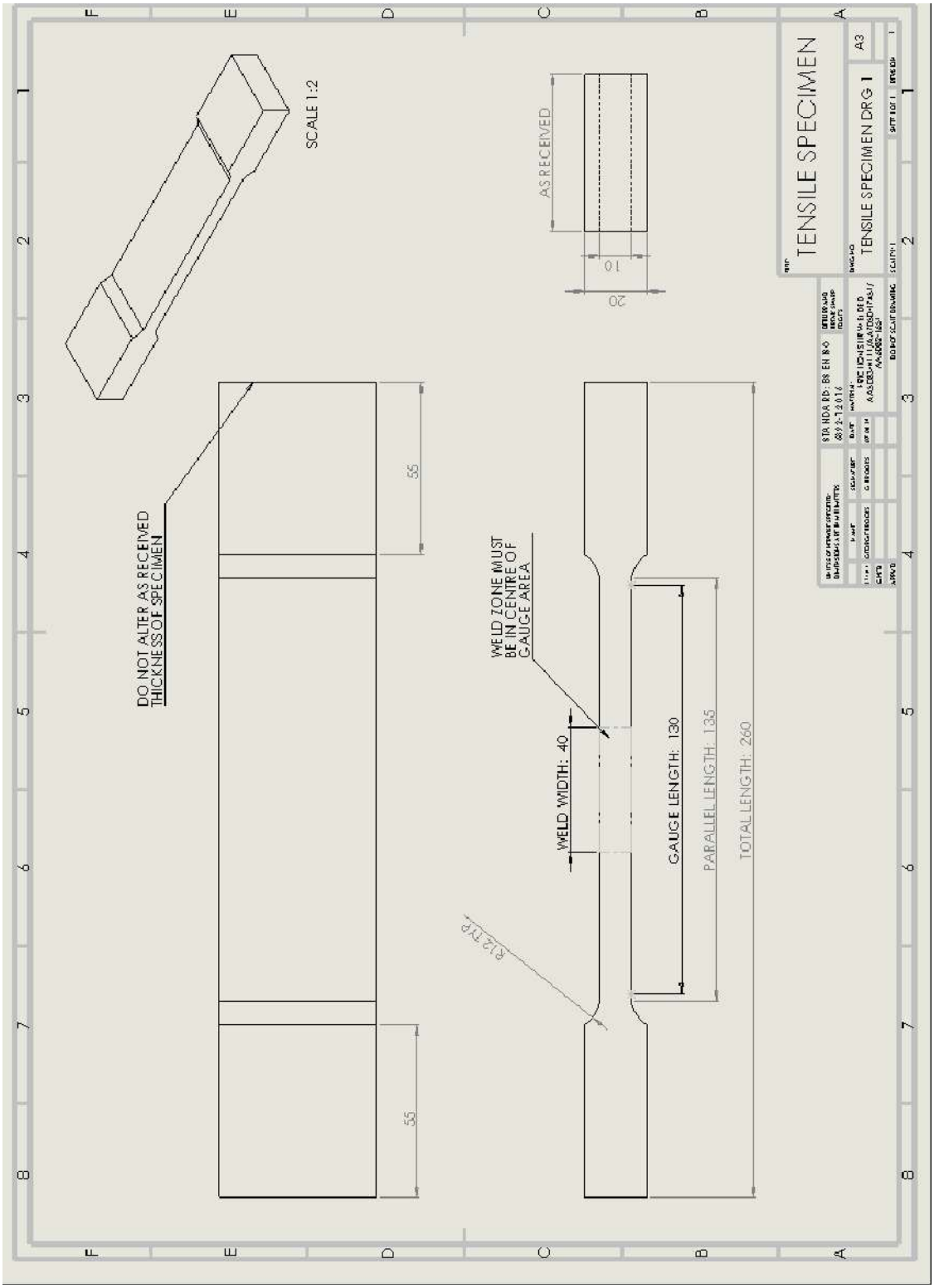

Figure 73 - Tensile test dog bone geometry.

For all materials tested a theoretical value for failure load was calculated by rearranging the stress equation to form Equation 3 below and applying a retention factor to account for the drop in properties due to the welding process. From research

conducted previously by Brooks (2018); K. V. Jata, Sankaran, and Ruschau (2000); Kumar V. Jata et al. (2003); Zhou et al. (2016) it was found that welded material retained ~73-80%. The retention factor used was 80% so that the upper end of the retention was suitably accounted for.

$$Failure\ Stress, \sigma_{UTS}\ (Nm^{-2}) = \frac{Force}{Gauge\ area} = \frac{F}{A}$$

$$\therefore Force, F\ (N) = \sigma_{UTS} A \quad (kN) \qquad \text{Equation 3}$$

The force required to cause failure within welded 50mm thick AA5083, AA6082 and AA7050 specimens was calculated as being 116, 124 and 209.6 kN respectively (see Table 12), when the UTS stress was given as 290, 310 and 524 MPa respectively ('ASM Material Data Sheet - AA5083-O' (n.d.); 'Aluminum 6082-T6' (n.d.), 60; 'ASM Material Data Sheet - AA7050-T7451' (n.d.)) and the gauge area as 500mm^2;

AA5083-H111	**AA6082-T651**	**AA7050-T7451**
$F = \sigma_{UTS} A$	$F = \sigma_{UTS} A$	$F = \sigma_{UTS} A$
$F = 290E6 \times 500E-6$	$F = 310E6 \times 500E-6$	$F = 524E6 \times 500E-6$
$F = 145\,000N = 145kN$	$F = 155\,000\,N = 155kN$	$F = 262\,000\,N = 262kN$
$F_{WELD} = 0.8 \times 145$	$F_{WELD} = 0.8 \times 155$	$F_{WELD} = 0.8 \times 262$
$F_{WELD} = 116\,kN$	$F_{WELD} = 124\,kN$	$F_{WELD} = 209.6\,kN$

Table 12 - Table of example tensile strength calculations for the materials investigated.

3.6.2.2 Hardness testing

Hardness testing was conducted to standard BS EN ISO 6507-1:2005. The hardness samples were prepared using the semi-automatic grinder/polishers available in SHU Labs. The samples were prepared using grit paper of 120 up to 2500 grit. Diamond suspension polish; 6 µm and 1 µm were then used to further improve the surface.

Once the surface was prepared the Wilsons VH3300 hardness machine was used to take micro hardness readings of the sample. Micro hardness was chosen as a hardness map containing a large number of measurements would better identify the hardness variation through the thickness of the material and across the various weld zones. A force of 0.5 kg was used to indent the material with a dwell time of 10 s for each indent, the schematic shown in Figure 74 identifies the location of these indents. As is shown, the first point is taken 4 mm from the furthest left edge of sample and 2 mm from the bottom of the sample. The hardness map was made up of 1368 points from 24 rows, each spaced 2 mm apart, and 57 columns each spaced 2 mm apart.

Following the completion of the measuring stage, each result was checked to ensure the measurement markers were indeed located at the corners of the indent. The data was then exported to 'Origin' where it was formatted to conform to the matrix required to produce the colour contour maps presented in the results section in section 4**.**

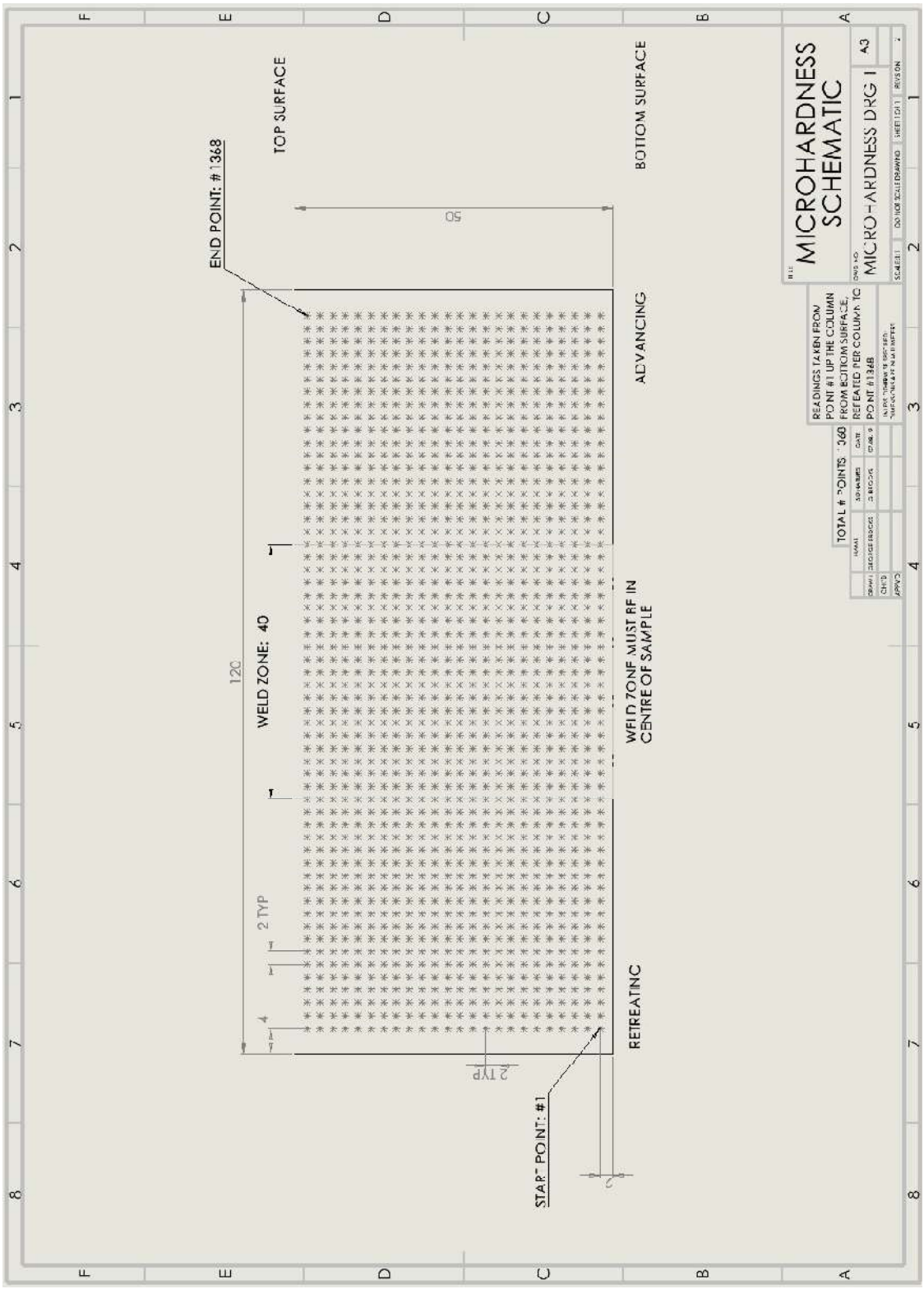

Figure 74 - Schematic of micro hardness readings.

Similar to the tensile samples, a hardness value was calculated, using Equation 4, for the welded materials, as demonstrated below in Table 13. The force and angle of diamond were pre-determined by the machine's capabilities while the diagonal distance, d, was determined through trial tests in spare material.

$$HV = \frac{2F\sin(\frac{\theta}{2})}{d^2} \quad \textit{(Kgf/mm}^2\textit{)} \qquad \text{Equation 4}$$

Where;

Angle of diamond, θ = 136 °

Force applied, F = 0.5 kgf

Diagonal distance across indenter = d (measured in mm).

AA5083-H111	**AA6082-T651**	**AA7050-T7451**
$Hardness = \frac{2F\sin\left(\frac{\theta}{2}\right)}{d^2}$ $Hardness = \frac{2 \times 0.5\sin\left(\frac{136}{2}\right)}{0.12^2}$ $Hardness = 64.39HV0.5$	$Hardness = \frac{2F\sin\left(\frac{\theta}{2}\right)}{d^2}$ $Hardness = \frac{2 \times 0.5\sin\left(\frac{136}{2}\right)}{0.10^2}$ $Hardness = 92.71HV0.5$	$Hardness = \frac{2F\sin\left(\frac{\theta}{2}\right)}{d^2}$ $Hardness = \frac{2 \times 0.5\sin\left(\frac{136}{2}\right)}{0.075^2}$ $Hardness = 164.83HV0.5$

Table 13 - Table of example hardness calculations for the materials investigated.

3.6.3 Microstructural analysis

The process for preparing the samples for microstructural analysis was the similar to that detailed in the hardness testing preparation in section 3.6.2.2. however, samples were polished by hand from 6µm to improve quality. Following the polishing stage, the samples were reviewed unetched and images captured for analysis. A sample of

G07/08, G13, G34 and parent material for AA5083-H111 was left for seven days in an oven heated to 150 °C. This was done to improve the visibility of the grain structure once etched and therefore aid in measuring the distance between grain boundaries. Lin et al. (2017) have previously shown that heating AA5083 aided in revealing the grain structure and this could be done to 300 °C before the grain structure started to recrystalize. These samples were not used for any other testing or analysis except to measure grain size.

A sample from each weld/parent material was then etched. All etched samples were done so by submersion etching in stages of 15 seconds after which time the sample was rinsed with water and reviewed under an Optical Light Microscope (OLM). For AA5083, Barkers Reagent was used following a review of 'Metallographic Etchants for Aluminium Alloys' (n.d.), while Keller's reagent was used for AA6082 samples and AA7050 was etched in Krolls Reagent following review of Vander Voort (2004). The composition of the etchants used is provided in Table 14.

Etchant	Composition	Material
Barkers Reagent	5ml HBF_4, 200ml H_2O	AA5083-H1
Keller's Reagent	190ml H_2O, 5ml HNO_3, 3ml HCl, 2ml HF	AA6082-T6
Krolls Reagent	2ml HF, 6ml HNO_3, 92ml H_2O	AA7050-T7

Table 14 - Etchant composition 'Metallographic Etchants for Aluminium Alloys' (n.d.).

Two sample sizes were investigated. Firstly, a 50x50 mm section of the stir zone and immediate surrounding area was used to produce the macrograph and nine regions of analysis as indicated by Figure 75.

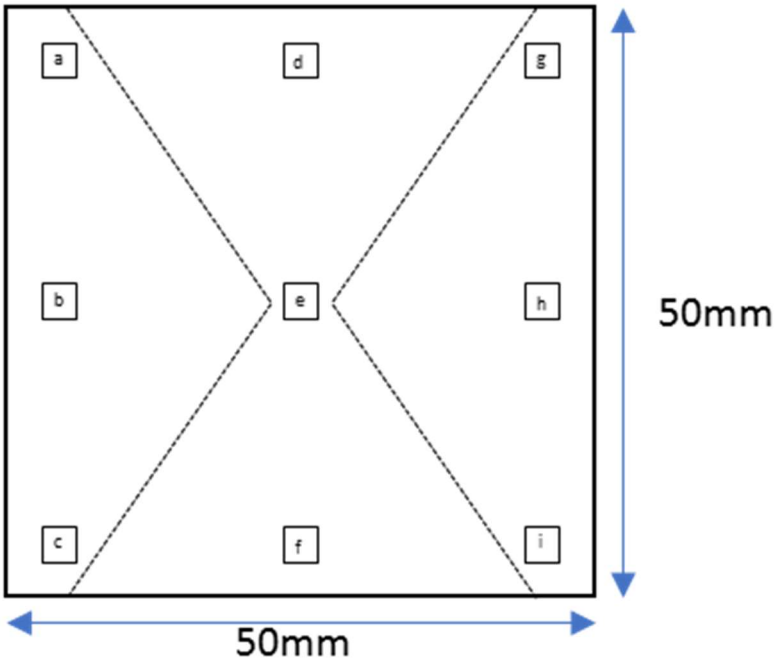

Figure 75 - Macrograph sample with identifying labels of the nine regions captured using OLM.

Secondly, 15x15 mm samples (mounted in 30 mm cold mount) of the stir zone, transition region, HAZ and PM were produced for SEM work – see Figure 76 for locations. Cold mount was used to prevent the thermal reaction taking place affecting the solution state of the material. In tests prior to mounting the samples, it was shown that the cold mount would reach 82 °C during the curing stage. This was deemed close to the ageing temperature of AA7050-T7451 which was 120 °C and therefore to further reduce the mounting stages impact, all mounting was conducted on a copper plate which had been left in the freezer (set to -18 °C) for a minimum of 24 hours each time. The samples were prepared in a similar fashion to those used in the hardness tests; grit paper of 120 up to 2500 grit was used to before diamond suspension polish of 6 µm and 1 µm was applied to further improve the surface. A line of conductive silver paint was then drawn from one corner of the polished metallic surface to the underside of the sample to improve the electrical conductivity between the sample and the aluminium stub which was used to hold the samples in place during EDX analysis.

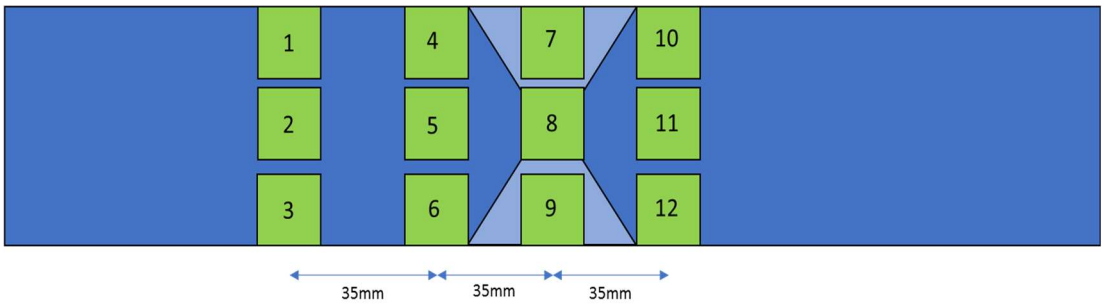

Figure 76 – Locations of samples taken for cold mounting purposes.

3.6.3.1 Infinite Focus Microscopy

An Infinite Focus Microscope (IFM) was used to produced macrographs of the parent and welded material. The IFM was used at 5x the objective lens and in a 2D configuration, using the parameters shown in Table 15, to capture images of the 50x50 mm samples.

Exposure	60.0 µs
Contrast	0.82
Polarizer	OFF
Vertical Resolution	986 nm
Lateral Resolution	28.07 µm
Auto Vignetting	ON

Table 15 – Parameters used for capturing macrographs.

3.6.3.2 Optical Emission Spectroscopy

Optical Emission Spectroscopy was used to determine the composition of the as-received material on three occasions, with an average being taken from these tests. Before testing could be undertaken, the sample was prepared by using grinding pads from 80 grit to 600 grit to produce a surface sufficient. The SpectroMaxx spectrometer was then calibrated, and the appropriate electrode was selected for the aluminium alloy in question. (e.g., Al-Mg for 5xxx series or Al-Si for 6xxx). Using the SpectroMaxx

spectrometer (the schematic of which is detailed in Figure 77) an electrical current is used to trigger the atoms within the metal in order to produce characteristic light. This is achieved using a high voltage source through an electrode. The difference in potential between the electrode and the sample generates discharge which causes the surface of the material to heat up and the atoms to excite, emitting an emission line characteristic of the elements. The light produced enters the spectrometer and is split so that the specific wavelengths of elements can be determined. The intensity of the wavelength is proportional to the concentration of the element present. A third component of the system is a computer. This obtains the measured intensity of each element and is processed through a predefined calibration to produce elemental concentrations.

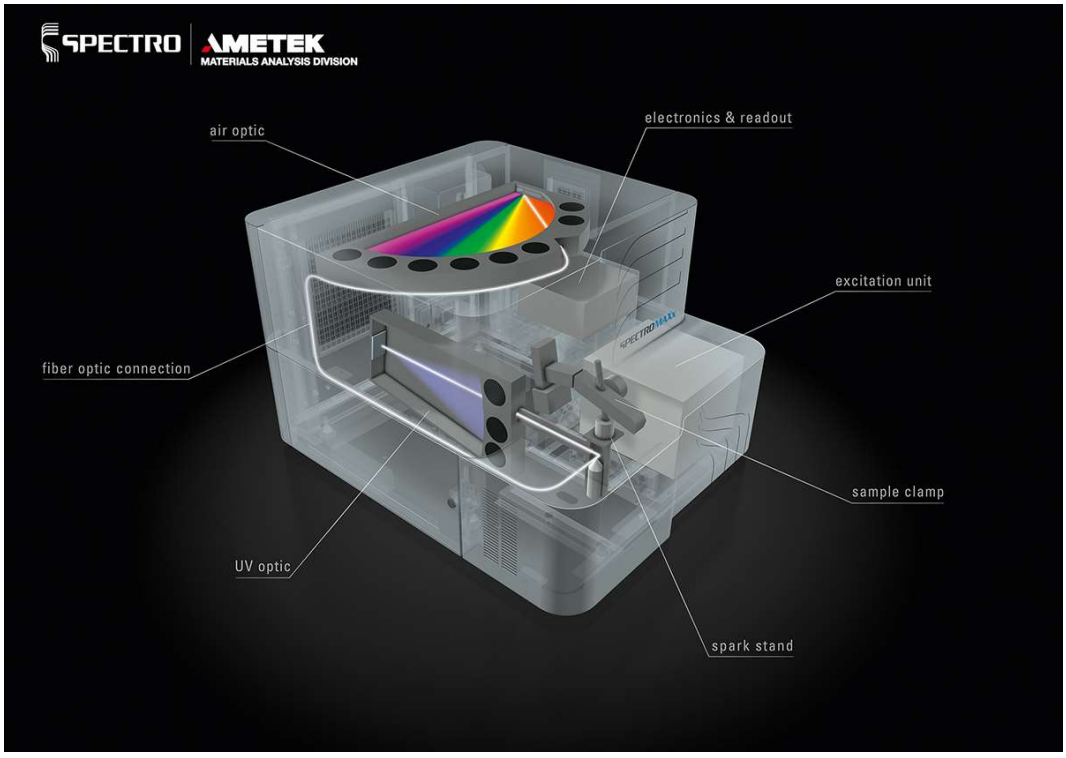

Figure 77 - SpectroMaxx analyser used in Optical Emission Spectroscopy ('SPECTROMAXx Metal Analyzer | SPECTRO Analytical' n.d.).

3.6.3.3 Scanning Electron Microscopy

A Quanta 650 Scanning Electron Microscope (SEM) was used to conduct Energy Dispersive X-Ray Spectroscopy (EDX). This provided qualitative data on the composition of regions and individual points within the alloys. EDX was initially conducted on three PM samples and positions 7, 8 and 9 of Figure 76. These positions were chosen as they were within the SZ of the weld and therefore the most diverse from the PM due to their experience of thermal and mechanical working during the welding process. If these three positions showed significant differences to the PM samples, then the remaining regions shown in Figure 76 would then be subsequently analysed. However, it was assumed that if the SZ particles analysed resembled the PM then the HAZ regions would likely also resemble the PM as the HAZ is subjected to only thermal working during the welding process.

Three map and five-point spectrums were produced per sample. Each spectrum was conducted with the following parameters;

Frame number	3
Dwell time	15 000 µs
Resolution	512
Process time	4

Table 16 - Parameters used for EDX map analysis.

3.6.3.4 Average grain boundary distance

The average distance between grain boundaries in each of the nine regions captured using OLM was measured using the mean linear intercept method, as per ASTM E112. The method uses a straight line, drawn over the captured image, to count grains that are intercepted, tangential or partially intercepted to establish an average distance between boundaries. The mean linear intercept is measured as per Equation 5;

$$Mean\ linear\ intercept, \bar{d} = \frac{L}{N} \qquad \text{Equation 5}$$

Where;

L = Length of line

N = Number of grains intercepted

The value of N is dependent on whether the line begins/ends inside, intercepts or is tangential to a grain. Where the line begins and ends within a grain the value of N is considered 0.5. For each grain the line fully intercepts an N value of 1 is used. Finally, where the line is tangential to a grain (see Figure 78) the value of N is considered to be 0.5. The total value of N for the length of the line is then used in the equation above to establish the average distance between the grain boundaries.

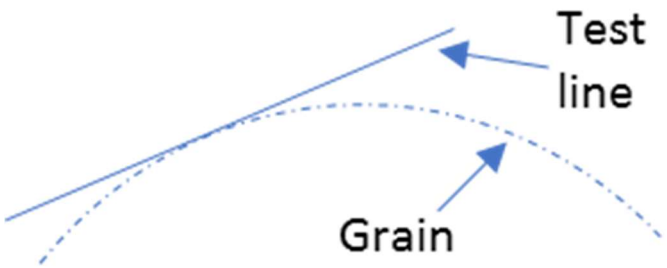

Figure 78 - Where the line is tangential to a grain; N = 0.5.

For grain structures that were visibly equiaxed, a vertical line measurement was taken three times to establish an average. However, in order to establish the average distance between grain boundaries where the structure was not equiaxed (e.g. the HAZ), two orientations (vertical and horizontal) were taken, demonstrated in Figure 79. These were again, repeated three times to establish an average for each orientation.

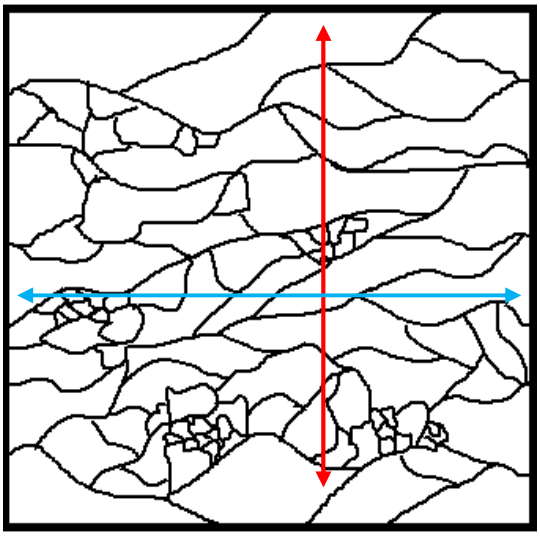

Figure 79 - Average distance between the grain boundaries measurements in non-equiaxed structures were taken in both the horizontal and vertical directions. Red line denotes the vertical measurement. Blue line denotes the horizontal measurement.

4 Results

4.1 Microstructural and mechanical analysis of AA5083-H111

Welds using the techniques discussed previously were produced in AA5083-H111 for analysis. These welds were identified by the ID numbers indicated in Table 17.

Material	AA5083-H111		
Weld ID	G07/08	G13	G34
Weld Type	WFW-FSW	SDS-FSW	SSS-FSW

Table 17 - Weld identification numbers for welds in AA5083-H111.

4.1.1 Weld Data

Data such as traverse and rotational speeds, torque and Z-force were recorded during welding. These are graphically represented in section 4.1.1.1 to 4.1.1.3.

4.1.1.1 Weld-Flip-Weld FSW

Pass	Traverse speed (mm/min)	Rotational speed (rpm)	Torque - Avg (Nm)	Z-force - Avg (kN)
First	130	129.70	761.45	101.00
Second	130	129.50	749.01	101.11

Table 18- Parameter information for G07/08, the WFW-FSW of AA5083-H111.

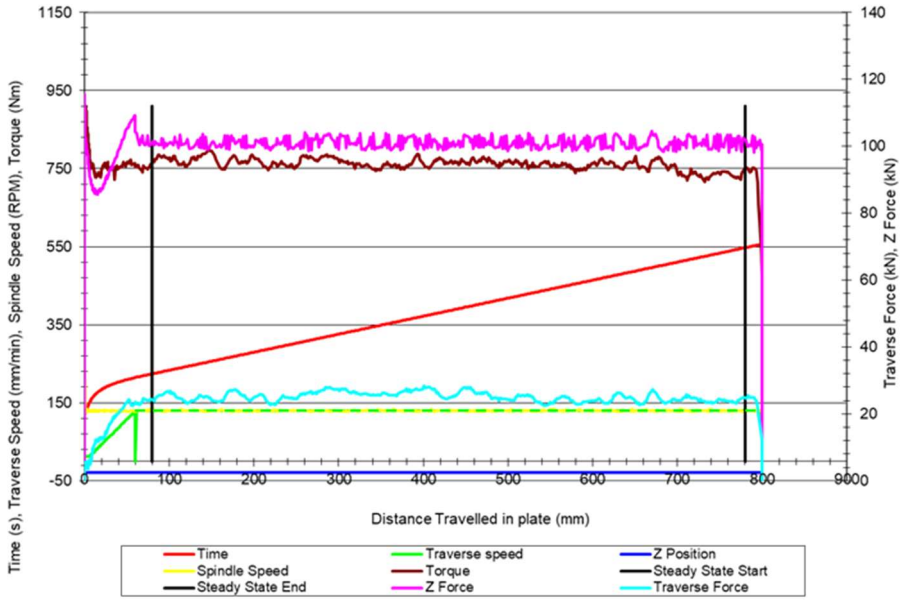

a) Weld data of first pass

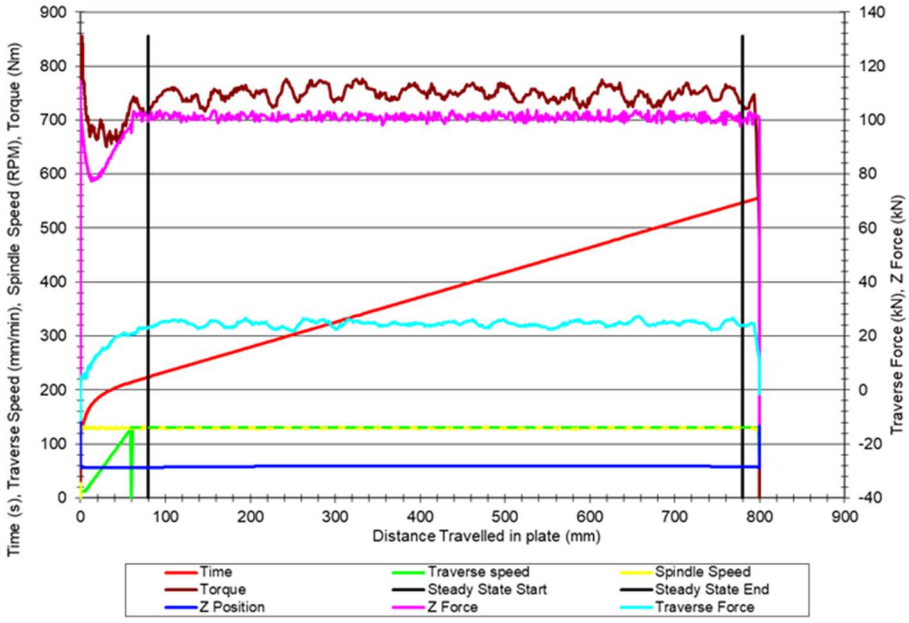

b) Weld data of second pass

Figure 80 - Weld data for WFW-FSW of AA5083-H111. Note: Due to data logger error, the traverse speed was not recorded during the steady state. This has been approximately represented by the green dashed line shown in both a) and b).

4.1.1.2 Simultaneous Double Sided FSW

Pass	Traverse speed (mm/min)	Rotational speed (rpm)	Torque - Avg (Nm)	Z-force - Avg (kN)
Upper	130	109.49	666.58	71.16
Lower	130	109.85	548.59	89.03

Table 19 - Parameter information for G13, the SDS-FSW of AA5083-H111.

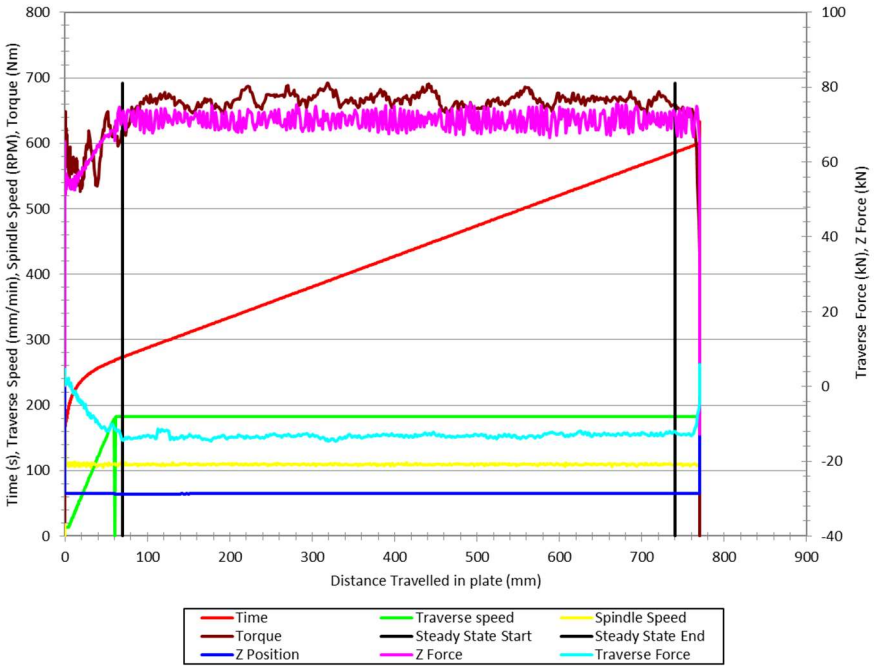

a) Weld data of upper pass

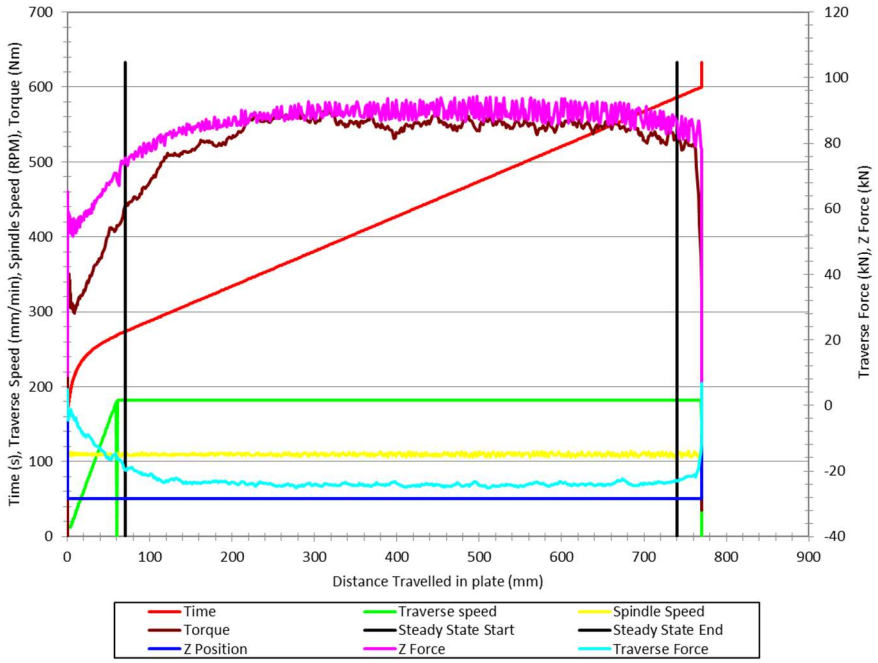

b) Weld data of lower pass

Figure 81 - Weld data for SDS-FSW of AA5083-H111.

4.1.1.3 Supported Stationary Shoulder FSW

Pass	Traverse speed (mm/min)	Rotational speed (rpm)	Torque - Avg (Nm)	Z-force - Avg (kN)
Single	60	182.00	1209.59	122.80

Table 20 - Parameter information for G34, the SSS-FSW of AA5083-H111.

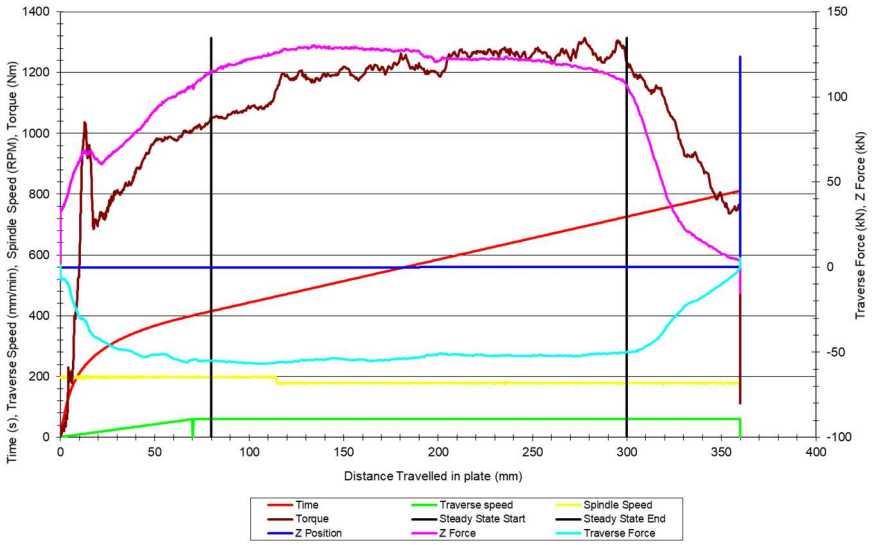

Figure 82 - Weld data for SSS-FSW of AA5083-H111.

4.1.2 Chemical analysis

4.1.2.1 Optical Emission Spectroscopy (OES)

Optical Emission Spectroscopy (OES) was conducted to quantify the elements and their weight percentages (wt%) within AA5083-H111. The chemical composition of the alloy is shown in Table 21, against the standard composition, and the OES data sheet is provided in Appendix 7. Table 21 shows the alloy AA5083-H111 an Al-Mg based alloy although several other alloying elements were detected, such as Si, Mn, Fe and Cr. The contents of these elements are well within the range specified by the standard composition. Literature (Altenpohl (1982); Vander Voort (2004)) supports the conclusion that AA5083-H111 is an aluminium-magnesium based alloy.

Element	Element wt%	
	Received material	Standard composition
Al	94.200	92.4 - 95.6
Cr	0.110	0.05 - 0.25
Cu	0.070	Max 0.1
Fe	0.350	Max 0.4
Mg	4.430	4 - 4.9
Mn	0.480	0.4 - 1
Si	0.240	Max 0.4
Ti	0.017	Max 0.15
Zn	0.075	Max 0.25
Other, each	Max 0.005	Max 0.05
Other, total	0.028	Max 0.15

Table 21 - Element wt% for parent material AA5083-H111 as provided by OES analysis.

4.1.3 Microstructural analysis

4.1.3.1 Macrograph

Macrographs of the as-received and welded samples were taken using an Infinite Focus Microscope (IFM), these are shown from Figure 83 through to Figure 86. Figure 83 showed no outstanding features in the PM, although some through thickness variation is discernible as the structure visibly changes as denoted by the yellow dashed border within the figure. The grain structure within this region is larger and the black particles are less frequent within the yellow dashed region, as evident in the pop-out images of Figure 83. The tool profile visible in Figure 84 shows that the probes overlap to produce a central region that is double processed, although some minor skewing of the probes is visible. However, in Figure 85, which shows G13 (SDS-FSW in AA5083-H111) the probes are skewed; a result of the forces acting on them while traversing.

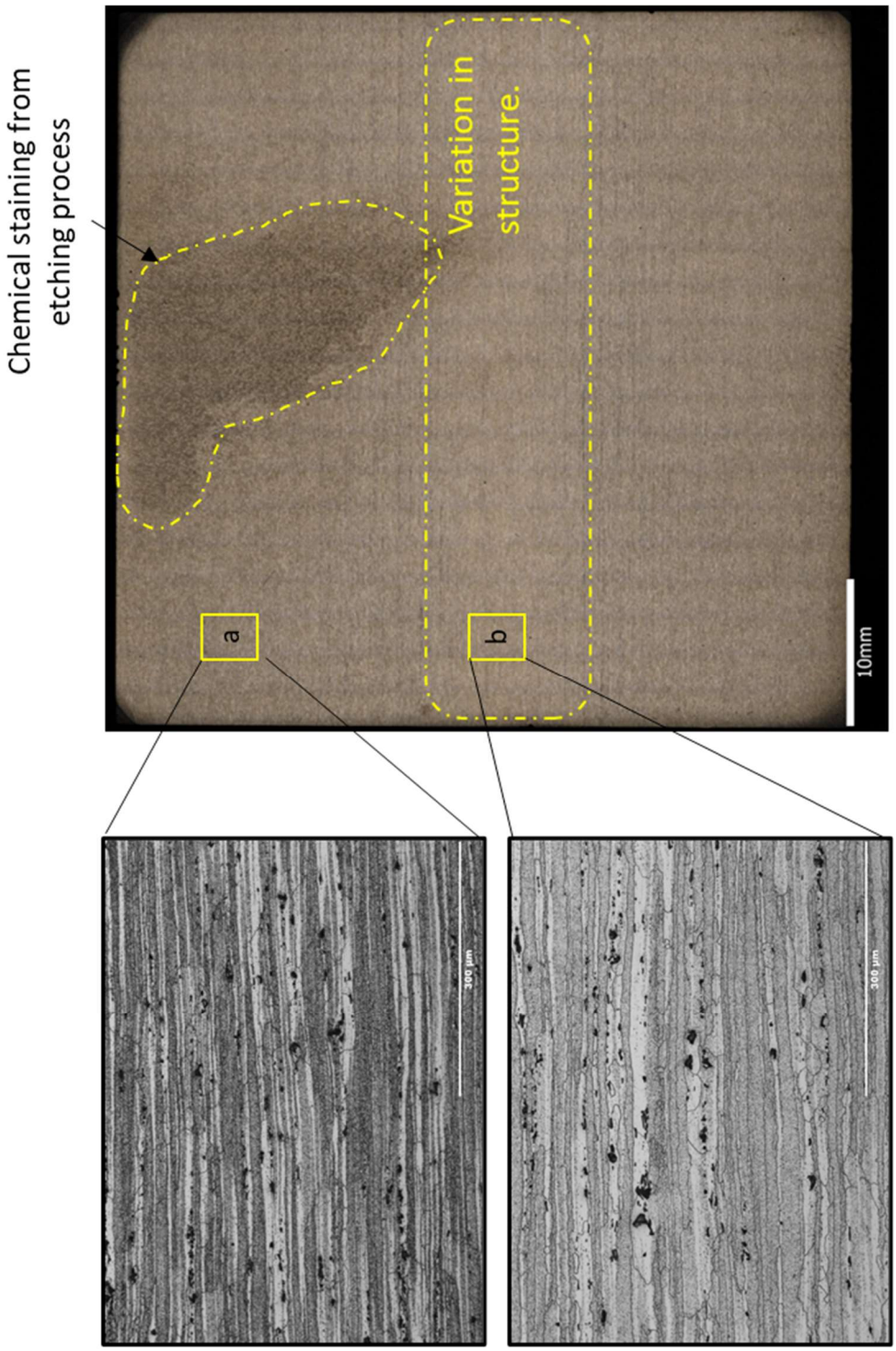

Figure 83 - Macrograph of as received AA5083-H111 - etched in Barker's reagent. Yellow dashed region indicates a variation in microstructure that differs from that visible above as demonstrated by the pop-out images. Chemical staining is identified at the top of the image.

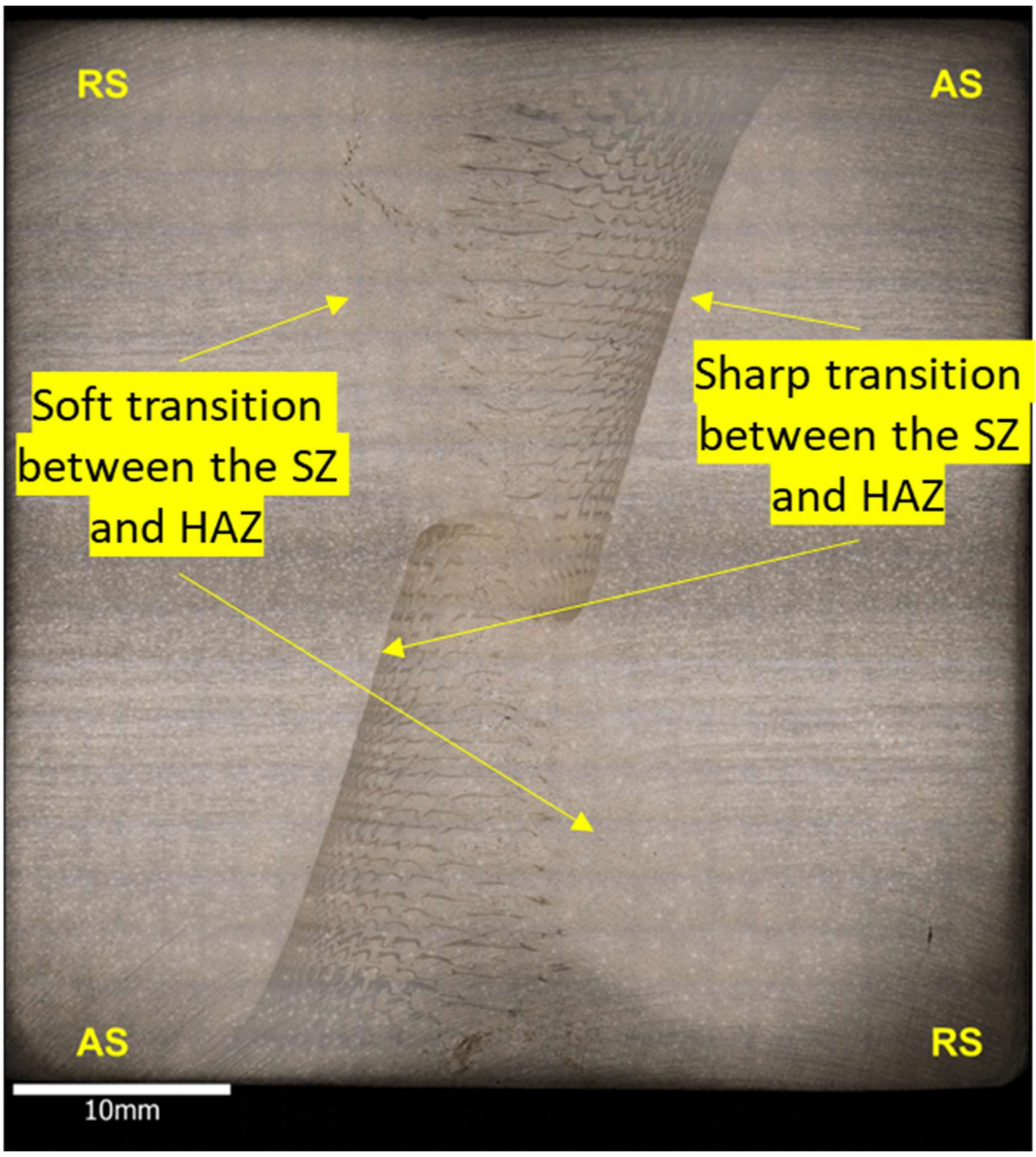

Figure 84 - Macrograph of weld G07/08 - etched in Barker's reagent. Both passes of the weld are visible and overlap at the tip of each weld. In both passes, as indicated, the advancing side is a starker transition to the HAZ than the retreating side.

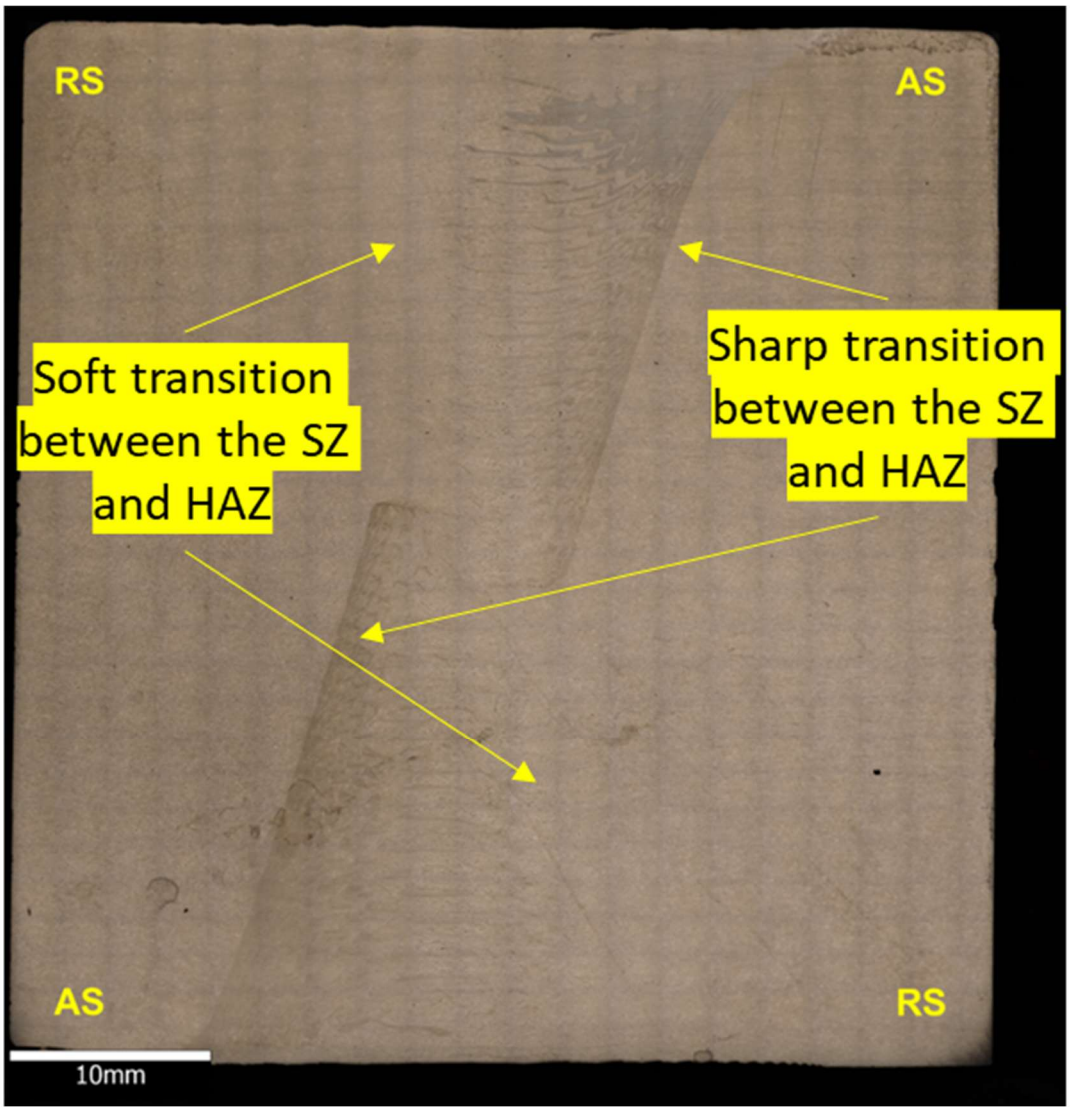

Figure 85 - Macrograph of weld G13 - etched in Barker's reagent. Both passes of the weld are visible and a small amount of skewing is evident by the offset tips of the two passes. In both passes, as indicated, the advancing side is a starker transition to the HAZ than the retreating side.

The SSS-FSW weld, G34, is shown in Figure 86. A collection of voids is visible in this weld and are highlighted using a yellow circle in the figure. The weld in question used a full-length bobbin probe with an anti-clockwise rotation, contrary to the rotational direction used in the other welds investigated. As such the advancing and retreating sides of the weld are reversed.

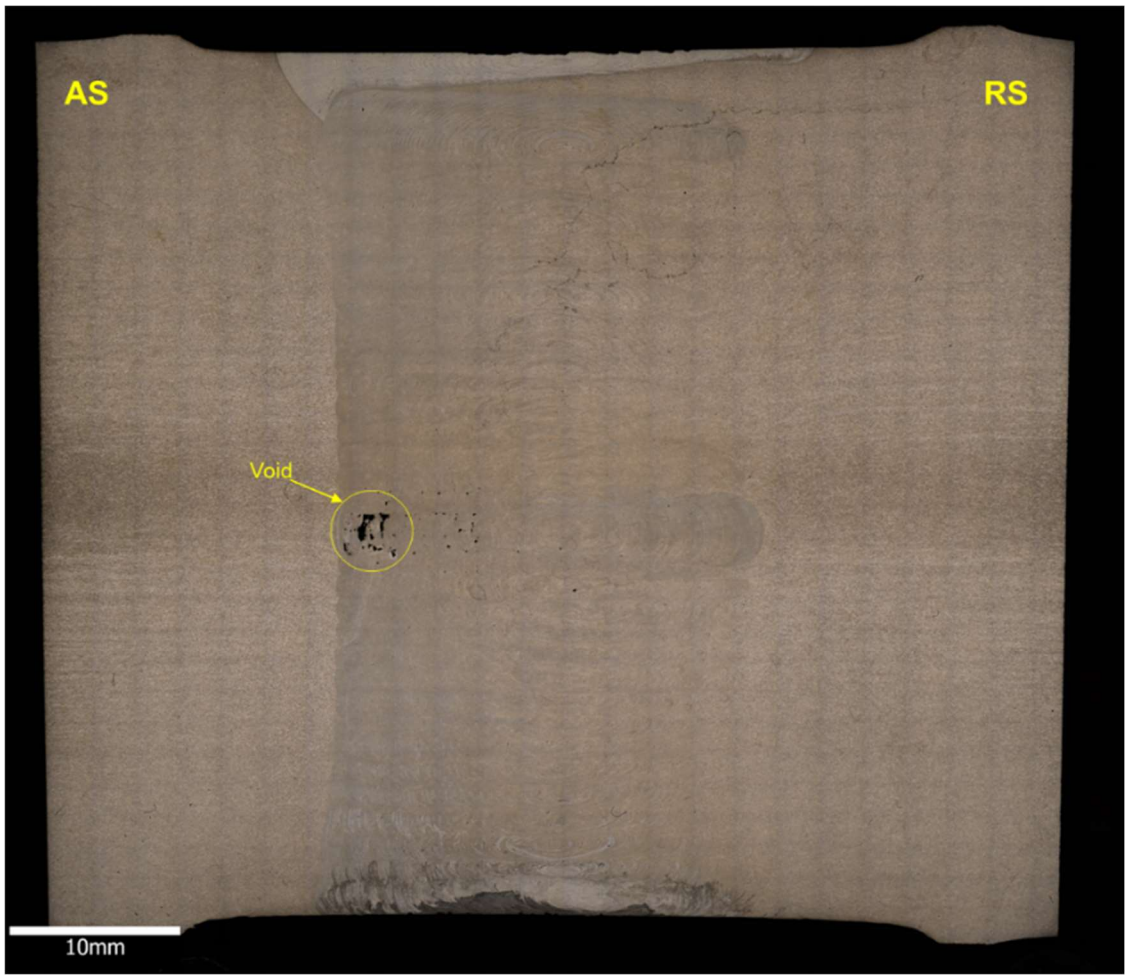

Figure 86 - Macrograph of weld G34 - etched in Barkers Reagent. Yellow circle has been used to highlight the presence of a void within the stir zone.

4.1.3.2 Optical Light Microscopy (OLM)

The microstructure of the as-received AA5083-H111 and stir zone of each of the three welds, etched in Barker's reagent, is shown from Figure 87 to Figure 90. Only the stir zone of each weld is shown in this section however, as per section 3.6.3, nine regions were captured in each sample, these are shown between Appendix 8 and Appendix 10. As the stir zone was the area of most significant change compared to the as-received material, this area is presented in this section.

Although the grain structure was not evident until the samples were heat treated (demonstrated from Appendix 12 to Appendix 14), as detailed in section 3.6.3, the

figures show the change in particle size from the ‘large black’ particles present in the PM to more refined and dispersed particles in each of the stir zones. The joint line remnant is also visible in Figure 88b indicating the presence of oxide build up.

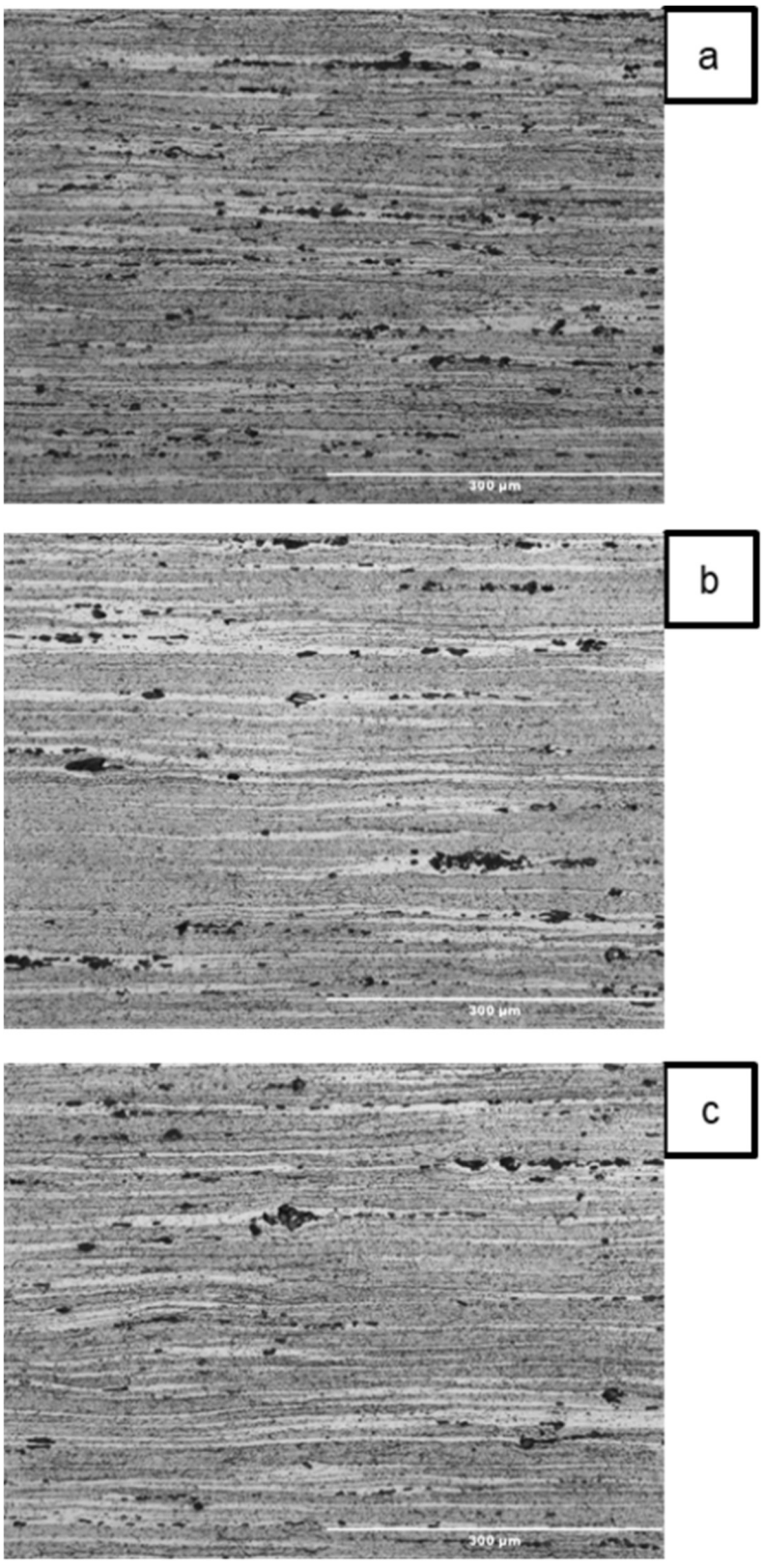

Figure 87 - Microstructure of as-received AA5083-H111. A) top of material, b) centre of material and c) bottom of material.

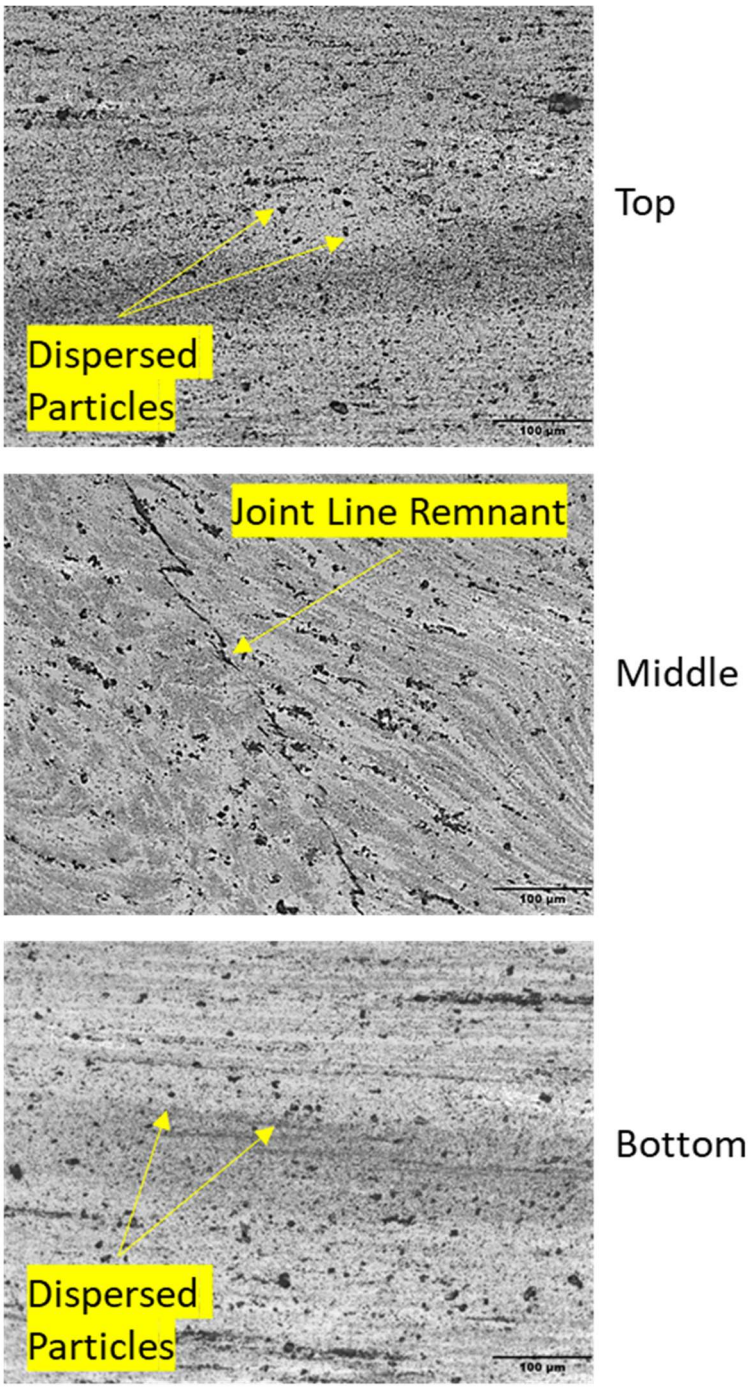

Figure 88 - Microstructure of WFW-FSW, G07/08, stir zone. (Top) shows a dispersed distribution of particles in the upper pass of the weld. (Middle) The joint line remnant is prominent in the double processed region of G07/08. (Bottom) shows finer dispersed particles, compared to the parent material, in the lower pass of the weld.

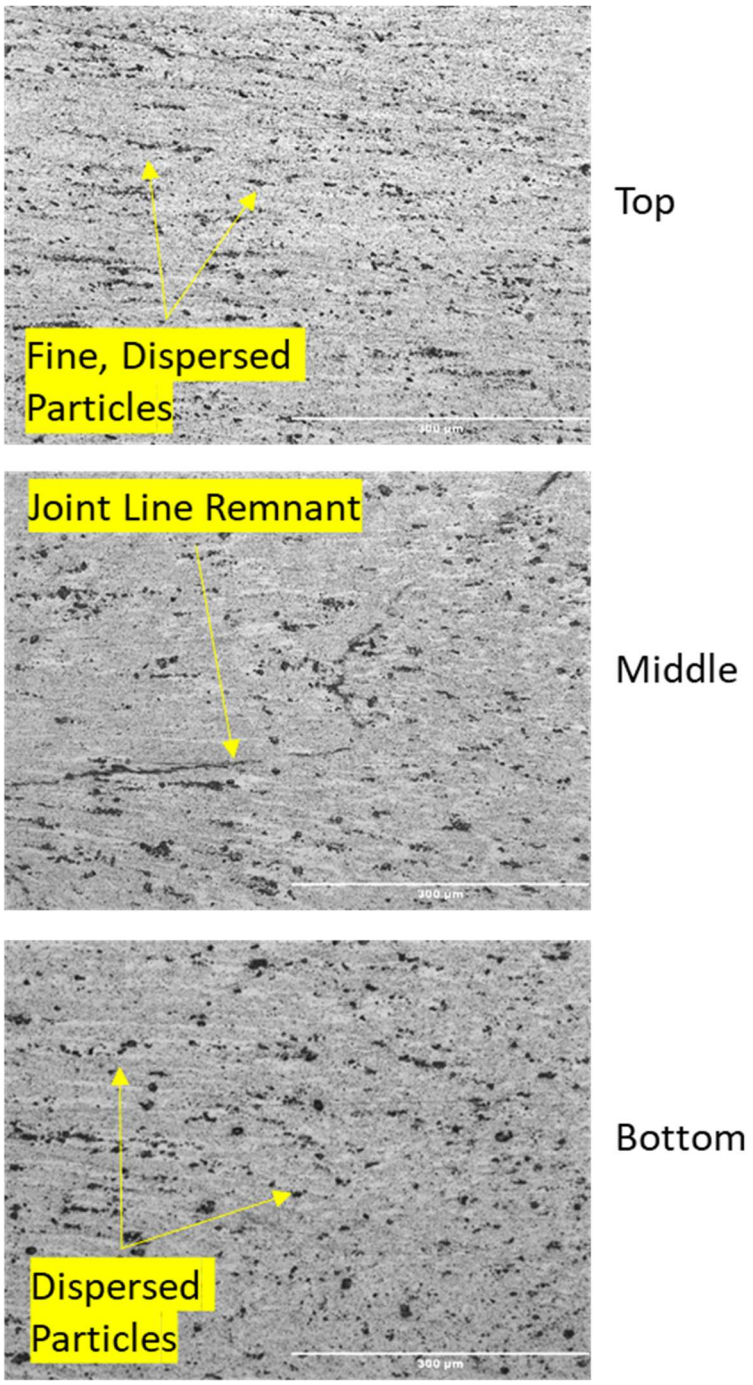

Figure 89 - Microstructure of SDS-FSW, G13, stir zone. (Top) shows a dispersed distribution of fine particles in the upper pass of the weld. (Middle) The joint line remnant passes diagonally from the lower left to upper right side of the image. (Bottom) shows finer dispersed particles, compared to the parent material, in the lower pass of the weld.

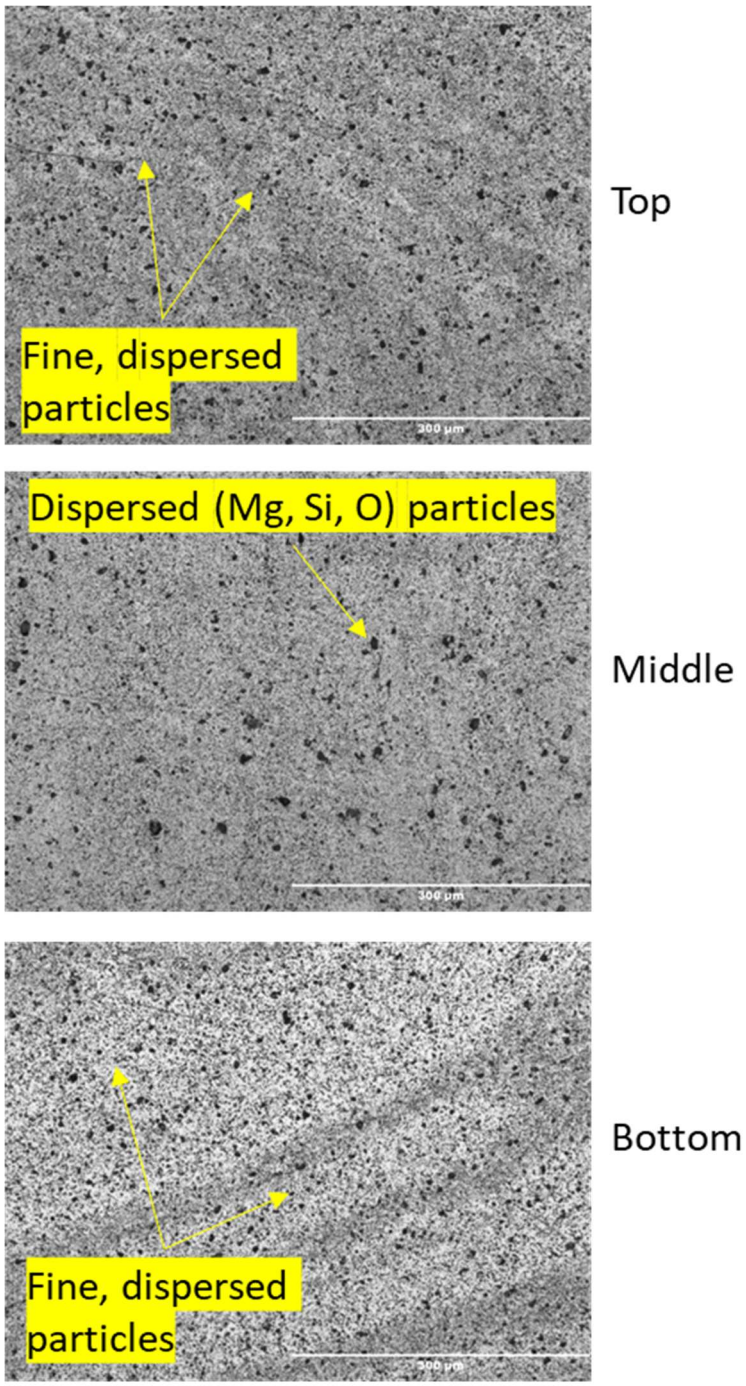

Figure 90 - Microstructure of SSS-FSW, G34, stir zone. (Top) fine dispersed particles present. (Middle) Particles of (Mg, Si, O) are not as fine as those seen in the top and bottom of the weld but are still dispersed throughout the image. (Bottom) Similar to the top image, the particles appear fine and well distributed.

4.1.3.3 Energy Dispersive X-Ray Spectroscopy (EDX Analysis)

Particles within the PM and welded material were analysed using EDX as demonstrated from Figure 91 to Figure 97. Light grey particles were the prominent feature of the SEM images, these were shown by EDX analysis to be of Al-Fe-Mn-Si composition while black particles, Mg-Si-O in nature, were less frequent, these are shown in Figure 92 and Figure 97.

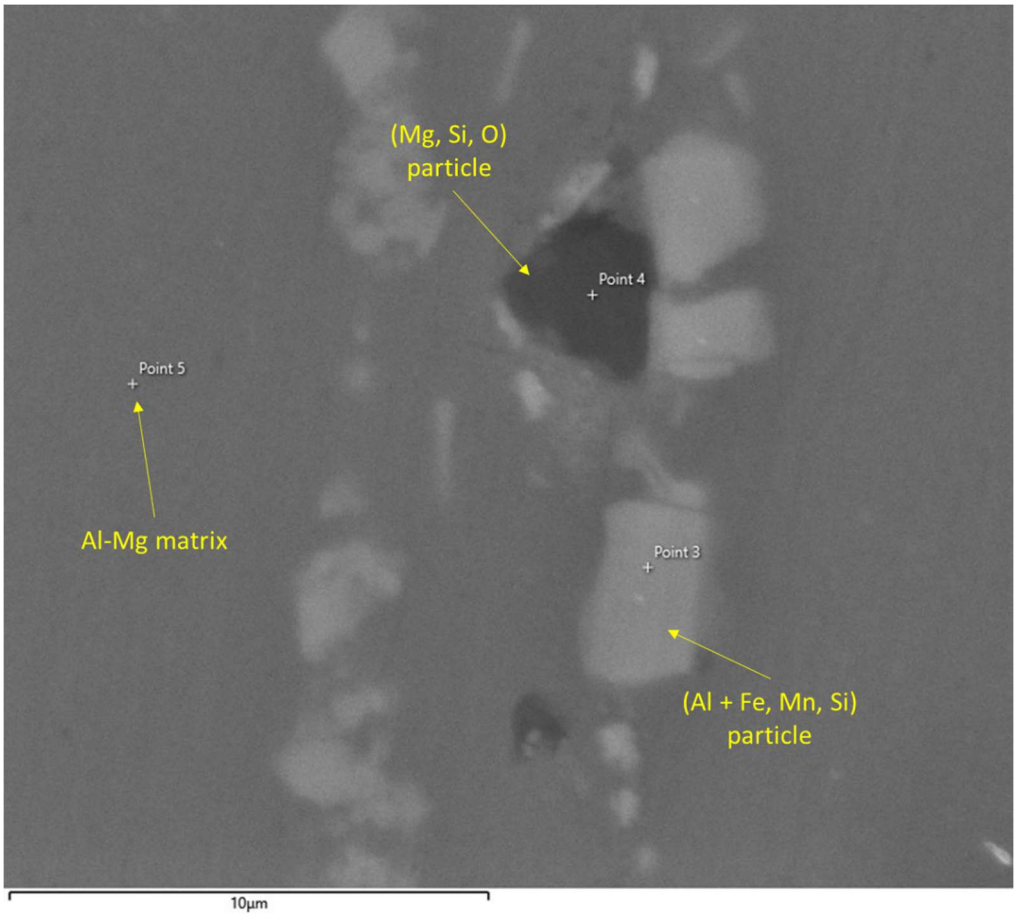

Figure 91 – SEM image of as-received AA5083-H111 showing locations of EDX spectra obtained within the matrix and visible particles.

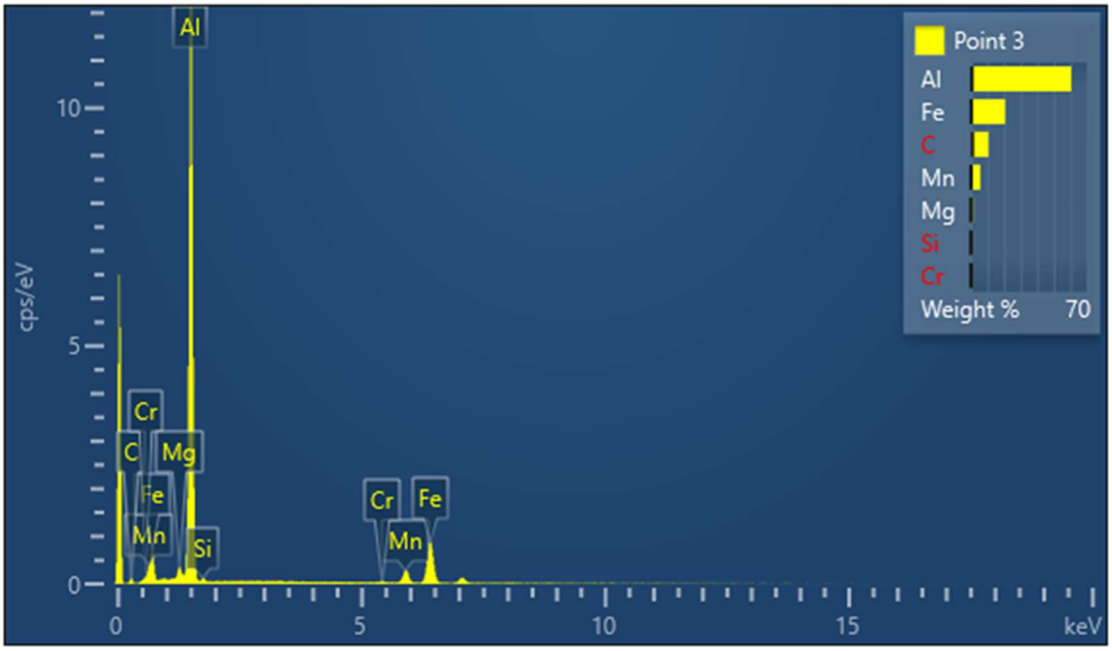

Figure 92 – EDX spectra of point 3 from Figure 91 indicating the presence of a (Al + Fe, Mn, Si) particle.

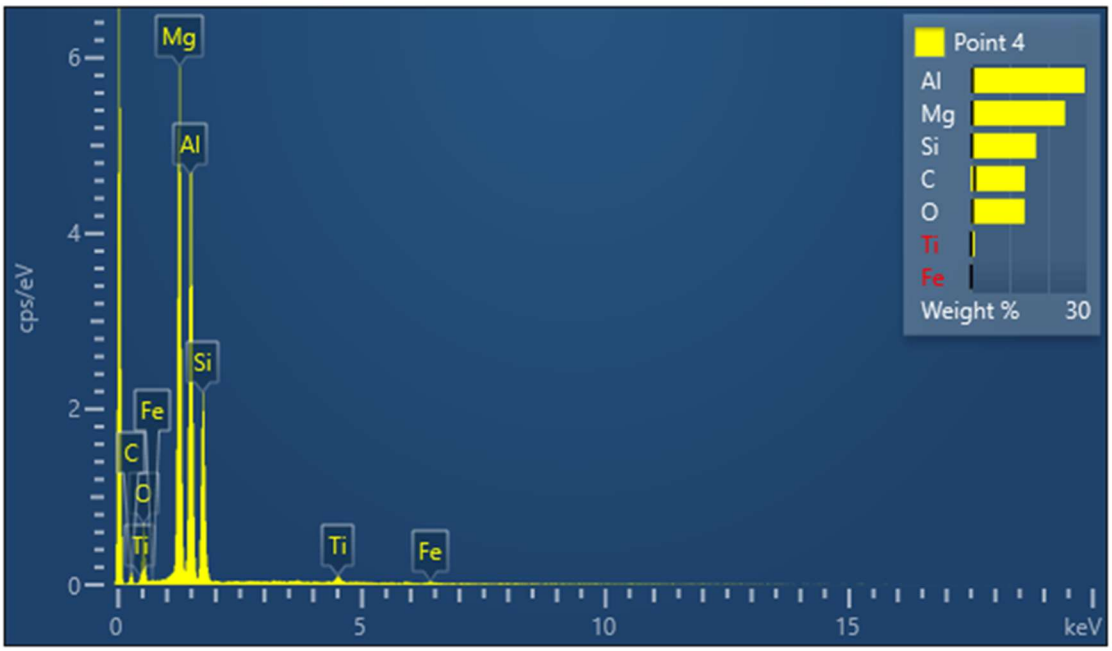

Figure 93 - EDX spectra of point 4 from Figure 91 indicating the presence of a (Mg, Si, O) particle.

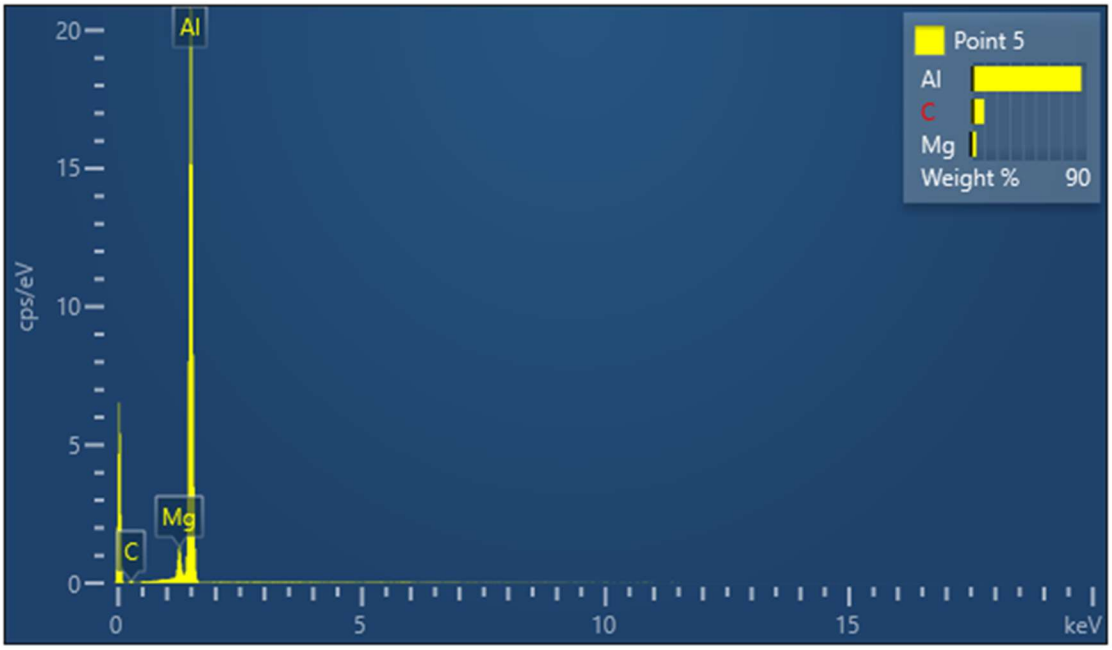

Figure 94 - EDX spectra of point 5 from Figure 91 indicating the Al-Mg matrix.

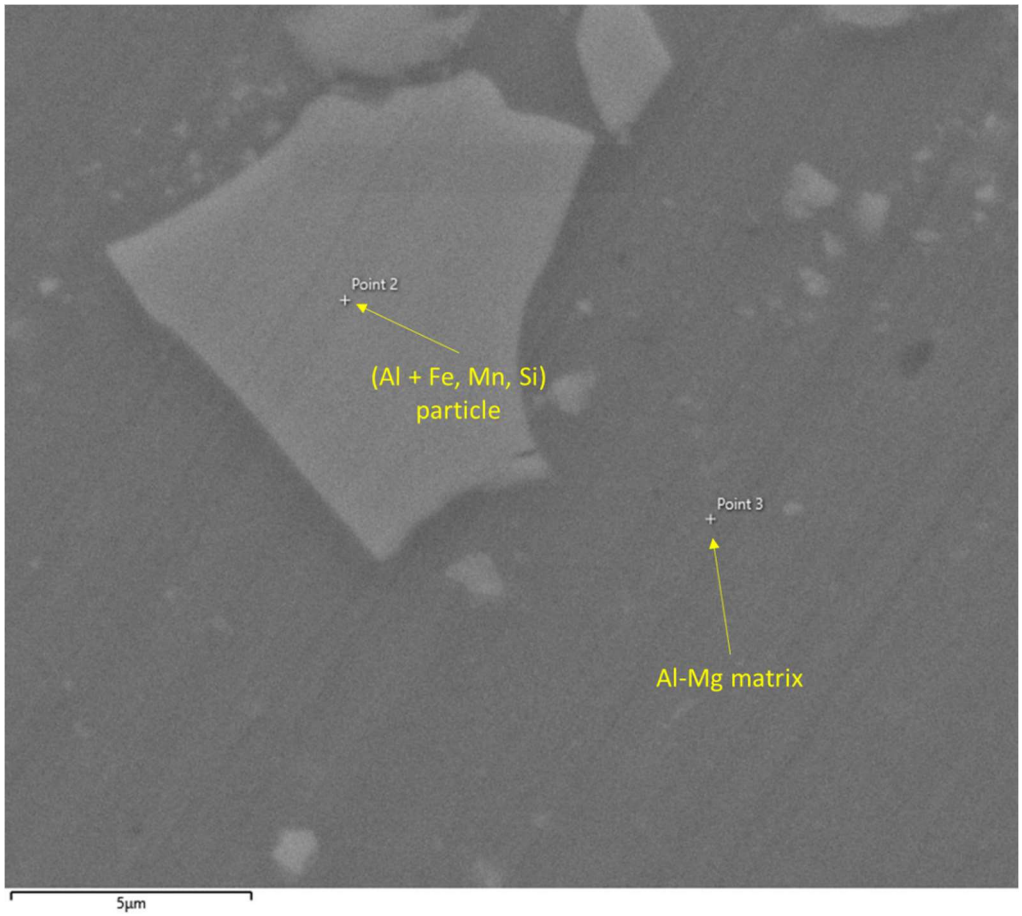

Figure 95 - SEM image of the first pass SZ in G07/08 showing an Al-Mn-Fe-Si based particle.

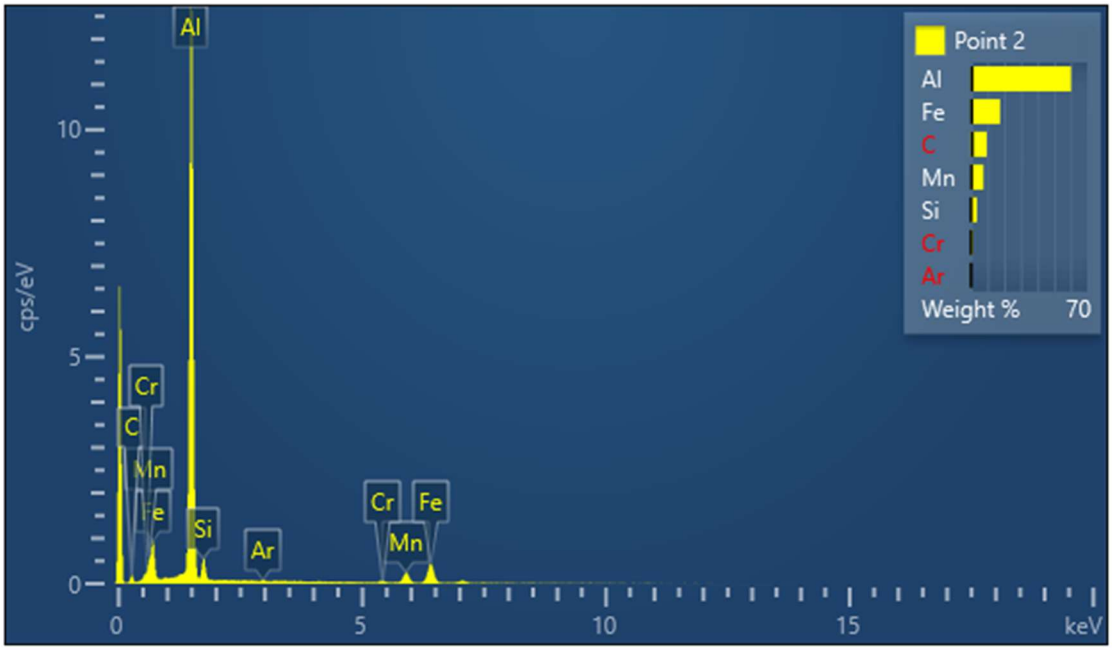

Figure 96 – EDX spectra of the particle in Figure 95 found to be (Al + Fe, Mn, Si) in nature.

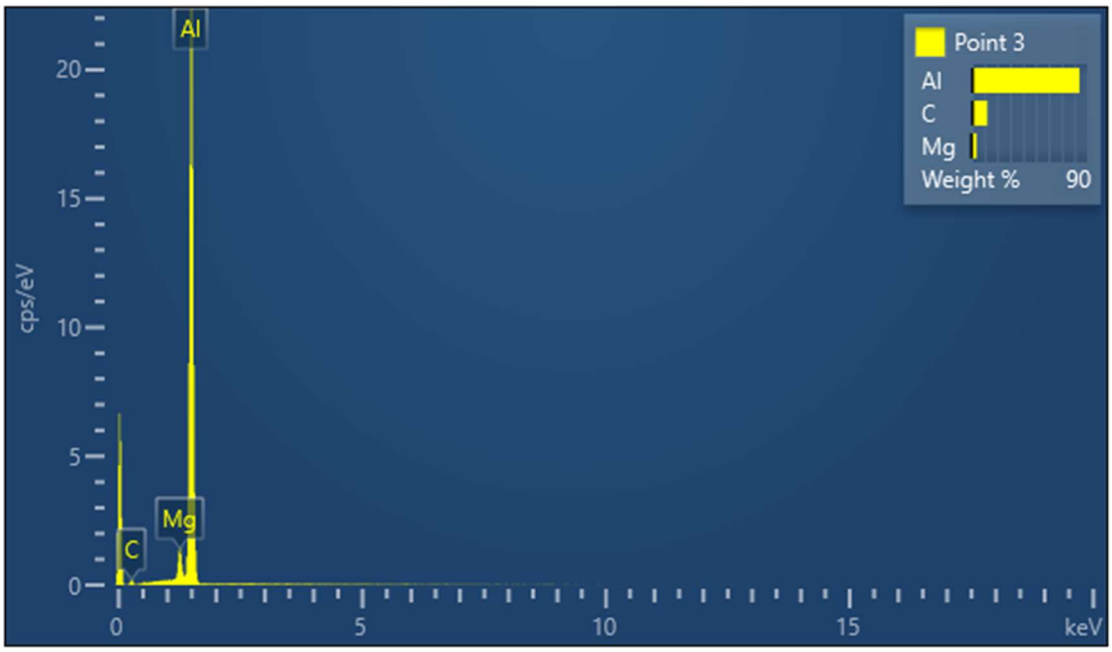

Figure 97 – EDX spectra of the Al-Mg matrix in Figure 95.

4.1.3.4 Average distance between grain boundaries

Average distance between grain boundaries was measured in line with the standard ASTM E112 as detailed in section 3.6.3.4 of the Methodology. Table 22 shows the average distance between grain boundaries of the PM which suggests the grains are not equiaxed with the horizontal measurements for all three areas measured being significantly greater than those of the vertical axis. The bottom position has the largest ratio between the height and width of the grains with the average distance between boundaries being 8.69 and 40.69 µm for the vertical and horizontal axes respectively.

Position	Average grain size (µm)	
	Vertical	Horizontal
Top	6.53	18.64
Middle	9.57	43.90
Bottom	8.69	40.69

Table 22 – Average distance between grain boundaries of the as-received AA5083-H111 in the transverse orientation, through the thickness of the plate.

The average distance between grain boundaries of the welded material was measured at each of the nine regions shown in Figure 98, the results of this are presented in Table 23. The regions d, e and f (the regions representing the SZ) show an equiaxed grain structure whereas the remaining regions suggest that the HAZ is not equiaxed and are similar to the PM in that the horizontal distance is greater than the vertical measurement. Values for regions b and c in G07/08 were not measured due to the grains not being revealed in the sample.

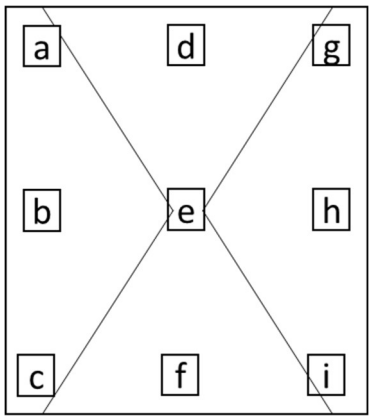

Figure 98 – Schematic of the nine regions in which average distance between grain boundaries was measured.

Positional ID	Average distance between grain boundaries (μm)					
	G07/08		G13		G34	
	Vertical	Horizontal	Vertical	Horizontal	Vertical	Horizontal
a	7.48	14.94	7.88	14.63	34.88	70.99
b	-	-	6.73	11.83	20.34	49.11
c	-	-	6.53	15.74	18.08	81.38
d	5.79	6.89	6.39	6.33	11.74	11.39
e	1.46	1.60	2.66	2.47	8.14	7.40
f	8.59	7.95	3.95	4.26	11.52	12.31
g	16.86	41.10	8.03	19.74	29.41	57.53
h	7.63	9.47	7.88	19.18	16.61	83.41
i	9.52	14.76	7.58	14.63	22.40	41.19

Table 23 – Average distance between grain boundaries of welded AA5083-H111 measured in the transverse orientation in both the vertical and horizontal axis.

4.1.4 Mechanical properties

4.1.4.1 Tensile

The parent and as-welded materials tensile data is summarised in Table 24. The as-received AA5083-H111 UTS was measured as 296 MPa after three tests and failed at an elongation of 23.7%. Whereas G07/08 failed comparatively weaker (277 MPa) than the as-received material, G13 exceeded the strength of the as-received PM, failing at 298 MPa. This is a retention of 93% and 101% respectively versus the as-received material. In contrast to the high retention of both G07/08 and G13, G34 retained just 56% the UTS of the PM failing at 165 MPa.

I.D	Yield Strength (MPa)	UTS (MPa)	Elongation (%)
P.M	180	296	23.7
G07/08	165	277	2.8
G13	157	298	20.5
G34	140	165	4.2

Table 24 – Principle tensile data for tests conducted in PM and FSWed AA5083-H111.

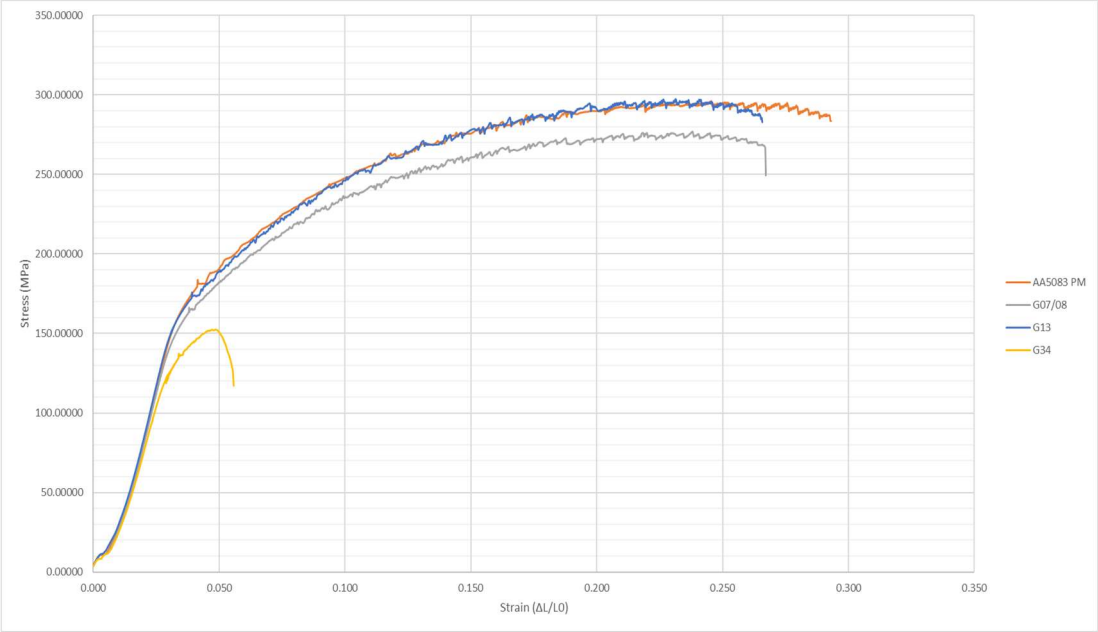

Figure 99 - Tensile data of as-received and welded AA5083-H111.

The failed tensile specimens are documented in Appendix 17 to Appendix 20, while the failure locations are identified in Table 25. Only G34 failed between the tool shoulders with both G07/08 and G13 failing between the HAZ and PM.

Weld #	Test 1	Test 2	Test 3
G07/08	Retr HAZ/PM	Adv HAZ/PM	Retr HAZ/PM
G13	Adv HAZ/PM	Ret HAZ/PM	Adv PM
G34	Adv SZ/TMAZ	Adv SZ/TMAZ	Adv SZ/TMAZ

Table 25 - Failure location of welds made in AA5083-H111.

4.1.4.2 Hardness

The hardness of the PM, illustrated in Figure 100, shows a variation of 10 HV0.5 throughout the sample which is predominantly distinguishable through the thickness of the test area. The hardness data of G07/08, G13 and G34, shown from Figure 101 to Figure 103, shows how FSW has impacted on this property.

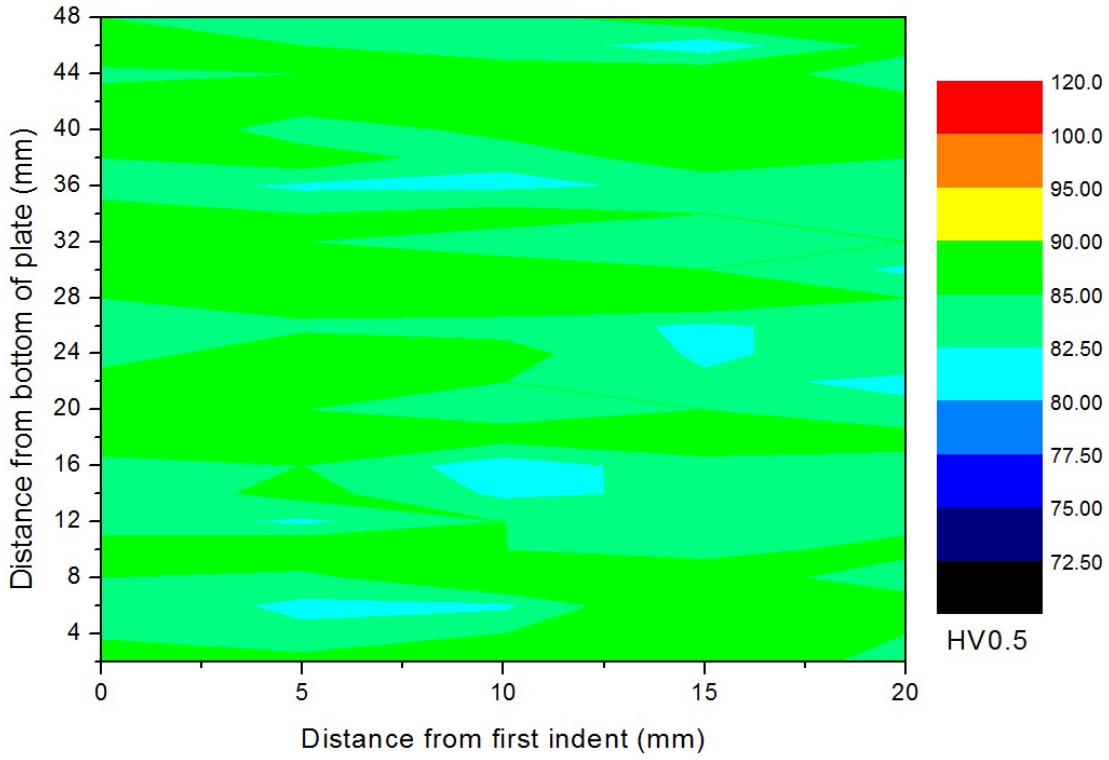

Figure 100 – Micro-hardness contour map of as received AA5083-H111.

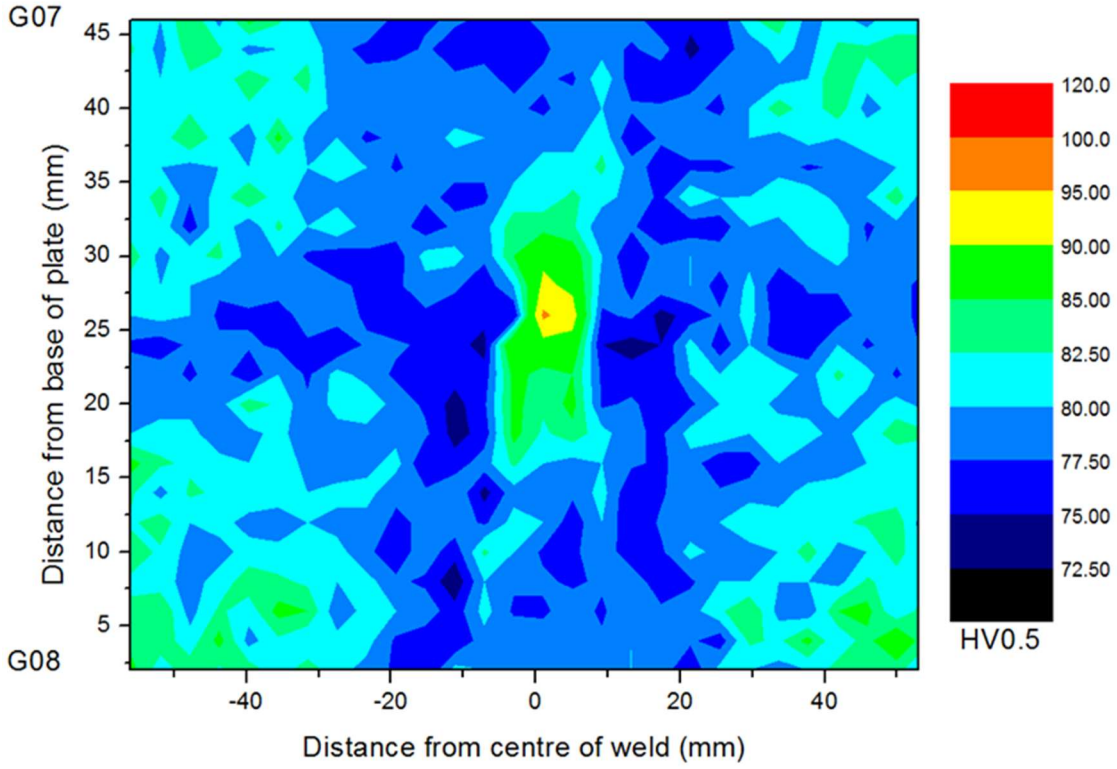

Figure 101 - Micro-hardness contour map of welds G07 and G08 - WFW-FSW in AA5083.

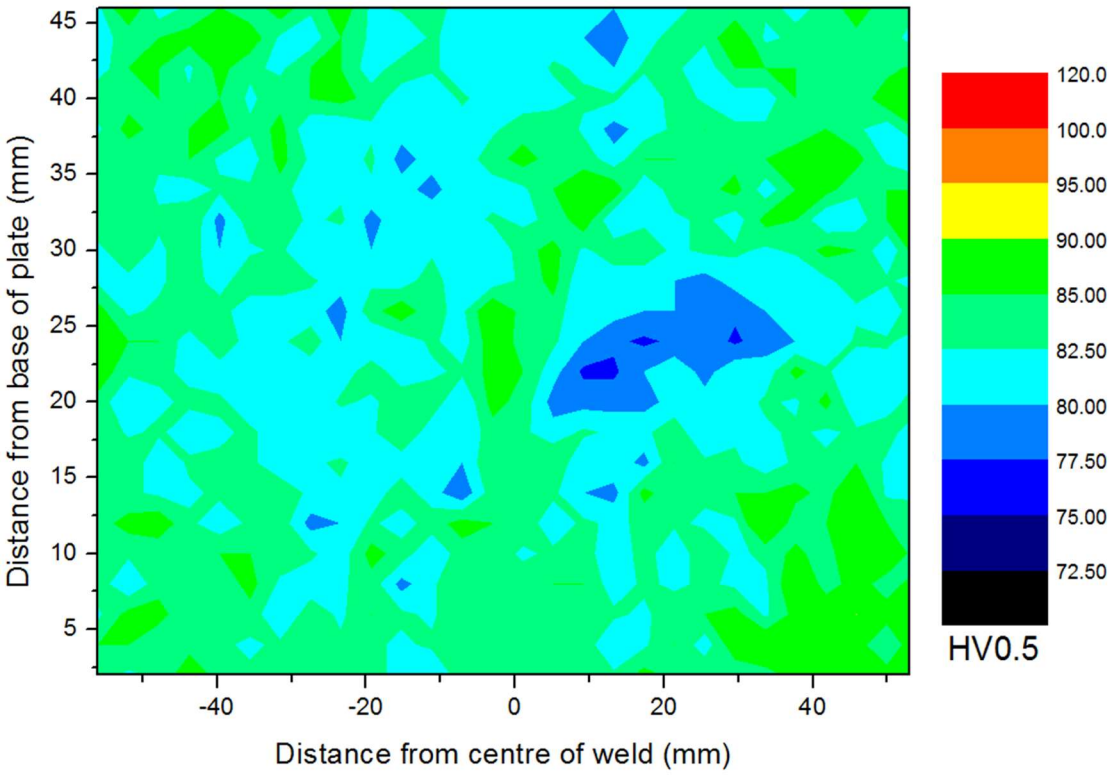

Figure 102 - Micro-hardness contour map of weld G13 - SDS-FSW in AA5083.

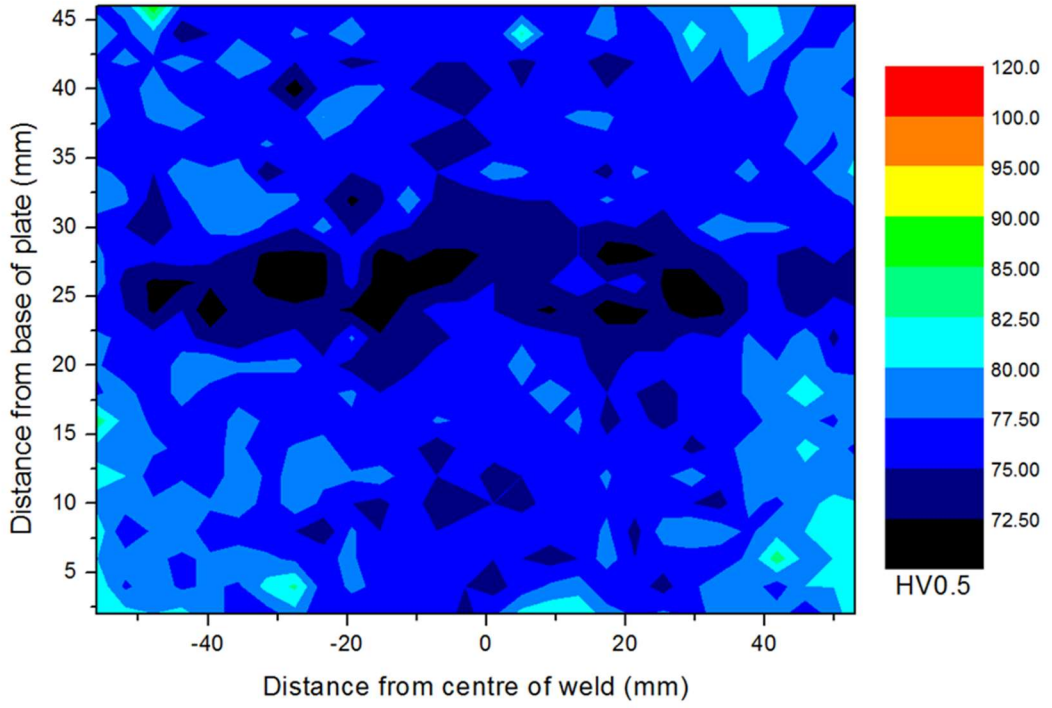

Figure 103 - Micro-hardness contour map of weld G34 - SSS-FSW in AA5083.

4.1.4.3 Swept volume

The calculated swept volume per revolution for each pass is detailed in Table 26. G07/08 and G13 show that the influence of the process parameters on the swept volume as both used nominally half-length probes yet the upper and lower passes of G13 (734.74 and 752.29 mm^3/rev respectively) swept between 100-120 mm^3/rev more than 1st and 2nd passes of G07/08 (637.18 and 638.16 mm^3/rev respectively). The full-length probe used in G34 was calculated as sweeping 535.71 mm^3/rev.

	G07/08	G13	G34
1st Pass/ Upper Pass	637.18	734.74	535.714
2nd Pass/ Lower Pass	638.16	752.29	-

Table 26 - Swept volume per revolution (mm^3/rev) of the FS welds in AA5083-H111.

4.1.4.4 Energy input

The energy required to produce the welds using WFW-FSW and SDS-FSW in AA5083-H111 is shown in Table 27. Here it is illustrated that by running the tools simultaneously the energy input is notably lower. The SDS-FSW weld investigated, G13, had a calculated mean energy input of 3.46 and 2.85 kJ/mm for the upper and lower passes respectively. Therefore, the total energy input into this weld is 6.31 kJ/mm. This is 32% less energy required than the WFW-FSW technique in the same alloy grade. WFW-FSW required 4.68 and 4.59 kJ/mm per pass respectively (totalling 9.27 kJ/mm).

Weld Number	Traverse Speed	Spindle Rotation	Torque (Mean)	Torque (Max)	Efficiency factor	Energy Input (Mean)	Energy Input (Max)
#	mm/min	rpm	Nm	Nm		kJ/mm	kJ/mm
G07	130	129.70	761.45	798.69	0.98	4.68	4.91
G08	130	129.50	749.01	776.30	0.98	4.59	4.76
G13 Upper	130	109.49	666.58	692.14	0.98	3.46	3.59
G13 Lower	130	109.85	548.59	568.85	0.98	2.85	2.96
G34	60	182.00	1209.59	1314.45	0.98	22.59	24.55

Table 27 - Energy input for welds produced in AA5083-H111. Energy efficiency factor is an assumed value.

4.2 Microstructural and mechanical analysis of AA6082-T651

Welds using the techniques discussed previously were produced in AA6082-T651 for analysis. These welds were identified by the ID numbers indicated in Table 28.

Material	AA6082-T651					
Weld ID	G20/21	G22	G14	G16	G17	G19
Weld Type	WFW	SDS	SSS	SSS	SSS	SSS

Table 28 - Weld identification numbers for welds in AA6082-T651.

4.2.1 Weld Data

Data such as traverse and rotational speeds, torque and Z-force were recorded during welding. These are graphically represented in section 4.2.1.1 to 4.2.1.6.

4.2.1.1 Weld-Flip-Weld FSW

Pass	Traverse speed (mm/min)	Rotational speed (rpm)	Torque - Avg (Nm)	Z-force - Avg (kN)
First	150	130.00	846.17	76.17
Second	150	130.00	851.45	78.20

Table 29 - Parameter information for G20/21, the WFW-FSW of AA6082-T651.

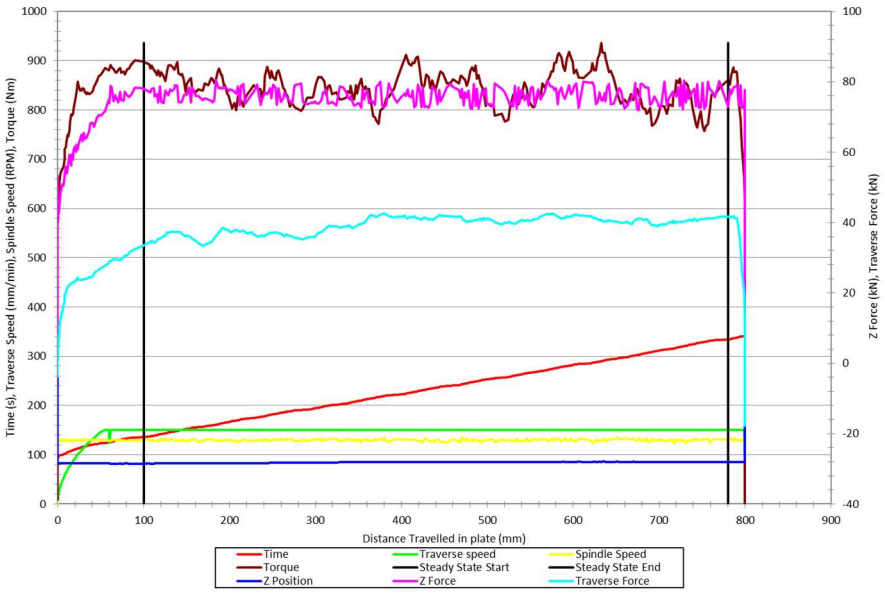

a) Weld data of first pass

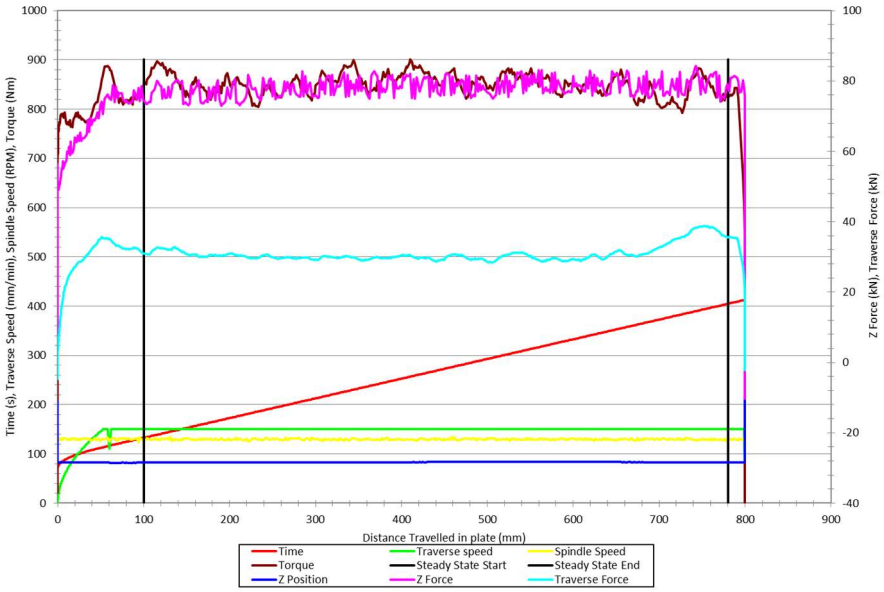

b) Weld data of second pass

Figure 104 - Weld data for WFW-FSW of AA6082-T651.

4.2.1.2 Simultaneous Double Sided FSW

Pass	Traverse speed (mm/min)	Rotational speed (rpm)	Torque - Avg (Nm)	Z-force - Avg (kN)
Upper	252	129.00	735.03	76.03
Lower	252	129.00	776.43	82.69

Table 30 - Parameter information for G22, the SDS-FSW of AA6082-T651.

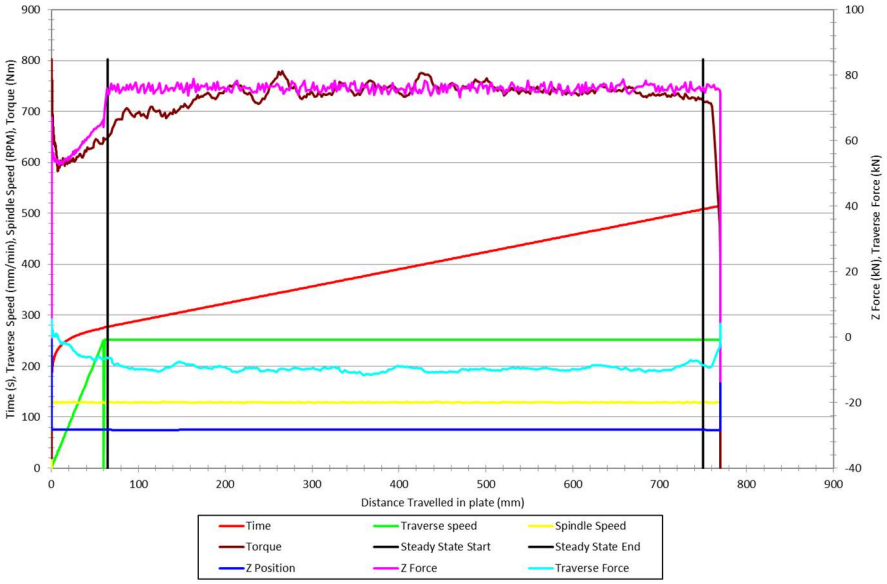

a) Weld data of upper pass

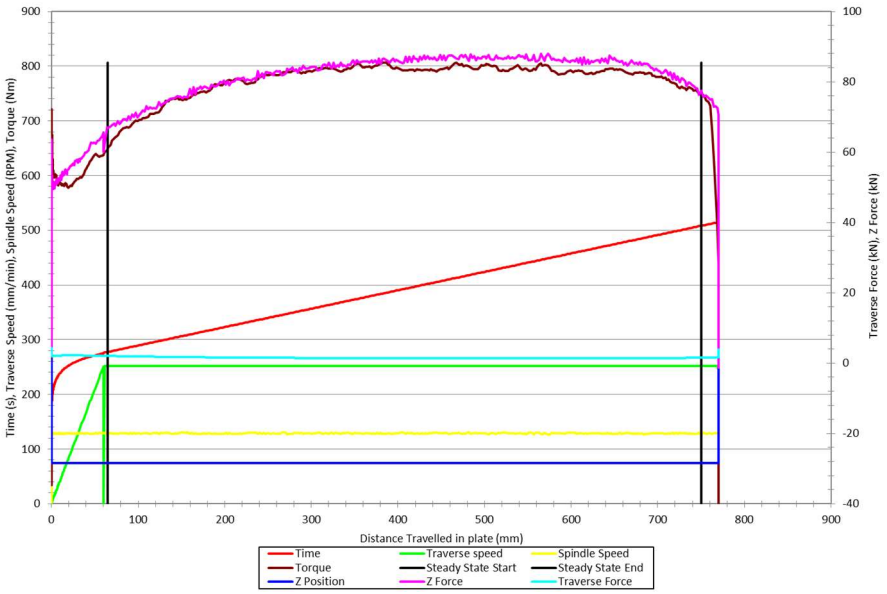

b) Weld data of lower pass

Figure 105 - Weld data for SDS-FSW of AA6082-T651.

4.2.1.3 Supported Stationary Shoulder FSW - Tool D060

Pass	Traverse speed (mm/min)	Rotational speed (rpm)	Torque - Avg (Nm)	Z-force - Avg (kN)
Single	245	199.00	1253.36	48.40

Table 31 - Parameter information for G14, an SSS-FSW of AA6082-T651.

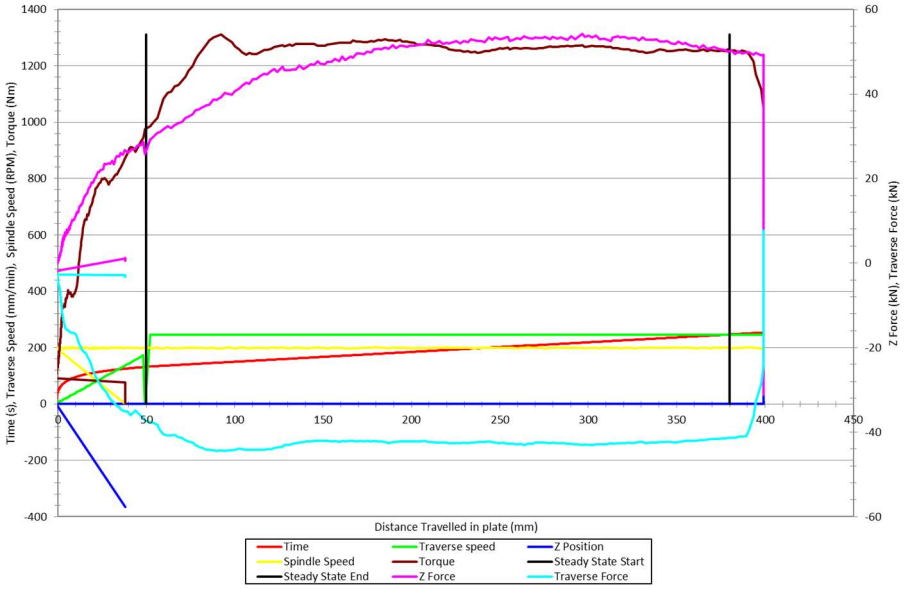

Figure 106 - Weld data for SSS-FSW of AA6082-T651 using tool D060.

4.2.1.4 Supported Stationary Shoulder FSW - Tool D070

Pass	Traverse speed (mm/min)	Rotational speed (rpm)	Torque - Avg (Nm)	Z-force - Avg (kN)
Single	245	199.00	1146.52	44.88

Table 32 - Parameter information for G16, an SSS-FSW of AA6082-T651.

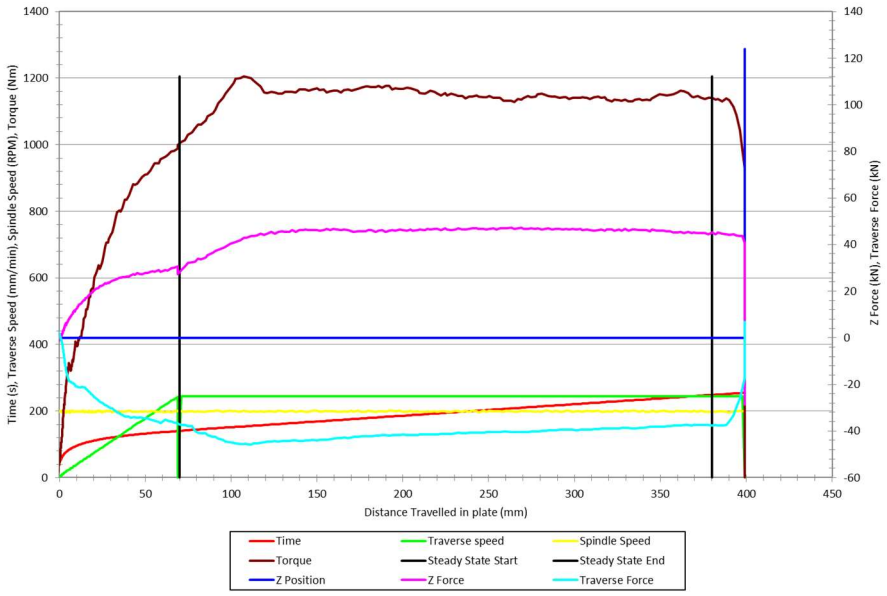

Figure 107 - Weld data for SSS-FSW of AA6082-T651 using tool D070.

4.2.1.5 Supported Stationary Shoulder FSW - Tool D080

Pass	Traverse speed (mm/min)	Rotational speed (rpm)	Torque - Avg (Nm)	Z-force - Avg (kN)
Single	245	199.00	1134.95	47.65

Table 33 - Parameter information for G19, an SSS-FSW of AA6082-T651.

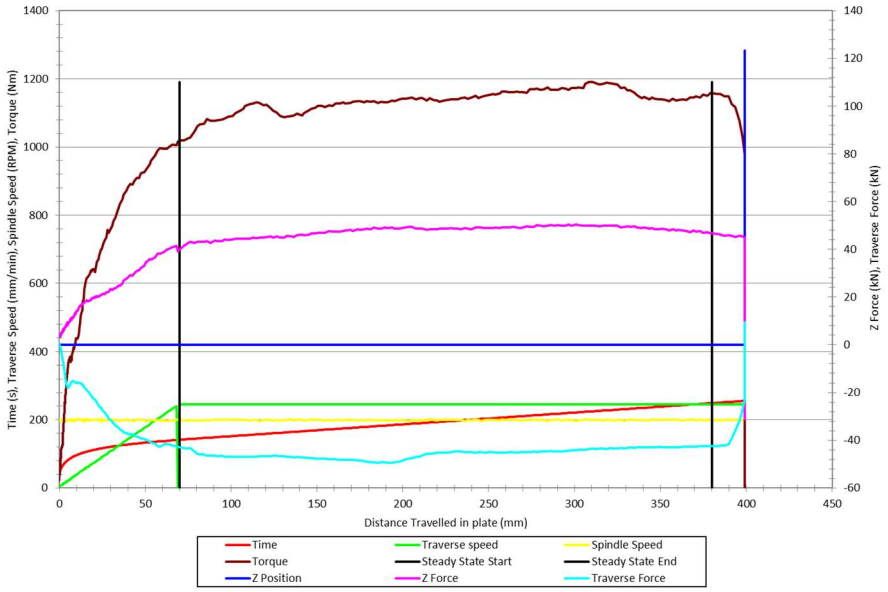

Figure 108 - Weld data for SSS-FSW of AA6082-T651 using tool D080.

4.2.1.6 Supported Stationary Shoulder FSW - Tool D030

Pass	Traverse speed (mm/min)	Rotational speed (rpm)	Torque - Avg (Nm)	Z-force - Avg (kN)
Single	245	199.00	1092.00	39.43

Table 34 - Parameter information for G17, an SSS-FSW of AA6082-T651.

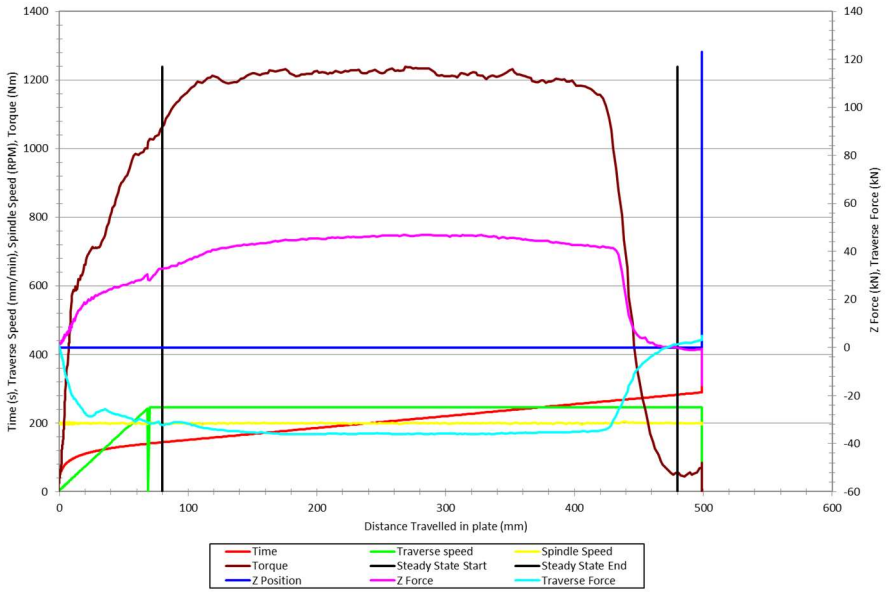

Figure 109 - Weld data for SSS-FSW of AA6082-T651 using tool D030.

4.2.2 Chemical analysis

4.2.2.1 Optical Emission Spectroscopy (OES)

Optical Emission Spectroscopy (OES) was conducted to quantify the elements and their weight percentages within AA6082-T651. The results of this are shown in Table 35, alongside the standard composition of the alloy, and the OES data sheet is provided in Appendix 21.

The alloy is heavily aluminium based (97.5 wt.%) however there are several primary alloying elements which showed increased weight percentages versus the other elements. These were shown to be magnesium (0.74 wt.%), manganese (0.53 wt.%) and silicon (0.92 wt.%).

Element	Element wt%	
	Received material	Standard composition
Al	97.5	95.2-98.3
Cr	0.011	Max 0.25
Cu	0.016	Max 0.1
Fe	0.19	Max 0.5
Mg	0.74	0.6-1.2
Mn	0.53	0.4-1.0
Si	0.92	0.7-1.3
Ti	0.010	Max 0.1
Zn	0.007	Max 0.2
Other, each	Max 0.008	Max 0.05
Other, total	0.076	Max 0.15

Table 35 - Element wt% for parent material AA6082-T651 as provided by OES analysis.

4.2.3 Microstructural analysis

4.2.3.1 Macrograph

Macrographs of the as-received, WFW and SDS-FSWed samples were taken using an Infinite Focus Microscope (IFM), these are shown from Figure 110 through to Figure 112. The as-received material, shown in Figure 110, appears uniform through the thickness.

As well as the tool profile being visible and signs of skewing in Figure 111, a void of approximately 3.5mm in width is evident by the yellow circle highlighting it. This void is what is referred to as a 'chip lack of fill' or Chip LOF defect. This is a cold weld defect that is caused by insufficient heating resulting in shearing and cutting of the parent material leaving chips or shards of metal within the tunnel void (Arbegast (2003)).

The weld G22 (SDS-FSW in AA6082-T651), in Figure 112, shows that the probes did not experience skewing, and the central region has been double processed as expected. Banding is prominent on the advancing side of both passes and the retreating side stir zone has a gradual transition into the HAZ.

Figure 110 - Macrograph of as received AA6082-T651 showing a consistent microstructure throughout the thickness of the material - etched in Kellers reagent.

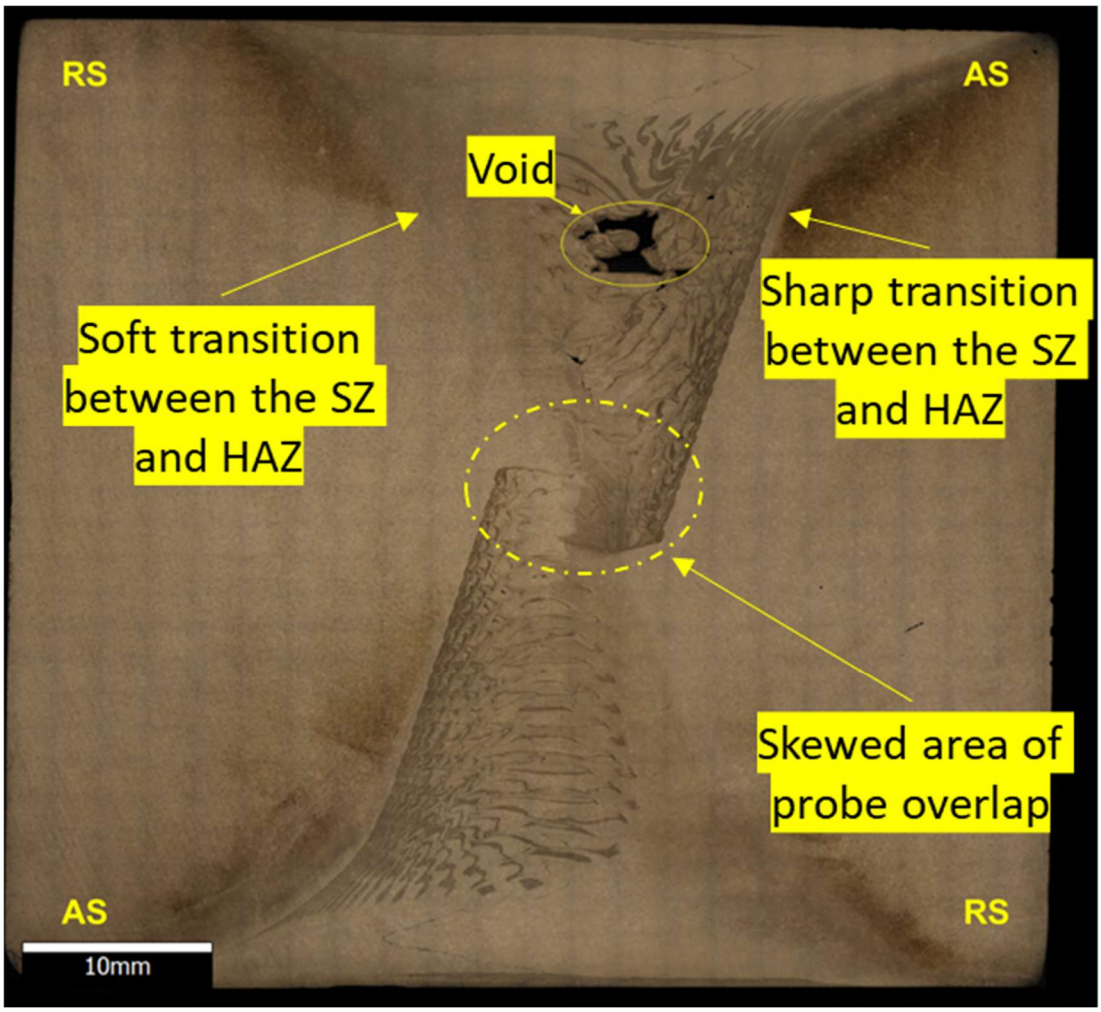

Figure 111 - Macrograph of weld G20/21 - etched in Kellers reagent. Solid yellow ring indicating the presence of a void. Dashed yellow ring indicates skewed nature of probes. A sharp and soft transition is visible on either side of the weld, as indicated by the arrows.

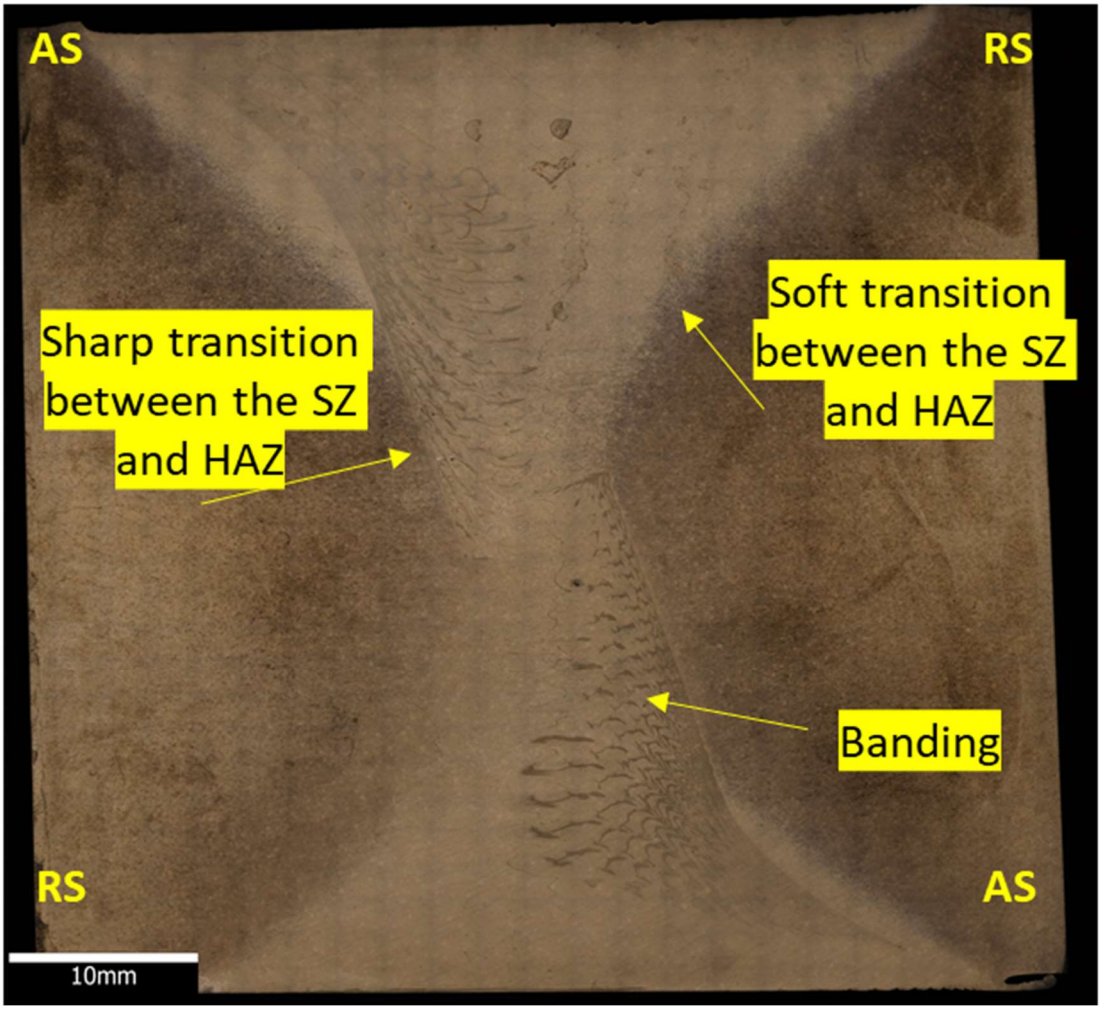

Figure 112 - Macrograph of weld G22 - etched in Kellers reagent. Profile of the probe is visible and the sharp and soft transitions on the advancing and retreating sides respectively are identified. Banding is also identified within the stir zone.

In this grade of material, four SSS-FS welds were produced as outlined in section 1.3. Figure 113 through to Figure 116 show the macrographs of these welds. Figure 116 shows the presence of voids in the weld. This weld used a 3 flat, coarse thread probe and may have ultimately not generated enough frictional heat to aid in consolidating the weld.

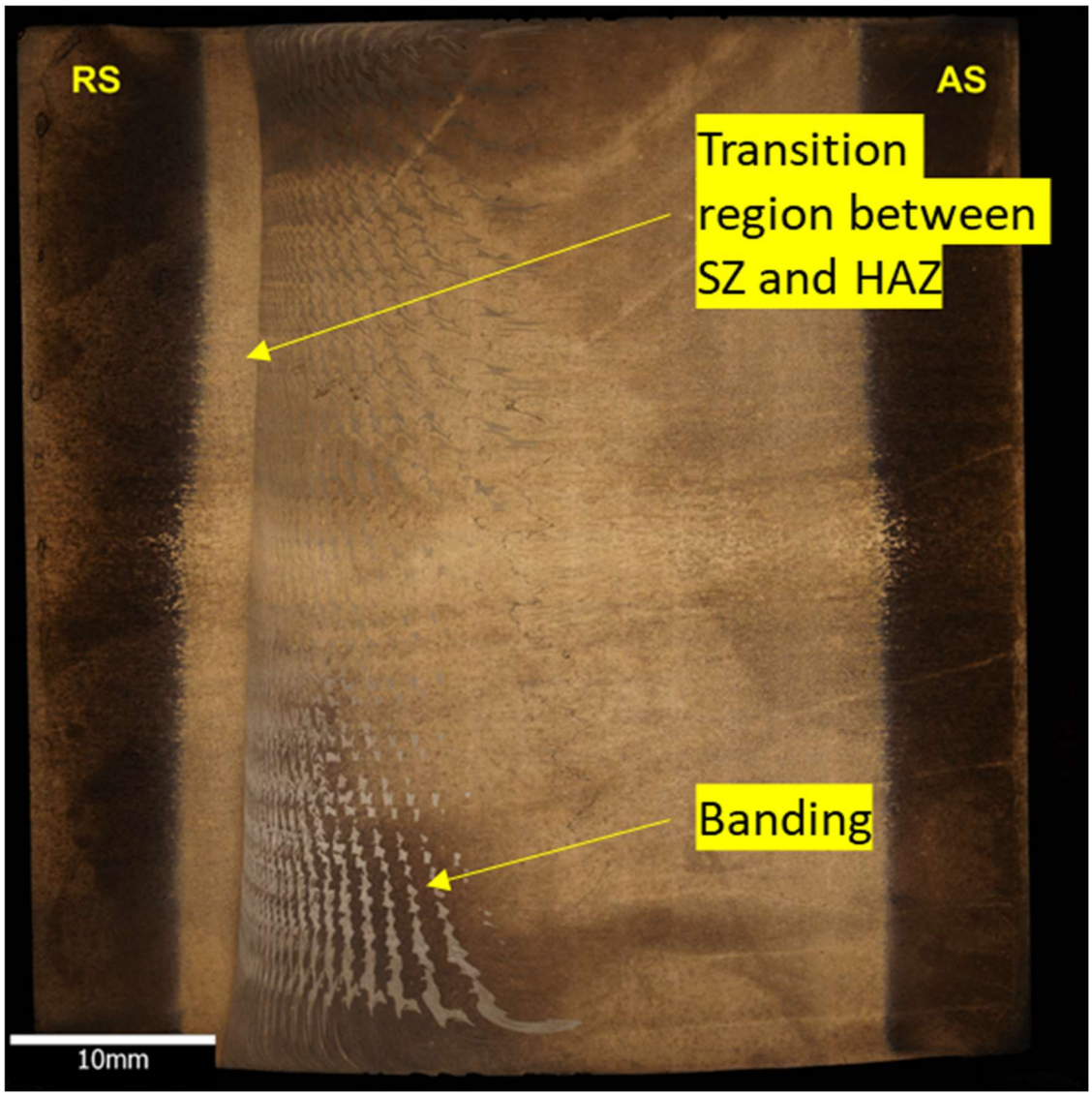

Figure 113 - Macrograph of weld G14 - etched in Kellers reagent. Profile of the probe is visible and a transition between the SZ and the HAZ is identified on the retreating side. Banding is also identified within the stir zone.

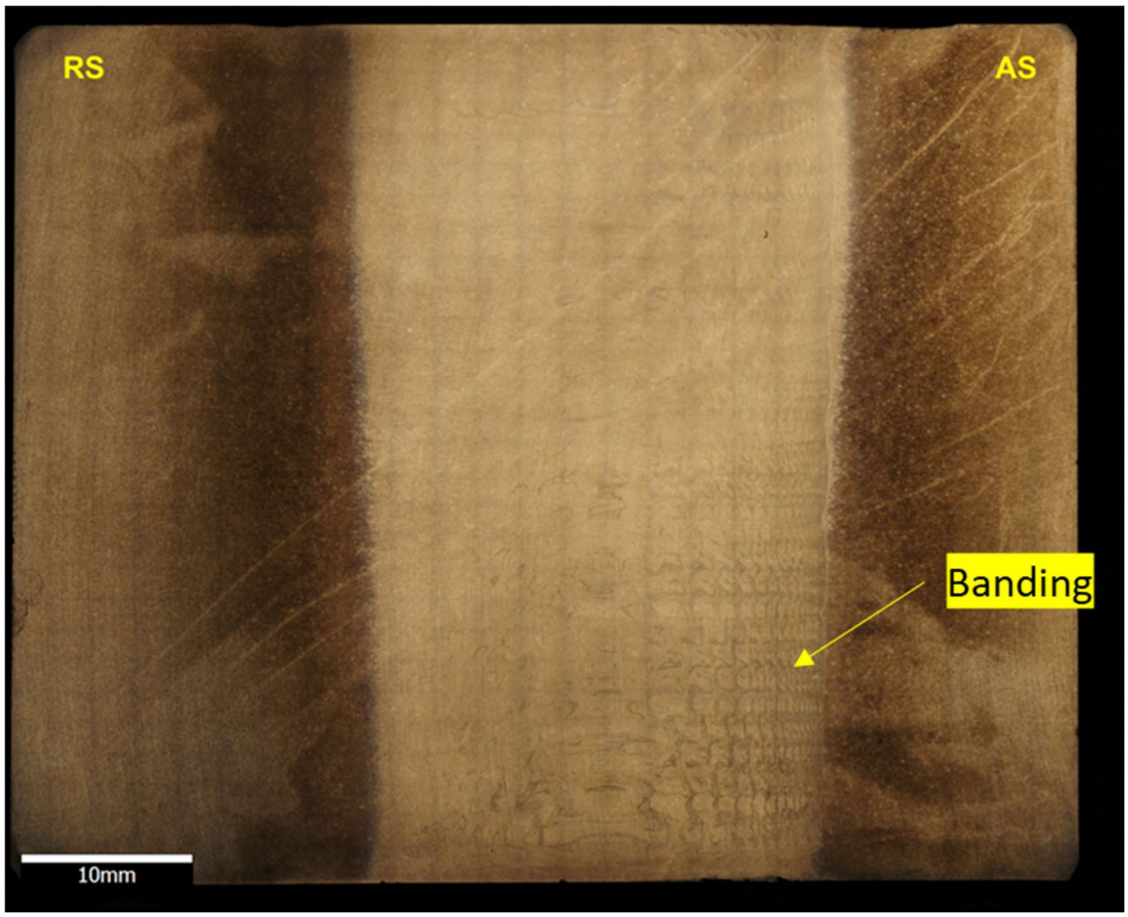

Figure 114 - Macrograph of weld G16 - etched in Kellers reagent. Profile of the probe is visible, and banding is also identified within the stir zone.

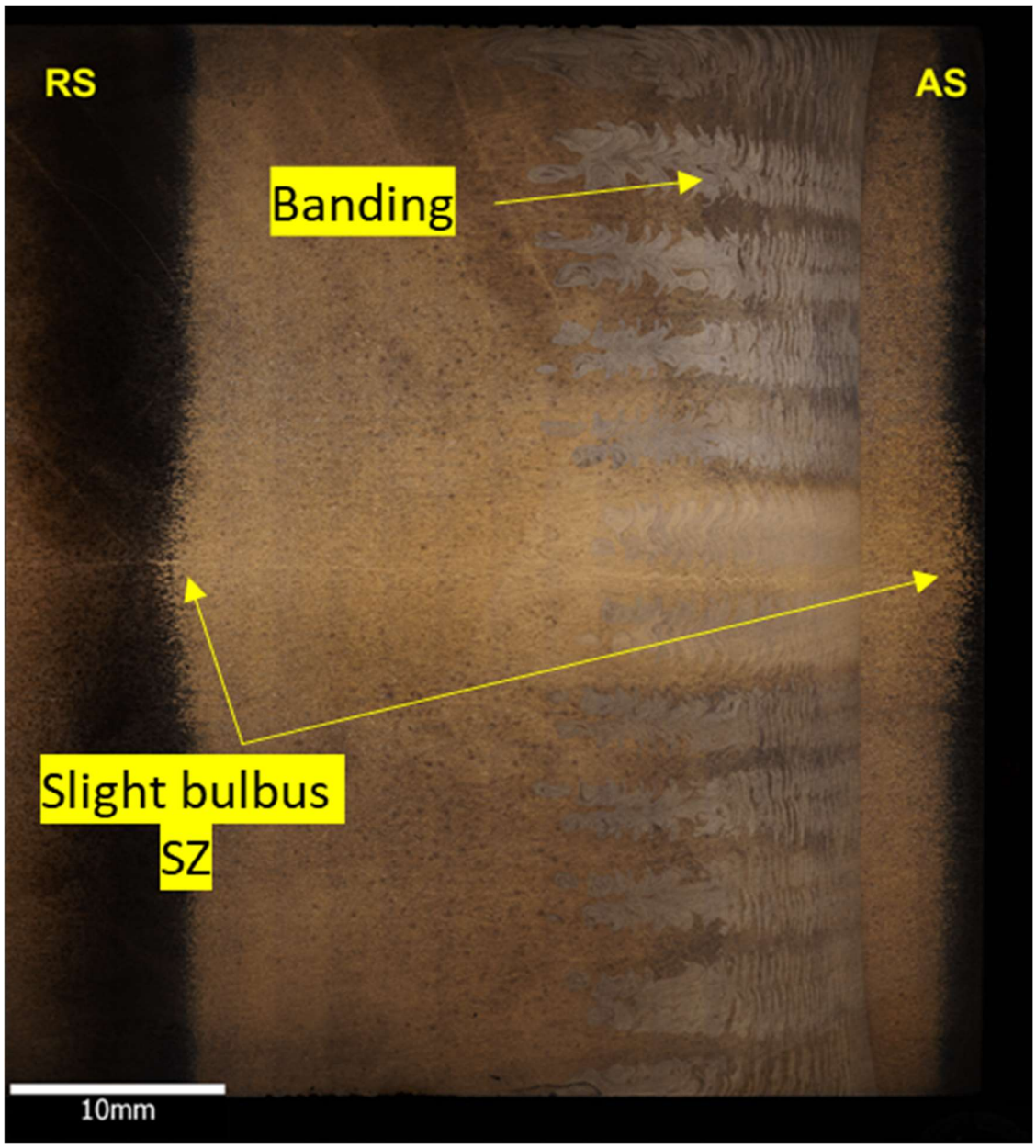

Figure 115 - Macrograph of weld G17 - etched in Kellers reagent. Profile of the probe is visible although the SZ also appears slightly bulbus at centre thickness. Banding is also identified within the stir zone.

Figure 116 - Macrograph of weld G19 - etched in Kellers reagent. Yellow ring indicating the presence of a void.

4.2.3.2 Optical Light Microscopy (OLM)

As per section 3.6.3, nine regions were captured for each sample. These are displayed in Appendix 22 to Appendix 27. However, in this section only the stir zone and as-received materials are presented as the stir zone was the area of most significant change due to both the thermal and mechanical impact of the FSW process. The microstructure of as-received AA6082-T651 is displayed in Figure 117 while the stir zone of each weld is shown in is shown from Figure 118 to Figure 124. All samples were etched in Kellers reagent. Figure 117 along with the macrograph shown in Figure 110 indicates a uniform through thickness microstructure with large black particles visible throughout. G20/21 is shown in Figure 118. Region b of this figure shows the skewed nature of probes as well as the joint line remnant which is also evident in G22 – see Figure 119(middle).

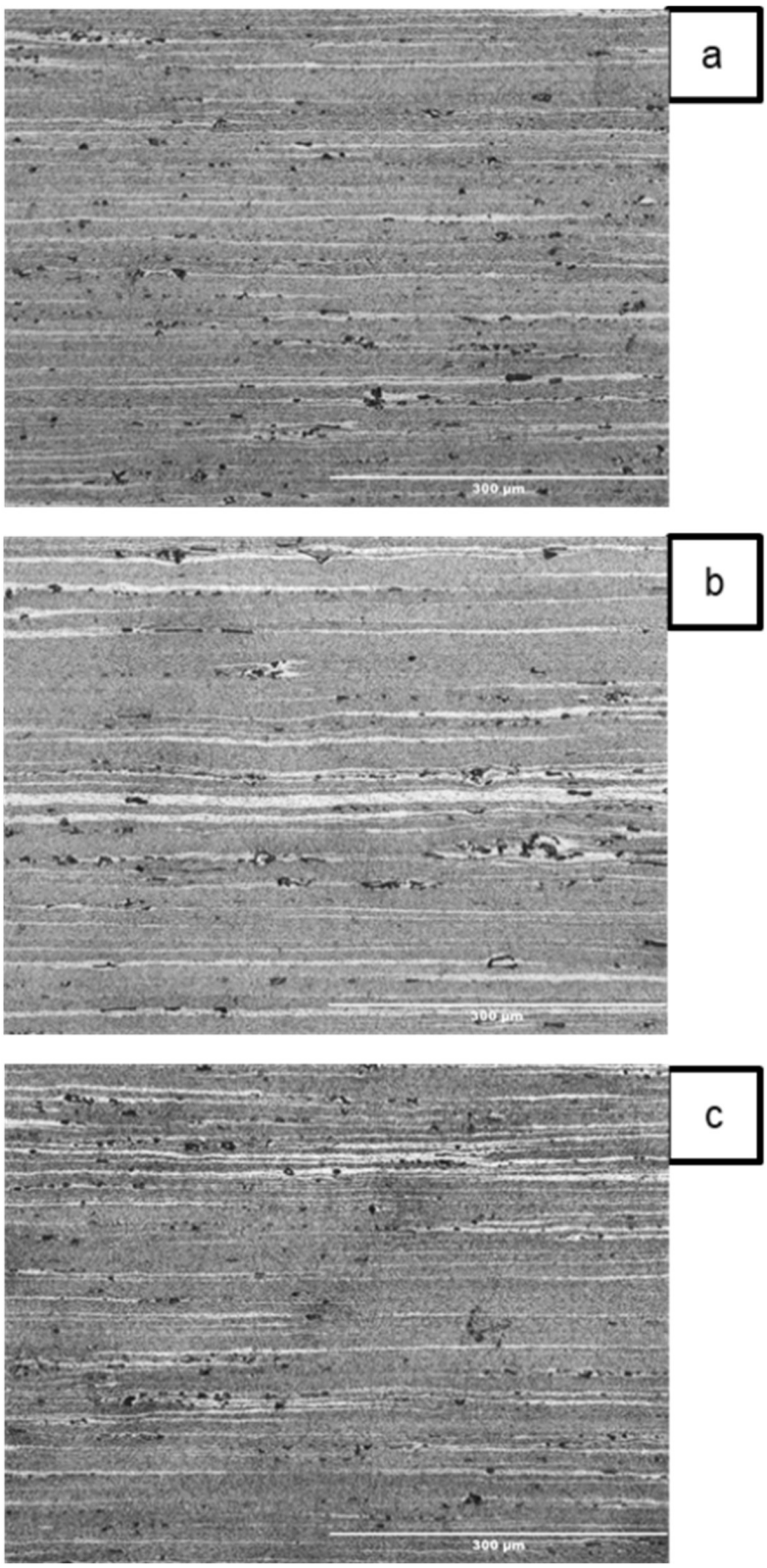

Figure 117 - Microstructure of as-received AA6082-T651. A) top of material, b) centre of material and c) bottom of material.

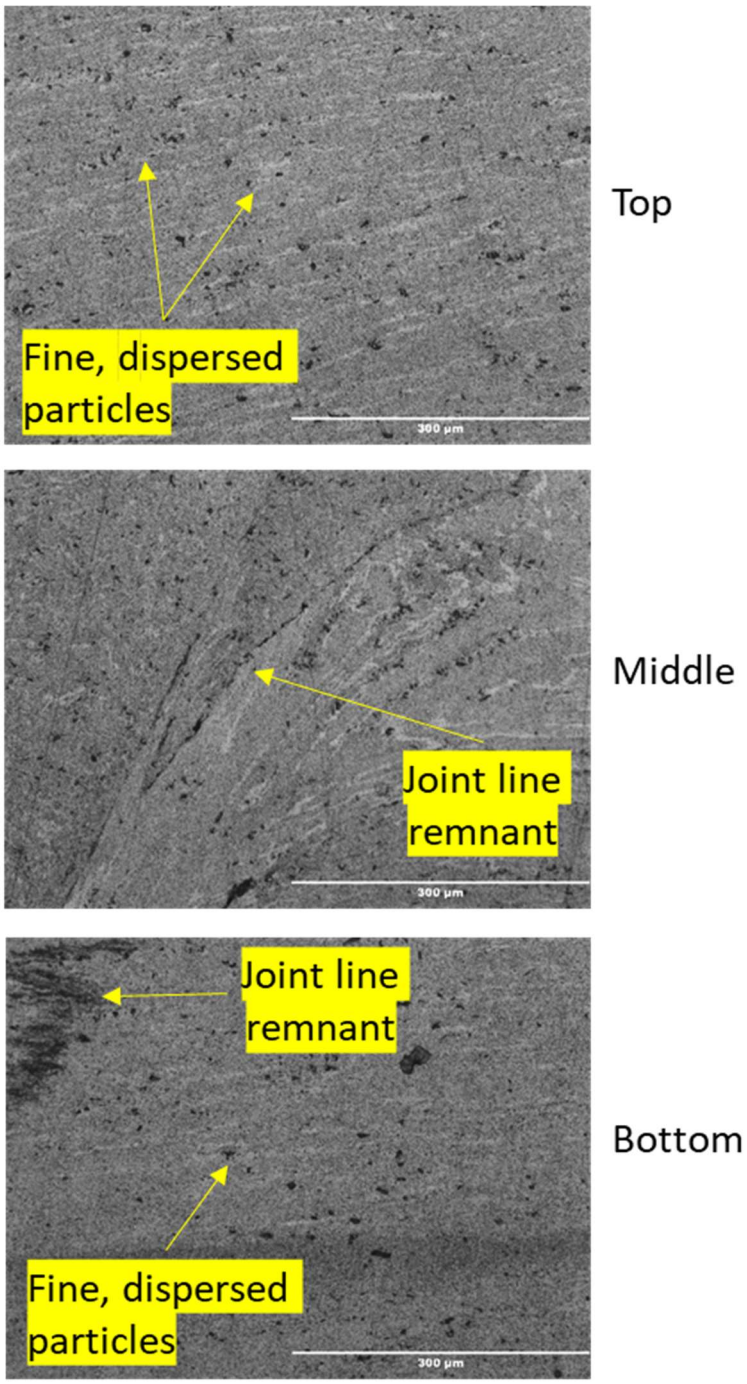

Figure 118 – Microstructure of WFW-FSW, G20/21, stir zone. (Top) shows a fine dispersed distribution of particles in the upper pass of the weld. (Middle) The joint line remnant is prominent in the double processed region of G20/21. (Bottom) shows finer dispersed particles, compared to the parent material, in the lower pass of the weld. The joint line remnant is also identified in the image.

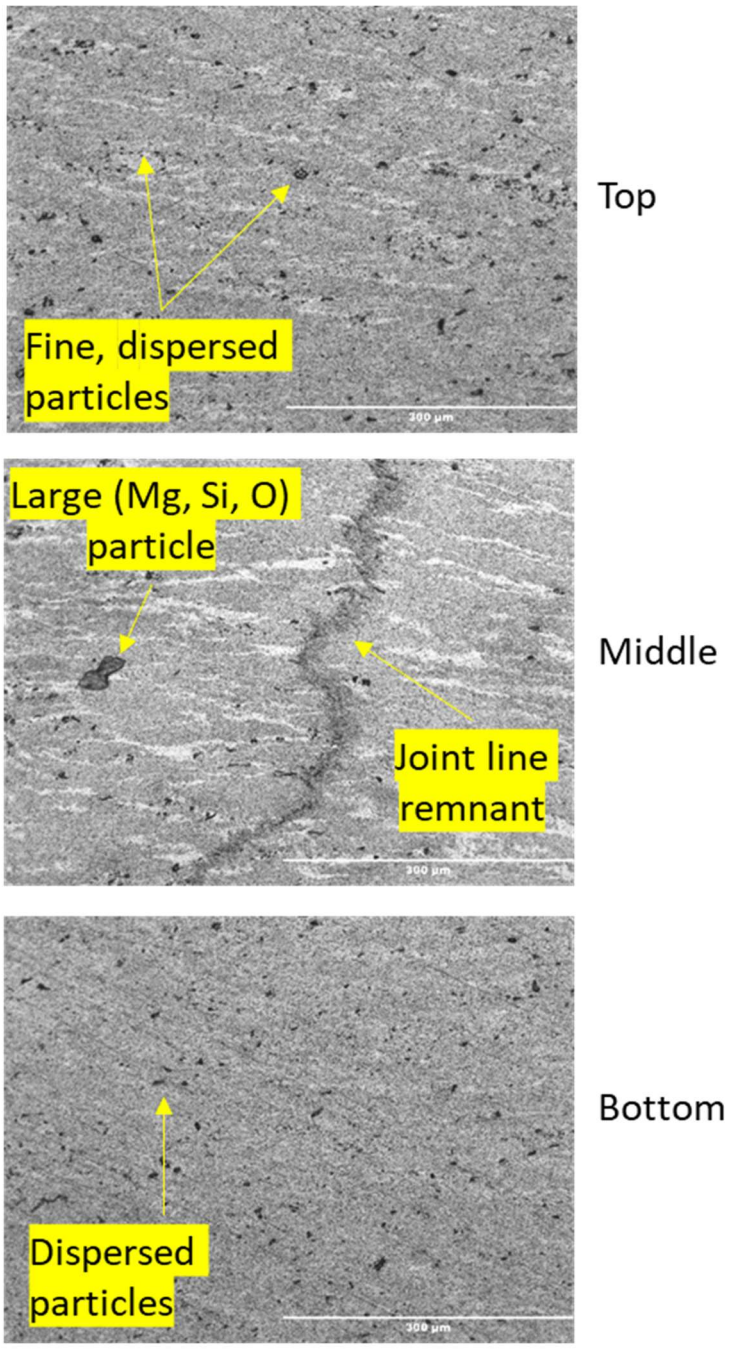

Figure 119 – Microstructure of SDS-FSW, G22, stir zone. (Top) shows a fine dispersed distribution of particles in the upper pass of the weld. (Middle) The joint line remnant is prominent in the double processed region of G22. A large (Mg, Si, O) particle is present. (Bottom) shows a less dispersed particles, compared to the upper pass, in the lower pass of the weld.

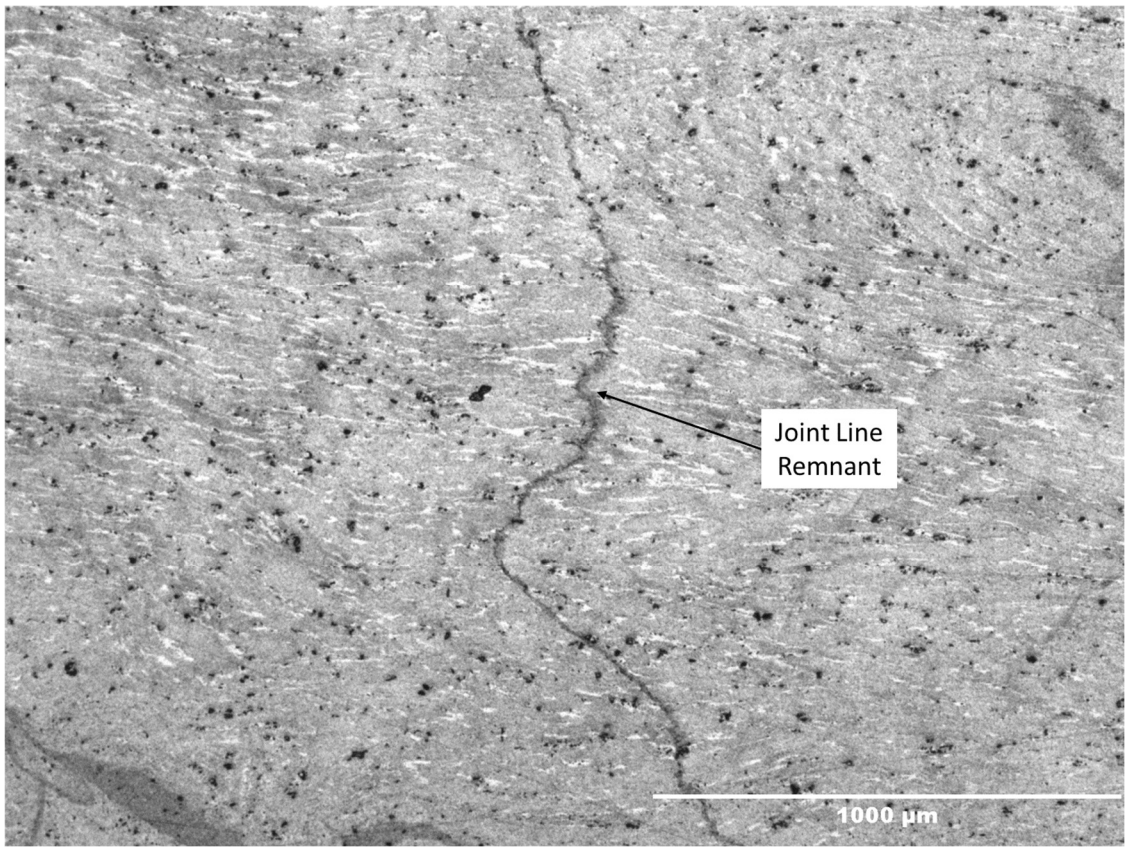

Figure 120 - Joint line remnant evident in G22.

The four SSS-FSW microstructures are shown from Figure 121 to Figure 124. There is little difference in the particle sizes and distribution between these welds and similarly there is little discrepancy between the microstructures of the SSS-FS welds and G20/21 and G22.

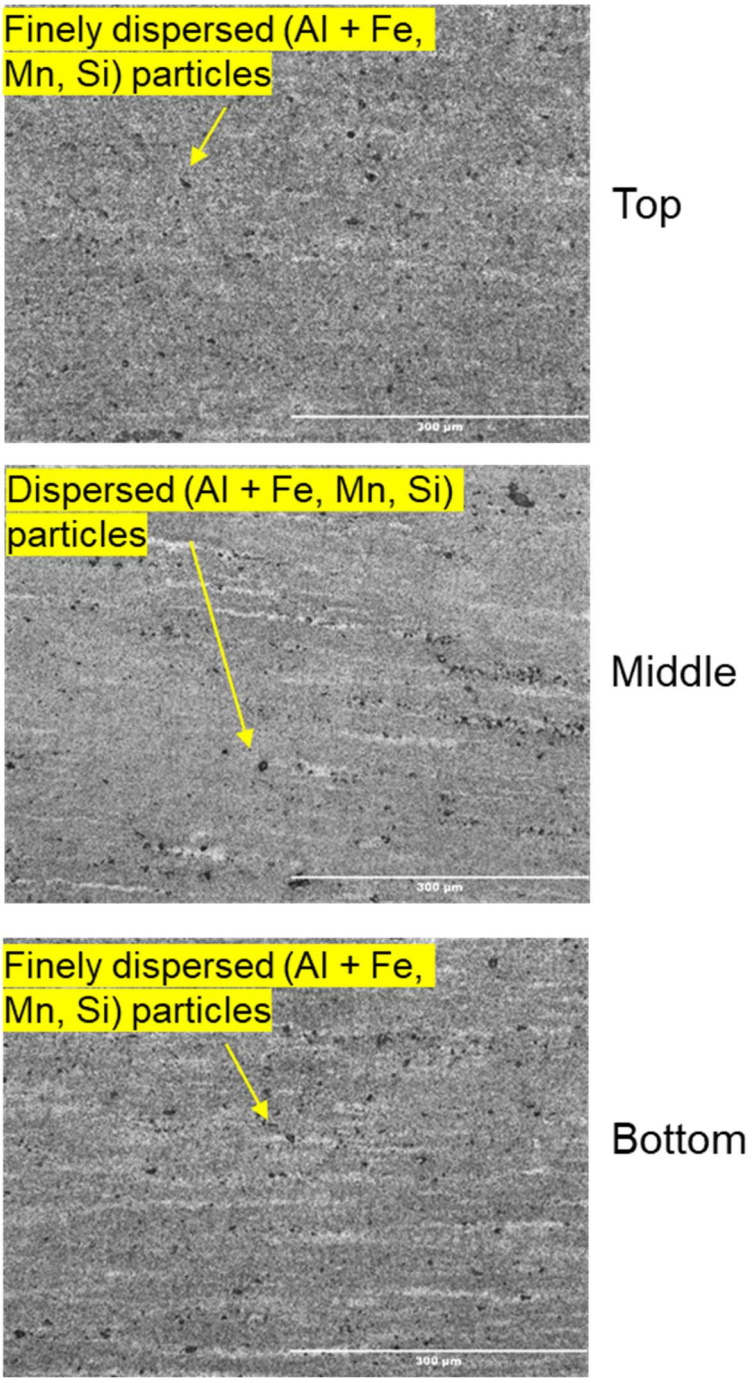

Figure 121 – Microstructure of SSS-FSW, G14, stir zone. (Top) shows a fine dispersed distribution of particles in the upper part of the weld. (Middle) Particles of (Al + Fe, Mn, Si) present in a dispersed manner (Bottom) shows finer dispersed particles, compared to the parent material, in the lower part of the weld.

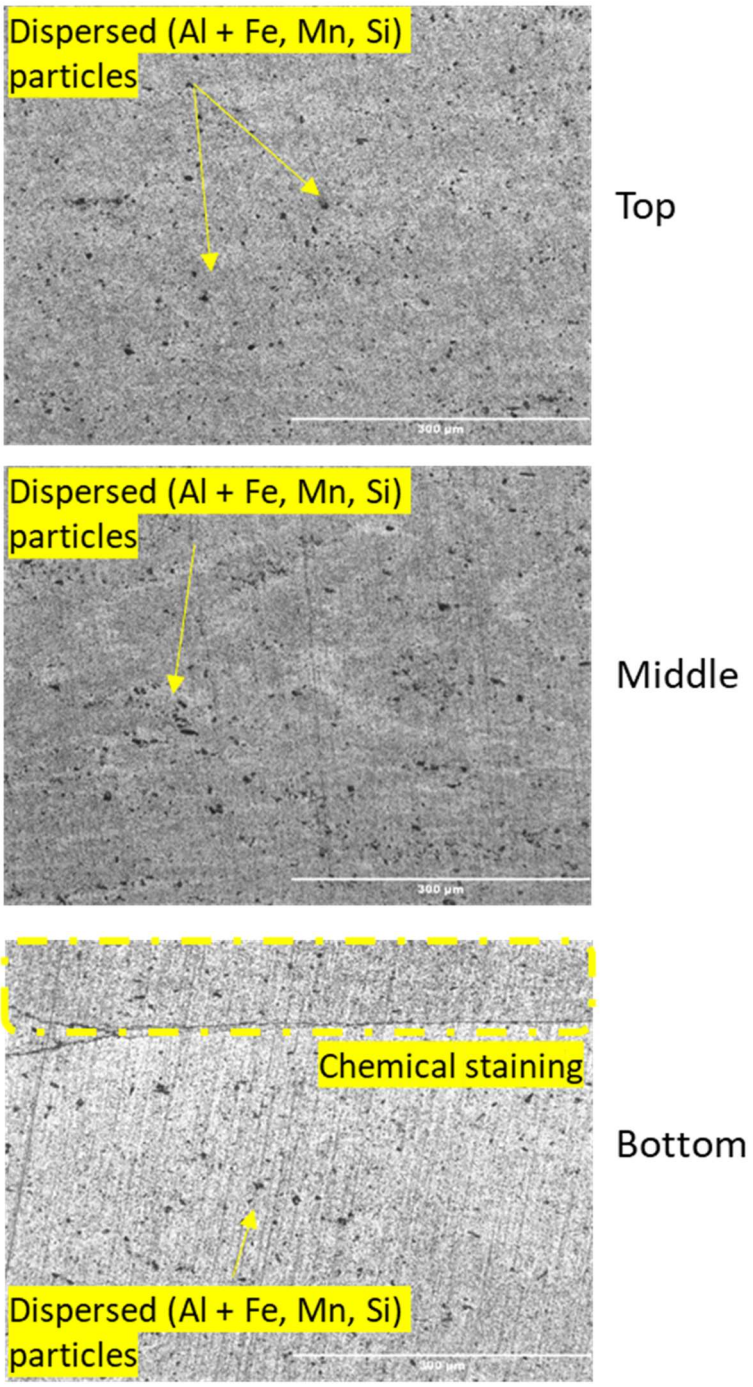

Figure 122 – Microstructure of SSS-FSW, G16, stir zone. (Top) shows a dispersed distribution of particles in the upper part of the weld. (Middle) Particles of (Al + Fe, Mn, Si) present in a dispersed manner (Bottom) Chemical staining observed at the top of the image.

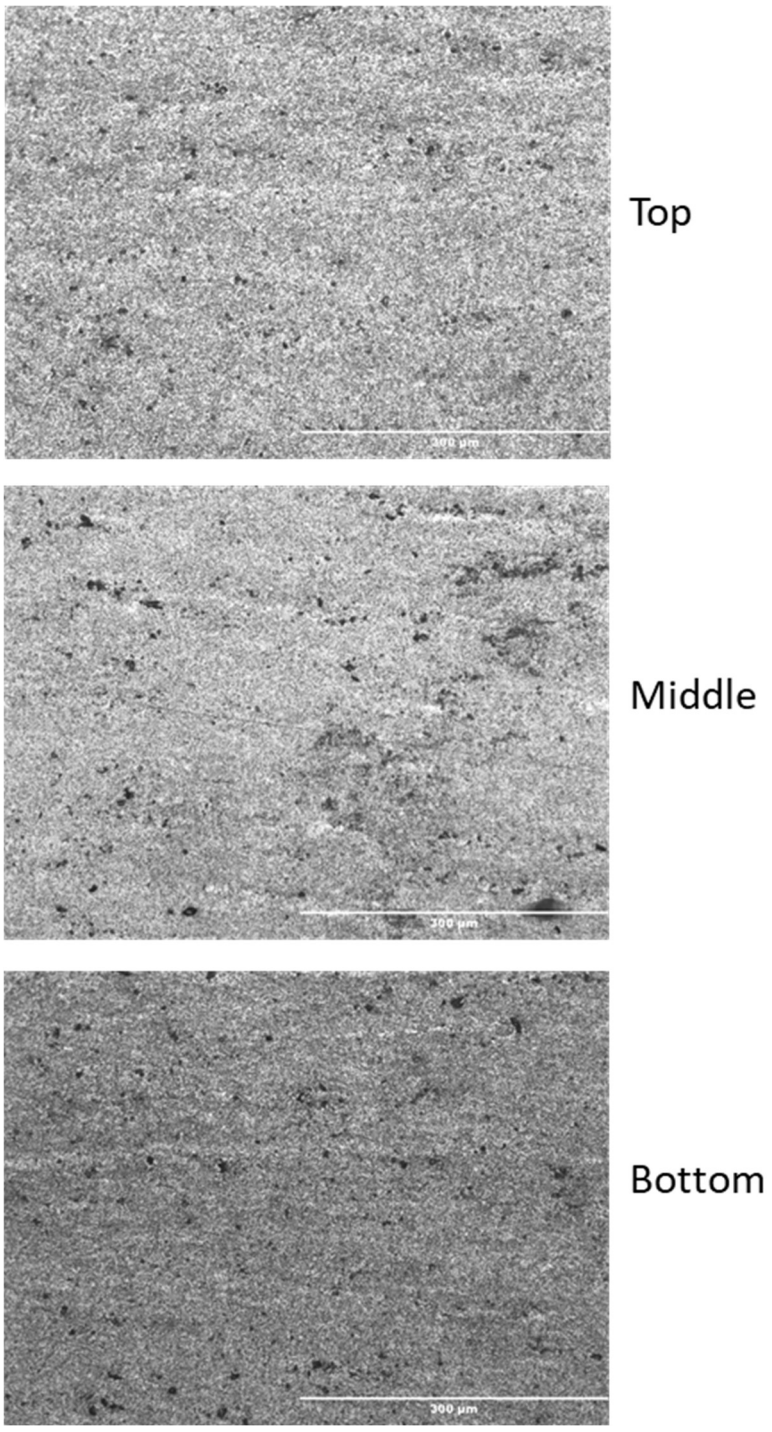

Figure 123 – Microstructure of SSS-FSW, G17, stir zone. (Top) shows a fine distribution of particles in the upper part of the weld. (Middle) Particles are distributed across the image. (Bottom) Similar to the top and middle images, the particles appear distributed across the region.

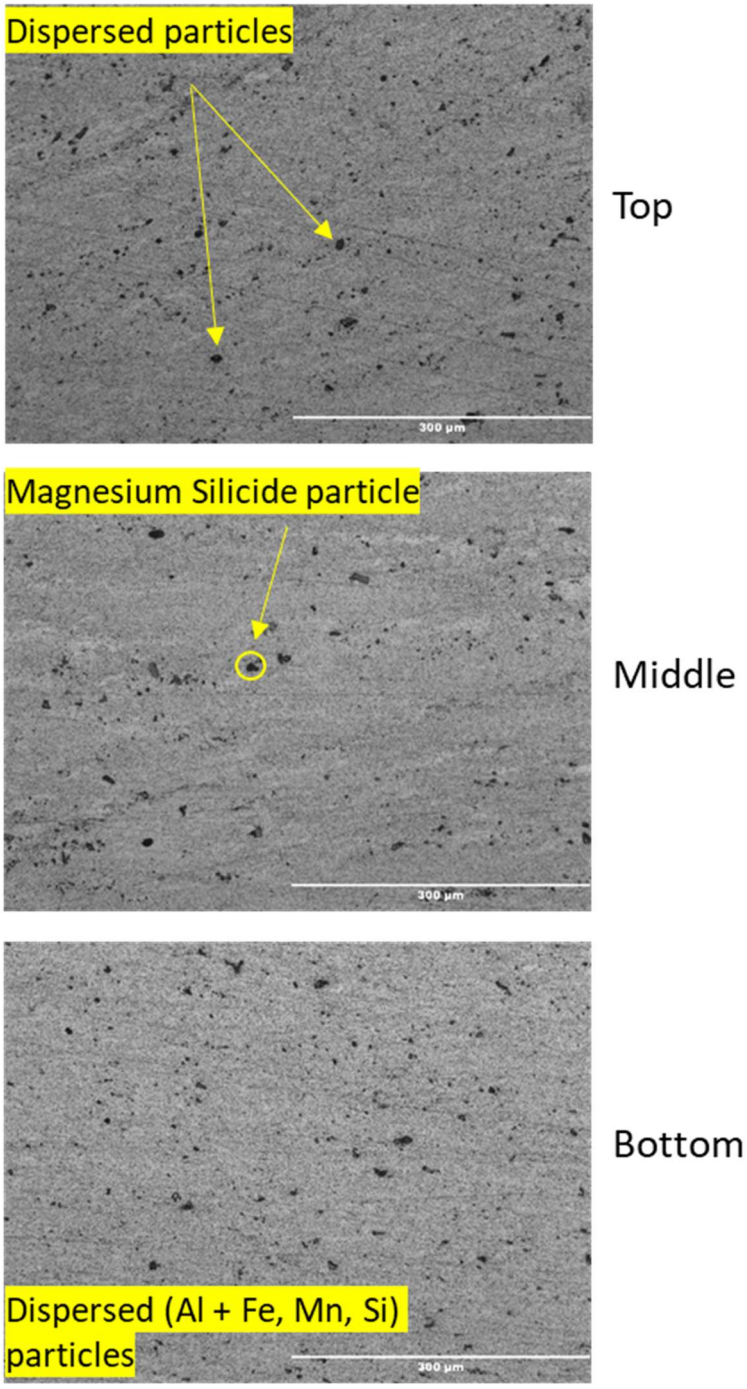

Figure 124 – Microstructure of SSS-FSW, G19, stir zone. (Top) shows a dispersed distribution of particles in the upper part of the weld. (Middle) Magnesium silicide and lighter particles of (Al + Fe, Mn, Si) present in the centre of the weld. (Bottom) shows (Al + Fe, Mn, Si) particles in the lower part of the weld.

4.2.3.3 Energy Dispersive X-Ray Spectroscopy (EDX Analysis)

EDX analysis was conducted on as-received and welded AA6082-T651. Figure 125 to Figure 135 represent some of this data. From this it was clear that much like AA5083, a light grey particle that was Al-Fe-Mn-Si based is prominent. The EDX analysis for Figure 125 also suggests the presence of magnesium in the matrix with the aluminium. Figure 132 also highlights the presence of black particles within G14, found to be Mg_2Si – the primary strengthening phase for AA6082.

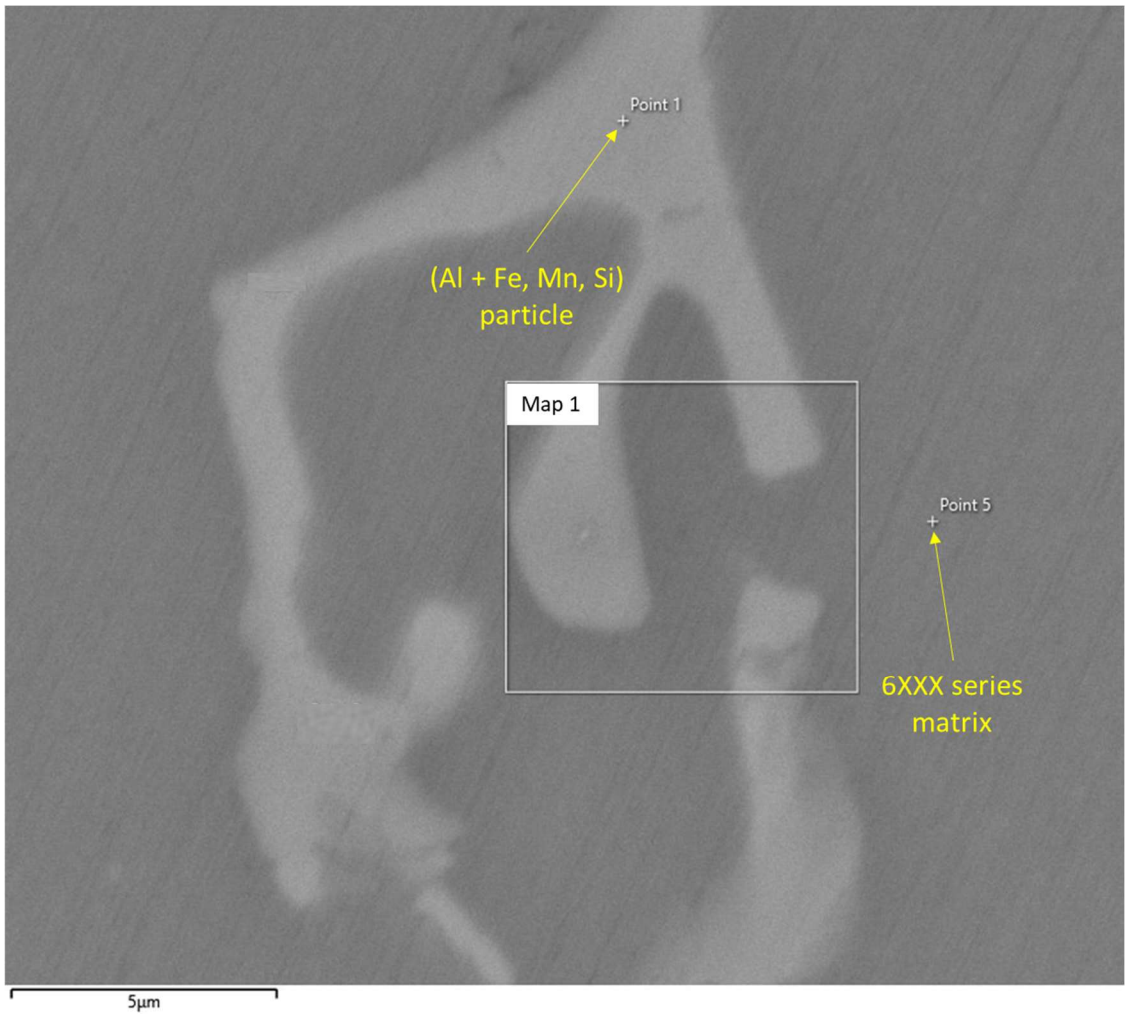

Figure 125 – SEM image of as-received AA6082-T651 showing an (Al+Fe, Mn, Si) based particle and Al-Mg matrix.

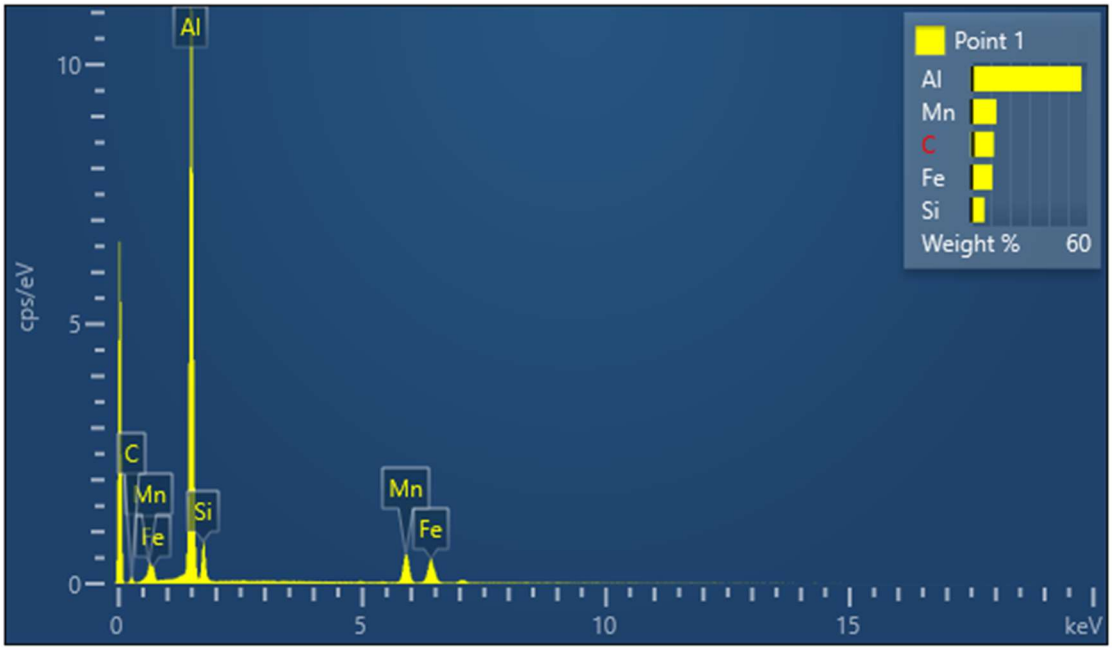

Figure 126 - EDX spectra of the particle in Figure 125.

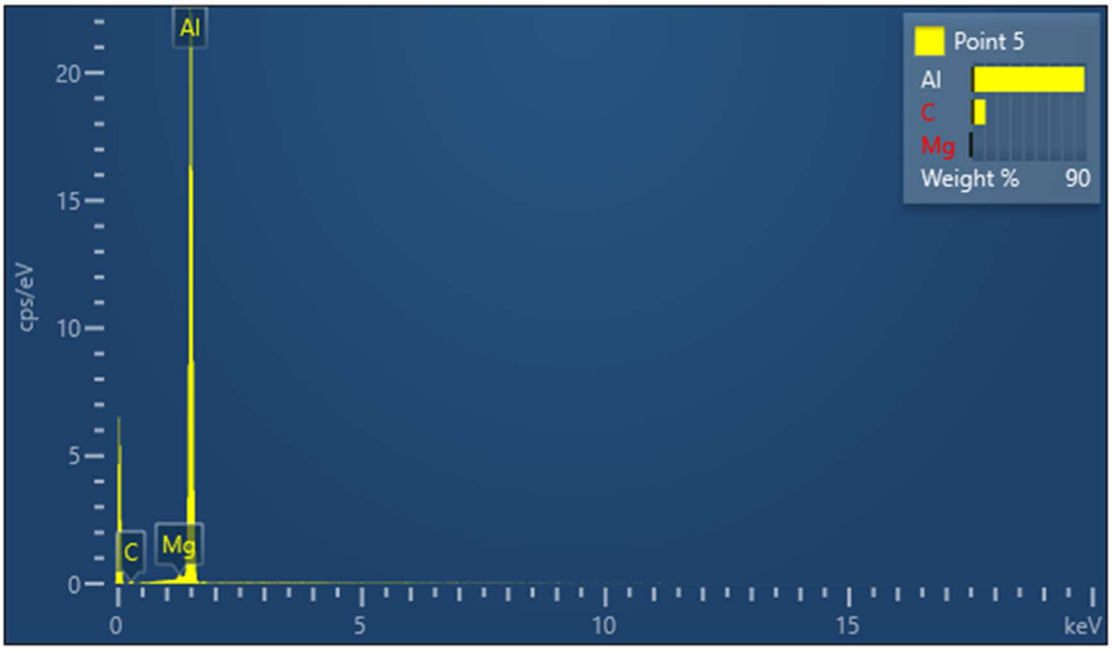

Figure 127 - EDX spectra of the Al-Mg matrix in Figure 125.

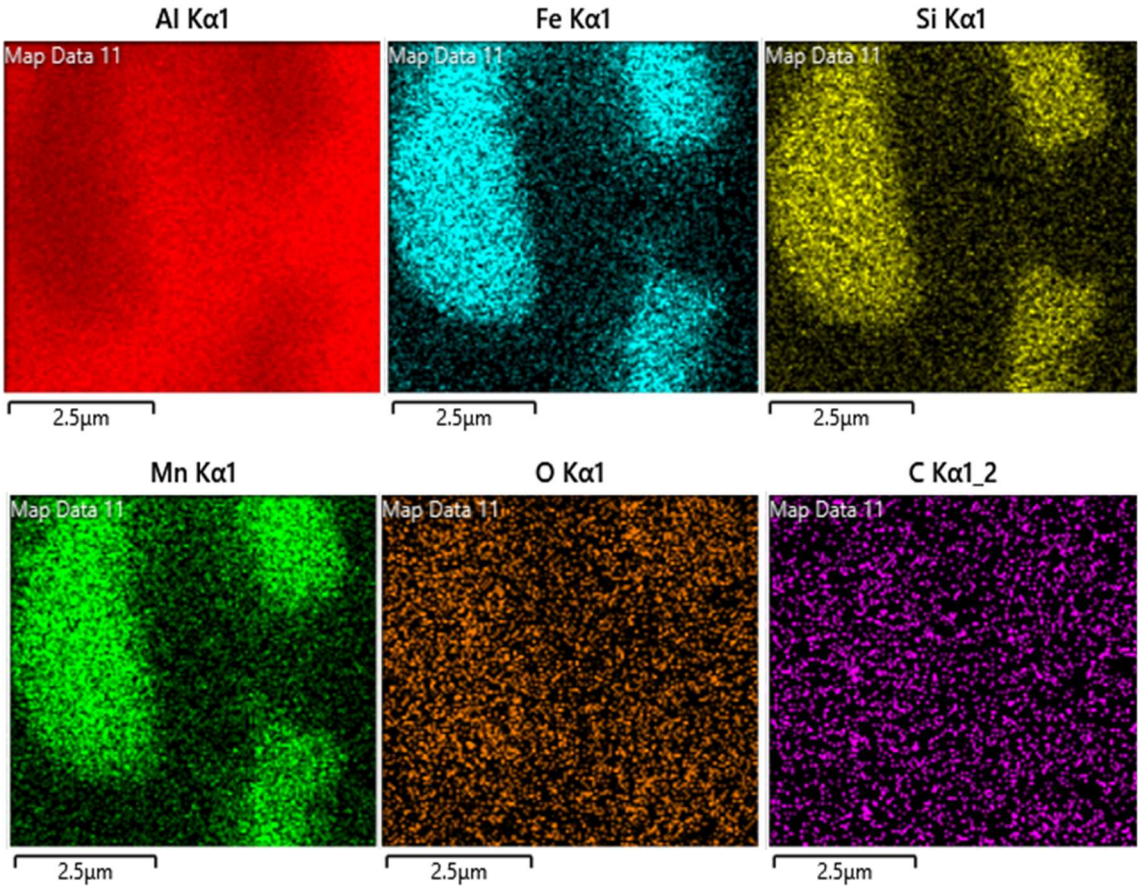

Figure 128 - EDX map of the (Al + Fe, Mn, Si) particle and surrounding matrix in Figure 125.

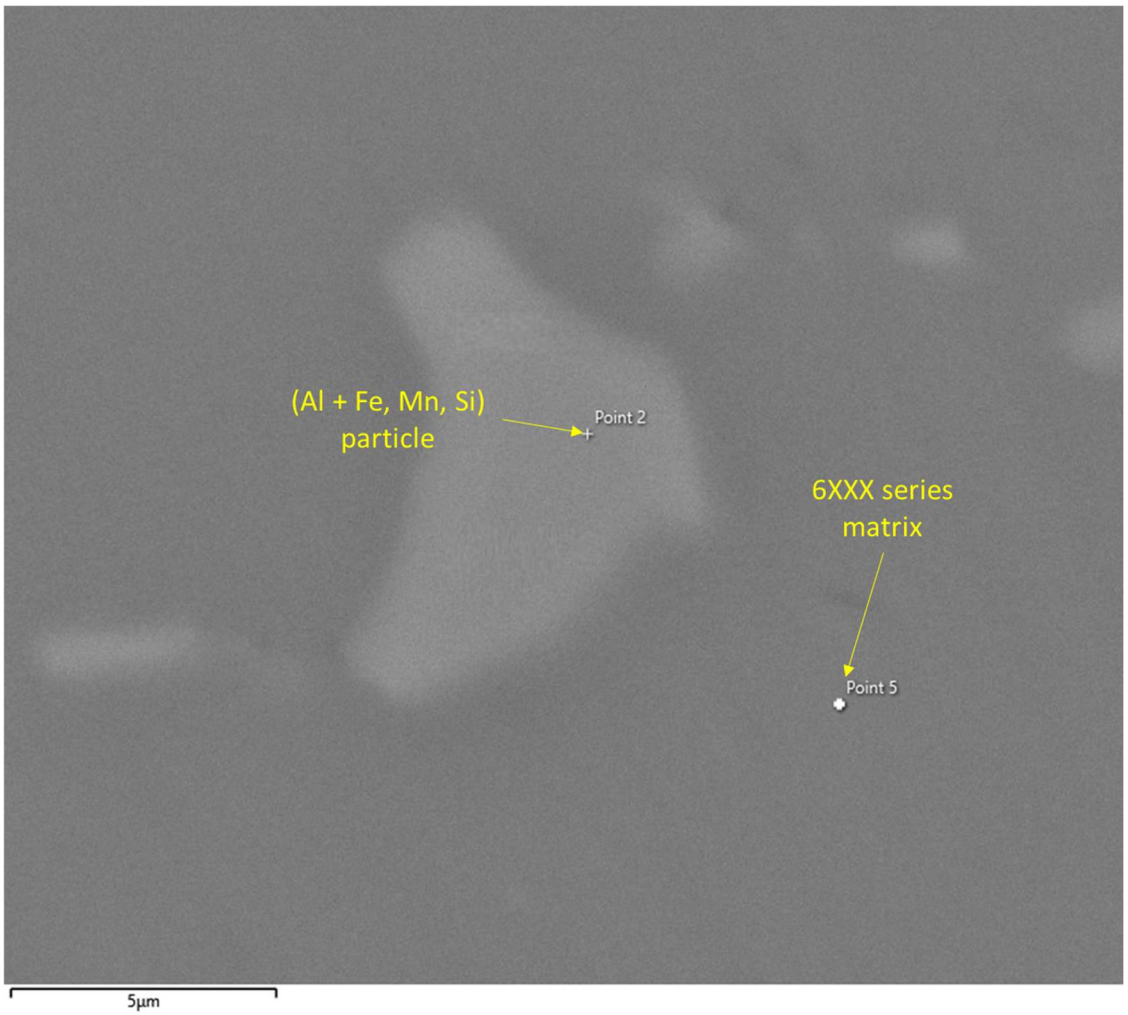

Figure 129 - SEM image of the SZ near the upper should of SDS-FSW, G22, showing an Al-Fe-Mn-Si based particle.

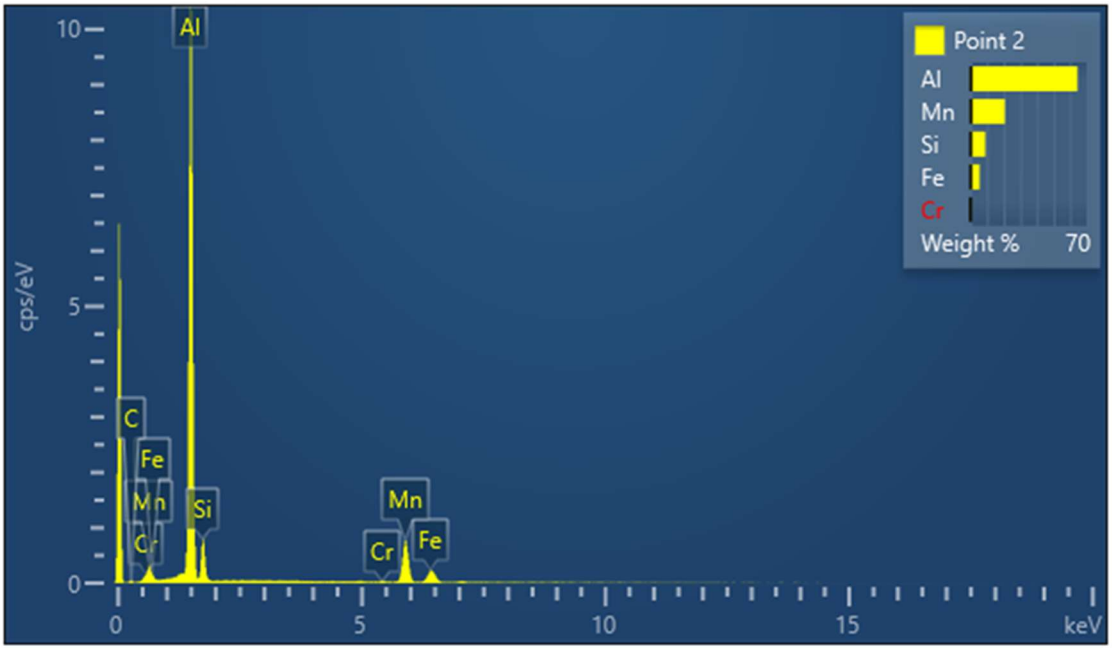

Figure 130 - EDX analysis of the particle in Figure 129.

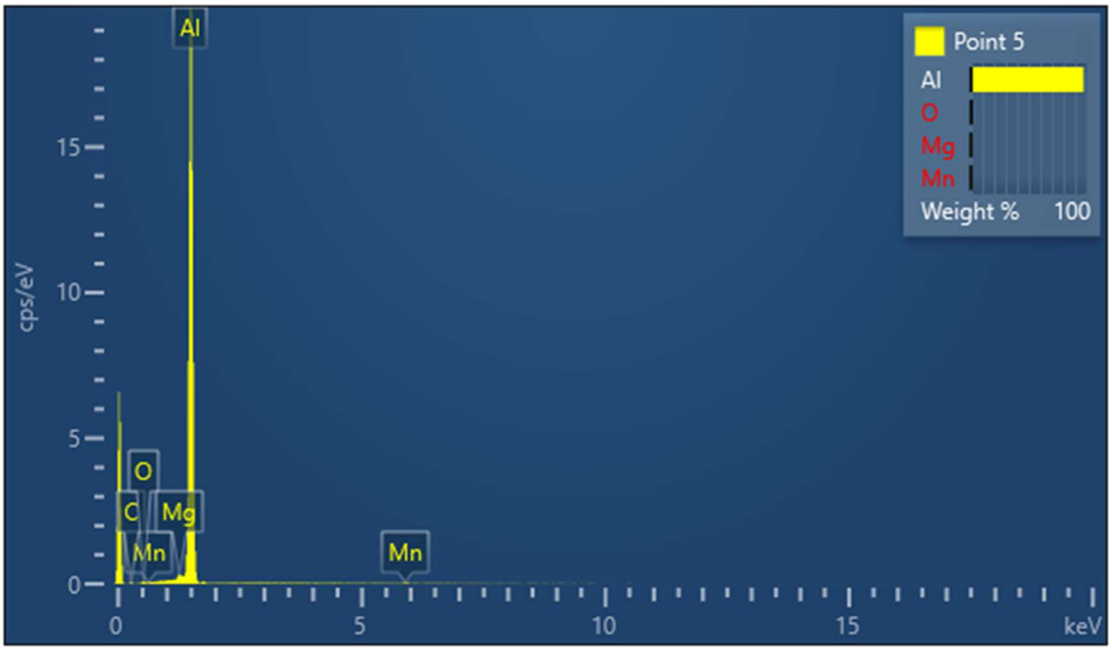

Figure 131 - EDX analysis of point 5, the matrix, in Figure 129.

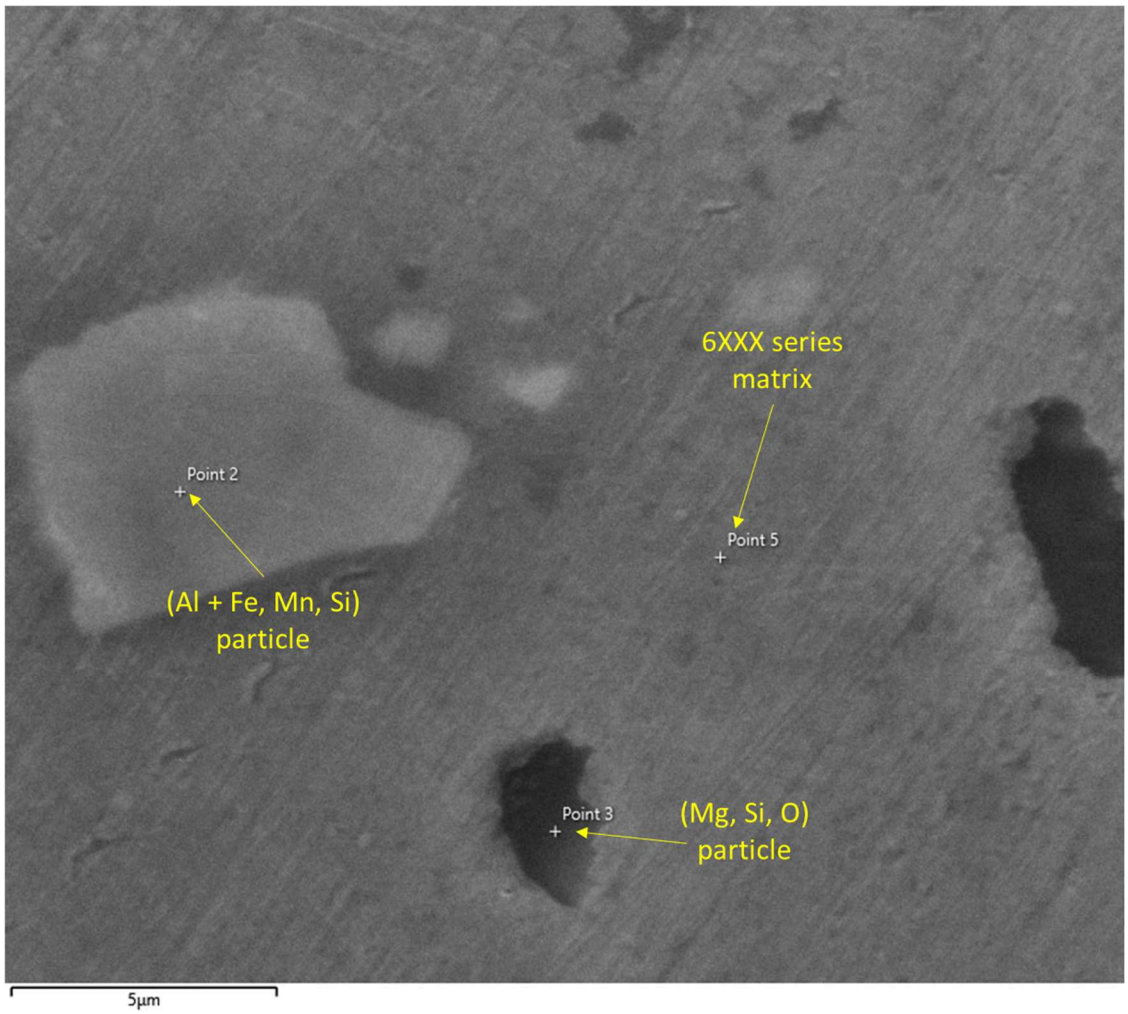

Figure 132 – SEM image of the SZ near the upper should of SSS-FSW, G14, showing an Mg-Si-O based particle.

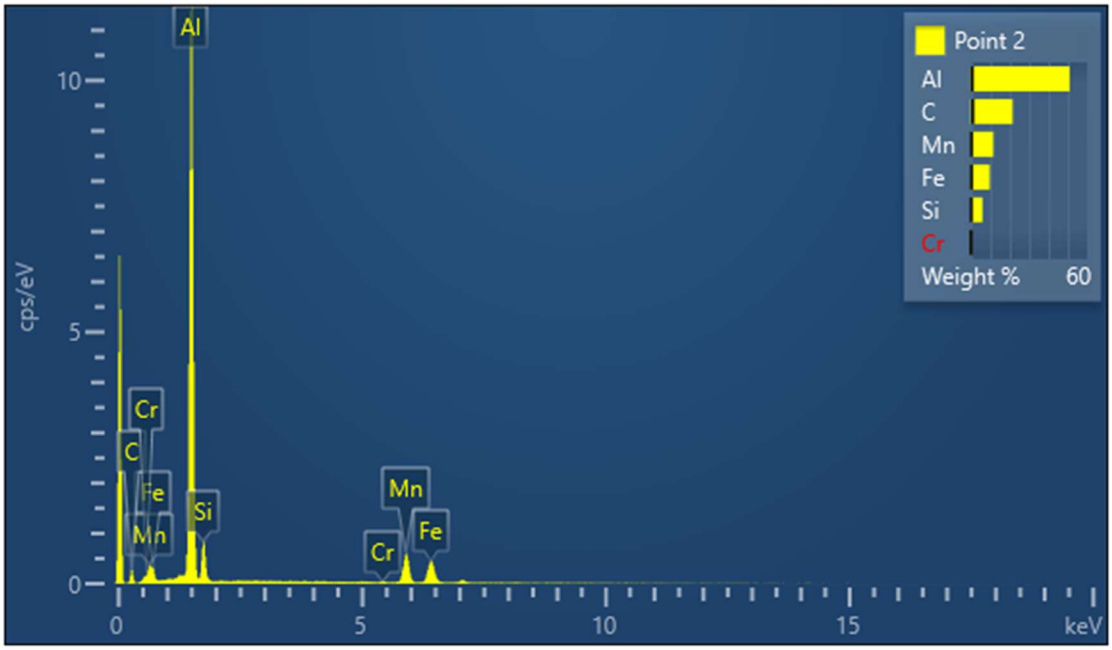

Figure 133 – EDX spectra of point 2, a (Al + Fe, Mn, Si) particle, in Figure 132.

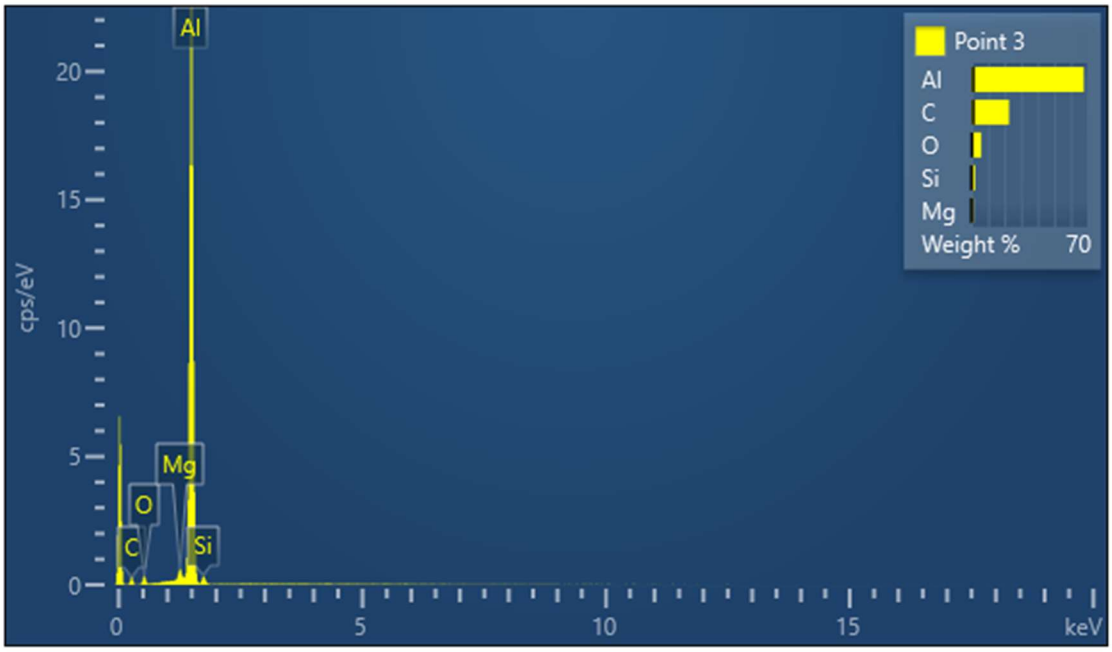

Figure 134 – EDX spectra of the black particle in Figure 132.

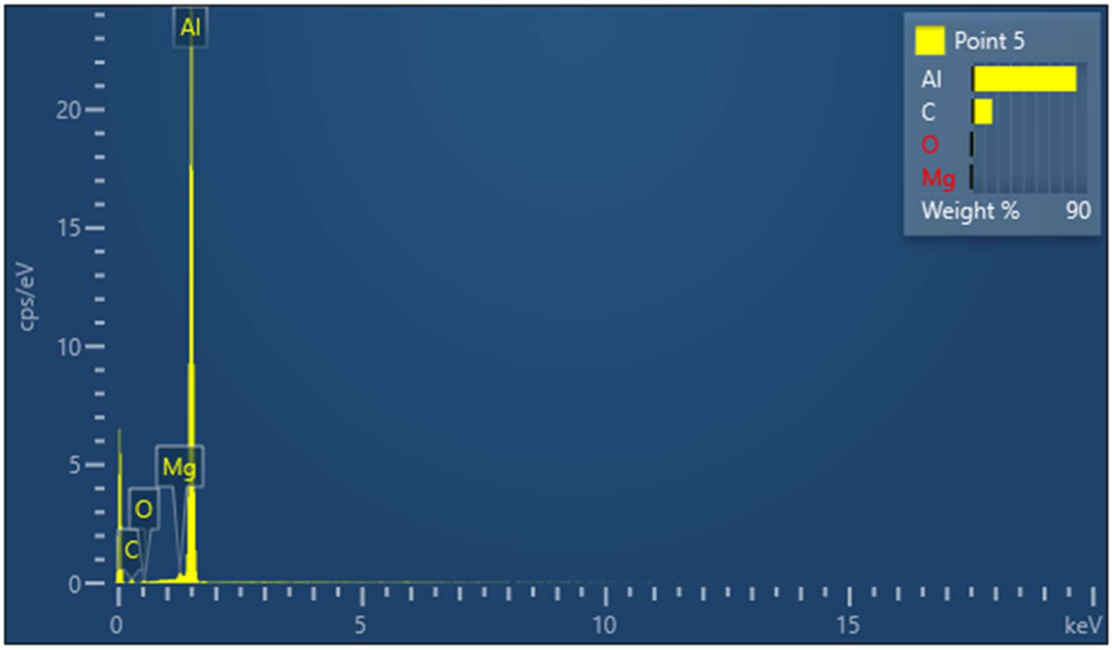

Figure 135 – EDX spectra of the matrix of G14, Figure 132.

4.2.3.4 Average distance between grain boundaries

The grain structure of this alloy was not revealed in this project. Despite the use of four etchants (Wecks, Kellers, Krolls and Barkers) and the introduction of heat treatments (250, 350 and 400 °C all for both 4 and 7 minutes) it was not possible to reveal the grain structure.

4.2.4 Mechanical properties

4.2.4.1 Tensile

The parent and as-welded materials tensile data is summarised in Table 36. The as-received AA6082-T651 UTS was measured as 334 MPa after three tests and failed at an elongation of 15.3%. Each of the 6 welds produced in AA6082-T651 failed comparatively weaker than the as-received material with G20/21 failing with the lowest UTS (185 MPa). The four SSS-FSW samples, G14, G16, G17 and G19, failed within 19 MPa of each other (221, 218, 212 and 203 MPa respectively).

I.D	Yield Strength (MPa)	UTS (MPa)	Elongation (%)
P.M	308	334	15.3
G20/21	173	185	4.3
G22	143	205	7.8
G14	167	221	5.5
G16	108	218	6.3
G17	98	212	6.4
G19	98	203	4.6

Table 36 – Principle tensile data for tests conducted in PM and FSWed AA6082-T651.

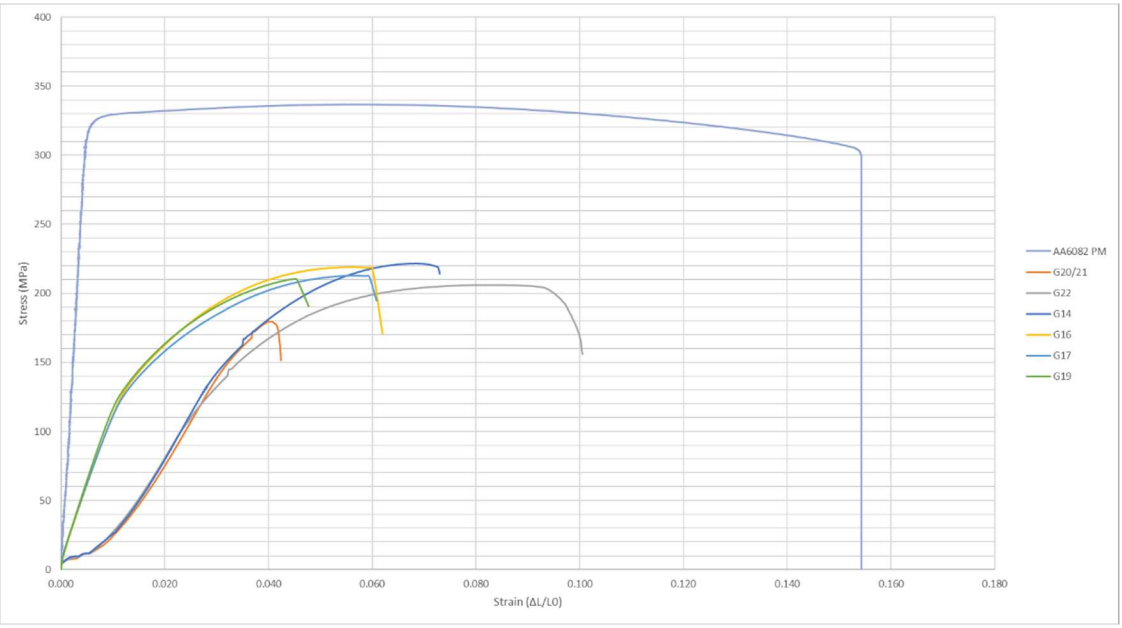

Figure 136 - Stress vs Strain plot for as-received and FSWed AA6082-T651.

Weld #	Test 1	Test 2	Test 3
G20/21	SZ	SZ	SZ
G22	Adv TMAZ/HAZ	Adv TMAZ/HAZ	Ret TMAZ/HAZ
G14	Ret TMAZ/HAZ	Ret TMAZ/HAZ	Ret TMAZ/HAZ
G16	Advancing	Advancing	Retreating
G17	Advancing	Advancing	Advancing
G19	Adv TMAZ/HAZ	Adv TMAZ/HAZ	Adv TMAZ/HAZ

Table 37 - Failure locations of welds produced in AA6082-T651.

The failure location of each of the samples was recorded in Table 37. The fracture surface of weld G20/21 is shown in Figure 137 and Figure 138. This highlights a 'honeycomb' fracture surface where the second pass, G21, was conducted.

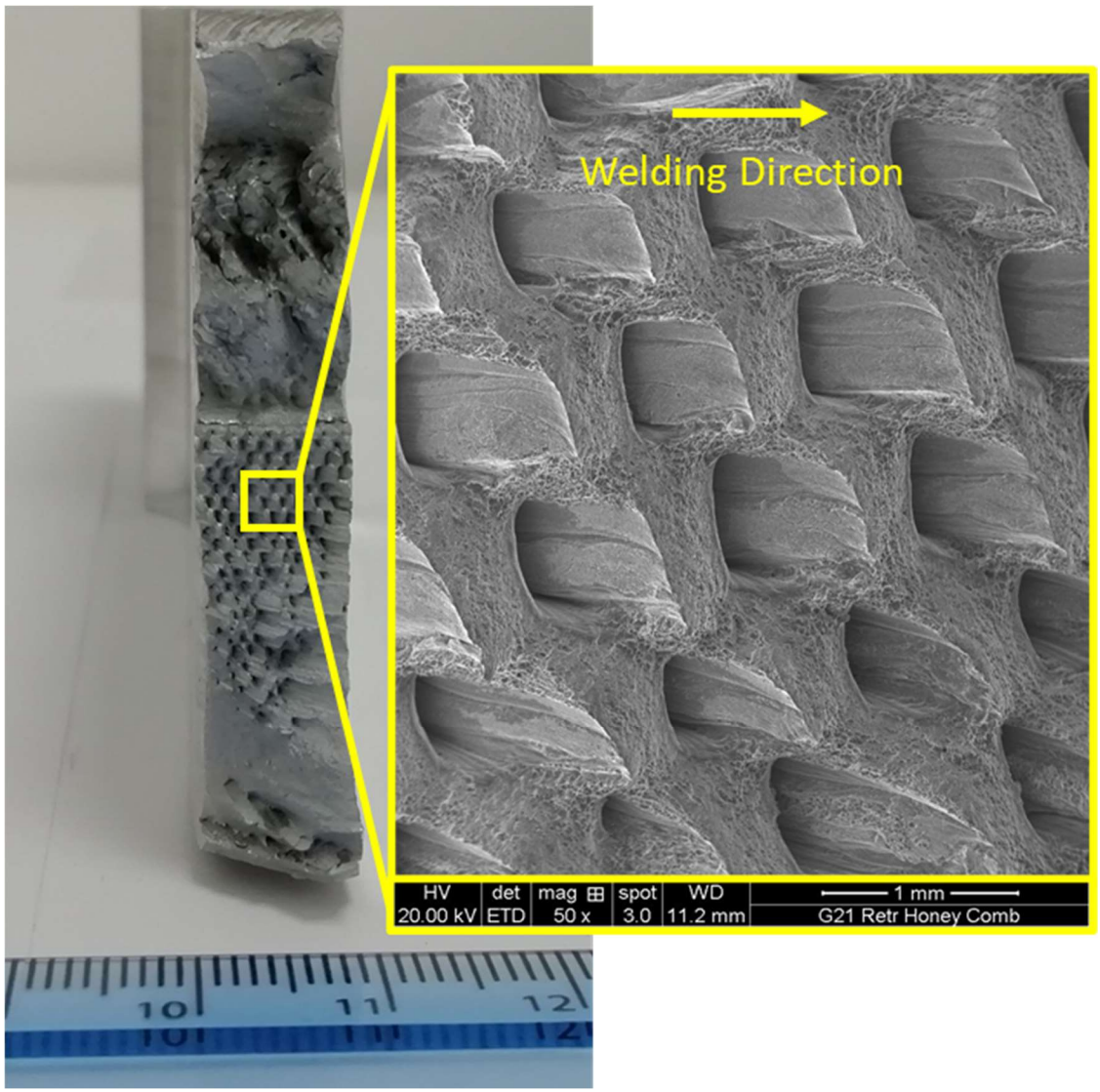

Figure 137 - Fracture surface of G20/21.

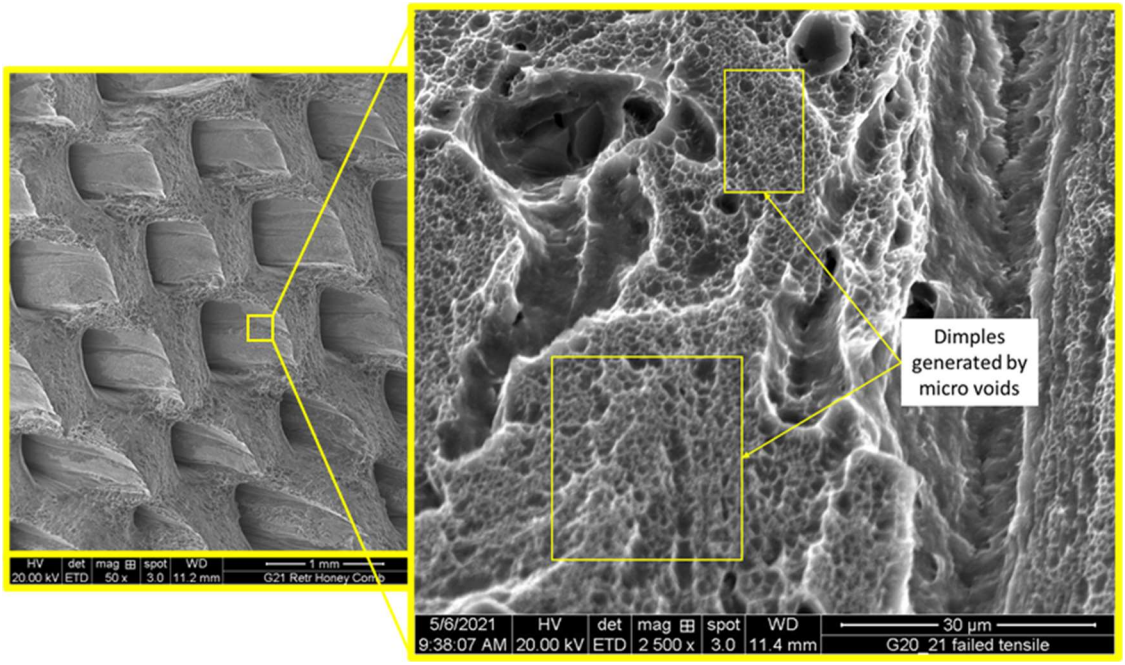

Figure 138 - Dimpled fracture surface of G22 indicating ductile failure.

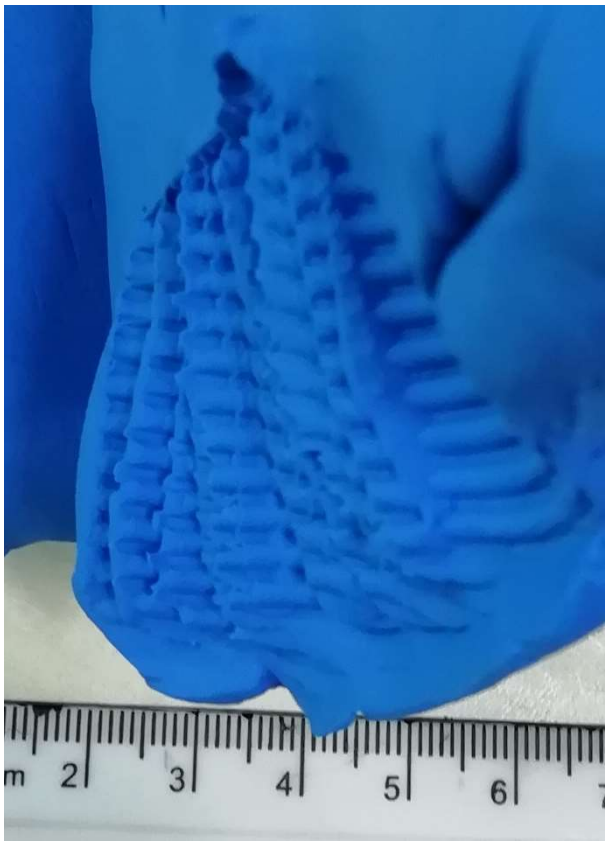

Figure 139 - Probe translated over putty to replicate the honeycomb feature found in G20/21 tensile samples.

4.2.4.2 Hardness

The as-received AA6082-T651 hardness data is presented in Figure 140 which suggests that the material was homogenous prior to welding. Figure 141 and Figure 142 suggest that by welding using either the WFW or SDS techniques respectively results in a reduction in hardness within the SZ and HAZ. Contrastingly to G22, the SZ in G20/21 is softer than the transition between the TMAZ and HAZ. The contour map indicates a hardness of 50-58.75 HV0.5 within the SZ of G20/21 which is lower than the TMAZ/HAZ interface in this weld (67.50-76.25 HV0.5).

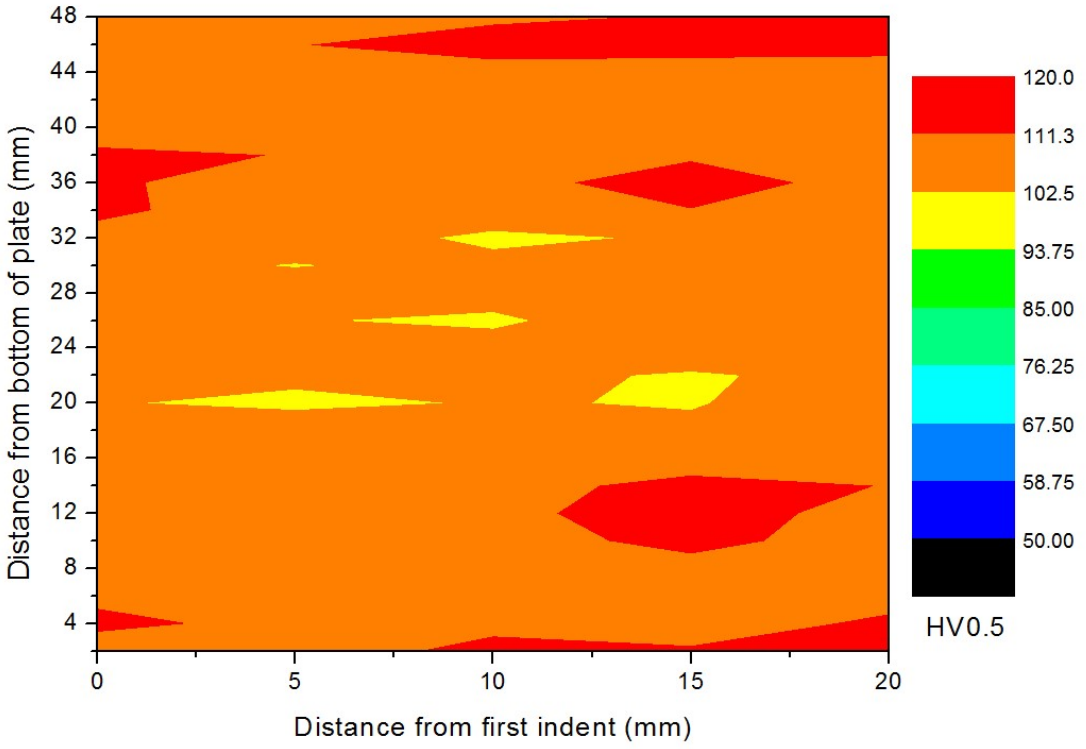

Figure 140 - Hardness map of as-received AA6082-T651.

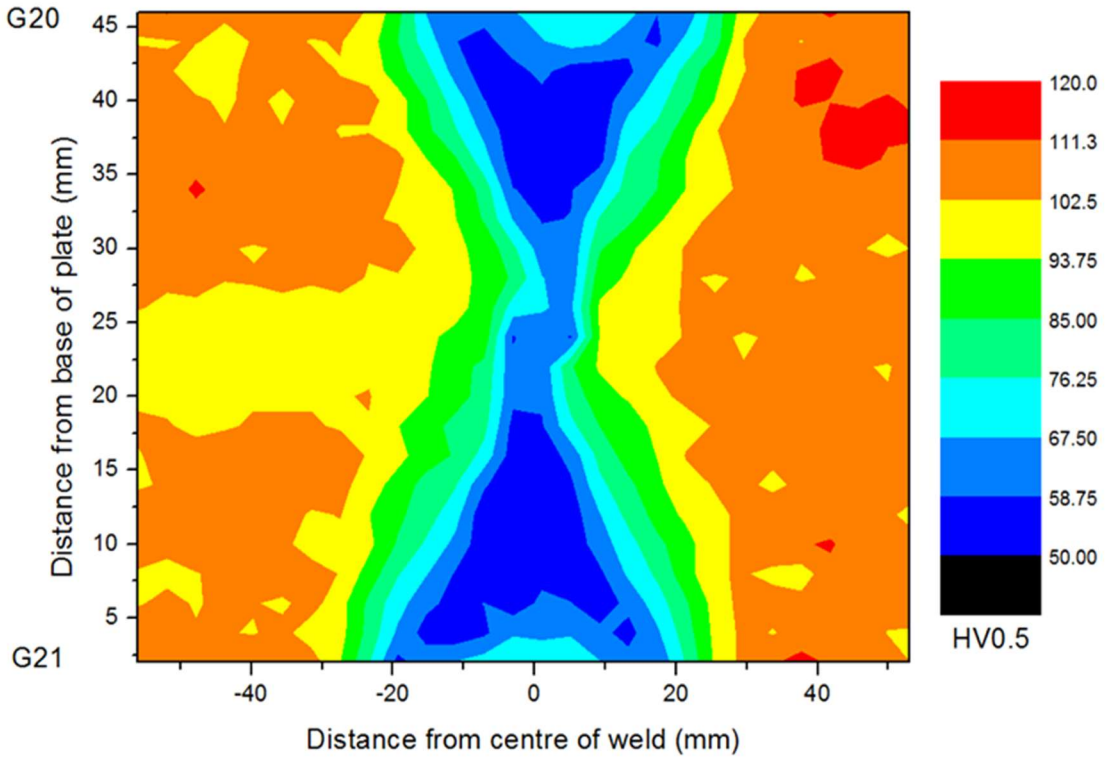

Figure 141 - Micro-hardness contour map of weld G20 and G21 - WFW-FSW in AA6082-T651.

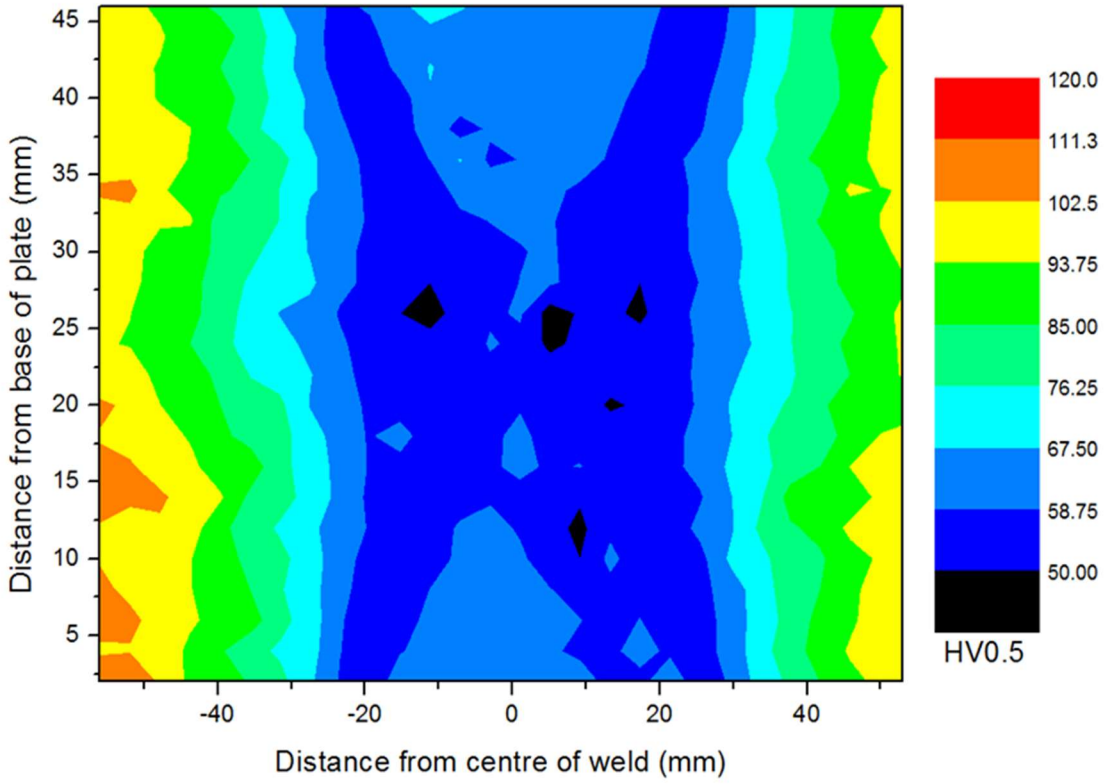

Figure 142 - Micro-hardness contour map of weld G22 - SDS-FSW in AA6082-T651.

The four SSS-FSW contour maps all highlight the linear nature of the SZ, this is shown from Figure 143 to Figure 146. Figure 143 is the contour map of G14 and suggests the through thickness hardness of the SZ is uniform, something cannot be said for the other three welds which all show some variation. The size of the HAZ also varied slightly across these welds from ~20 to 35 mm wide.

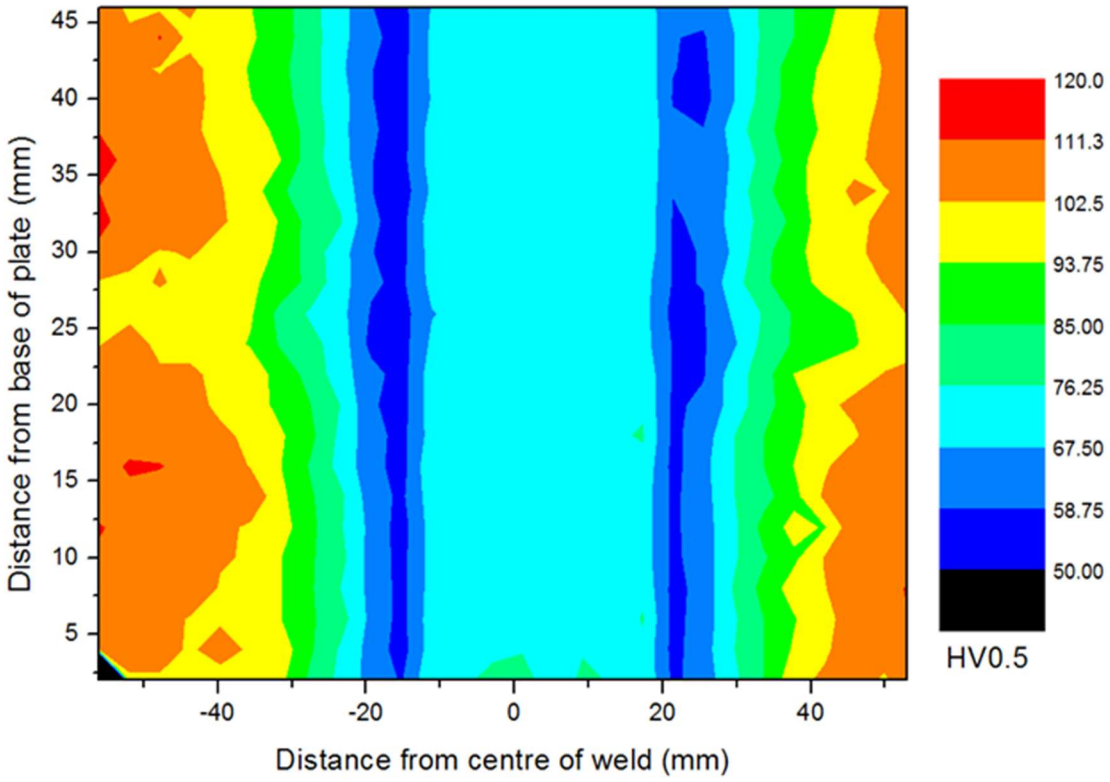

Figure 143 - Micro-hardness contour map of weld G14 - SSS-FSW using tool D060 in AA6082-T651.

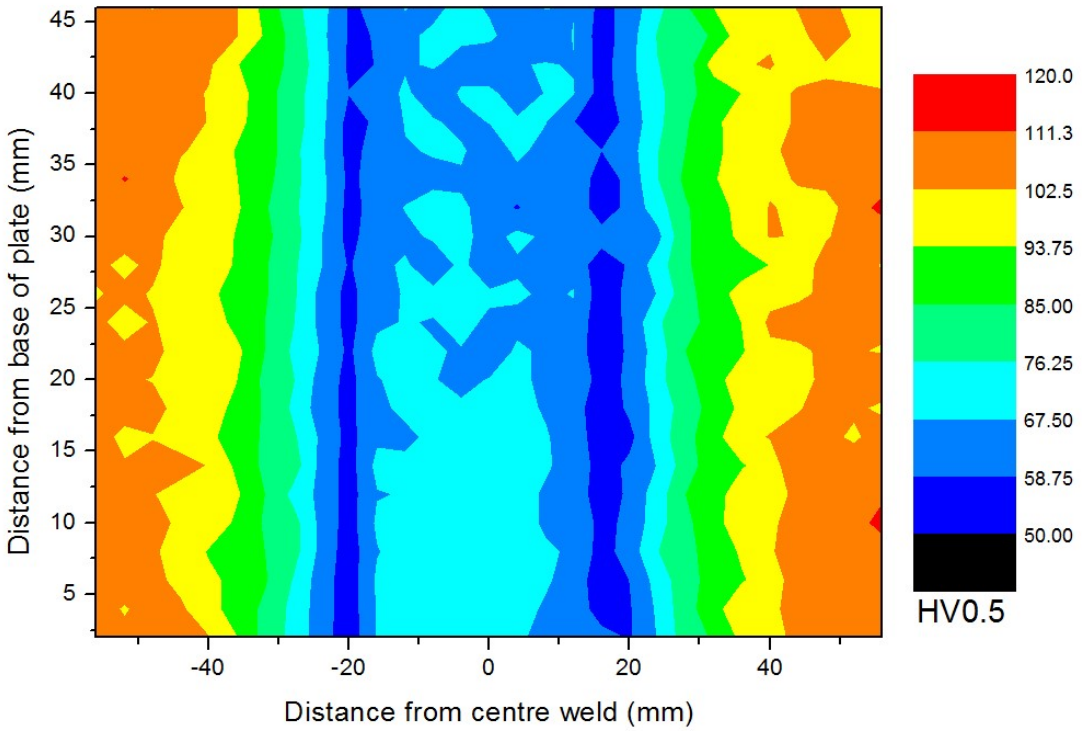

Figure 144 - Micro-hardness contour map of weld G16 - SSS-FSW using tool D070 in AA6082-T651.

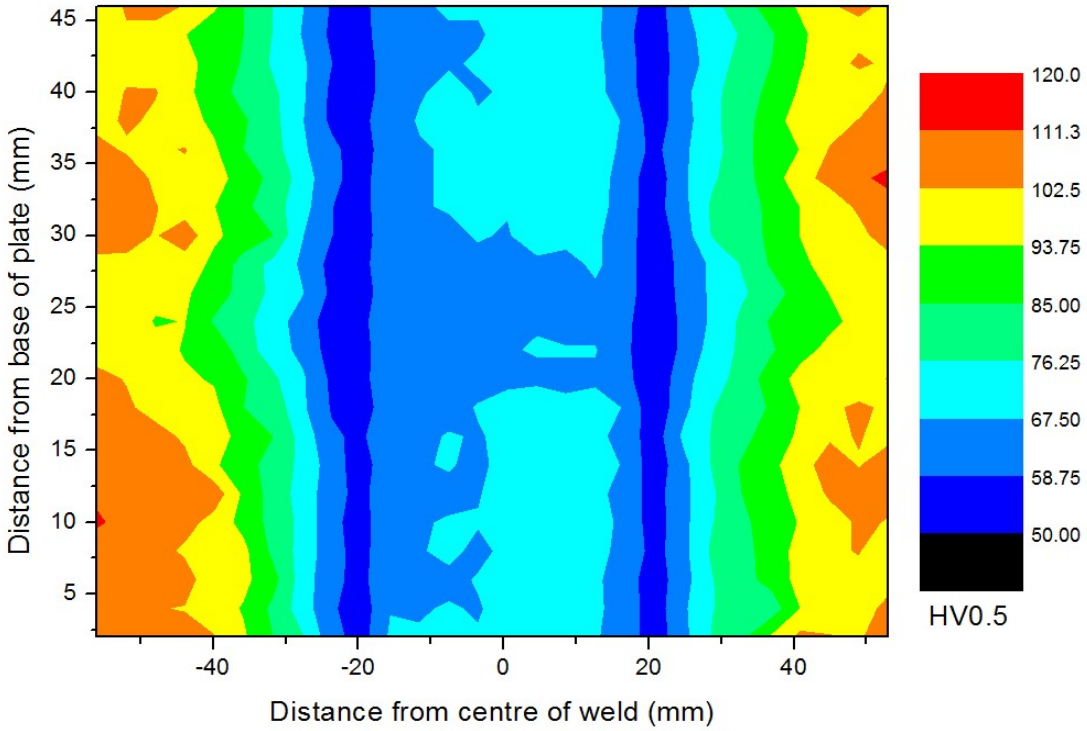

Figure 145 - Micro-hardness contour map of weld G17 - SSS-FSW using tool D030 in AA6082-T651.

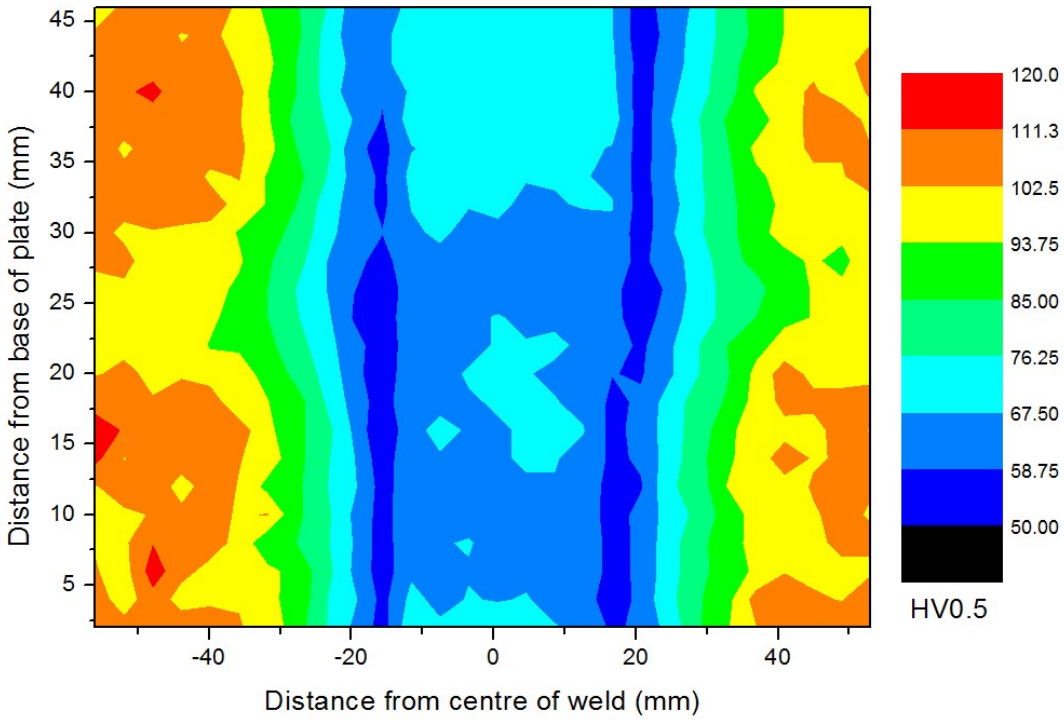

Figure 146 - Micro-hardness contour map of weld G19 - SSS-FSW using tool D080 in AA6082-T651.

4.2.4.3 Swept volume

Table 38 presents the calculated swept volume per revolution of each pass during welding. The data suggests that the full-length linear probes used during the SSS-FSW technique swept a greater volume per revolution than the two tapered nominally half-length probes, used in the WFW and SDS welds, combined. Of the four SSS-FS welds, G19 (the 3 flat, coarse pitch probe) swept the most material per revolution (1997.98 mm^3/rev) though G17 (the 4 flat, fine pitch probe) swept a very similar amount and was the second highest volume swept suggesting there was no correlation between the number of flats/pitch and volume swept.

	G20/21	G22	G14	G16	G17	G19
1st / Upper Pass	725.14	1224.97	1978.02	1985.34	1995.97	1997.98
2nd / Lower Pass	725.56	1224.97	-	-	-	-

Table 38 - Swept volume per revolution (mm^3/rev) of the FS welds in AA6082-T651.

4.2.4.4 Energy input

The energy input required to FS weld AA6082-T651 by the techniques described previously is shown in Table 39. Here it is established that the SDS-FSW technique used 47% less energy than the WFW-FSW technique, despite traversing 100 mm/min faster. This suggests that although the weld was run 'colder', the local temperature surrounding the probes was higher and therefore the material nearest the probes was more plasticised, lowering the torque required and consequently the energy needed.

The SSS-FSW welds produced in AA6082-T651 used four different tool designs. Welds G14 and G17, which use a thread pitch of 2.8 mm, were shown to produce the largest maximum energy inputs (6.56 kJ/mm and 6.19 kJ/mm respectively), however, G17 also experienced the lowest mean energy input into the weld zone - 5.46 kJ/mm. G16 and G17 were produced using tools with 4 flats. There was little variation in the energy input between the coarse and fine thread tools as evident in these welds which had a variation of 0.27 kJ/mm. The same can be argued between the 3 flat tool welds, G14 and G19, which had a variation in mean energy input of 0.59 kJ/mm. It can, therefore, be argued that the variations in tool design investigated had little impact on the energy input into the weld zone. As SSS-FSW in 50 mm thick aluminium alloy is still a relatively untried joining method the parameters selected were focused on sustaining tool life and not optimising the weld quality.

Weld Number	Traverse Speed	Spindle Rotation	Torque (Mean)	Torque (Max)	Efficiency factor	Energy Input (Mean)	Energy Input (Max)
#	mm/min	rpm	Nm	Nm		kJ/mm	kJ/mm
G20	150	130	846.17	935.86	0.98	4.52	4.99
G21	150	130	851.45	901.05	0.98	4.54	4.81
G22 Upper	252	129	735.03	778.56	0.98	2.32	2.45
G22 Lower	252	129	776.43	806.64	0.98	2.45	2.54
G14	245	199.00	1253.36	1312.50	0.98	6.27	6.56
G16	245	199.00	1146.52	1205.32	0.98	5.73	6.03
G17	245	199.00	1092.00	1237.83	0.98	5.46	6.19
G19	245	199.00	1134.95	1191.22	0.98	5.68	5.96

Table 39 - Energy input for welds produced in AA6082-T651. Energy efficiency factor is an assumed value.

4.3 Microstructural and mechanical analysis of AA7050-T7451

Welds using the techniques discussed previously were produced in AA7050-T7451 for analysis. These welds were identified by the ID numbers indicated in Table 40.

Material	AA7050-T7451		
Weld ID	G03/04	G12	G18
Weld Type	WFW-FSW	SDS-FSW	SSS-FSW

Table 40 - Weld identification numbers for welds in AA7050-T7451.

4.3.1 Weld Data

Data such as traverse and rotational speeds, torque and Z-force were recorded during welding. These are graphically represented in section 4.3.1.1 to 4.3.1.3.

4.3.1.1 Weld-Flip-Weld FSW

Pass	Traverse speed (mm/min)	Rotational speed (rpm)	Torque - Avg (Nm)	Z-force - Avg (kN)
First	130	129.64	778.21	120.96
Second	130	129.47	766.31	121.16

Table 41 - Parameter information for G03/04, the WFW-FSW of AA7050-T7451.

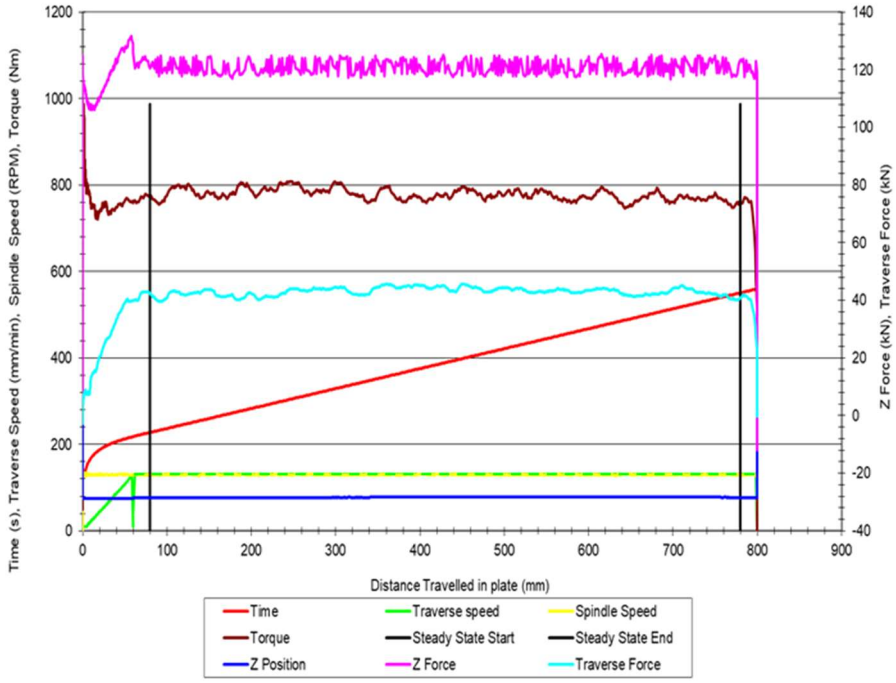

a) Weld data of first pass

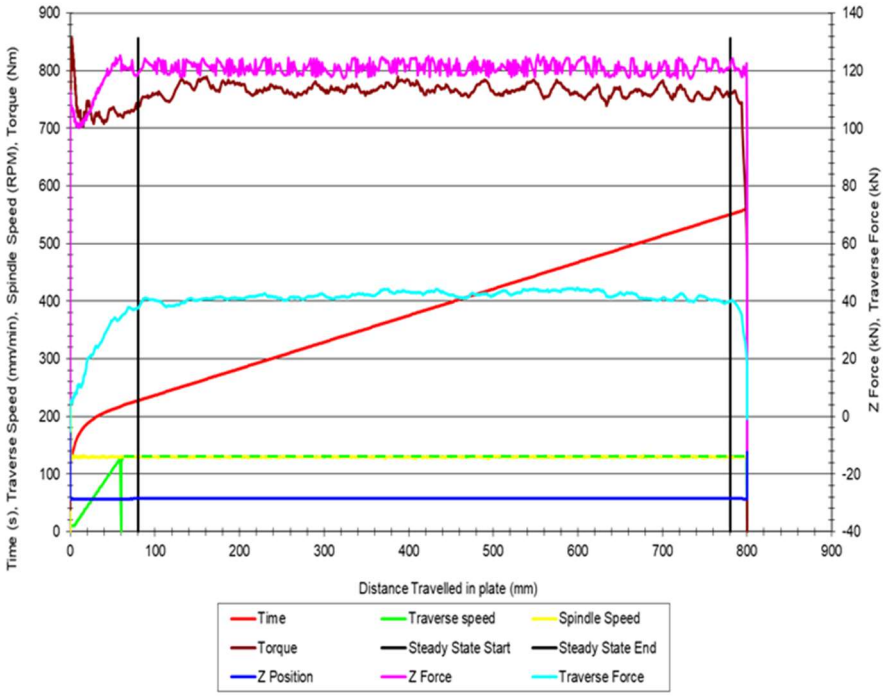

b) Weld data of second pass

Figure 147 - Weld data for WFW-FSW of AA7050-T7451. Note: Due to data logger error, the traverse speed was not recorded during the steady state. This has been approximately represented by the green dashed line shown in both a) and b).

4.3.1.2 Simultaneous Double Sided FSW

Pass	Traverse speed (mm/min)	Rotational speed (rpm)	Torque - Avg (Nm)	Z-force - Avg (kN)
Upper	130	109.57	640.16	81.06
Lower	130	109.91	574.04	103.64

Table 42 - Parameter information for G12, the SDS-FSW of AA7050-T7451.

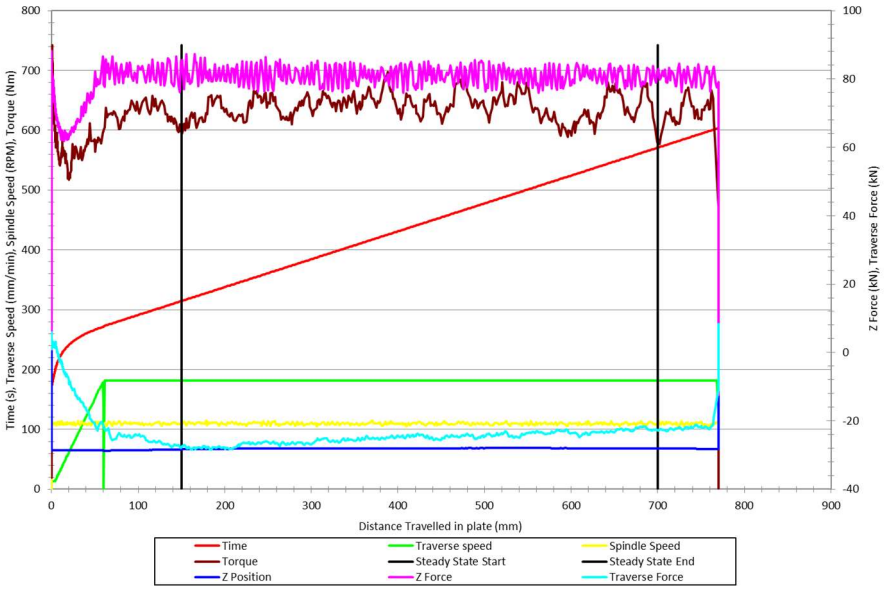

a) Weld data of upper pass

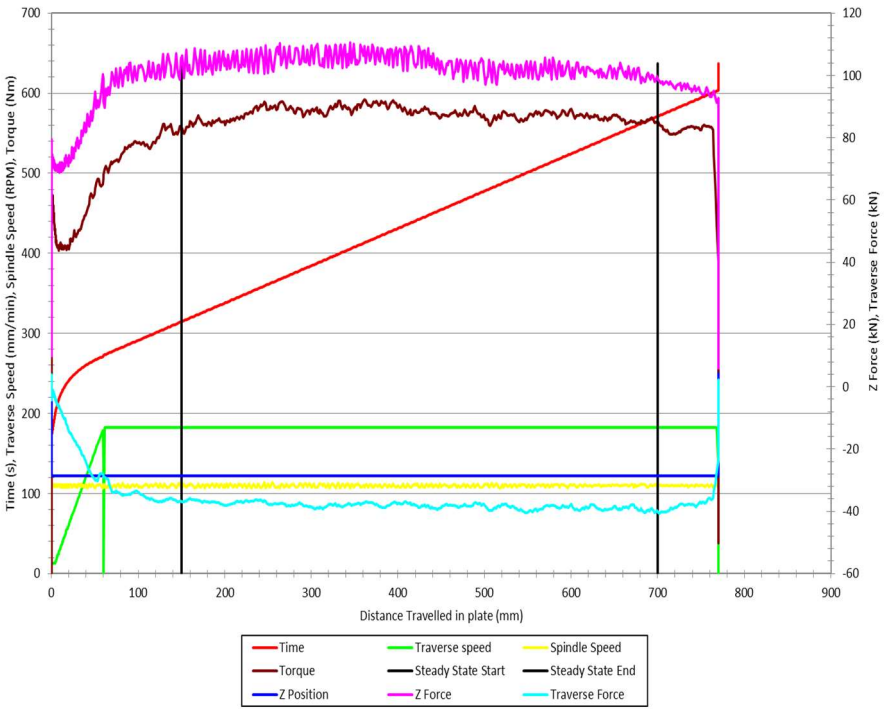

b) Weld data of lower pass

Figure 148 - Weld data for SDS-FSW of AA7050-T7451.

4.3.1.3 Supported Stationary Shoulder FSW – Tool D090

Pass	Traverse speed (mm/min)	Rotational speed (rpm)	Torque - Avg (Nm)	Z-force - Avg (kN)
Single	59	122.00	1101.94	55.72

Table 43 - Parameter information for G18, the SSS-FSW of AA7050-T7451.

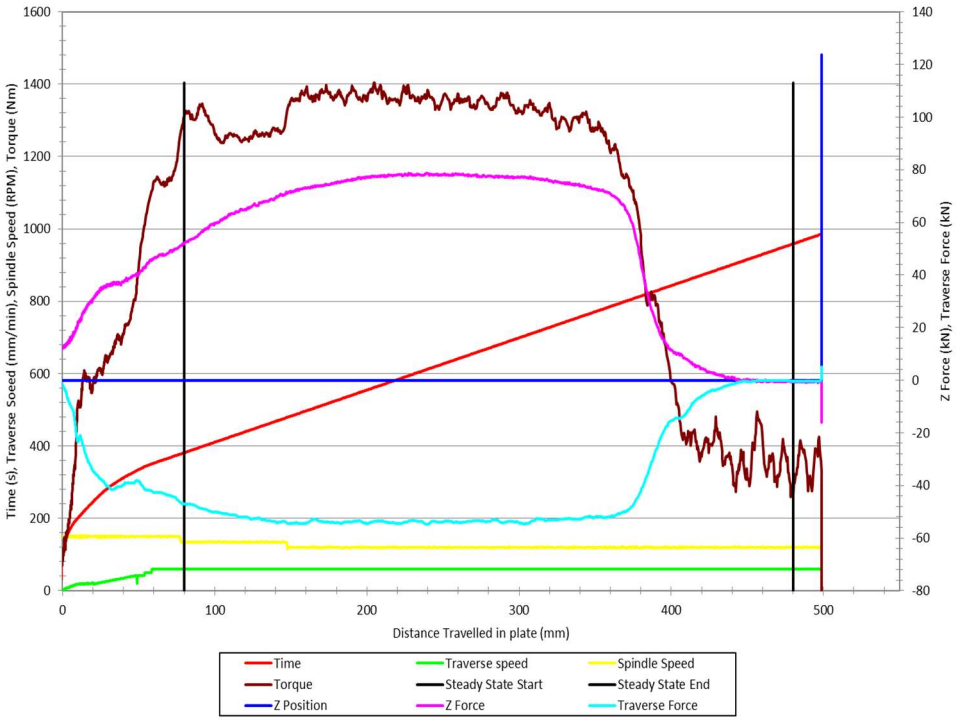

Figure 149 - Weld data for SSS-FSW of AA7050-T7451 using tool D090.

4.3.2 Chemical analysis

4.3.2.1 Optical Emission Spectroscopy (OES)

Optical Emission Spectroscopy (OES) was conducted to quantify the elements and their weight percentages within AA7050-T7451. The results of this are shown in Table 44, against the standard composition, and the OES data sheet is provided in Appendix 34. The primary alloying elements, alongside aluminium (90.60 wt%), were copper (1.85 wt%), magnesium (1.83 wt%) and zinc (5.29 wt%), which although the elements were

in line with the literature ('ASM Material Data Sheet - AA7050-T7451' n.d.; Sha and Cerezo (2004)) confirming that the material was a 7xxx series alloy, did not meet the standard composition expressed in Table 44 for AA7050.

Element	Element wt%	
	Received material	Standard composition
Al	90.600	87.3 - 90.3
Cr	0.008	Max 0.04
Cu	1.850	2 - 2.6
Fe	0.120	Max 0.15
Mg	1.830	1.9 - 2.6
Mn	0.010	Max 0.1
Si	0.054	Max 0.12
Ti	0.058	Max 0.06
Zn	5.290	5.7 - 6.7
Zr	0.140	0.08 - 0.15
Other, each	Max 0.005	Max 0.05
Other, total	0.04	Max 0.15

Table 44 - Element wt.% for parent material AA7050-T7451 as provided by OES analysis. Highlighted elements did not meet the standard composition values stated in 'ASM Material Data Sheet - AA7050-T7451' (n.d).

4.3.3 Microstructural analysis

4.3.3.1 Macrograph

Macrographs of the as received and welded samples were taken using an Infinite Focus Microscope (IFM), these are shown from Figure 150 through to Figure 153. The tool profile visible in Figure 151 shows that the probes overlap to produce a central region that is double processed, as mentioned previously for welds in the other material grades. However, in Figure 152, which shows G12 (SDS-FSW in AA7050-T7451) the probes are skewed; a result of the forces acting on them while traversing.

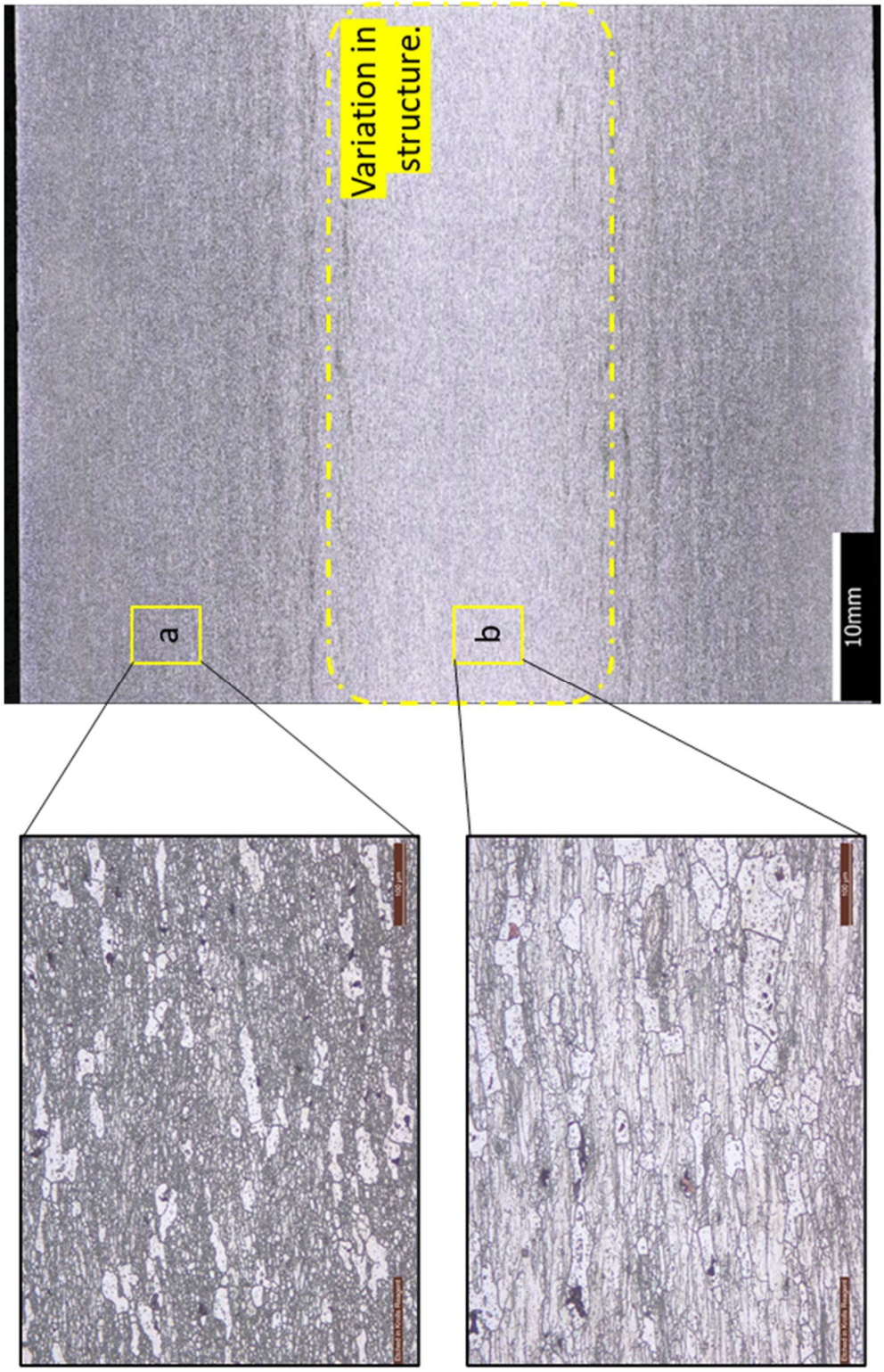

Figure 150 - Macrograph of as received AA7050-T7451 - etched in Krolls reagent. Yellow dashed region indicates a variation in microstructure that differs from that visible above as demonstrated by the pop-out images.

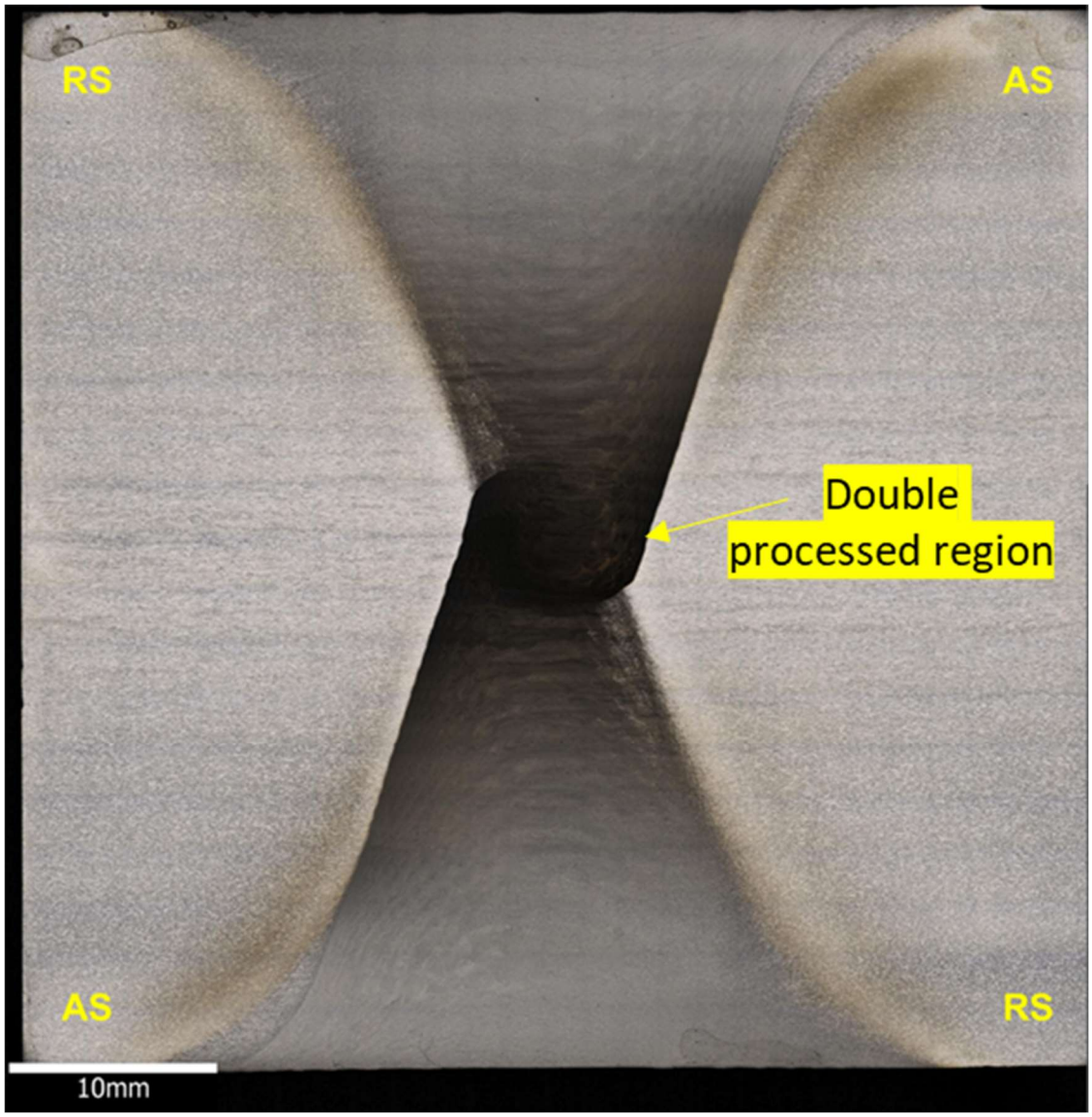

Figure 151 - Macrograph of weld G03/04 - etched in Krolls reagent. Tapered profile of each probe is visible and the double processed region, where the two probes overlap, is identified.

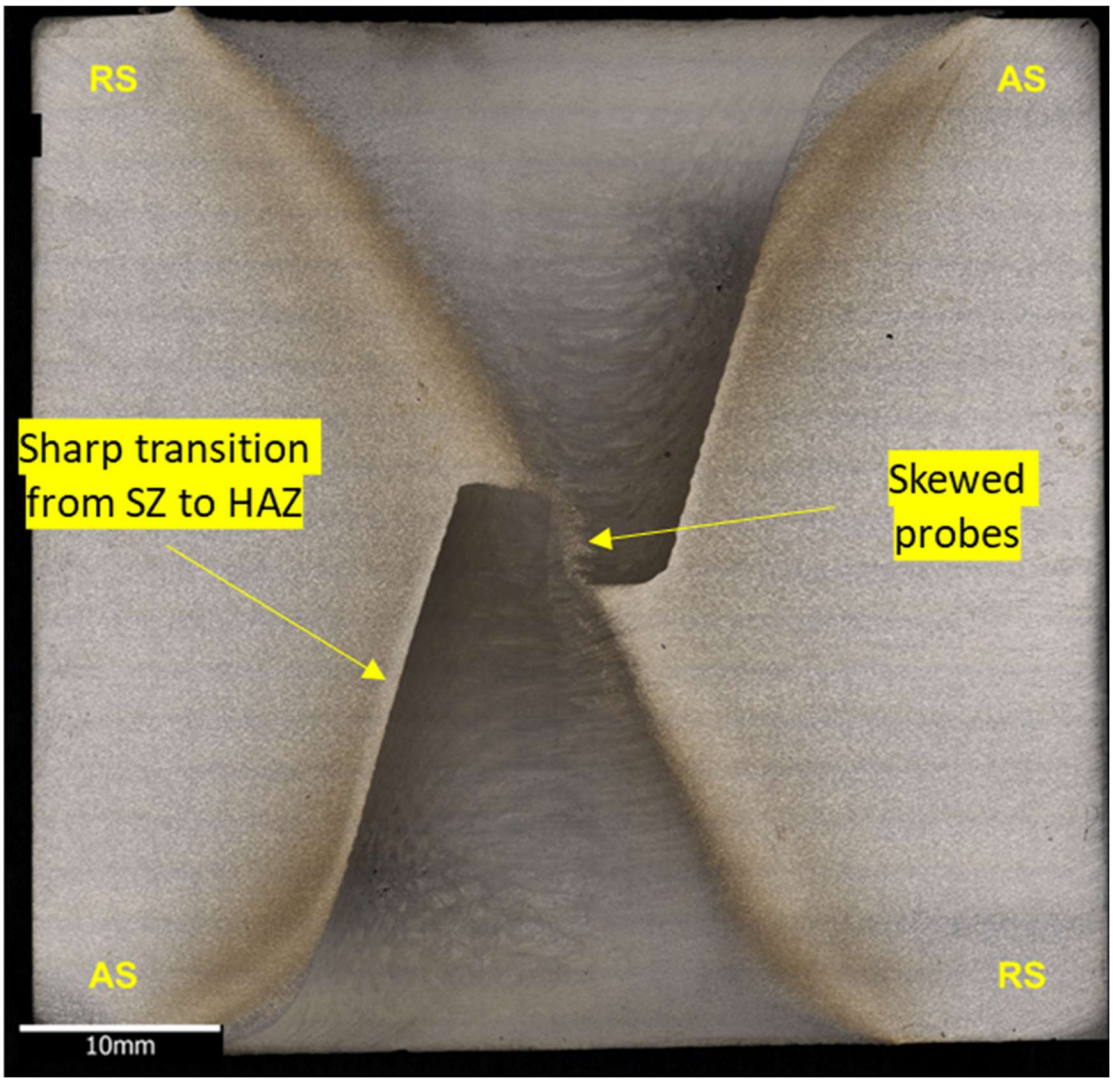

Figure 152 - Macrograph of weld G12 - etched in Krolls reagent. Tapered profile of each probe is visible. Evidence of skewing identified where the probes should overlap. The sharp transition between the SZ and HAZ is identified.

Unlike the welds shown in Figure 151 and Figure 152, the weld in Figure 153 was produced using a single, full length probe. This figure shows the most prominent banding in any of the three welds.

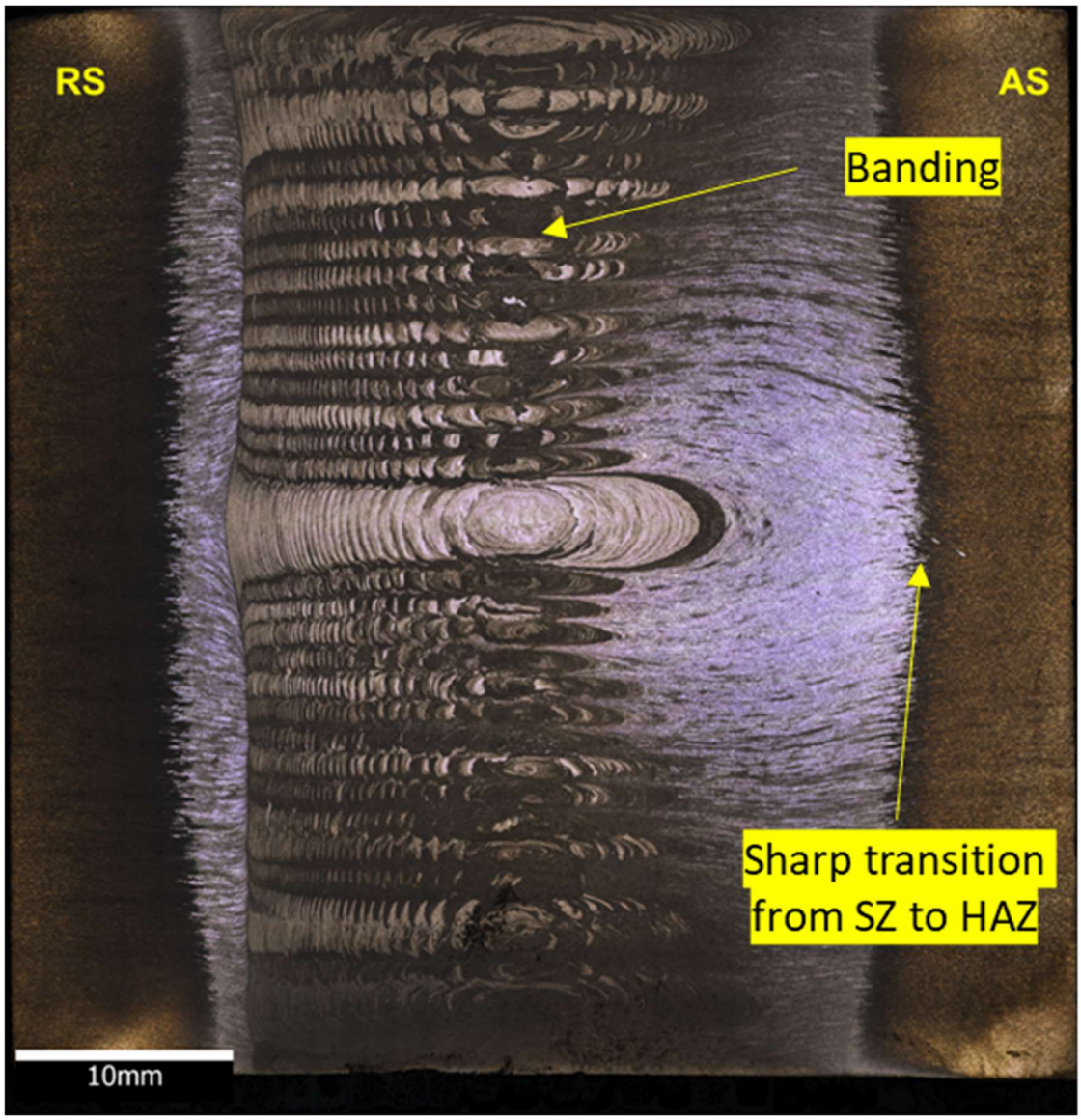

Figure 153 - Macrograph of weld G18 - etched in Krolls reagent. Linear profile of the probe is visible, and banding is prevalent throughout the SZ. The advancing side of the weld shows a sharp transition between the SZ and HAZ.

4.3.3.2 Optical Light Microscopy (OLM)

In each of the three welds there is a difference between the advancing (AS) and retreating (RS) sides. The transition from SZ to HAZ in the AS is sharper than in the RS, as demonstrated in Figure 154.

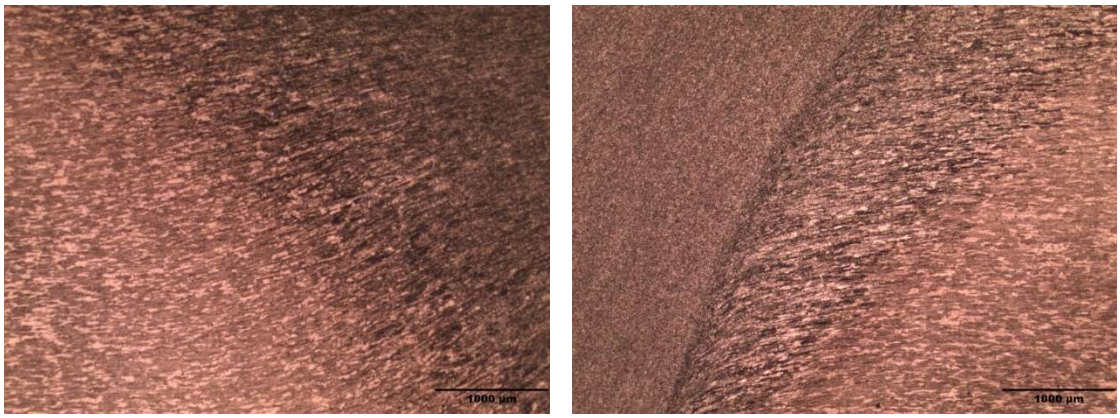

a) Retreating side b) Advancing side

Figure 154 - Transition region between SZ and HAZ of G03 taken near the shoulder.

The microstructure of each sample was captured in nine regions as detailed in Figure 155 using an OLM, and are presented in Appendix 35 to Appendix 37. Only one region from the top, middle and bottom of the sample are presented for the as-received material as variations were only noted through the material thickness. The as-received AA7050 (Figure 156) comprised of a bimodal grain structure with elongated grains stretching across the region separating clusters of much smaller grains. The precipitates were shown at high magnification to be mostly intergranular with few particles lying within the grains. There is a slight through thickness variation in the as-received material with regions b containing a greater number of elongated grains.

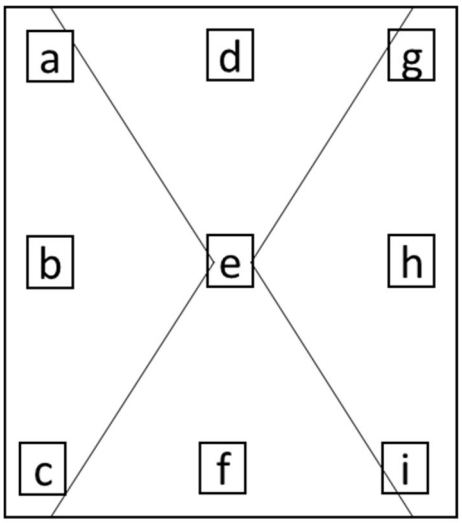

Figure 155 - Layout of microstructural images captured using optical light microscopy.

Figure 157 to Figure 159 provide the microstructure of each stir zone (SZ) of the three welds produced in AA7050-T7451. In Figure 157 the top and bottom regions show the single processed SZ is equiaxed and refined while the middle region is within the double processed area of the weld and shows that the grain structure is highly refined as at the same level of magnification individual grains cannot be identified. Figure 158(middle) highlights the effects of the skewing identified in Figure 152. The microstructure in this region has remained bimodal (such as the PM and HAZ) although some refinement has occurred which is evident by reduction in size of the clusters of small grains. Similar to the single processed regions of G03/04, Figure 158(top and bottom) show an equiaxed and refined grain structure versus the parent.

The final microstructure presented is that of the SSS-FS weld, G18, seen in Figure 159. The SZ of this weld is linear and as such the equiaxed nature of the single processed regions of G03/04 and G12 are visible throughout the SZ of G18. This weld was produced using ‘hot parameters’ which has resulted in a HAZ that appears significantly larger than that of the other two welds in this material grade. The particles present in each of the welds continued to adhere to the intergranular nature noted in the PM

with few large black particles still present within the grains. The intergranular particles were the focus of EDX analysis conducted in section 4.3.3.3.

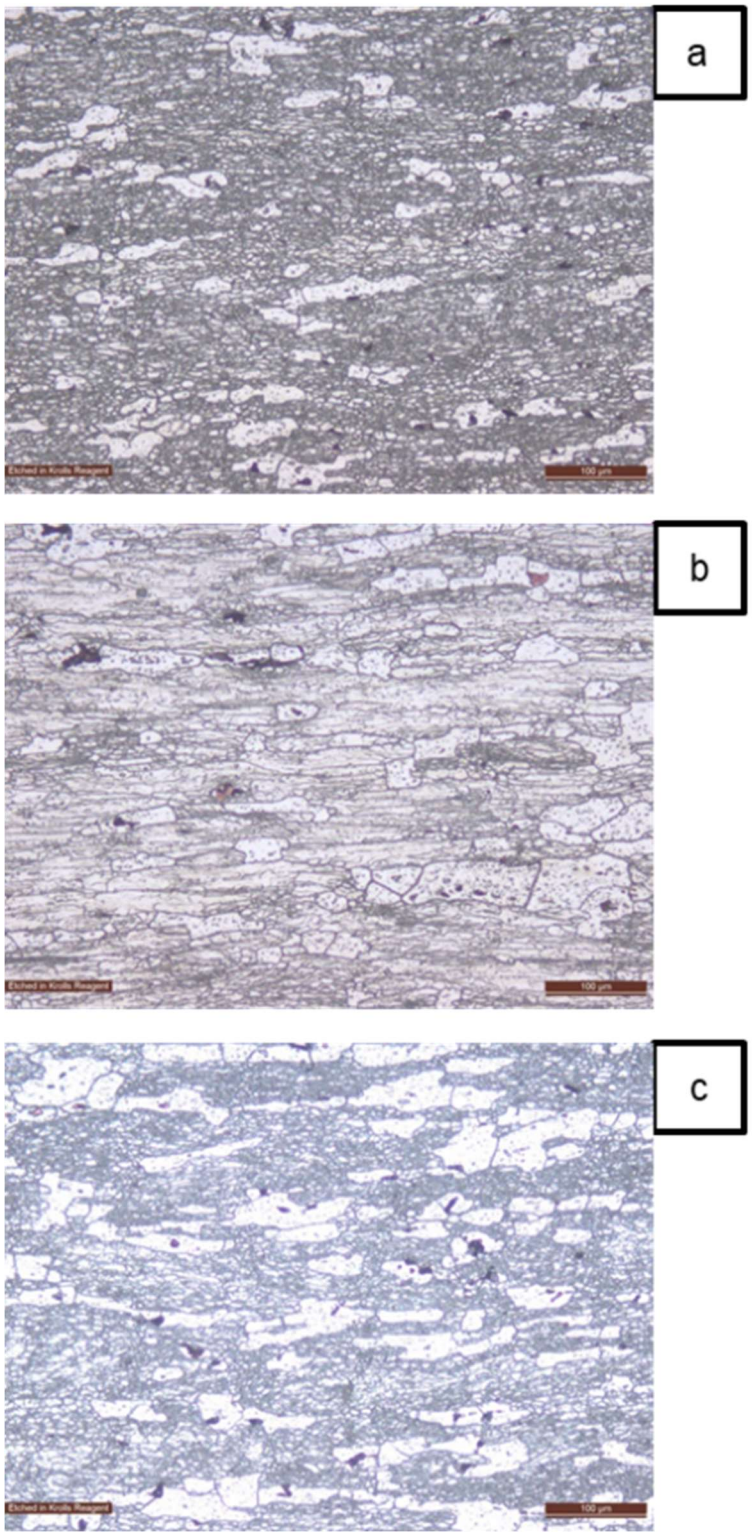

Figure 156 - Microstructure of as-received AA7050-T7451. A) top of material, b) centre of material and c) bottom of material.

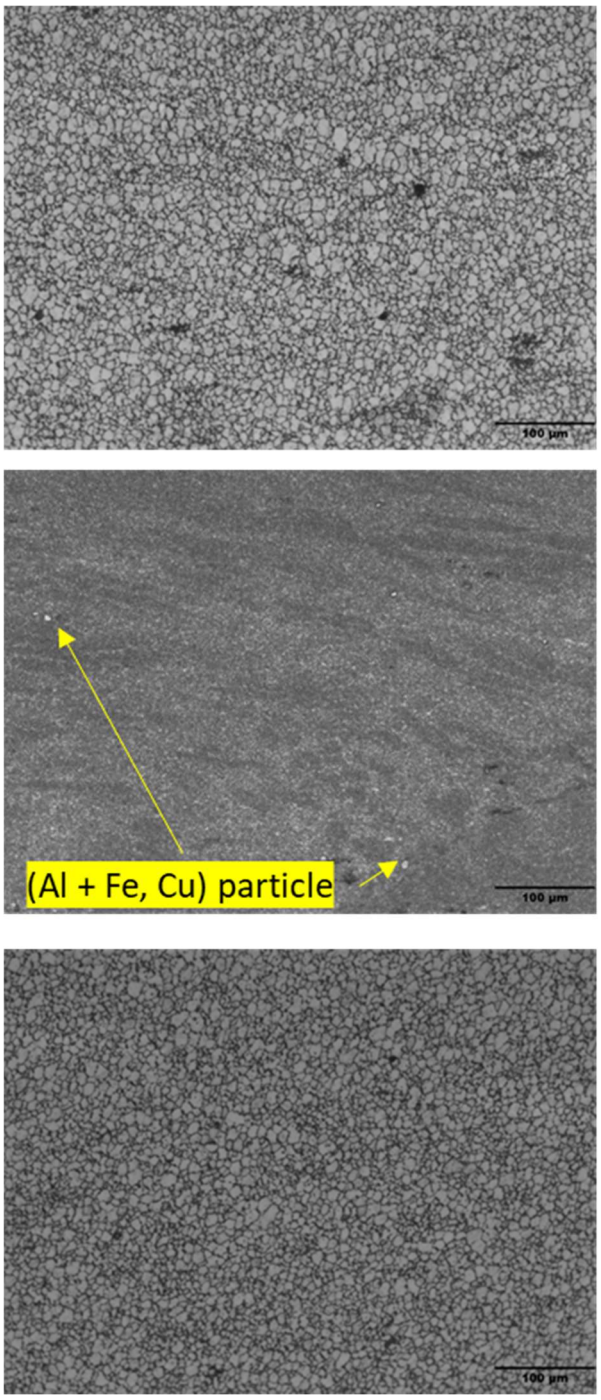

Figure 157 - Microstructure of WFW-FSW, G03/04, stir zone. (Top) shows an equiaxed and refined grain structure present in the upper pass of the weld. (Middle) Particles of (Al + Fe, Cu) present within a grain structure that is too refined to be visible at this level of magnification. (Bottom) Lower pass of the weld, similar to upper pass with regards to equiaxed grain structure.

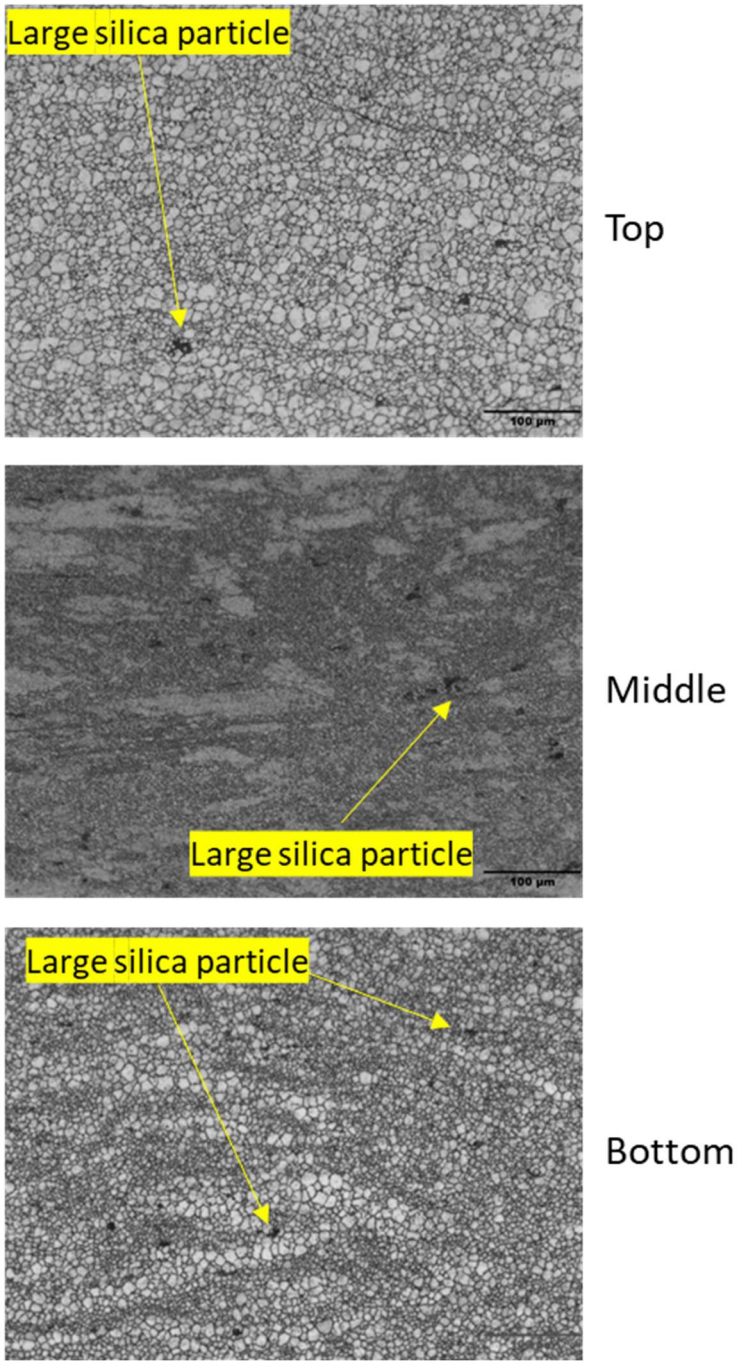

Figure 158 - Microstructure of SDS-FSW, G12, stir zone. (Top) shows an equiaxed and refined grain structure present in the upper pass of the weld. A large silica particle is identified by the arrow. (Middle) Central region of the stir zone, identifiable by the bimodal grain structure comparable to the HAZ. Large silica particles, similar to the top and bottom regions, identified. (Bottom) Lower pass of the weld, similar to upper pass with regards to equiaxed grain structure and particle distribution.

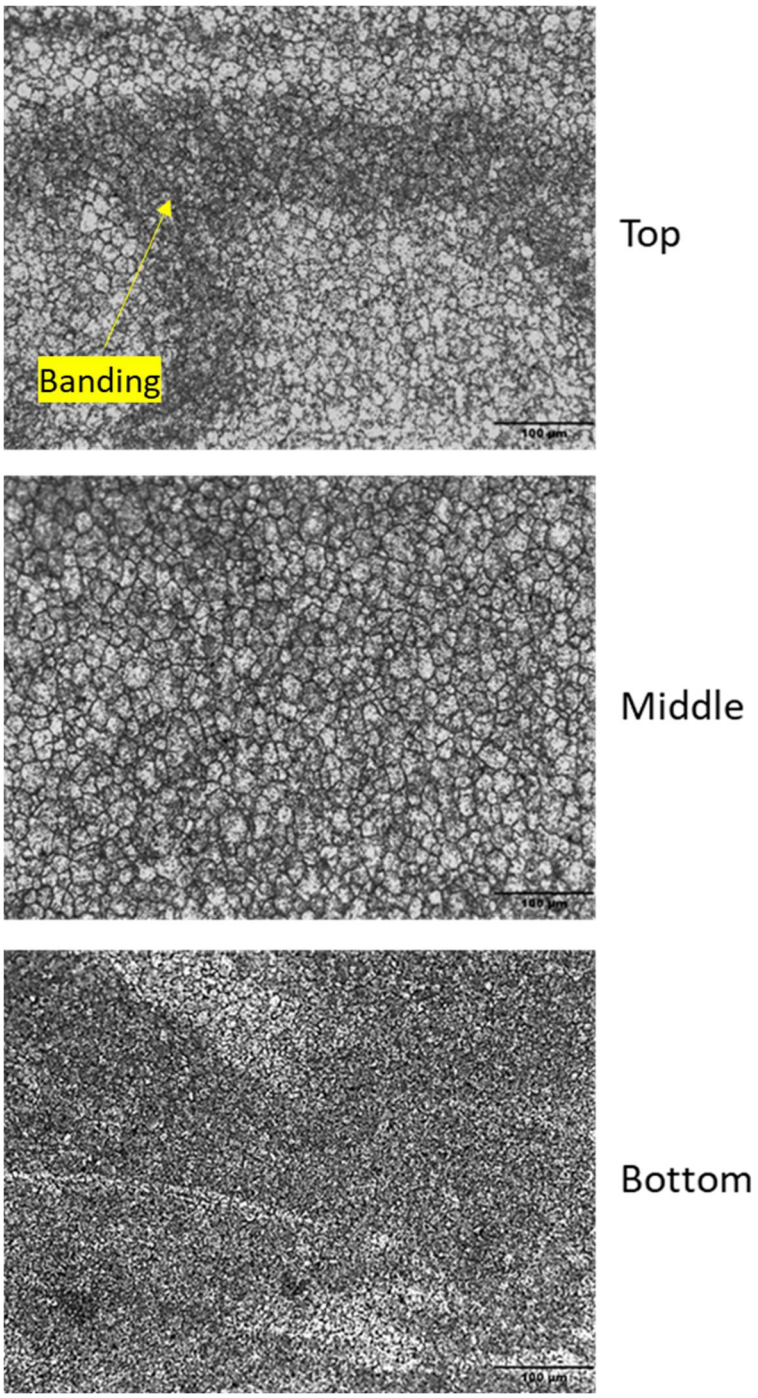

Figure 159 - Microstructure of SSS-FSW, G18, stir zone. (Top) shows an equiaxed grain structure present in the upper part of the weld. Banding is also visible as outlined. (Middle) Use of a bobbin tool has resulted in a central stir zone region that is similar to the top and bottom regions. Here the grain structure is equiaxed and particles appear to be intergranular. (Bottom) Lower part of the weld, similar to upper pass with regards to equiaxed grain structure and banding.

4.3.3.3 Energy Dispersive X-Ray Spectroscopy (EDX Analysis)

EDX analysis was conducted on both as-received and welded AA7050-T7451. Figure 160 to Figure 170 show three particles found in the PM, G03/04 and G12 respectively. Oxide particles were noted in the PM, silica particles were found in G12 (see Figure 167) and (Al + Fe, Cu) particles were observed in each of the three samples along with the Al-Mg-Zn matrix.

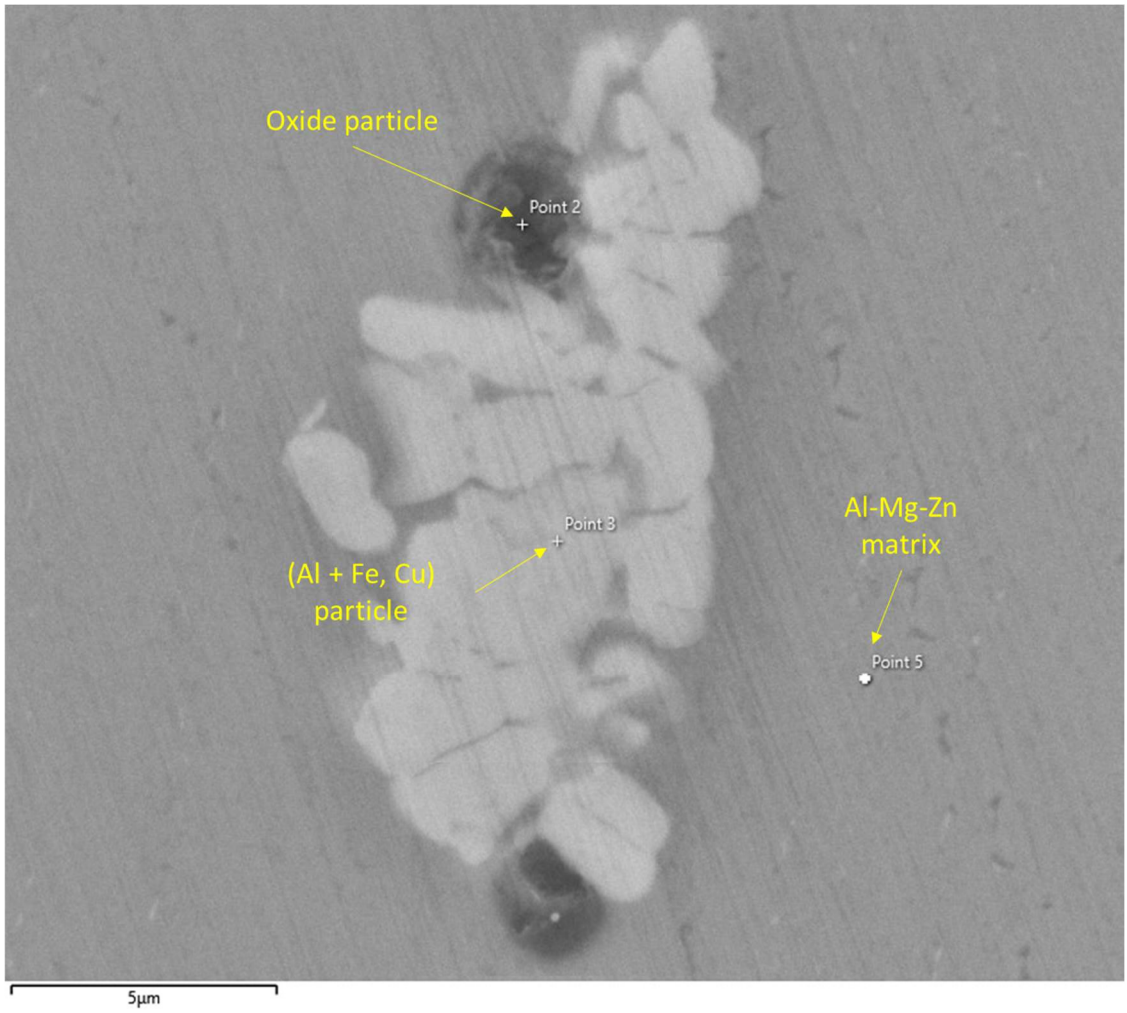

Figure 160 - SEM image of as-received AA7050-T7451 showing an Al-Cu-Fe based particle.

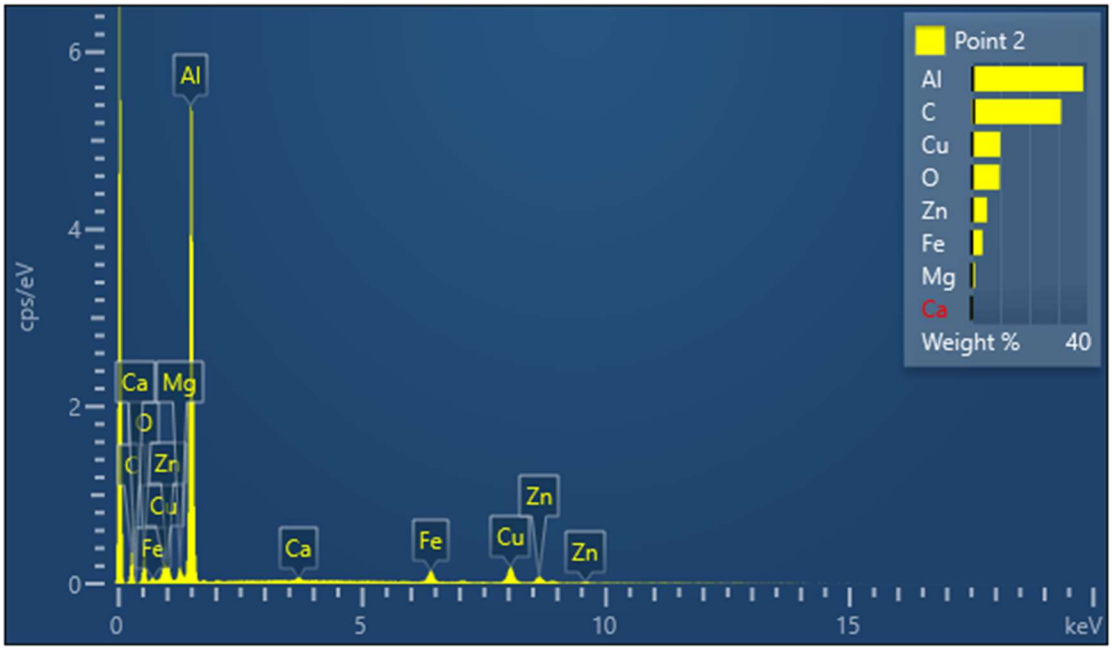

Figure 161 - EDX spectra of point 2 in Figure 160.

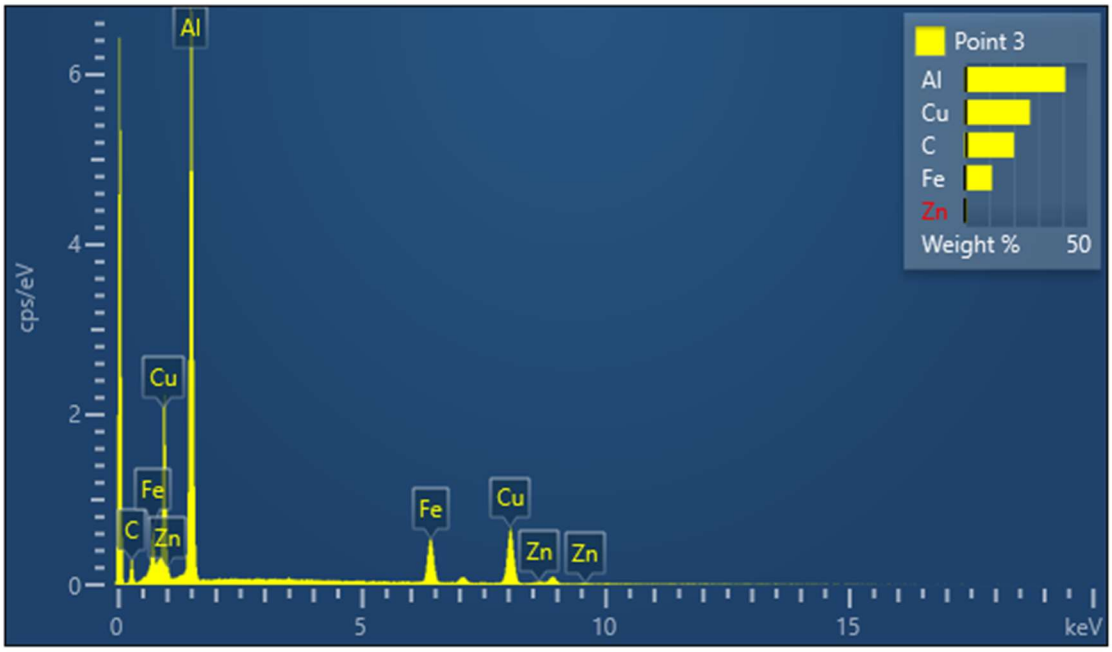

Figure 162 - EDX spectra of point 3 in Figure 160.

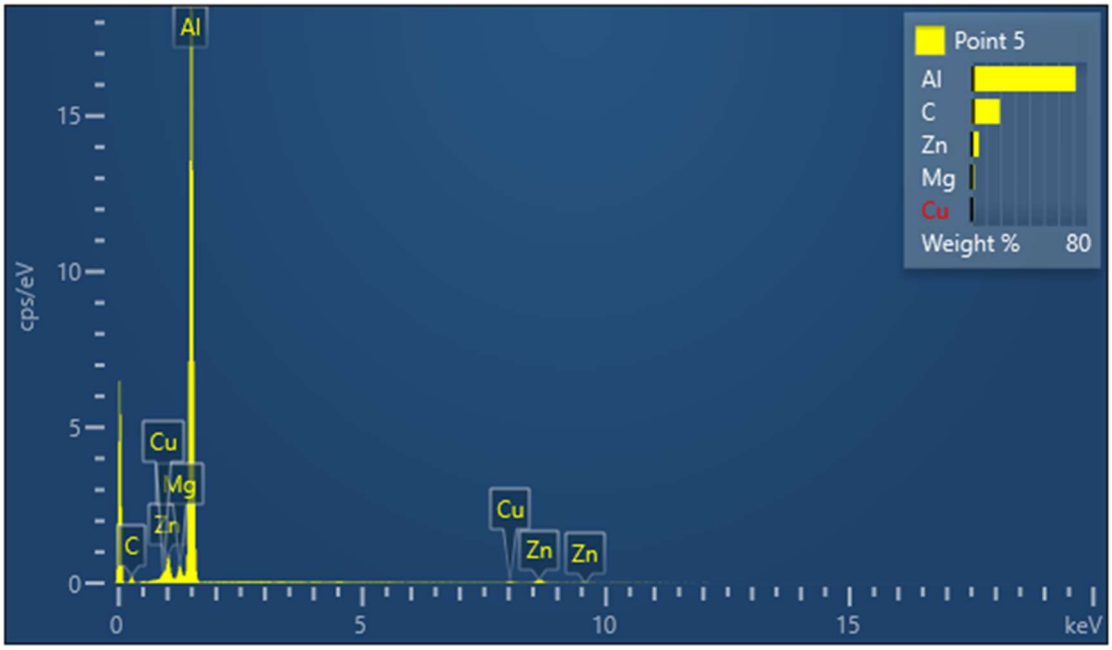

Figure 163 - EDX spectra of point 5 in Figure 160.

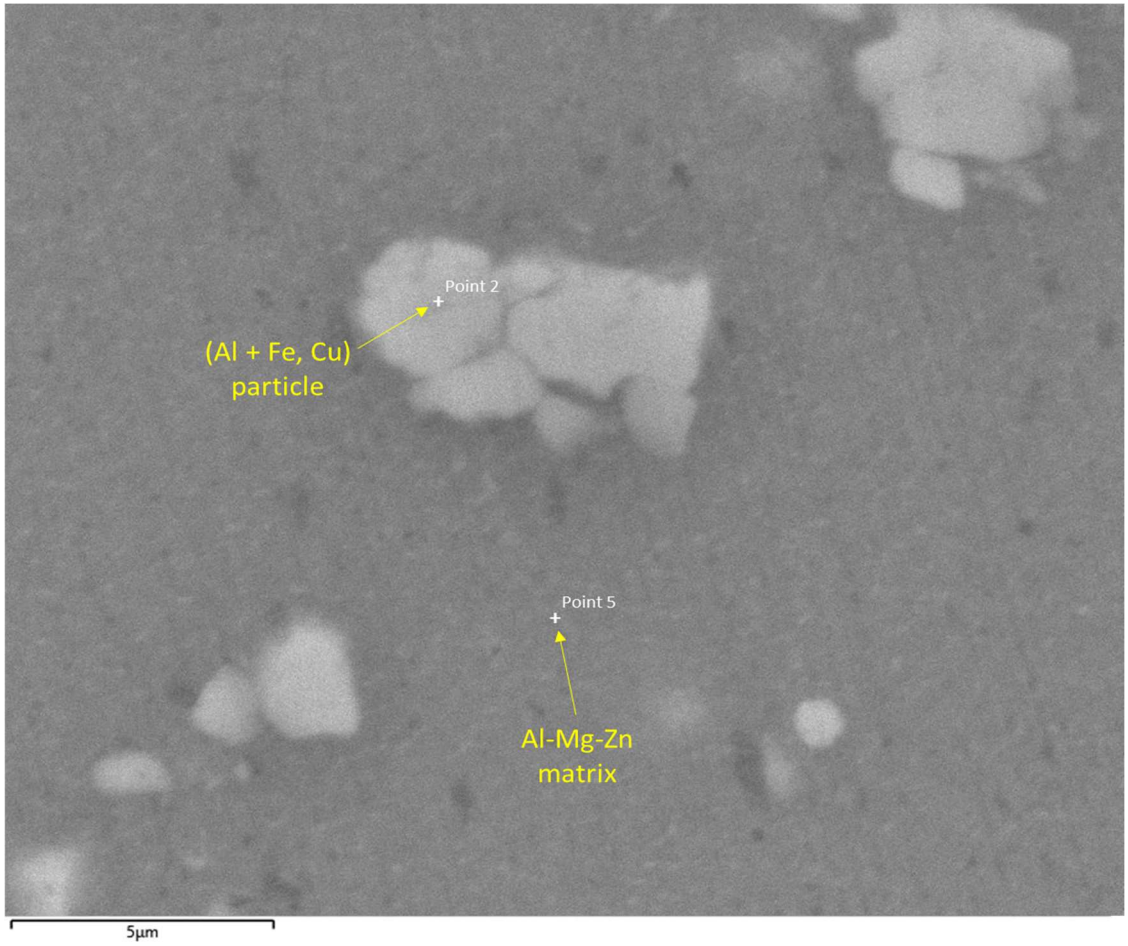

Figure 164 - SEM image of the double processed stir zone region in G03/04 showing an Al-Cu-Fe based particle.

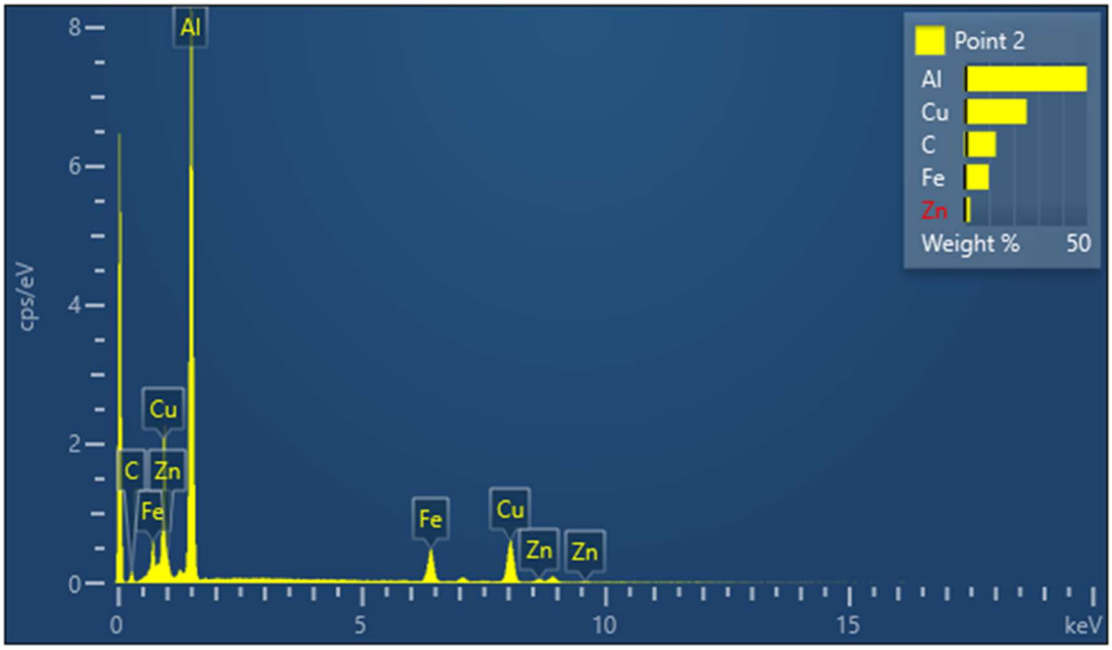

Figure 165 – EDX analysis of the particle in Figure 164.

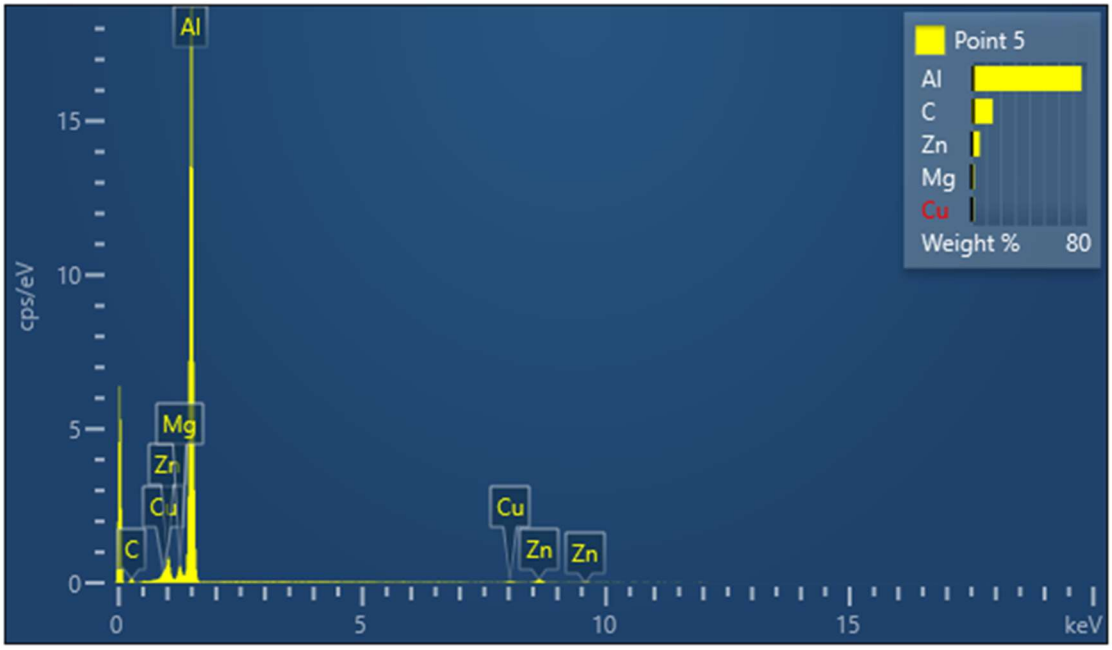

Figure 166 – EDX analysis of the particle in Figure 164.

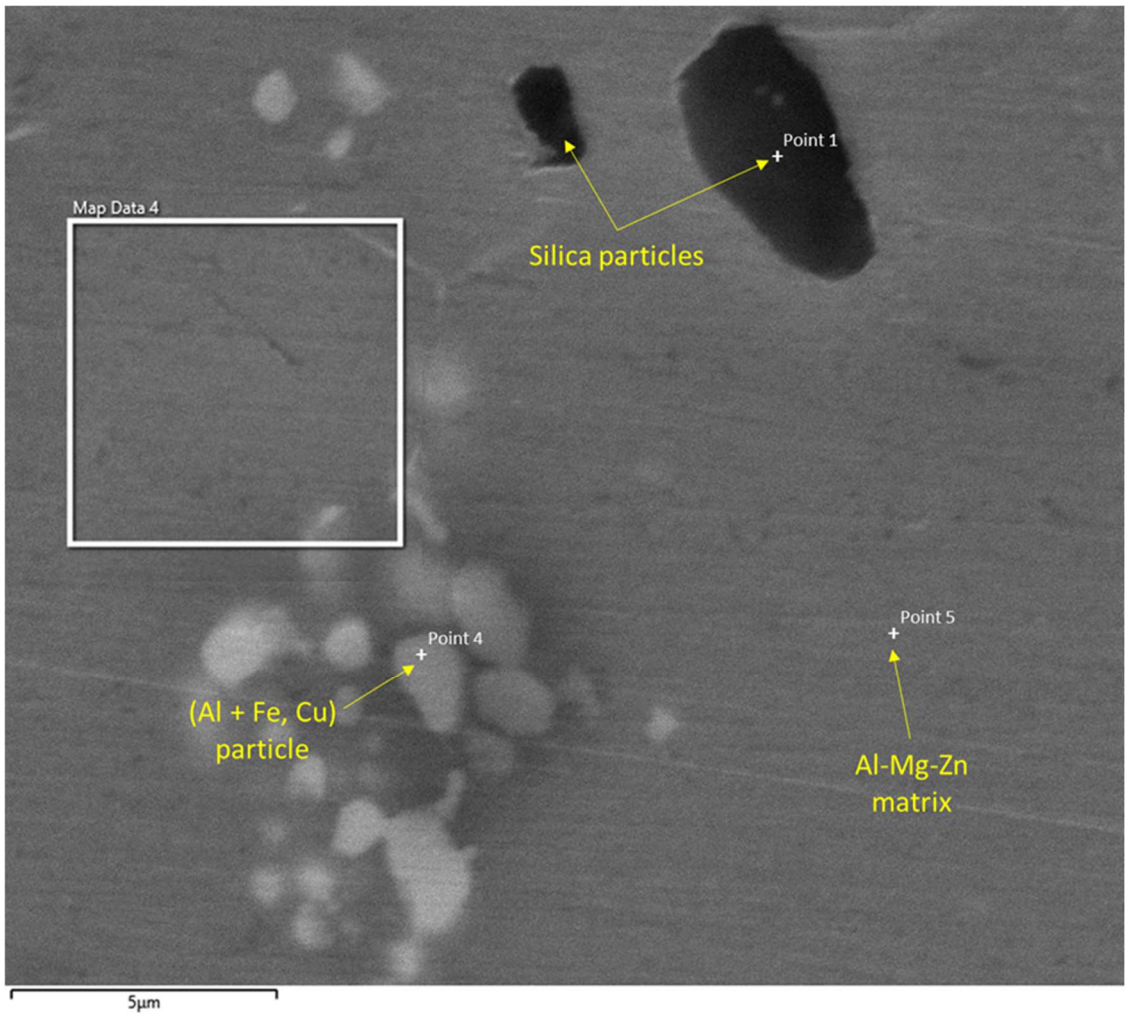

Figure 167 - SEM image of the upper pass stir zone in G12 showing an Al-Cu-Fe based cluster of particles and silica.

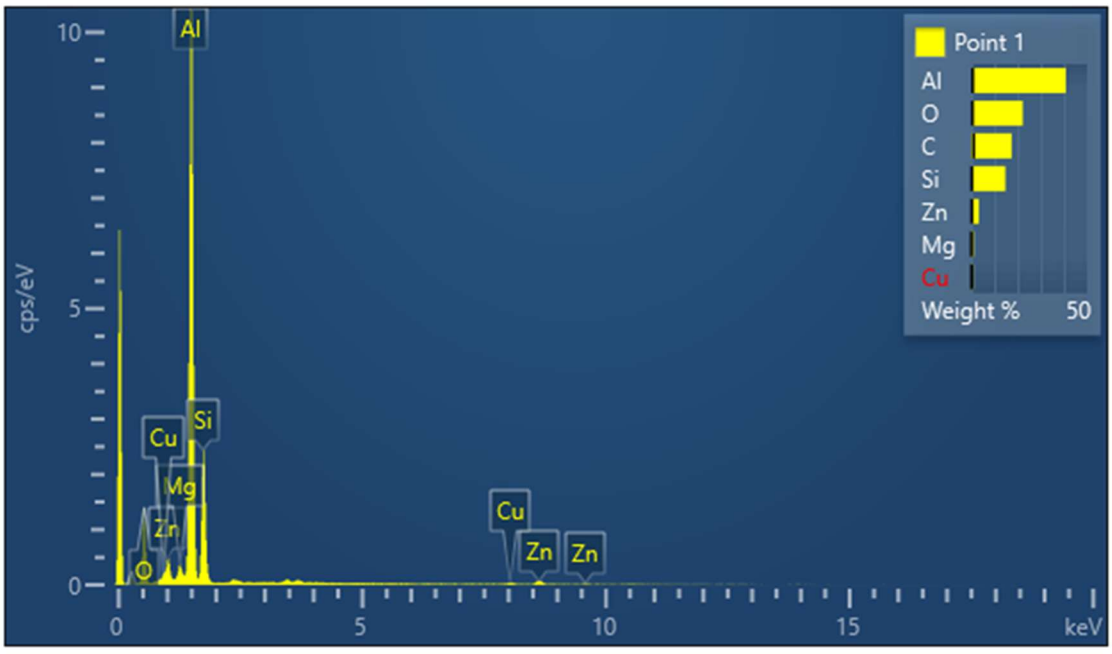

Figure 168 – EDX spectra 1 in Figure 167 indicating the presence of silica.

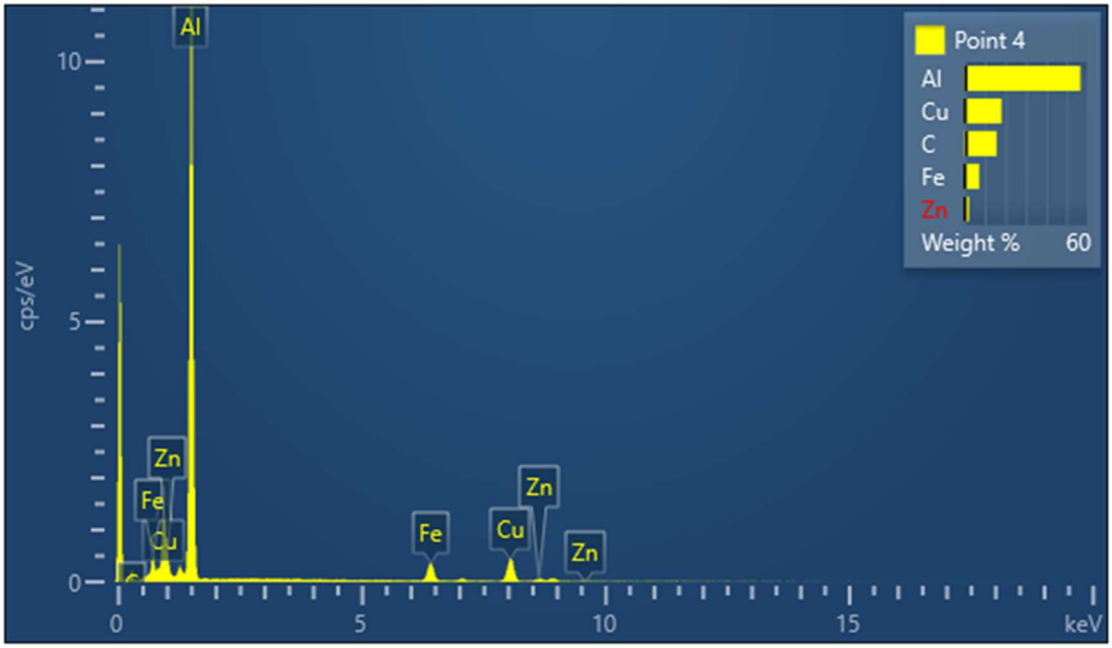

Figure 169 - EDX spectra 4 in Figure 167 taken from a Al-Cu-Fe particle.

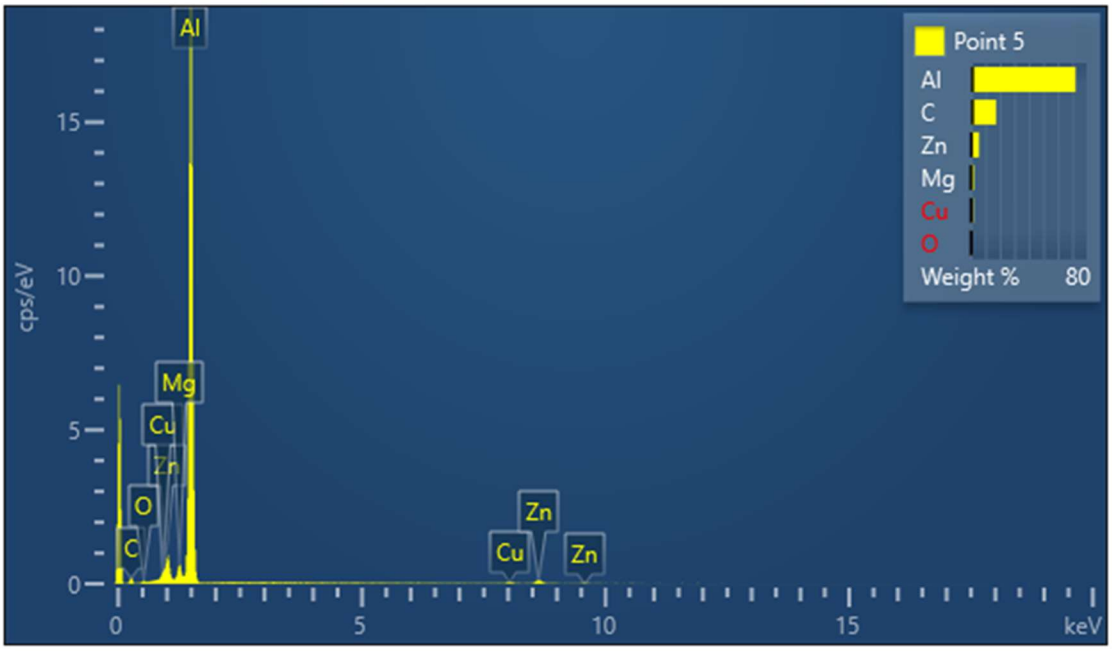

Figure 170 - EDX spectra 5 in Figure 167 showing the Al-Mg-Zn matrix.

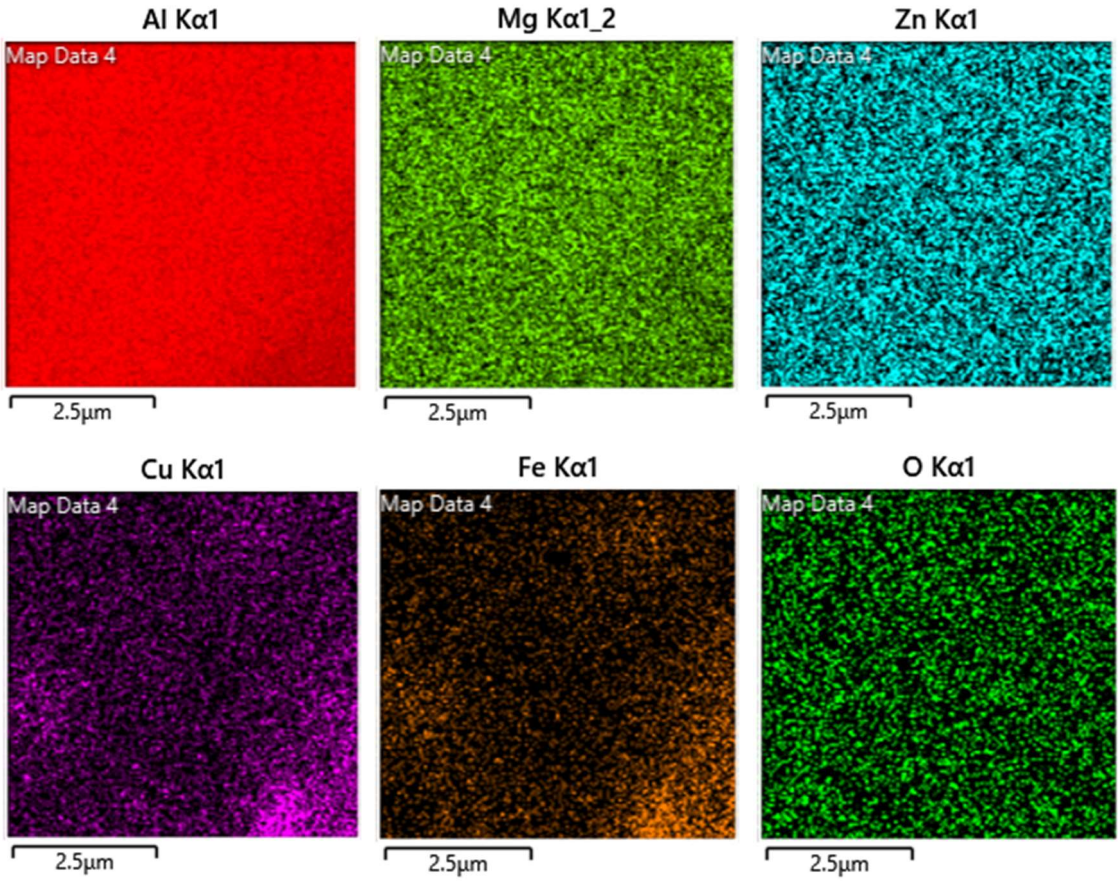

Figure 171 – EDX colour map 4 of the matrix present in weld G12.

4.3.3.4 Average distance between grain boundaries

The average distance between grain boundaries of the as-received AA7050-T7451 is presented in Table 45. The table shows that grains at centre thickness are larger than those nearer either surface of the plate. The grain structure was shown in section 4.3.3.2 to be bimodal which is supported by the data in the table which indicates a difference in grain size between the vertical and horizontal measurements.

Position	Average distance between grain boundaries (µm)	
	Vertical	Horizontal
Top	5.15	6.60
Middle	6.30	7.56
Bottom	3.39	5.68

Table 45 - Average distance between grain boundaries of the as-received AA7050-T7451 in the transverse orientation, through the thickness of the plate.

The average distance between grain boundaries of the welded material was measured at each of the nine regions shown in Figure 172, the results of this are presented in Table 46. It is clear the grains in the SZ (IDs d, e and f) for both G03/04 and G12 are more equiaxed by the consistency in the grain boundary distance for these regions. No measurement was secured for position ‘e’ for G03/04 due to the grain structure being too refined to be visible under an OLM, SEM was also used however the grain structure was still unidentifiable and as such this position was not recorded.

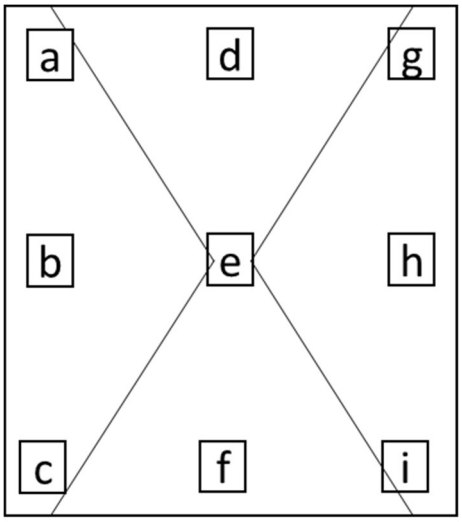

Figure 172 – Schematic of the nine regions in which average distance between grain boundaries was measured.

Positional ID	Average distance between grain boundaries (µm)					
	G03/04		G12		G18	
	Vertical	Horizontal	Vertical	Horizontal	Vertical	Horizontal
a	5.19	8.94	4.53	6.20	4.19	5.08
b	7.41	10.03	4.89	11.29	3.85	5.74
c	8.83	8.72	4.39	7.09	3.49	3.86
d	9.31	9.31	6.60	6.60	7.92	7.88
e	-	-	3.96	4.19	16.14	10.54
f	7.95	7.95	5.90	5.90	8.48	7.08
g	5.23	9.01	4.42	5.31	4.68	6.24
h	6.07	9.39	4.86	8.31	4.33	5.48
i	6.27	7.52	4.84	7.63	3.58	4.31

Table 46 - average distance between grain boundaries of welded AA7050-T7451 measured in the transverse orientation in both the vertical and horizontal axis.

4.3.4 Mechanical properties

4.3.4.1 Tensile

The parent and as-welded materials tensile data is summarised in Table 47. The as-received AA7050-T7451 UTS was measured as 538 MPa after three tests and failed at an elongation of 12.5%. The welds G03/04 and G12 failed comparatively weaker than the as-received material; 419 MPa and 352 MPa respectively. This is a retention of 78% and 66% respectively versus the as-received material.

I.D	Yield Strength (MPa)	UTS (MPa)	Elongation (%)
P.M	475	538	12.5
G03/04	330	419	4.0
G12	297	352	3.0

Table 47 – Principle tensile data for tests conducted in PM and FSWed AA7050-T7451.

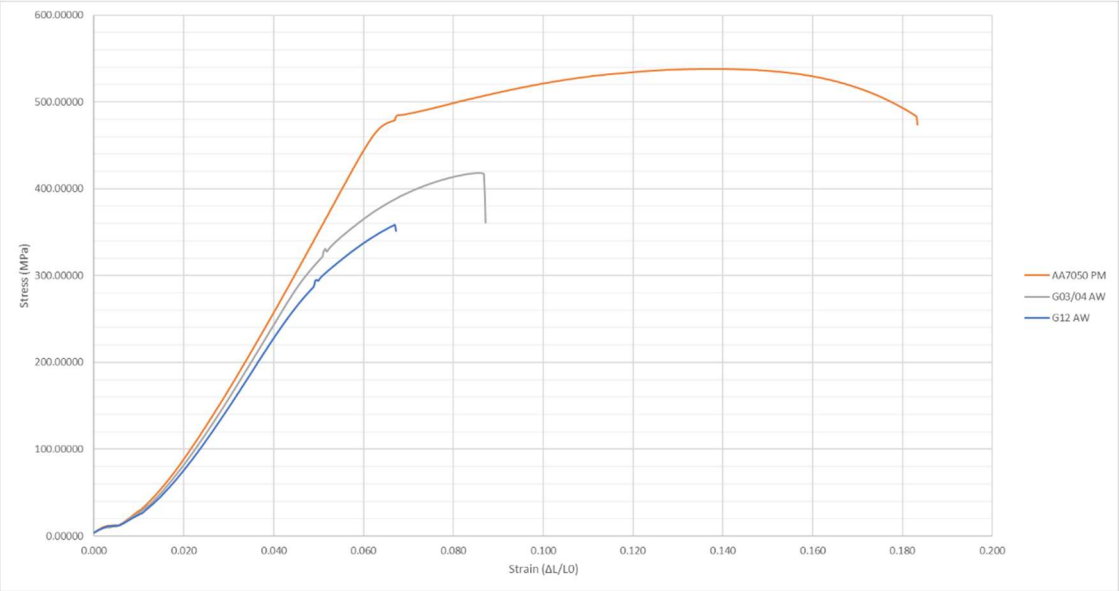

Figure 173 - Stress-Strain plot of as-received and as-welded AA7050-T7451.

The failed tensile specimens are documented in Appendix 38 to Appendix 40 while the failure locations are identified in Table 48. G03/04 failed at the TMAZ/HAZ interface on the retreating side in all three specimens. The failure followed this line for both passes and therefore intercepts the double processed region at the centre of the weld. Contrastingly, as-welded G12 fracture path travels through the SZ of the upper pass to the retreating side of lower pass.

Weld #	Tensile failure location		
	Test 1	Test 2	Test 3
G03/04 As welded	Ret to Ret	Ret to Ret	Ret to Ret
G03/04 6 Months	Ret to Ret	Ret to Ret	Ret to Ret
G03/04 12 Months	Ret to Ret	SZ to Ret	Ret to Ret
G03/04 18 Months	Ret to Ret	Ret to SZ	Adv to Adv
G12 As welded	SZ to Ret	SZ to Ret	SZ to Ret
G12 6 Months	SZ to Ret	SZ to Ret	Ret to Ret
G12 12 Months	SZ	SZ	SZ
G12 18 Months	SZ	SZ	SZ

Table 48 - Failure locations of as welded and naturally aged WFW and SDS welds in AA7050-T7451.

The effect of natural ageing on the tensile properties for both G03/04 and G12 is shown in Figure 174 and Figure 175 and the failed samples are presented in Appendix 41 to Appendix 46. For both welds there is an improvement in the properties with a clear correlation between increasing time aged and improved tensile strength evident for G03/04. Over the 18 months of ageing the UTS increases by 11% from 419 MPa after 0 months aged to 463 MPa while the yield strength of the weld improved from 330 MPa to 370 MPa (an increase of 12%).

I.D	Yield Strength (MPa)	UTS (MPa)	Elongation (%)
G03/04 6 Months	358	450	4.5
G03/04 12 Months	365	460	4.3
G03/04 18 Months	370	463	4.2
G12 6 Months	336	461	3.2
G12 12 Months	322	387	2.7
G12 18 Months	264	391	3.2

Table 49 – Principle tensile data for tests conducted in naturally aged FSWed AA7050-T7451.

The correlation between natural ageing and improved properties is not as evident in G12 due to a spurious result during the 6 months aged testing. The third test at this ageing period recorded a UTS ~75 MPa greater than the other two tests (387, 389 and 461 MPa) which has skewed the average. Ignoring this final value would still suggest little difference between the aged samples; each showing an increase of ~8-10%.

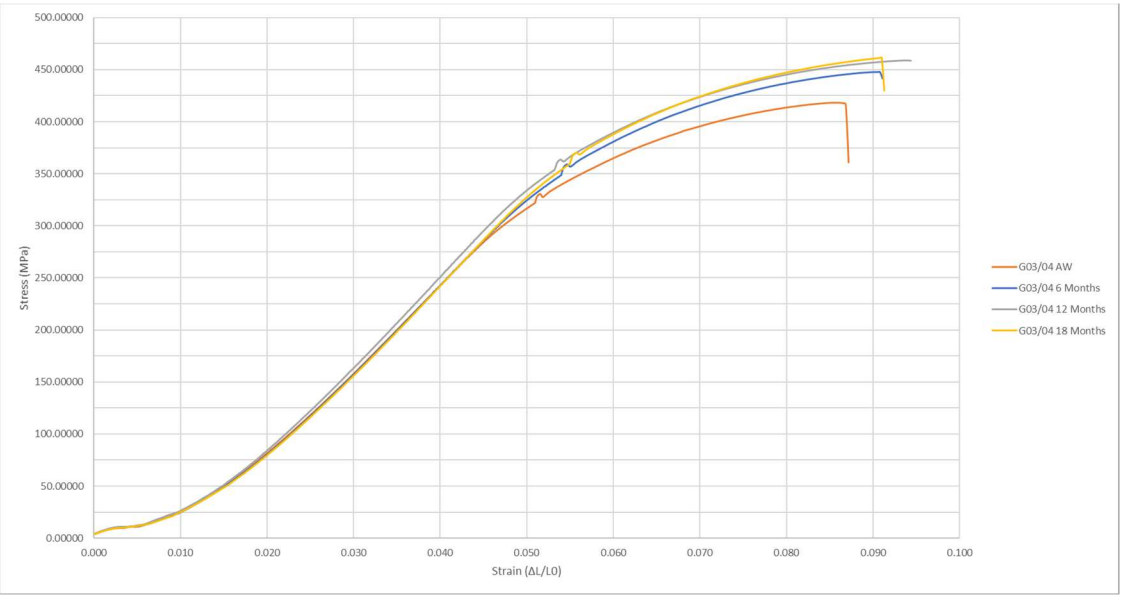

Figure 174 - Plot showing the impact natural ageing has on the mechanical properties of G03/04.

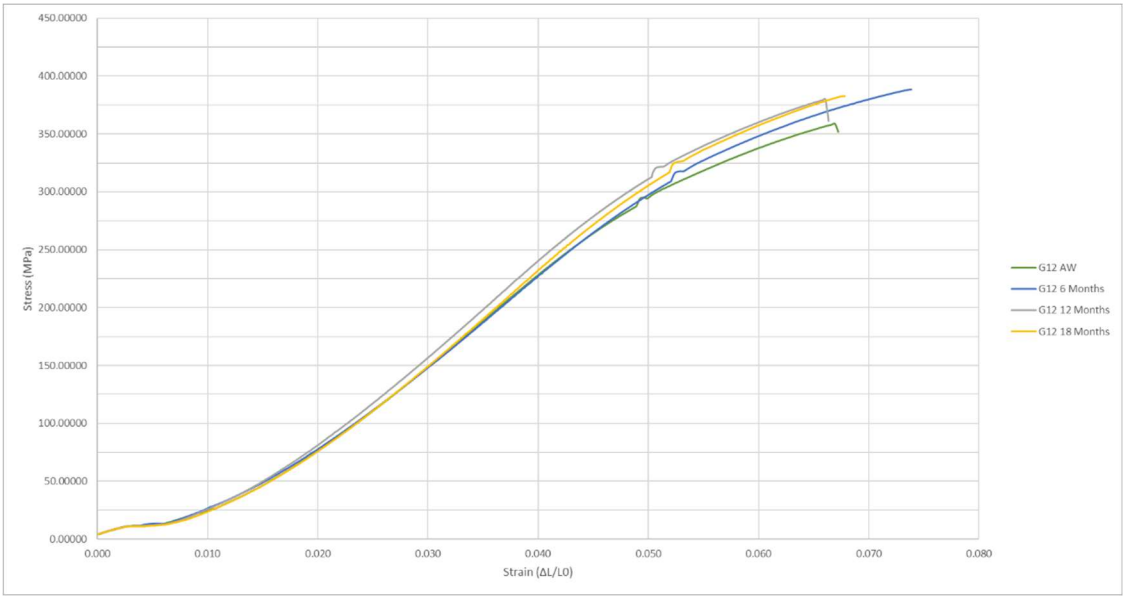

Figure 175 - Plot showing the impact natural ageing has on the mechanical properties of G12.

4.3.4.2 Hardness

Hardness mapping, shown in Figure 176a, reinforced that the microstructure of the as-received AA7050-T7451 varied through the thickness of the material, as demonstrated in Figure 176b.

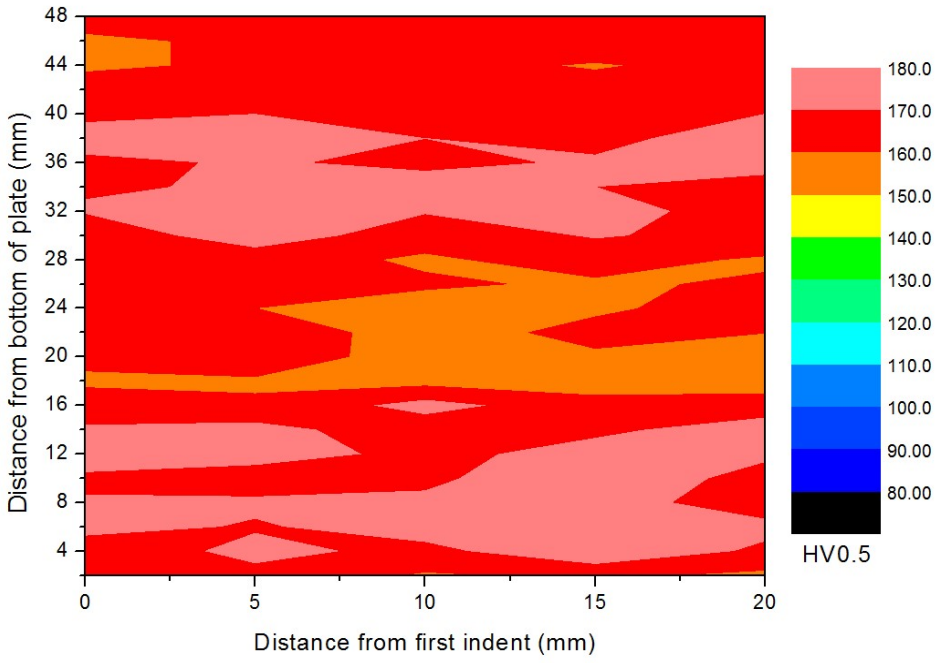

a)

b)

Figure 176 – a) Hardness map of as-received AA7050-T7451. b) Macrograph and hardness map overlayed.

The hardness plots for the three welds are presented in Figure 177 to Figure 179. Two points within the SSS-FSW hardness map, Figure 179, were statistically calculated as a result of the machine overloading and failing to record an indent. These points were consecutive at coordinates (-48, 32) and (-48, 34). To overcome having no data at these points, the average of the surrounding five points was taken for each coordinate. For example, at (-48, 32) the value taken was 132 HV [(134+140+129+129+129)/5 = 132.2 HV].

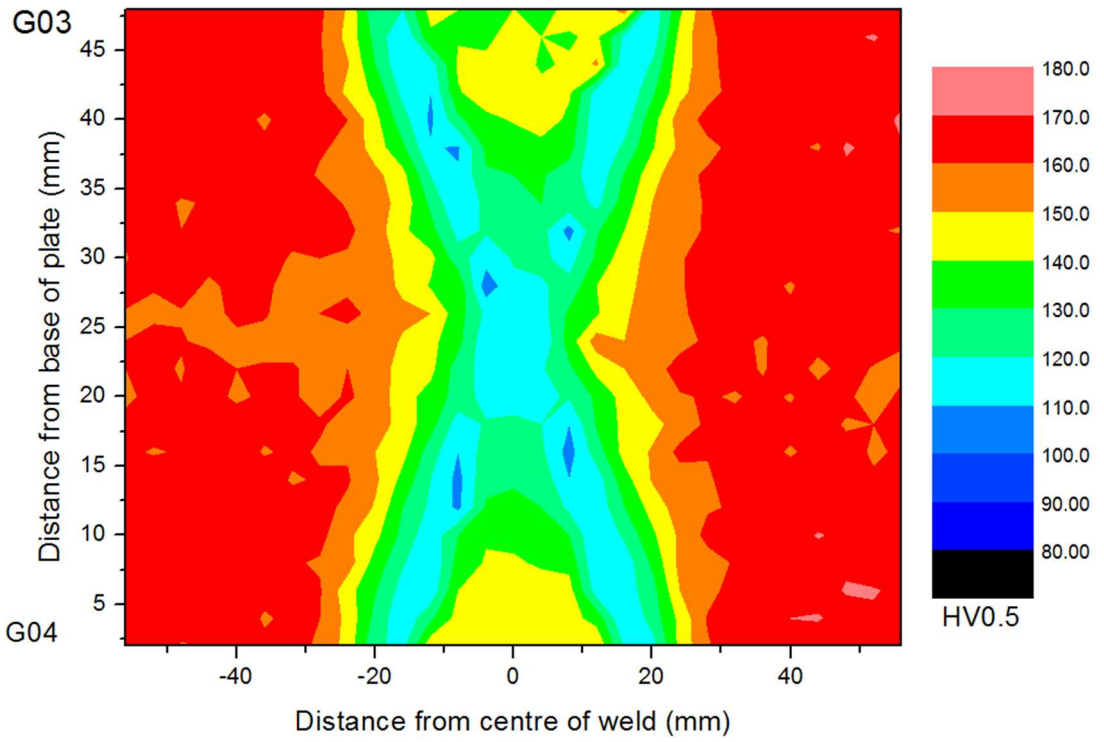

Figure 177 - Micro-hardness contour map of weld G03 and G04 - WFW-FSW in AA7050-T7451.

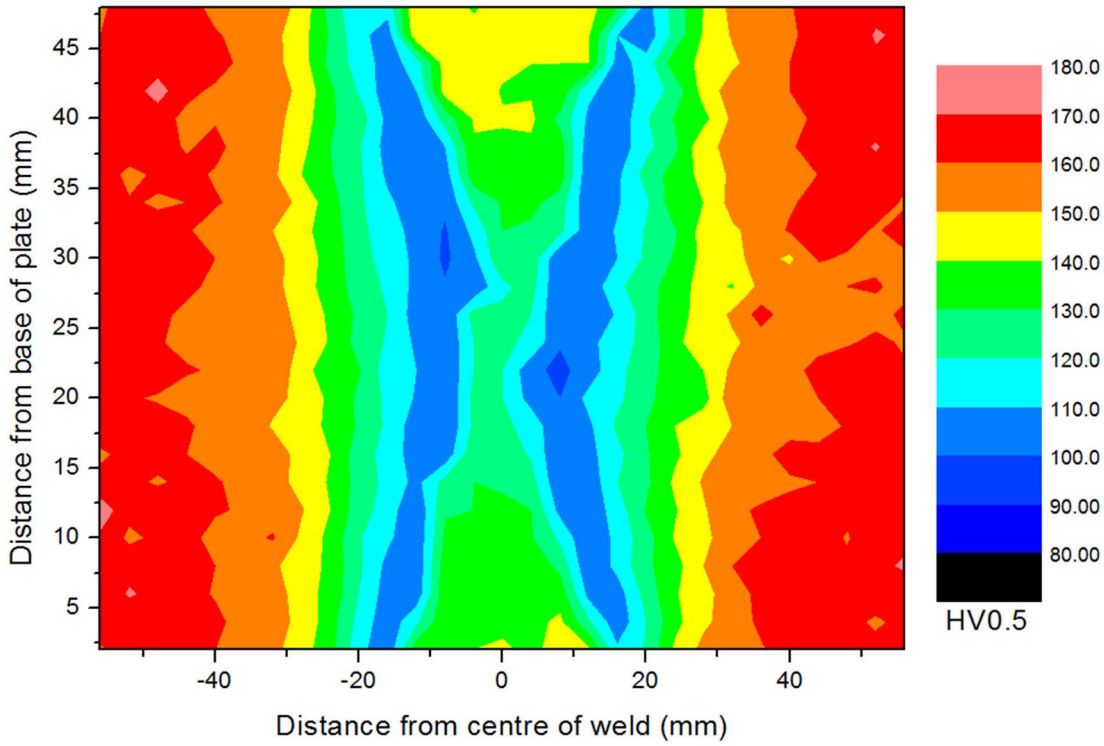

Figure 178 - Micro-hardness contour map of weld G12 - SDS-FSW in AA7050-T7451.

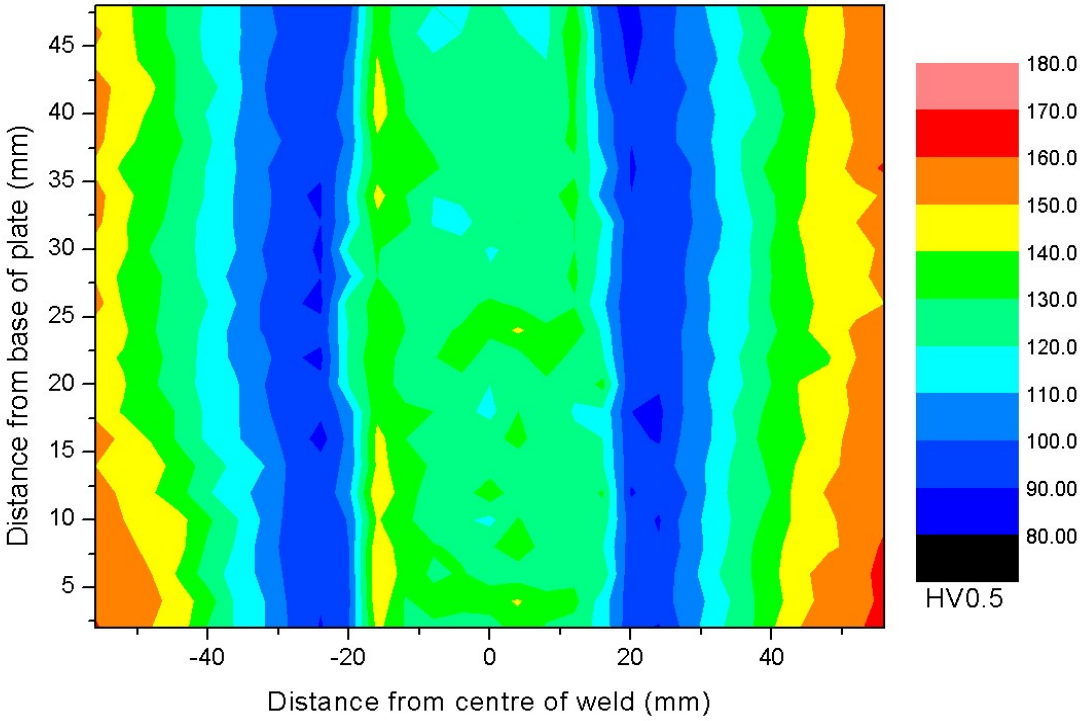

Figure 179 - Micro-hardness contour map of weld G18 - SSS-FSW in AA7050-T7451.

4.3.4.3 Swept volume

The swept volume per revolution for each of the three welds produced in AA07050-T7451 is presented in Table 50. G12 (734.23 and 751.90 mm^3/rev), despite using the same probe design as G03/04, swept more material per revolution than the WFW-FSW (637.47 and 638.31 mm^3/rev). The SSS-FSW, G18, swept the most material (785.86 mm^3/rev) for a single pass, however, the combined volume per revolution for G12 in order to produce a full penetration weld sizeably exceeds this at 1486.13 mm^3/rev.

	G03/04	G12	G18
1st Pass/ Upper Pass	637.47	734.23	785.86
2nd Pass/ Lower Pass	638.31	751.90	-

Table 50 - Swept volume per revolution (mm^3/rev) of the FS welds in AA7050-T7451.

4.3.4.4 Energy input

Table 51 shows the energy input required for welding using WFW-FSW, SDS-FSW and SSS-FSW techniques in 50 mm thick AA7050-T7451.

Weld Number	Traverse Speed	Spindle Rotation	Torque (Mean)	Torque (Max)	Efficiency factor	Energy Input (Mean)	Energy Input (Max)
#	mm/min	rpm	Nm	Nm		kJ/mm	kJ/mm
G03	130	129.64	778.21	808.45	0.98	4.78	4.96
G04	130	129.47	766.31	789.17	0.98	4.70	4.84
G12 Lower	130	109.57	640.16	697.63	0.98	3.32	3.62
G12 Upper	130	109.91	574.04	591.67	0.98	2.99	3.08
G18	59	122.00	1101.94	1404.30	0.98	14.03	17.88

Table 51 - Energy input for welds produced in AA7050-T7451. Energy efficiency factor is an assumed value.

5 General Discussion

This chapter discusses the results obtained during this research. The results are examined as a collective, and unique findings from each material or technique are presented.

5.1 AA5083-H111: Results Discussion

5.1.1 Microstructure

5.1.1.1 Effect of alloy composition on the microstructure

Both the parent and FS welded material used during this project were reviewed against several articles of previous work (Scamans, Holroyd, and Tuck (1987); Yan and Hodge (2017); Chen et al. (2016); Rahmatian, Mirsalehi, and Dehghani (2019)) which identified the material was similar in structure; this reiterated the conclusions from the OES (Table 21) and EDX (section 4.1.3.3) analysis and confirmed the alloy investigated as being AA5083.

EDX analysis displayed constituent particles of (Al + Fe, Mn, Si) and a matrix consisting of (Al + Mg). Constituents such as those found during EDX analysis are widely considered to be not beneficial despite claims that iron-rich particles are one of the main types of intermetallic particles present in AA5083 (Scamans, Holroyd, and Tuck (1987) and Lucadamo et al. (2006)). The size of the constituents identified ranged from micrometres to tens of micrometres. These particles are not beneficial as the presence of iron reduces the strengthening effect of the transition elements, manganese and chromium, because it readily forms insoluble, more brittle compounds that are prone to cracking during future processing as discussed by Anderson, Weritz, and Kaufman (2018b). Similar particles have been found within AA5083 by Segal et al. (2019) which states the presence of a 'multicomponent' system within the AA5083. This forms three groups of intermetallic compounds; '(i) constituent particles (Al + Fe, Mn, Si) with a size range of 0.5–10 µm; (ii) dispersions (Al + Mg, Mn, Cr, Zn) with a size range 0.05–0.5 µm; and (iii) precipitates (beta-phase Mg_2Al_3) of a nanometer size'. Further literature

agrees with the presence of these constituent particles, identifying the composition as α-Al(Mn,Fe)Si (Yi et al., (n.d.); Wang (2020)).

EDX analysis also indicated the presence of (Mg + Si + O) within the PM. These particles may have been magnesium orthosilicate (Mg_2SiO_4), however, it is far more likely that these particles are magnesium silicide (Mg_2Si) that have been oxygenated prior to analysis. In 5xxx alloys silicon is considered an impurity and the presence of Mg_2Si would subsequently reduce the plasticity of the metal. This is because there is an excess of magnesium over the required amount to form the phase which sharply reduces the solid solubility of the compound (Anderson, Weritz, and Kaufman (2018)).

5.1.1.2 Effect of FSW technique and process parameters

Both the tool design and the energy input of the weld influenced the microstructure of the alloy. The tool design influenced the profile of the SZ and consequently the variation in microstructure through the thickness of the material, demonstrated by section 4.1.3.1. G07/08 and G13 both produced hourglass SZs in line with their tapered probes whereas G34 produced a linear SZ due to the bobbin tool used in this weld. The profile of the probe also influenced the degree of deformation the microstructure experienced and the direction of material flow. The E011 probe used in G07/08 and G13 is designed with a 2.5 mm pitch thread whereas the D090 probe used in the welding of G34 has a 4.0 mm pitch thread. This resulted in differing levels of deformation and recrystallization of the grain structure. The pitch of the probe, along with other factors including process parameters, influences the energy input into the weld which effects the grain growth during welding. The thread on the probe generates friction which impacts on the energy required to produce the weld. This is due to the frictional heat determining the level of plasticity of the material which in turn determines how much energy is required to translate the probe.

There is a positive correlation between the energy input and the average distance between grain boundaries. G34 used a traverse to rotational speed ratio of 1:3 that

produced an energy input (22.59 kJ/mm) significantly higher than either G07/08 or G13 (9.27 kJ/mm and 6.31 kJ/mm respectively). The result is the largest grain growth of any HAZ in the AA5083 material. The HAZ present in G34 was bimodal with the horizontal length of the grains in each region exceeding 40 µm. Of the 9 predetermined regions where measurements were made (see Figure 98) only one, G07/08 g, exceeded 40 µm in the horizontal axis, showing the extent of influence the increased energy input had on G34s HAZ. Dawood, Mohammed, and Rajab (2014) also highlights the influence of energy input on grain growth signalling that a greater rpm, and therefore higher energy input, resulted in a larger range of grain size in the HAZ, supporting the view that there is a positive correlation between energy input and grain size. Dawood et al (2014), however, also indicates that a faster rpm results in a smaller grain size range in the SZ, a product of the refinement and recrystallization that occurs in this region.

The positive correlation between energy input and grain size is also evident in the SZ. Table 23 shows that the grain size for G34 ranged between 8.14-11.74 µm and 7.40-12.31 µm vertically and horizontally respectively. Where the energy input is lowest in G13, the average distance between grain boundaries of the SZ ranged between 2.66-6.39 µm and 2.47-6.33 µm in the vertical and horizontal axes respectively. The lower limit of G13s ranges is due to the area where the probes pass through the same material refining the grain structure further than in the single processed regions.

5.1.2 Hardness

5.1.2.1 Effect of microstructure on the hardness

The through thickness variation in the grain structure in as-received AA5083, shown in Figure 83, corresponds to variations in the hardness of the PM, as demonstrated by Figure 100. Where the average distance between grain boundaries of the PM is larger the hardness is shown to be softer, suggesting that the PM adheres to the Hall-Petch relationship (illustrated in Equation 6).

$$HV = HV_0 + \frac{k}{\sqrt{d}} \qquad \text{Equation 6}$$

The welded material, however, did not appear to adhere to the Hall-Petch relationship. The average distance between grain boundaries is inversely proportional in FSWed AA5083 to the hardness suggesting no correlation between the hardness and the Hall-Petch relationship. Sato, Park, and Kokawa (2001) suggest that the relationship between the microstructure and hardness profile remains unclear, though they continue by indicating solid-solution alloys often contain high densities of particles (Hu, Ikeda, and Murakami (1996); R. E. Sanders, Baumann, and Stumpf (1989)). The particles both within the grains and on grain boundaries are expected to be modified by the FSW process and this can lead to more or less solute Mg available for strengthening, depending on the location in the weld. This is likely to be a significant factor in explaining the observed hardness distribution.

5.1.2.2 Effect of FSW technique and process parameters

In non-heat treatable AA5083 the process of FSW showed changes in hardness that did not fit the profile of the tool, as is the case with heat-treatable AA6082 and AA7050. Figure 101 to Figure 103 show this trait, which leads to the conclusion that not only is the heat generated during welding more influential in heat-treatable alloys, such as AA6082 and 7050, than in AA5083 (the non-heat-treatable alloy) but the generated heat is also more influential in defining the hardness profile than the plastic deformation produced during welding. The heat input during welding induces coarsening of the particles and grains in the HAZ and aids with recrystallization in the SZ while plastic deformation also impacts the degree of recrystallization.

Moreover, it was noted that the WFW and SDS techniques produced overlapped regions that affected the hardness. Figure 101 shows the hardness at centre thickness of G07/08 is greater than the hardness of the PM. Rahmatian, Mirsalehi, and Dehghani (2019) also demonstrate an increase in hardness in the region (albeit in thinner 10 mm AA5083) citing a high density of dislocations as well as uniform distribution of

intermetallic particles as the cause. It was also cited that the hardness is independent of the grain size and therefore of the Hall-Petch relationship (further supporting Sato, Park, and Kokawa (2001)). It is explained that adhering to the Hall-Petch relationship would imply a significant increase in hardness within the SZ where the grain structure has been refined (as per Equation 6) however only a minor increase in hardness was recorded. This is because Hall-Petch is dependent on high angle grain boundaries acting as obstacles for dislocation motion, however, the production of a refined, equiaxed structure caused a high density of dislocations and dislocation entanglement limiting the mobility of future dislocations at smaller intervals than the grain size suggested by Hall-Petch.

It was anticipated that the SDS weld, G13, would exhibit similar hardness properties to G07/08 as it also uses two nominally half-length probes. However, as Figure 102 shows the SZ and HAZ are predominantly harder than the corresponding WFW regions while the double processed region is far smaller and does not exceed the PM. The probes in G13 skewed during welding reducing the size of the double processed region, though the hardness map in Figure 102 would suggest a small region is still harder than the surrounding material. The parameters effected the extent of the skewing and therefore the impact on hardness. The traverse/rotational speed ratio for G13 was 1.2 (whereas G07/08 was 1.0) which produced greater forces in the X and Y axis' due to the material not being as plasticised but still requiring to be displaced. This pushed the probes off centre, causing the skewing to occur. In contrast to this, G34 used a ratio of 0.3 which produced a 'hot' weld and Figure 103 shows the effect of SSS-FSW. As shown, the hardness is lower in this weld retaining ~75% the hardness of the PM vs the ~80-90% retained by the WFW and SDS-FSW techniques. Again, the SZ is not distinguishable from the HAZ.

5.1.3 Tensile properties

5.1.3.1 Effect of microstructure on the tensile properties

The microstructure of FSWed AA5083 influences the failure location during tensile testing. Table 25 identifies the failure location in each weld indicating that G07/08 and G13 both failed between the HAZ and PM on either the AS or RS. Despite differing grain structures on either side of the weld, as demonstrated by Appendix 15 and Appendix 16, there was no consistency as to the side of the weld where failure occurred. As the samples failed in the HAZ/PM, it can be concluded that the transition grain structure depicted is stronger than the elongated and coarsened grain structure shown to be present in the HAZ.

Defects in the microstructure, such as the void visible in the macrograph of G34 (see Figure 86), have a substantial effect on the tensile properties of the weld. G34 retained 56% of the PM UTS, whereas G07/08 and G13 retained 93 and 101% respectively, showing that G34 was comparatively weaker than either of the other two welds. Appendix 20 also illustrates that the failure location, unlike the other two welds, was within the SZ and originated in the void on the AS. Not only was a sizeable defect present in G34 but the average distance between grain boundaries was also considerably larger in each of the regions measured resulting in a weaker material due to the fewer grain boundaries hindering dislocation movement.

5.1.3.2 Effect of FSW technique and process parameters

Different FSW techniques affected the tensile properties to differing degrees. G13, for example, has been shown to retain a UTS (298 MPa) slightly greater than the PM (296 MPa) following welding, whereas G07/08 retained 277 MPa. Therefore, AA5083 responds better to the simultaneous welding of G13 better than the weld-flip-weld technique used for G07/08. The difference between the two techniques is the energy input. The energy input in G13 is lower (6.31 kJ/mm) than that of G07/08 (9.27 kJ/mm) though as the energy is inputted simultaneously, the resulting energy input is greater than either the first or second pass of G07/08. Subsequently, the swept volume (SV) is

~100 mm^3/rev greater for both probes in G13. This results in more material being plastically deformed and as the material is work hardened G13 will strengthen to a greater extent than G07/08.

G34 has been shown to contain a void defect which is the product of the anti-clockwise rotation of the full-length bobbin probe. The probe profile was designed for clockwise rotation so that the thread directed plasticised material towards the centre of the weld. However, attempts at producing the SSS-FSW weld using a clockwise rotation failed to consolidate and fuse the material instead machining the material away as the probe traversed along the joint line. An anti-clockwise rotation was subsequently tested and was found to consolidate the material far better than the clockwise rotation. However, a void defect was still produced in G34, which resulted in a reduction in the strength of the weld. As Figure 99 shows, G34 failed with far less strain than any of the other samples tested and within the SZ unlike the other samples which all demonstrate the effect of the void produced by the SSS-FSW technique on the tensile properties.

5.2 AA6082-T651: Results Discussion

5.2.1 Microstructure

5.2.1.1 Effect of alloy composition on the microstructure

Both the parent and FS welded material used during this project were reviewed against several articles of previous work (such as 'Aluminum 6082-T6' (n.d.) & Liang et al. (2019)) which supported the conclusions from the OES (Table 35) and EDX (section 4.2.3.3) analysis that the alloy was AA6082. The OES data confirms the alloy analysed was AA6082 as the wt% of magnesium (0.74), manganese (0.53) and silicon (0.92) were within the ranges stated by 'Aluminum 6082-T6' (n.d.) for this alloy.

EDX analysis was used to review the particles present in both the as-received and FS welded material. The EDX analysis (shown in section 4.2.3.3)indicates the presence of both (Mg, Si) and (Al + Mn, Fe, Si) based particles which was also the case for Birol et al. (2014) who found the precipitates present were predominately Mg_2Si (the main strengthening phase) and α-$Al_{12}(Fe,Mn)_3Si$ (a constituent particle). Although the grain structure was not successfully revealed by etching, as previously mentioned in section 4.2.3.4, Birol et al (2014) present the image displayed in Figure 180a which highlights similarities in the two materials, reiterating the OES data that the alloy investigated was AA6082.

The EDX analysis shown in Figure 129 to Figure 135 highlights an Al-Mn-Fe-Si based particle and a surrounding matrix which consisted of Al+Mg. Given the temperature during welding exceeds the solution temperature for magnesium (450 °C) but does not for iron, manganese, or silicon (655, 660 and 580 °C respectively) it is assumed that the magnesium present in the alloy has gone into solution (Vander Voort (2004)) within the matrix but as the particle elements did not the particles size is far more considerable than that of magnesium.

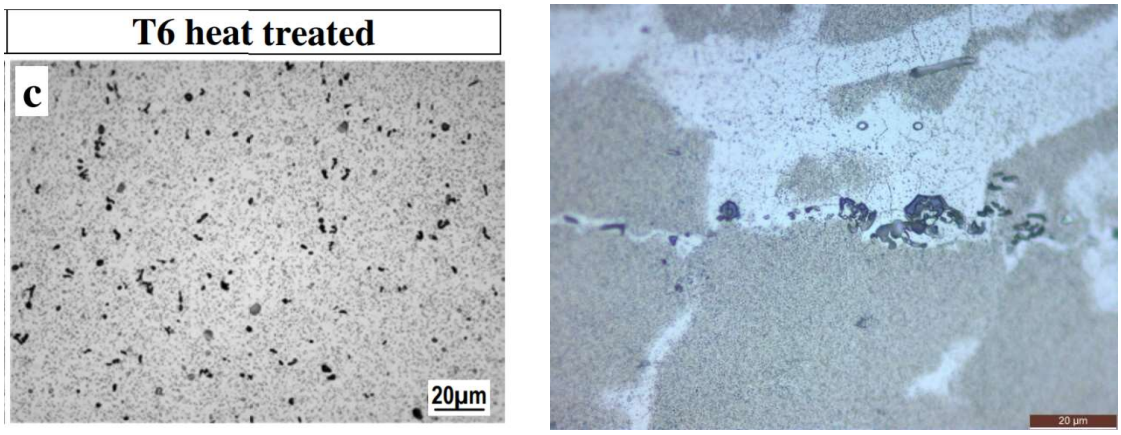

a) Grain structure of T6 heat treated AA6082 (Birol et al (2014)).

b) As-received AA6082-T651 used in this project. Etched in Krolls Reagent.

Figure 180 – Microstructure comparison between T6 heat treated AA6082 used by Birol et al (2014) and AA6082-T651 used in this project.

5.2.1.2 Effect of FSW technique and process parameters

The magnitude of influence FSW has on the microstructure of AA6082-T651 is dependent on the FS variant and process parameters. As stated by Birol et al (2014) in section 5.2.1.1, the primary particles present in the as-received AA6082-T651 were Mg_2Si and α-$Al_{12}(Fe, Mn)_3Si$. These particles, though smaller, were also the principle particles found in the FS welded samples. The particle within the PM, shown in Figure 125, was recorded as 11.66 µm in length whereas the particle from G14, see Figure 132, was 8.13 µm in length.

The four SSS-FSW macrographs all displayed linear SZ, as expected, though the two produced using fine thread pitches (G14 and G17) appear broader than those with coarse pitch (G16 and G19). This is due to the increased surface area of the probe generating greater friction and consequently plasticising more material. Weld G19 (which used a 3 flat, coarse pitch probe) contains voids, indicated in Figure 116, which suggest the parameters used didn't generate sufficient heat. Although the energy input (5.68 kJ/mm) of the weld is greater than that of G17 (5.46 kJ/mm), G19 is the only SSS weld produced in AA6082 to contain voids. This would suggest that the profile of the probe requires a greater energy input to plasticise the material sufficiently to consolidate the weld and therefore, the probe used in G19 is not as efficient. Contrastingly, G17 had the lowest energy input of the four SSS welds and produced a consolidated weld indicating that this probe design may be the most energy efficient and fit for purpose of the four designs.

Another effect of FSW on the microstructure is the presence of the Joint Line Remnant (JLR). The JLR is a trace of where the joint line previously existed prior to welding but has been displaced by the tool. It is visible by virtue of the presence of oxides and other surface contaminants. Figure 120 shows that the JLR resembles the lazy Z shape of a kissing bond, however, this is not the same feature and should be treated differently. The JLR is labelled a 'flaw' and as such is considered a cosmetic blemish

rather than a ‘defect’ which has a detrimental impact on the mechanical properties of the weld.

5.2.2 Hardness

5.2.2.1 Effect of microstructure on the hardness

The hardness of the as-received AA6082-T651 was very consistent through the thickness of the sample, as presented in Figure 140, suggesting that the microstructure was homogeneous. Once FS welded the material is no longer homogenous and a difference in the hardness is observable. The HAZ grain structure and precipitates coarsen compared to the PM and the SZ becomes refined and equiaxed. The only instance in which the hardness minima was found within the SZ is G20/21 which experienced cold lapping. This is a phenomenon in which two sheets of material are pressed together by the forces exerted on the material instead of the material being plasticised enough to fuse together during the stirring. A large void was also noted in the G20/21 SZ which reduces the resistance to the indentation force as the material can move into the void thus causing a reduction in hardness of the surrounding material. As such the materials hardness minima was located within the SZ in this instance.

The hardness profiles of G20/21 and G22 (the two tapered probe welds) form a ‘U’ shape although G22 showed signs of a small recovery on the advancing side approximately 4 mm from the centre of the weld. All four SSS-FSW samples presented broader ‘W’ shapes indicating a recovery within the SZ towards parent hardness. The linear profile of the probe meant a consistent microstructure through the transverse plane and as such resulted in a broader SZ than that of G20/21 or G22. In FS welds in AA6082, the SZ peak hardness does not return above 80HV at ~25 mm thickness however it would be achievable to do so if the material was artificially aged after FSW (Sato et al. (1999)). By artificially ageing AA6082 post weld, Al-Fadhalah and Asi (2018) indicated a recovery of hardness within the SZ comparable to the base material, though the TMAZ only partially recovered. This recovery is possible as result of the

reprecipitation of a ‘high density of needle-shaped’ precipitates β’’ in the SZ due to an abundance of solute magnesium and silicon atoms. Al-Fadhalah and Asi (2018) also attributes the recovery of hardness within the TMAZ to the formation of a high density of β’ but concluded that formation of this precipitate made it difficult to form β’’.

5.2.2.2 Effect of FSW technique and process parameters

The FSW techniques and parameters used have varying impacts on the location of the hardness minima, SZ hardness retention and width of HAZ. Both WFW and SDS-FSW have been shown to produce macrographs resembling hourglasses. The hardness data, presented in section 4.2.4.2, reinforces this. From the hardness contour colour maps in Figure 141 and Figure 142 it is clear that the two processes have produced welds with through thickness variation, with the SZ narrowing near the centre of the materials thickness. The SSS-FSW technique, contrastingly, was shown to produce minimal through thickness variation. The probe design in this weld was linear and as such produced a SZ that did not alter in width through the thickness. This has resulted in the hardness distribution presented between Figure 143 and Figure 146.

In heat-treatable alloys such as AA6082, the energy input for each weld was expected to influence the HAZ width as well as the welds’ ability to retain hardness. However, this was not the case in the six welds produced in this alloy. G20/21 experienced the greatest total energy input (9.06 kJ/mm), although, the simultaneous energy input of G22 (4.77 kJ/mm) marginally exceeded the energy input of each pass for G20/21 (4.52 kJ/mm and 4.54 kJ/mm). The HAZ of G20/21 was the narrowest of all six welds (~60 mm), aligning with the predicted energy input/HAZ width relationship. However, the four SSS welds were each produced using greater energy inputs than G22; yet G22 had the largest HAZ width (~110 mm), disputing the relationship.

5.2.3 Tensile properties

5.2.3.1 Effect of microstructure on the tensile properties

The microstructure of the weld influences the failure location of the sample. For example, G22 failed within the TMAZ/HAZ interface where the grain structure is changing from refined and equiaxed within the SZ to the bimodal HAZ, as demonstrated by Figure 181. Tamadon et al. (2017) show the grain distribution in both sides of the weld indicating the different zones of the weld. The failure site of G22 can be compared to this and correlates to the stark change in grain structure between the TMAZ and HAZ of Tamadon et al (2017).

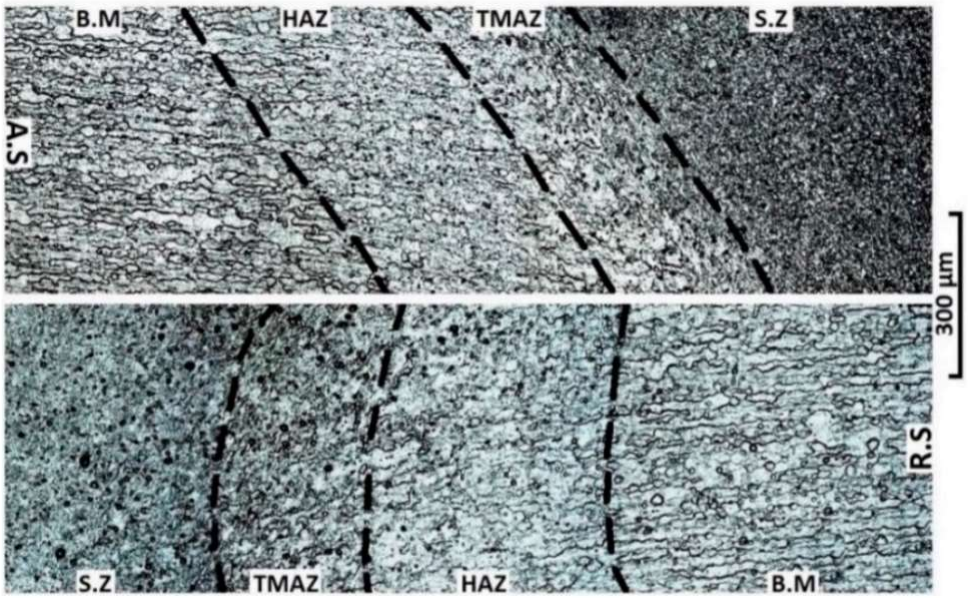

Figure 181 – Microstructure of the grain distribution in the advancing side (A.S, top) and the retreating side (R.S, bottom) of the A6082-T6 weld (Tamadon et al. (2017)).

The Hall-Petch relationship is valid for these welds which show that yield strength is increased with the reduction of grain diameter. However, grain diameter is inversely proportional to UTS which decreases with grain size.

5.2.3.2 Effect of FSW technique and process parameters

The FSW process has a comprehensive impact on the tensile properties of the AA6082. The macrograph of G20/21, see Figure 111, shows a large void (~3 mmx3 mm) in the first/upper pass, as stated in section 4.2.3.1 this is a Chip LOF defect. Voids within the SZ can be produced as a result of several issues such as tool damage, cold process parameters and material defects. The same probe was used for the second pass which had no visible voids, discrediting tool damage as the cause of the voids production. There was also no visible damage to the as-received material. Therefore, it is suggested that the process parameters were responsible for the formation of the void.

The fracture path and surface of G20/21, stated in Table 37 and demonstrated in Figure 137, reveal the failure occurred in the SZ of the weld and a 'honeycomb' style surface is visible in the second pass SZ. An investigation of this has revealed that the rotational speed was too low to plasticise the material to the extent required and as a result 'cold lapping' occurred. The fracture surface also reveals the presence of kissing bonds (see Figure 182b), another feature that reinforces the view that this fracture surface was a result of cold weld parameters. Kissing bonds are discernible as 'lazy zigzags' but are actually broken oxide particles of Al_2O_3 produced by the insufficient stirring of the metal (Kah et al. (2015)). Oosterkamp, Oosterkamp, and Nordeide (2004) identifies similarities with the kissing bonds witnessed in this projects tensile testing, as illustrated in Figure 182a.

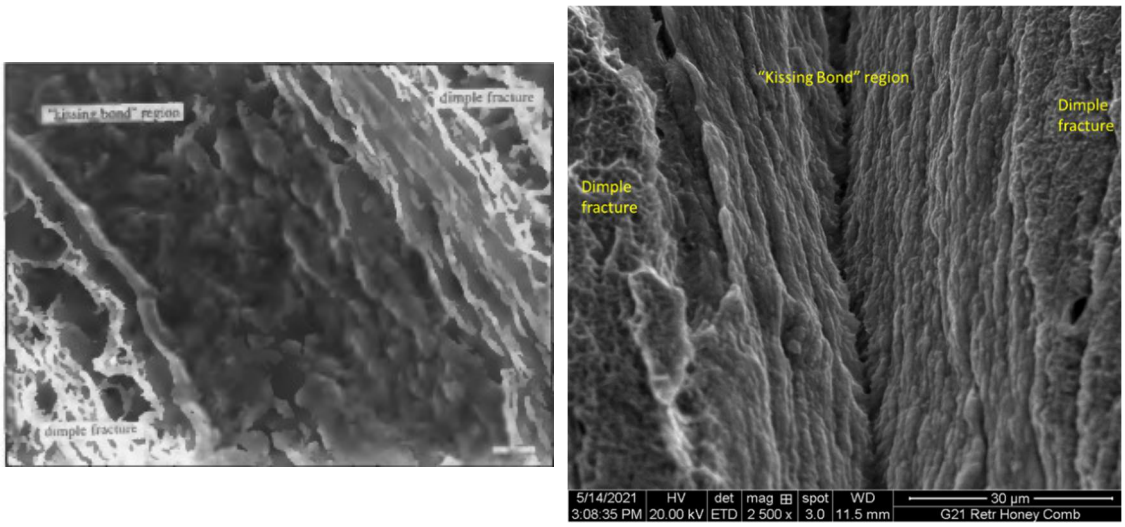

(a) (b)

Figure 182 – (a) Close-up of the kissing bond present in FSWed AA6082 (Oosterkamp et al 2014). (b) Kissing bond from G20/21 of this project.

Dimples were also visible in the SEM images presented in Figure 138 suggesting that the fracture was ductile. Following FSW these dimples, compared to those present in the PM, appear to remain equiaxed however each dimple appears to be smaller in size. As the fracture occurred in the SZ where the grains and precipitates have been refined it can be argued that the dimples, which form from micro voids produced by high plastic deformation (Halahan (1997)), are smaller in size as a result of the reduction in size of the particles and grains within the SZ.

The honeycomb feature was identified as being related to the probe profile. A rudimentary experiment was conducted whereby the probe was translated over putty, see Figure 139. Although not identical it can be seen that the shape is similar to that seen within the weld.

5.3 AA7050-T7451: Results Discussion

5.3.1 Microstructure

5.3.1.1 Effect of alloy composition on the microstructure

Both the parent and FS welded material used during this project were reviewed against several articles of previous work (such as Shahzad et al. (2010), Wang (2020) and Magalhães, Hupalo, and Cintho (2014)) which identified the material was similar in structure, this reiterated the conclusions from the OES (Table 44) and EDX (section 4.3.3.3) analysis that the alloy was as expected.

The images in Figure 183 show the microstructures of AA7010-T7451 and AA7050-T7451, the latter taken from the material used in this project. It is visible in both these images that there are sizeable grey/black particles within the elongated grains. Shahzad et al. (2010) qualified these as being 'constituent particles or inclusions of mainly two types: Mg_2Si and Al_7Cu_2Fe' and stated that the grains they resided in were elongated following recrystallization. Comparing the image by Shahzad et al. (2010) with the microstructure of the AA7050-T7451 in Figure 183b it is evident that the two alloys grain structures bear similarities with clusters of small grains being separated by elongated grains containing the inclusions Shahzad et al. (2010) discusses, although they are separated by variations in the quantity of copper and magnesium used.

Magalhães, Hupalo, and Cintho (2014) also describes, with the aid of the image in Figure 184a, the microstructure of AA7050-T7451. Magalhães et al. (2014) described the grain size distribution (which is similar to that of the material shown in Figure 184b albeit not as directional) as 'bimodal' with the grain size of the coarse and fine grains differing by a factor of 10. Magalhães et al (2014) also highlights the 'noticeable presence of a significant' amount of undissolved coarse intermetallic particles along the grain boundaries, shown in Figure 184b.

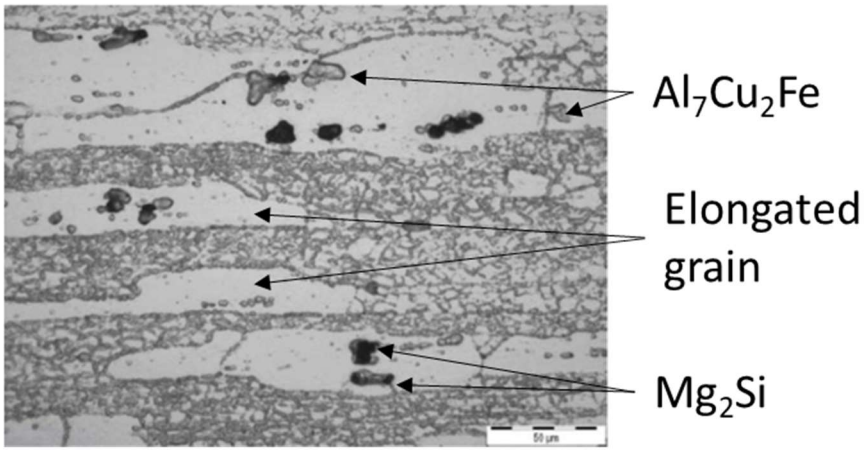

a)

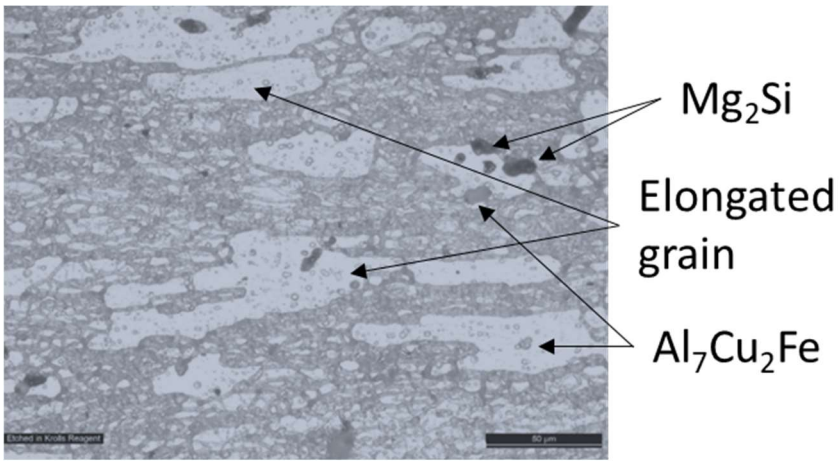

b)

Figure 183 – Optical microscopy of A) AA7010-T7451 showing constituent particles in the recrystallized grains (Shahzad et al. (2010)). B) AA7050-T7451 used in this project. Material etched in Krolls Reagent.

It is reported that these particles were observed as either insoluble iron-rich intermetallic Al_7Cu_2Fe or undissolved S phase (Al_2CuMg) or T phase ($Al_2Zn_3Mg_3$) (Fan et al. (2006)). EDX analysis, shown in Figure 160 to Figure 167, indicates that there are several instances of particles, ranging between 5-20 µm in size, that are rich in copper and iron. By referring back to literature such as Shahzad et al. (2010) and Magalhães, Hupalo, and Cintho (2014) this would suggest the formation of Al_7Cu_2Fe inclusions. Map and point analysis of the matrix, see Figure 170 and Figure 171, also indicates an abundant (albeit not visible) presence of copper, magnesium and zinc which Magalhães et al (2014) describe as dissolvable intermetallic phases consisting of η($MgZn_2$) and Cu-Mg enriched non-equilibrium aluminides. The solution heat

treatment temperature for plate AA7050-T7451 is 475 °C (ASM Handbook Comittee (1991)) which is lower than the temperature generated through FSW, as reported by Silva-Magalhães et al. (2019) this exceeds 500 °C. Therefore, elements including magnesium and zinc whose solubility in aluminium is achieved at below this temperature are likely to be in solution and will not form larger particles such as the constituents containing iron and copper.

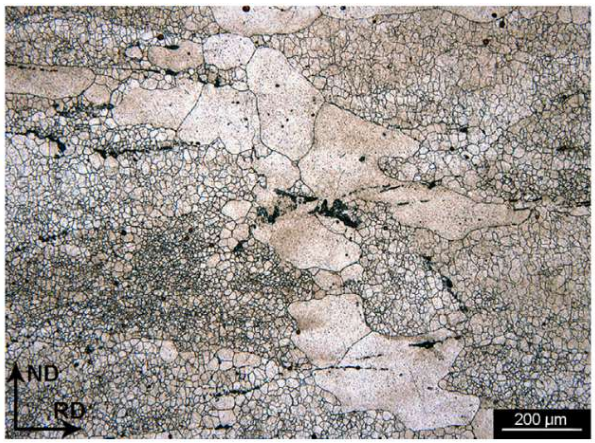

a)

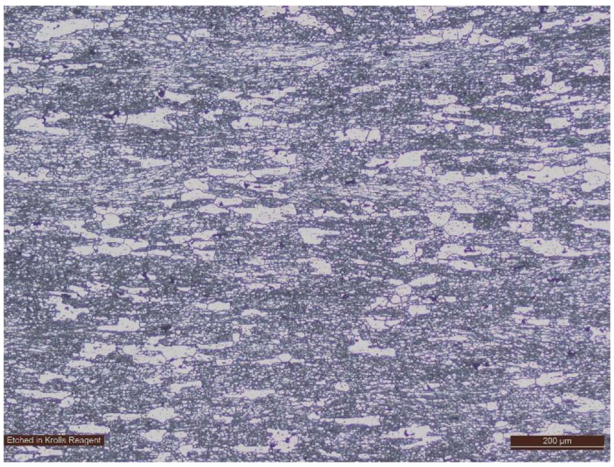

b)

Figure 184 - Optical micrographs showing the microstructure of AA7050 alloy in the as-received condition (T7451): (a) low magnification showing a bimodal grain size distribution from (Magalhães, Hupalo, and Cintho (2014)), and (b) AA7050-T7451 used in this project. Material etched in Krolls Reagent.

5.3.1.2 Effect of FSW technique and process parameters

The magnitude of the influence FSW has on the microstructure of AA7050-T7451 is dependent on the FS variant and process parameters. The macrographs of G03/04, G12 and G18, see Figure 151, Figure 152 and Figure 153, show the outline of the SZ is dependent on the profile of the probe. G03/04 and G12 use two half-length probes to produce a full penetration weld that resembles an hourglass shape, this is in comparison to the linear profile of the G18 SZ.

Banding is evident in all three welds, though it has been stated in section 4.3.3.1 that this is most prominent in G18. Although the onion layer effect is visible in both the WFW and SDS welds, it is most discernible in the SSS shown in Figure 153. J. H. Yan, Sutton, and Reynolds (2007) state that there is no direct evidence to clearly demonstrate the relationship between banding and FSW processing, however, Krishnan (2002) suggests that banding results from the process of frictional heating due to tool rotation so that tool translation extrudes the heated metal around to the retreating side of the tool. Cavaliere et al. (2004) and Ceschini et al. (2007), also, discuss how the flow behaviour of the plasticised material and the differences in dislocation density are responsible for this phenomenon.

Another feature of the microstructure is the transition between the refined, equiaxed grain structure of the SZ and the bimodal structure of the HAZ. This feature, shown in Figure 154, differs on the advancing (AS) and retreating (RS) sides. On the AS the shear resulting from the probes rotation is greater leading to a steeper transition. Also, as discussed previously by Silva-Magalhães et al. (2019) , the peak temperature occurs at the probe/shoulder interface at the rear of the retreating side which would mean this side of the weld would have a greater grain growth rate than the AS.

FSW has been widely recorded as refining and recrystallizing the grain structure of the SZ as well as generating a HAZ. The process parameters used during welding determine the energy input and deformation experienced by the material. This in turn impacts

grain growth and degree of recrystallization that occurs. It has been mentioned previously that the process parameters for G18, the SSS-FSW, were designed to preserve tool life as much as possible. This produced a 'very hot' weld, the result of which was a wide HAZ and more grain growth. The HAZ of G18 extends ~60mm from the centre of the weld which is twice the width of G03/04s HAZ (~30mm from centre of weld). The reduced traverse speed of G18 resulted in the probe lingering in the stirred material for longer, which in turn has meant the HAZ is wider and the grains in this region are larger due to the longer time taken to return to below 250 °C (the temperature exceeded to define a region as heat affected).

From Table 51 it was shown that the energy input of G12 was greater than a single pass of G03/04 and thermocouple data (see Appendix 53 to Appendix 55) gathered illustrates a higher surface temperature and longer time at ≥250 °C (the temperature the material must experience to be defined as the HAZ) were achieved also. Therefore, it was anticipated greater grain growth would occur for this weld. However, despite the elevated temperatures and longer time at this, G12s average distance between grain boundaries in the HAZ was smaller than that of G03/04. The times at which thermocouples 1 and 2 during G12 were held at ≥250 °C (71 s and 51 s respectively) was longer than that of the corresponding thermocouples for both passes of G03/04 (20 s and 27 s for G03 and 27s and 20 s for G04 respectively). It is concluded therefore that the greater energy input spread over two separate passes during G03/04 was more influential on the average distance between grain boundaries of the HAZ than the energy input simultaneously inputted during G12.

EDX analysis, shown in section 4.3.3.3, highlighted that post welding the particles present were consistent albeit reduced in size to those in the PM and those found by Wang (2020). In the WFW, Figure 164, this particle is 6.11 µm long while the area analysed in Figure 167 (Weld G12s upper pass) consisted of multiple smaller particles the longest measured was 1.99 µm. Both are considerably smaller to the particle analysed in Figure 160 which was recorded as 16.22 µm in length. Therefore, it is concluded that the probe rotation, which causes the deformation required for

recrystallization, is breaking up the particles present and distributing them throughout the SZ.

Both the as received and SDS samples also showed oxide particles present. However, unlike the small round oxide particles shown in Figure 160, Figure 167 and Figure 168 present a silica particle, similarly black in colour and 4.64 µm in size. As no stark differences were observed between the SZ and the PM in the as-welded condition, neither the HAZ nor naturally aged samples were investigated. It was deemed that any sizeable changes to the particles present was most likely to occur in the SZ and as this was not noted the HAZ would not be investigated.

5.3.2 Hardness

5.3.2.1 Effect of microstructure on the hardness

The hardness of the as-received AA7050-T7451 was shown to range between 150-180 HV0.5 with the softest region located at centre thickness. The reduction occurs between 18 and 28 mm from the bottom of the plate. This correlates to Figure 150 in section 4.3.3.1 which when overlayed with the hardness map (see Figure 176b) supports that the reduction in hardness corresponds to the change in microstructure. This has been considered a result of the manufacturing processes influence on the microstructure of the plate. The rolling required to form the plate means mechanical working is experienced by both top and bottom surfaces however the amount of mechanical working experienced by the centre of the plate is far lower. An additional factor is the time at which the material was held at temperature during this process. The material at centre thickness will retain the heat more so than the upper and lower surfaces which can dissipate to the surroundings. Unfortunately , it was not possible to image the strengthening precipitates found in AA7050-T7451, the size, fraction, and distribution of the which are expected to dominate the strength distribution (Kamp, Reynolds, and Robson (2009)). As such it is not possible to draw a definite conclusion regarding the underlying microstructural reasons for the observed hardness distribution. The grain structure is a secondary factor that contributes to

strengthening, and this discussion will focus on this aspect, since the grain structure was measurable using the techniques available in this research.

The Hall-Petch relationship implies that a reduction in average distance between grain boundaries results in an increase in hardness, this is demonstrated by Equation 3;

$$HV = HV_0 + \frac{k}{\sqrt{d}} \qquad \text{Equation 7}$$

Where HV_0 is a material constant, k is a strengthening constant and d is the average distance between grain boundaries.

In the HAZ the relationship between hardness and grain size adheres to Hall-Petch as the HAZ exhibits larger grains than the PM as well as reduction in the hardness. The HAZ is exposed to thermal damage from the welding process, however, the SZ is experiences both thermal and mechanical working resulting in an equiaxed and recrystallised grain structure which does not adhere to the Hall-Petch relationship compared to the as-received material.

The welded material is softest in each of the three welds at the interface between the TMAZ and HAZ. In this region the grain structure is elaborate, as demonstrated in Figure 154. Elongated, fine equiaxed and sub-grains are all present within the interface. EBSD conducted by Lin et al. (2019) on FS welded 12 mm thick 7N01 highlights the stark difference in a similar grain structure at the interface. The temperature and strain the TMAZ experiences are dependent on the distance from the SZ which results in an 'inhomogeneous' microstructure in this zone, as illustrated in Figure 185. The hardness at this region is labelled 'Hardness minima' by Lin et al (2019), which is attributed to the reduction in high angle grain boundaries compared to the SZ.

The hardness plots shown in Appendix 56 and Appendix 57 indicate that the welded material adhered to a 'W' shape, a characteristic that is widely seen in literature including Canaday et al. (2013); Zhou et al. (2016). The TMAZ and HAZ were softer than the SZ which recovered the greatest hardness of the welded zones. The softness of the TMAZ and HAZ is consistent with precipitate coarsening being a dominant feature while the SZ hardness was augmented by the deformation structure produced by the mechanical stirring from the probe (Threadgill et al. (2009)).

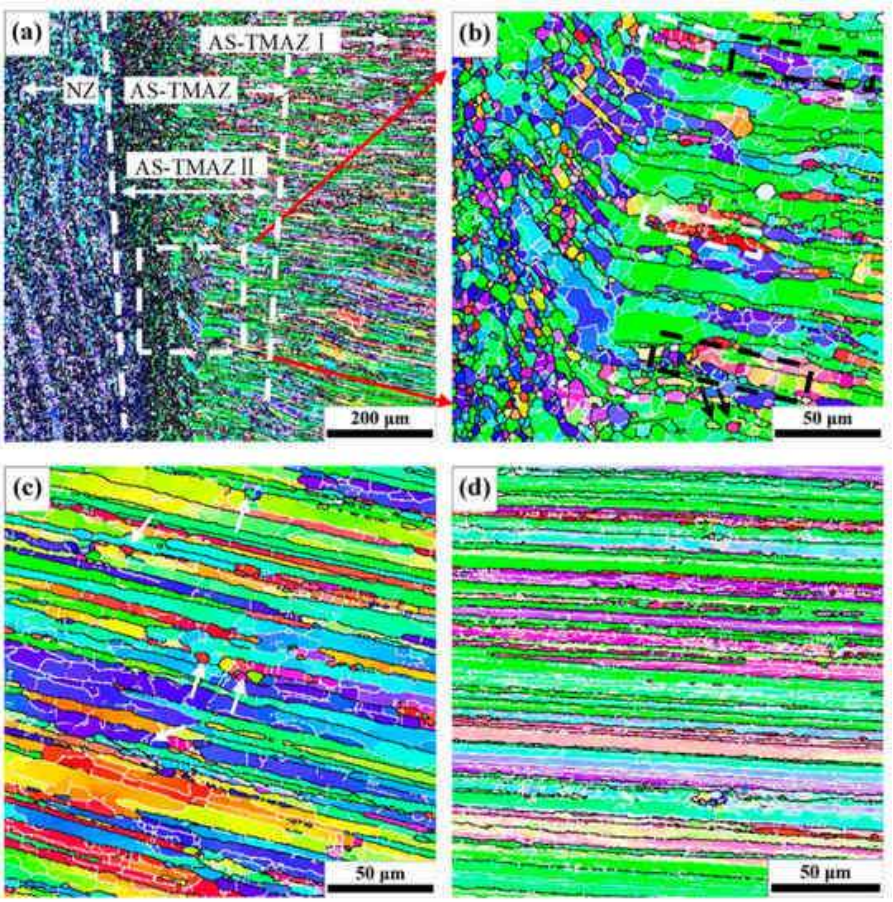

Figure 185 - EBSD orientation maps of TMAZ and HAZ for FS welded AA7N01: (a) NZ/AS-TMAZ; (b) AS-TMAZ II; (c) AS-TMAZ I; (d) HAZ at hardness minima. (Lin et al. (2019)).

5.3.2.2 Effect of FSW technique and process parameters

Process parameters have a substantial influence on the hardness. The energy input determines not only the width of the TMAZ/HAZ (the hardness minima) but also the retention of hardness across the multiple zones. For the weld G03/04 the total energy input was larger than that of G12, however, the individual energy inputs for each pass of the WFW were not as great as the energy input for the simultaneous passes of G12. Consequently, the HAZ of G03/04 was narrower than in G12, extending no more than ~30 mm from the centre of the weld. The inverse correlation between energy input and hardness is further supported in G18 (the weld with the greatest energy input). Here the HAZ extends ~60 mm from the centre of the weld and the weld retains as little as 45-50% that of the PM at hardness minima.

The tool profile is also influential on the hardness, effecting through thickness variation. G03/04 and G12 both use two tapered, half-length probes which produced an hourglass SZ which causes a variation in hardness through the thickness of the material. Reviewing the hardness map of G03/04 in Figure 177 shows that the between -20 and +20 mm from the centre of the weld (the maximum width of the SZ), the weld regions present are SZ and HAZ which leads to this through thickness variation in hardness. This can be compared with G18 (Figure 179) which used a linear probe and although there is some variation due to heat transfer through the material as well as the thread on the probe determining flow direction, the variation is minimal through the thickness of the material and therefore identifies the probe profile as an influencing factor on the nature of the hardness in the weld. G18 was produced as a 'hot' weld due to the desire to preserve tool life as much as possible in this relatively untested technique by reducing the torque and bending stresses the probe would experience. As such the HAZ is significantly larger than that of the WFW and SDS-FSW methods. The HAZ stretches almost the full width of the tested sample, although the hardness at 40 mm away from the centre of the weld was ~130 HV (72% retention of the PM). At the same distance from the centre of the weld, the WFW-FSW hardness was ~160-170 HV and the SDS-FSW hardness was ~150-160 HV. Therefore, the additional heat experienced by the material during the SSS-FSW negatively influenced

the hardness of the material, however it still retained a high percentage of the PM value.

5.3.2.3 Effect of natural ageing on the hardness

Natural ageing was shown to have a positive effect on the microhardness of the FS welded material. After 6 months the hardness of both G03/04 and G12 was shown to have increased (demonstrated in Appendix 47 and Appendix 52). Literature suggests that during natural ageing precipitates (which coarsen during the FSW process) grow which results in an increase in hardness (Anderson, Weritz, and Kaufman (2018)). Once the final ageing period of 18 months was complete it was recorded that the single processed SZ of G03/04 had a hardness of 150-160 HV (an increase of ~10 HV vs the as-welded material), an increase that was also seen in G12.

Natural ageing also had the effect of 'shrinking' the HAZ. In G03/04, it has already been stated that the HAZ extended 30 mm from the centre of the weld. However, after 18 months natural ageing the HAZ had reduced in size by a total of ~5-10 mm. A similar trend was observed in the G12 samples. Fuller et al. (2010) explain that the HAZ hardens over time due to the precipitation of GP (II) zones and η' precipitates which strengthen the alloy. In this instance it can be argued that the relationship between hardness and grain size in proportional and as such the Hall-Petch relationship is not adhered. This contrasts with the as-welded material which suggests the HAZ adheres to the relationship, as outlined in section 5.3.2.1.

The phenomenon 'over ageing' was not observed during natural ageing investigation. Between the final two time periods, 12 and 18 months, the material further increased in hardness. Literature has suggested that the material will not overage for 'several years' suggesting that the alloy would continue to harden after this project is complete (Totten (2016)). Dong, Zhang, and Luan (2014) illustrate that after 17, 520 hours (equivalent to 730 days) 'the microhardness values were 60 MPa higher in the nugget zone and thermal-mechanical-affected zone in the joint' than after 72 hours (or 3 days)

natural ageing. This would reaffirm the view that over ageing did not occur during this project.

5.3.3 Tensile properties

5.3.3.1 Effect of microstructure on the tensile properties

The tensile properties of the FS welded AA7050-T7451 are influenced by the microstructure. Across the transverse plane of the weld, the microstructure is inconsistent varying from a bimodal PM, coarsened bimodal HAZ and a refined equiaxed SZ. G03/04 failed consistently from retreating side TMAZ/HAZ interface (which the hardness data indicated was the softest region, and therefore the predicted failure site) through to the retreating side interface of the second pass, failing through the narrow double processed region at the tip of the two passes. The retreating side interface has a shallower gradient from the SZ to the HAZ (Prangnell and Heason (2005)) (as depicted in Figure 154a) which contains fewer high angle grain boundaries resulting in easier dislocation paths than on the advancing side. This would require EBSD to validate for this project, however, this was not possible during the project.

Another effect of the microstructure is the correlation between the average distance between grain boundaries and the yield strength of the material which correlates to the Hall-Petch relationship, this is also true with regards to the UTS. The tensile data presented in Table 47 and Figure 173 shows that G03/04 had the highest yield and UTS of the two welds (330 MPa and 419 MPa compared to G12 – 297 MPa and 352 MPa respectively) but also a smaller HAZ average distance between grain boundaries than G12.

5.3.3.2 Effect of FSW technique and process parameters

The tensile data shown indicates that a larger single energy input reduces the strength of the weld to a greater extent than a total energy input comprising of two lesser amounts. G12 was shown to retain 66% the strength of the PM, unlike G03/04 (78%)

and although the energy input in G12 (6.31 kJ/mm) is much lower than the total energy input of G03/04 (9.48 kJ/mm) it is inputted in a single, albeit two probe pass, meaning the weld is hotter. This led to a wider HAZ, the most susceptible zone to tensile failure.

The probe profile has affected the failure path, particularly in G03/04. From the failed tensiles captured in Appendix 39 the fracture path in G03/04 follows the edge of the retreating side of the probe, as discussed in section 5.3.3.1. However, in G12 the fracture path progresses through the SZ (slightly on the advancing side) of the upper pass before diverging towards the retreating side of the lower pass, see Appendix 40. This weld had significant skewing, demonstrated by Figure 152, of the lower probe (the leading probe) and the hardness map (see Figure 178) shows the softest region of the weld was adjacent to the tip of the lower probe and is likely the site of failure. The profile of the probe and the process parameters selected appear to have a significant effect on the tensile properties and fracture path of the FS welded material. The retention success of the weld is dependent on the EI as is the level of skewing between the probes which in turn impacts upon the fracture path.

5.3.3.3 Effect of natural ageing on the tensile properties

There was a positive effect on the tensile properties of the welded material when naturally aged. As per section 3.4 natural ageing was conducted for periods of 6, 12 and 18 months. During 18-months of natural ageing the UTS of G03/04 increased by 44 MPa meaning the strength of the alloy increased to 86% from 78% that of the PM. This exceeds the expectation of Anderson, Weritz, and Kaufman (2019) which states that the weld heat affected zone can age harden up to 80% that of the PM. Anderson et al (2019) discusses the effects of natural ageing with respect to fusion welding and therefore the retention of strength in the alloy in the as-welded condition is far lower than that of FSW.

In 7xxx alloys, natural ageing is not commonly used as a hardening method due to the unstable nature of the strength increase over a lengthening time period. As shown both G03/04 and G12 continued to return to pre-weld levels of strength however as the rate is unstable these alloys are more commonly artificially aged to produce a stable temper.

5.4 Sample defects

During the production of the welds there were several issues such as void production, blistering and tool failure that impacted on the quality of the samples. The production of voids can occur due to several factors (Threadgill et al. (2009)) such as such as the material not being clamped sufficiently, however in the case of the voids present in welds G19, G20/21 and G34 (see Figure 86, Figure 111 and Figure 116) a lack of consolidation was the cause of the voids produced. A lack of consolidation is a consequence of welding 'too cold' either by having a traverse rate that is too great or not having a large enough rotational speed. This can cause insufficient flow resulting in voids emerging near the edge of the SZ (Zeng et al. (2018)).

Blistering on the surface of the weld, demonstrated in Appendix 58, was another issue encountered, though only on the back-up WFW in AA7050. During the production of the back-up material the tip of the probe broke away, lodging in the material. This reduced the probe length from 28.70 mm to 27.97 mm resulting in a difference between the intended and actual plunge depth which was to be maintained by the software used and as such resulted in changes being made during welding that caused the blistering on the surface. This had minimal impact on the project as the material was to be used as 'back-up' to the material investigated however the tensile properties of this material would have been negatively influenced by the defect due to the creation of stress concentrations.

Another defect encountered in this project was probe failure during the SSS-FSW of AA7050-T7451, or weld G18. The probe failed within the material due to excessive

stresses acting on the length of the probe. The stresses exceeded the upper limit for the MP159 alloy tool and caused the tool to snap within the material. Consequently, the amount of welded material available for this weld was greatly limited and testing including tensile and natural ageing were both forfeited.

5.5 Industrial suitability

The results presented in section 4 allow for assessment of the welding variants industrial suitability's. Table 52 summaries the suitability of the processes for specific industrial needs including mass manufacturing components and components that require a high degree of property retention. Where the need is to manufacture a one-off or handful of components, WFW is an excellent choice. The machinery required is the simplest of the three variants, the weld properties are not significantly lower than the PM and as the production is of a low quantity of parts, the slower manufacturing time is not a key factor. This variant would be recommended for each of the three grades of alloy in this scenario as WFW performed in AA5083 and AA7050 and with more appropriate parameters would be a better choice in AA6082 also.

SDS has been shown to be an effective process and arguably the most appropriate for a wide range of industrial uses. In non-heat treatable AA5083 the process is not only greener but also retains higher strength than WFW. The retention of strength in SDS in heat-treatable alloys is not as high as that in WFW, however, coupled with the other benefits, such as faster production time and lower energy input, can be considered the most industrially suitable variant for heat treatable alloys AA6082 and 7050.

SSS was an exploratory technique which has indicated potential benefits in AA6082, though both WFW and SDS have better tool life due to the lower stresses experienced by the half-length probes. This is an important consideration when selecting a variant for large scale production. In both AA5083 and AA7050 probe failure occurred due to excessive bending stresses, indicating that this process may not be suitable for industrial use in these alloys at this thickness. It would therefore be recommended

that either WFW or SDS be selected for joining 50 mm aluminium alloys, depending on the scale of production required, as indicated by Table 52.

Aluminium alloy	FSW variant	Industrial need		
		One-off part	Mass production	High retention of properties
AA5083-H111	WFW	✓		✓
	SDS		✓	✓
	SSS			
AA6082-T651	WFW	✓		✓
	SDS		✓	✓
	SSS			
AA7050-T7451	WFW	✓		✓
	SDS		✓	✓
	SSS			

Table 52 - Summary of welding variants industrial suitability.

5.6 Summary Discussion

During the investigation it was found that the Simultaneous Double-Sided (SDS) technique was the best suited to industrial applications where fast production speed and good retention of mechanical properties were desired. In all three materials the SDS welds were produced in the shortest time, approximately 50% the welding time of the Weld-Flip-Weld (WFW) which negates the additional time between WFW welds to machine and clamp the sample resulting in a complete manufacturing time more than double that of SDS. Furthermore, the SDS weld retained 101%, 61% and 66% of the tensile strength of the parent material in each of AA5083-H111, AA6082-T651 and AA7050-T7451 respectively. Although this is not the strongest weld in all three materials, the retention coupled with weld speed and energy input make the process a desirable method for joining 50mm aluminium alloys.

A trend noted in the heat-treatable alloys, AA6082-T651 and AA7050-T7451, was the correlation of energy input and width of the Heat affected Zone (HAZ). Although the energy input of the combined passes for WFW was greater than that of the SDS process, the simultaneous nature of the process meant a greater energy input was generated at any given moment meaning a higher temperature occurred, as supported by Appendix 53 to Appendix 55. The higher temperatures resulted in greater HAZ width which is supported by the hardness data presented in sections 4.2.4.2 and 4.3.4.2. In G03/04, WFW of AA7050-T7451, the HAZ width was no greater than 60 mm, however, in G12 (the SDS weld in the same alloy) was approximately 80 mm in width. This trend was not noted in AA5083-H111 (the non-heat treatable alloy) suggesting that the heat generated by a greater energy input had a limited impact on this alloy, though a reduction in hardness was noted the width of the HAZ was not clearly defined as per section 4.1.4.2.

Failure location during tensile testing was another trend observed. In the non-heat treatable AA5083-H111 the samples failed, unless a defect such as a void was present, away from the stir zone between the HAZ and the parent. The weld retention in G07/08 and G13 (two defect free welds) was 93 and 101% respectively and both welds failed either in the parent or the HAZ/parent interface, as demonstrated by Appendix 18 and Appendix 19. Conversely, the heat-treatable alloys, AA6082 and AA7050, both tended to fail between the stir zone (SZ) and HAZ interface, unless a defect was detected. Although there was no correlation between failure and the advancing or retreating sides of the weld both materials failed along the interface between the SZ and the HAZ which was shown to be the softest region in the hardness data presented in sections 4.2.4.2 and 4.3.4.2.

6 Conclusion

This chapter summaries the findings of this project, the limitations encountered and recommends future work that would benefit this project.

6.1 Findings

This research set out to investigate the influence of three Friction Stir Welding (FSW) variants namely, Weld-Flip-Weld (WFW), Simultaneous Double Sided (SDS) and Supported Stationary Shoulder (SSS) in 50mm thick AA5083-H111, AA6082-T651 and AA7050-T745, determining the microstructural and mechanical changes the processes induce.

6.1.1 Material AA5083-H111

The following conclusions have been made with regards to the influence of FSW on the microstructural and mechanical properties of 50 mm thick AA5083-H111.

- The SDS process produced a stronger weld than the other two processes. The weld G13 failed at 298 MPa, the only weld with a strength greater than the parent material (296 MPa).
- The hardness map of G13 demonstrates a better retention of hardness than is evident in the hardness map of either G07/08 or G34.
- The grain structure of the stir zone was equiaxed and recrystallised whereas the HAZ was bimodal and the grains were elongated, something reaffirmed by literature.
- A positive correlation showing the effects of energy input on grain size was recorded. G13, the SDS weld, used the lowest energy and displayed the smallest grain structure which contrasted with G34, the SSS weld, which used the largest energy input and displayed the largest grains of the three welds.

- Welds in AA5083 also correlated to the Hall-Petch relationship suggesting that the average distance between grain boundaries determined the strength of the alloy rather than the particles present.
- Voids were generated in G34 due to a lack of consolidation, which impacted on the failure location and performance of the tensile properties.
- The above conclusions identify Simultaneous Double Sided (SDS) as the most appropriate process for industrial application for 50mm thick AA5083-H111.

6.1.2 Material AA6082-T651

Welds were manufactured in AA6082-T651 to determine the influence of the three FSW variants discussed throughout this research. The below conclusions have been made based on the microstructural and mechanical properties identified.

- Full penetration was achieved in G22 using just 4.77 kJ/mm energy input – the lowest energy required of the six welds produced.
- A chip lack of fill defect was observed in the upper pass of G20/21. This defect impacted on the mechanical performance of the weld and caused tensile failure to occur within the SZ.
- The primary particles in the welds, though approximately 3 µm smaller, were consistent with those of the parent material. Mg_2Si and α-$Al_{12}(Fe, Mn)_3Si$ were both confirmed by literature as these particles in AA6082-T651.
- Of all three materials investigated, the SSS process was most successful in AA6082-T651 producing three welds with no voids and good strength retention.
- The four SSS variations suggest that the different probe designs did not influence the mechanical properties by such an extent that the design of the probe is a significant concern.

- Only one SSS weld in AA6082, G19, contained a void caused by a lack of consolidation which would suggest that this probe design would require a greater energy input to ensure consolidation of the stirred material.

Based on the conclusions outlined in this section, the Simultaneous Double Sided (SDS) technique is most industrially applicable for 50mm thick AA6082-T651. Similar to its performance in other materials, the process used lower energy and manufactured the weld in a shorter time period. Further conclusions supporting the view SDS is the most industrially applicable are detailed below:

6.1.3 Material AA7050-T7451

Three welds were manufactured in AA7050-T7451 using three different FSW techniques and subsequently tested and analysed as per testing methods in section 3. The below conclusions have been made as a result.

- WFW produced the strongest weld (419 MPa) and retained the best hardness properties of any of the welds in AA7050-T7451.
- Using simultaneous probes reduced manufacturing time by greater than 50% compared to WFW.
- SDS required the lowest energy input (6.31 kJ/mm) of the three techniques examined in the study.
- Natural ageing had a positive impact on the performance tensile and hardness properties of the samples. Where the stir zone was single processed, hardness returned to as-received standards. This impact was confirmed by literature in thin section samples of the same alloy grade.
- AA7050-T7451 displayed an adherence to the Orowan mechanism, converse to the relationship demonstrated in AA5083, indicating that the precipitates were more influential in this alloy than the grain size. It was unlikely that only one of Orowan and Hall-Petch was present and therefore it is concluded that the non-

or heat-treatable nature of the alloy determined which mechanism was most prominent.

- Using the SSS technique would not be recommended due to failure of probe during weld and poor hardness properties.

Following the conclusions outlined in this section the most suitable FSW technique for joining 50 mm thick AA7050-T7451, on a large industrial scale, was determined to be Simultaneous Double Sided (SDS), though Weld-Flip-Weld (WFW) would also be suitable for limited production.

6.1.4 Parameter selection

Optimisation of the parameters was not part of this study. The parameters that were used were not optimal which in three welds (G20/21, 19 and 34) led to void production. These welds used parameters that were at the upper limit of the working envelope. Parameter optimisation has been recommended as a potential future work topic.

6.2 Future work

6.2.1 Repeating weld analysis

Repeating the welds would give further validity to the test results and would allow for minor corrections to accommodate a reduction in the presence of voids. In addition to repeating the testing already undertaken, further methods of testing, such as those discussed in 6.2.3 and 6.2.4, could also be explored by repeating the welds and increasing the amount of material available. This would provide a more in-depth review of the performance of the weld and the effects of FSW on the microstructure.

6.2.2 Parameter optimisation

Optimising the process parameters would remove the presence of voids and would provide insight into the optimal mechanical properties that could be provided to industrial consumers. Such optimisation would include the WFW manufactured in AA6082-T651. Here the sizeable void within the stir zone impacts the tensile properties greatly. By optimising this weld it would be possible to analyse the tensile strength of a successful weld.

6.2.3 Corrosion and fatigue testing

Corrosion and fatigue properties are highly sought after in marine and aerospace industries (the industries thick section FSW is attracting interest from). Conducting corrosion testing using salt water to British Standard BS EN ISO 16701:2008 would provide industry with a greater understanding of the process and allow them to consider the use of FSW in 50mm thick aluminium. Similarly, fatigue testing would be a beneficial analysis method for understanding how the welded material performs in a service environment. Fatigue testing could be conducted to BS ISO 23296:2022.

6.2.4 Further microstructural analysis

Further microstructural characterisation using EBSD analysis reviewing the effect of the FSW process on the angle of the grain boundaries, particularly at the interface between the SZ and the HAZ, as well as the degree of refinement within the SZ would have provided greater insight into the influence FSW has on the microstructure and subsequently the mechanical properties. TEM analysis would also provide greater insight into the influence of the welding method on the microstructure of the material. TEM could be used to analyse the strengthening precipitates that are not visible through the use of a scanning electron microscope and therefore provide more depth to the understanding of how the material retains strength as well as the impact natural ageing has on the strengthening precipitates in AA7050-T74151.

6.2.5 Post weld heat treatment

Another avenue for exploration would be to investigate the effects of heat treatment on post welded material. During this project natural ageing was investigated over periods of 6, 12 and 18-months. The result of which was an increase in strength and hardness from the as-welded condition. It would be of interest to conduct heat treatment post welding to investigate if the improvement in properties is replicated or even further enhanced beyond natural ageing. A series of different tempers would be used to investigate the effect of heat treatment on mechanical properties.

7 References

Alexander, D. T. L., and A. L. Greer †. 2004. 'Nucleation of the Al_6 (Fe, Mn)-to-α-Al–(Fe, Mn)–Si Transformation in 3XXX Aluminium Alloys. II. Transformation in Cast Aluminium Alloys'. *Philosophical Magazine* 84 (28): 3071–83. https://doi.org/10.1080/14786430410001701788.

Al-Fadhalah, Khaled, and Fahad Asi. 2018. 'Aging Behavior of Aluminum Alloy 6082 Subjected to Friction Stir Processing'. *Crystals* 8 (9): 337. https://doi.org/10.3390/cryst8090337.

Altenpohl, Dieter G. 1982. *Aluminium Viewed from within: An Introduction into the Metallurgy of Aluminium Fabrication*. 1st edition. Düsseldorf: Aluminium-Verlag.

Alumeco. n.d. 'Temper Designations'. Alumeco - Knowledge & Technique. Accessed 2 December 2021. https://www.alumeco.com/knowledge-technique/aluminium-data/temper-descriptions.

'Aluminum 6082-T6'. n.d. Matweb.Com/Aluminiumalloys. Accessed 3 October 2019. http://www.matweb.com/search/datasheet_print.aspx?matguid=fad29be6e64d4e95a241690f1f6e1eb7.

'Aluminum 7075-T6; 7075-T651'. n.d. Matweb.Com/Aluminiumalloys. Accessed 3 February 2021. http://www.matweb.com/search/DataSheet.aspx?MatGUID=4f19a42be94546b686bbf43f79c51b7d.

'Aluminum 7475-T7351'. n.d. Matweb.Com/Aluminiumalloys. http://www.matweb.com/search/DataSheet.aspx?MatGUID=92620a0b7b9a44fcb34799eda01d2b18.

Amini, A., P. Asadi, and P. Zolghadr. 2014. 'Friction Stir Welding Applications in Industry'. In *Advances in Friction-Stir Welding and Processing*, 671–722. Elsevier. https://doi.org/10.1533/9780857094551.671.

Andersen, S J, H W Zandbergen, J Jansen, C TRáHOLT, U Tundal, and O Reiso. 1998. 'THE CRYSTAL STRUCTURE OF THE B0 PHASE IN Al±Mg±Si ALLOYS', 16.

Andersen, Sigmund J., Calin D. Marioara, René Vissers, Malin Torsæter, Ruben Bjørge, Flemming J.H. Ehlers, and Randi Holmestad. 2010. 'The Dual Nature of Precipitates in Al-Mg-Si Alloys'. *Materials Science Forum* 638–642 (January): 390–95. https://doi.org/10.4028/www.scientific.net/MSF.638-642.390.

Anderson, Kevin, John Weritz, and J. Gilbert Kaufman, eds. 2018a. 'Friction Stir Welding of Aluminum Alloys'. In *Aluminum Science and Technology*, 748–62. ASM International. https://doi.org/10.31399/asm.hb.v02a.a0006500.

———, eds. 2018b. 'Metallurgy of Heat Treatable Aluminum Alloys'. In *Aluminum Science and Technology*, 411–37. ASM International. https://doi.org/10.31399/asm.hb.v02a.a0006509.

———, eds. 2019a. '7 *Xxx* Aluminum Alloy Datasheets'. In *Properties and Selection of Aluminum Alloys*, 410–12. ASM International. https://doi.org/10.31399/asm.hb.v02b.a0006726.

———, eds. 2019b. 'Aluminum Structural Design'. In *Properties and Selection of Aluminum Alloys*, 19–32. ASM International. https://doi.org/10.31399/asm.hb.v02b.a0006486.

Andrews, Dick, and Horrex. 2013. 'Tool Performance and Lifetime When Friction Stir Welding High Strength Aluminium Alloys'. https://www.twi-

global.com/technical-knowledge/industrial-member-reports/fsw-tool-performance-and-lifetime-in-high-strength-aluminium-1007-2012/.
Arbegast, William, J. 2003. 'Week 6: Friction Stir Joining: Characteristic Defects'. MET 492-Special Topics Friction Stir Processing, South Dakota School of Mines and Technology.
ASM Handbook Comittee. 1991. 'Heat Treating of Aluminum Alloys' 4: 841–79. https://doi.org/10.1361/asmhba0001205.
'ASM Material Data Sheet - AA5083-O'. n.d. Accessed 9 July 2019. http://asm.matweb.com/search/SpecificMaterial.asp?bassnum=MA5083O.
'ASM Material Data Sheet - AA7050-T7451'. n.d. Accessed 9 July 2019. http://asm.matweb.com/search/SpecificMaterial.asp?bassnum=MA7050T745.
Benedyk, J. C. n.d. '6061'. In *Aerospace Structural Materials Handbook*, Section 1.5.7:8. CINDAS.
Bergman, G., J. L. T. Waugh, and L. Pauling. 1957. 'The Crystal Structure of the Metallic Phase Mg32(Al, Zn)49'. *Acta Crystallographica* 10 (4): 254–59. https://doi.org/10.1107/S0365110X57000808.
Biallas, G, R. Braun, C Dalle Donne, G Staniek, and W.A Kaysser. 1999. 'Mechanical Properties and Corrosion Behaviour of Friction Stir Welded 2024-T3'. In *Weld Performance*. Thousand Oaks, California, USA: TWI, Abington.
Bigot, Annabelle, Pierre Auger, Sylvain Chambreland, Didier Blavette, and Andrew Reeves. 1997. 'Atomic Scale Imaging and Analysis of T' Precipitates in Al-Mg-Zn Alloys'. *Microscopy Microanalysis Microstructures* 8 (2): 103–13. https://doi.org/10.1051/mmm:1997109.
Birol, Yucel, Onur Ilgaz, Seracettin Akdi, and Erdem Unuvar. 2014. 'Comparison of Cast and Extruded Stock for the Forging of AA6082 Alloy Suspension Parts'. *Advanced Materials Research* 939 (May): 299–304. https://doi.org/10.4028/www.scientific.net/AMR.939.299.
Braga, D.F.O., A.C.F. da Silva, and P.M.G.P. Moreira. 2014. 'Mechanical Properties'. In *Advances in Friction-Stir Welding and Processing*, 141–97. Elsevier. https://doi.org/10.1533/9780857094551.141.
Brooks, George. H. 2018. 'A Study into the Impact of Corrosion on the Efficacy of Double Sided Friction Stir Welding in 50mm Thick Aluminium Alloy 7050-T7451'. Undergraduate Dissertation. Sheffield: Sheffield Hallam Univeristy.
Brush Wellman Inc. 2010. 'Strain Hardening & Strength'. *Technical Tidbits*, 2010.
Bucci, R.J. 1979. 'Selecting Aluminum Alloys to Resist Failure by Fracture Mechanisms'. *Engineering Fracture Mechanics* 12 (3): 407–41. https://doi.org/10.1016/0013-7944(79)90053-5.
Cáceres, C. H., I. L. Svensson, and J. A. Taylor. 2003. 'Strength-Ductility Behaviour of Al-Si-Cu-Mg Casting Alloys in T6 Temper'. *International Journal of Cast Metals Research* 15 (5): 531–43. https://doi.org/10.1080/13640461.2003.11819539.
Callister, William D. 2005. *Fundamentals of Materials Science and Engineering: An Integrated Approach*. 2. ed. Hoboken, NJ: Wiley.
———. 2007. *Materials Science and Engineering: An Introduction*. 7th ed. New York: John Wiley & Sons.
Callister, William D., and David G. Rethwisch. 2008. *Fundamentals of Materials Science and Engineering: An Integrated Approach*. 3rd ed. John Wiley & Sons.
———. 2014. *Materials Science and Engineering: An Introduction*. 9th edition. Hoboken, NJ: Wiley.

Canaday, Clinton T., Matthew A. Moore, Wei Tang, and A.P. Reynolds. 2013. 'Through Thickness Property Variations in a Thick Plate AA7050 Friction Stir Welded Joint'. *Materials Science and Engineering: A* 559 (January): 678–82. https://doi.org/10.1016/j.msea.2012.09.008.

Cater, Stephen. 2020. 'TWI Core Research Programme, Project No 30146, 2020'. 30146. Sheffield: TWI Ltd.

Cater, Stephen, Dick Andrews, and TWI Ltd. 2014. *Fundamentals of Friction Stir Welding*.

Cater, Stephen, and George. H Brooks. 2020. 'Establishing Baseline FSW Data for Aluminium Alloys up.Pdf'. *Welding and Cutting* 19 (3): 216–18.

Cater, Stephen, and TWI Ltd. 2018. *An Overview of Friction Stir Welding (Internal Use Only)*. 2nd ed.

Cavaliere, P, E Cerri, L Marzoli, and J Dos Santos. 2004. 'Friction Stir Welding of Ceramic Particle Reinforced Aluminium Based Metal Matrix Composites'. *Applied Composite Materials* 11: 247–58.

Cederqvist, L., C. D. Sorensen, A. P. Reynolds, and T. Öberg. 2009. 'Improved Process Stability during Friction Stir Welding of 5 Cm Thick Copper Canisters through Shoulder Geometry and Parameter Studies'. *Science and Technology of Welding and Joining* 14 (2): 178–84. https://doi.org/10.1179/136217109X400420.

Ceschini, L., I. Boromei, G. Minak, A. Morri, and F. Tarterini. 2007. 'Microstructure, Tensile and Fatigue Properties of AA6061/20vol.%Al2O3p Friction Stir Welded Joints'. *Composites Part A: Applied Science and Manufacturing* 38 (4): 1200–1210. https://doi.org/10.1016/j.compositesa.2006.06.009.

Chan, Kwai S. 2010. 'Roles of Microstructure in Fatigue Crack Initiation'. *International Journal of Fatigue*, 20.

Chen, Y, H Ding, J Li, Z Cai, J Zhao, and W Yang. 2016. 'Influence of Multi-Pass Friction Stir Processing on the Microstructure and Mechanical Properties of Al-5083 Alloy | Elsevier Enhanced Reader'. *Materials Science and Engineering A* 650: 281–89. https://doi.org/10.1016/j.msea.2015.10.057.

Cheng, W, and I Finnie. 1990. 'The Crack Compliance Method for Residual Stress Measurement'. *Weld World* 28 (5): 103–10. https://doi.org/10.1080/13621718.2017.1377335.

Chowdhury, S.M., D.L. Chen, S.D. Bhole, and X. Cao. 2010. 'Tensile Properties of a Friction Stir Welded Magnesium Alloy: Effect of Pin Tool Thread Orientation and Weld Pitch'. *Materials Science and Engineering: A* 527 (21–22): 6064–75. https://doi.org/10.1016/j.msea.2010.06.012.

Colligan, K.J. 2010. 'Solid State Joining: Fundamentals of Friction Stir Welding'. In *Failure Mechanisms of Advanced Welding Processes*, 137–63. Elsevier. https://doi.org/10.1533/9781845699765.137.

Columbia, University of British, Carleton University, Twitter Twitter, and LinkedIn LinkedIn. n.d. 'Key Properties and Effects of Common Steel Alloying Agents'. ThoughtCo. Accessed 4 June 2020. https://www.thoughtco.com/common-steel-alloying-agents-properties-and-effects-2340004.

'Conductive Heat Transfer'. n.d. Accessed 23 February 2019. https://www.engineeringtoolbox.com/conductive-heat-transfer-d_428.html.

'Crystal Structures of Metals | Chemistry for Non-Majors'. n.d. Accessed 21 May 2019. https://courses.lumenlearning.com/cheminter/chapter/crystal-structures-of-metals/.

Dawood, Hasan I., Kahtan S. Mohammed, and Mumtaz Y. Rajab. 2014. 'Advantages of the Green Solid State FSW over the Conventional GMAW Process'. *Advances in Materials Science and Engineering* 2014: 1–10. https://doi.org/10.1155/2014/105713.

De Backer, Jeroen. 2014. 'Feedback Control of Robotic Friction Stir Welding'. Trollhättan: University West.

Deveci, Murat. n.d. 'Residual Stresses Are Spontaneously in Equilibrium as Tensile Residual Stresses (Detrimental) and Compressive Residual Stresses (Beneficial). For Example, a Surface Formed in Tensile Stresses Will Comprise Compressive Residual Stresses, and a Surface Formed in Compressive Stresses Will Contain Tensile Residual Stresses.', 2.

Dilger, Daniel. 2013. 'Apple Slims down IMac 40% with "friction-Stir Welding" & Ditching the Disc Drive'. Apple Insider. 2013. https://appleinsider.com/articles/12/10/24/apple-slims-down-imac-40-with-friction-stir-welding-ditching-the-disc-drive.

Dong, Chun-lin, Kun Zhang, and Guo-hong Luan. 2014. 'Effect of Natural Aging on Mechanical Properties of 7050 Aluminum Alloy Friction Stir Welding'. *Transactions of the China Welding Institution* 35 (4): 15–18.

Du, Y., T. Mukherjee, P. Mitra, and T. DebRoy. 2020. 'Machine Learning Based Hierarchy of Causative Variables for Tool Failure in Friction Stir Welding'. *Acta Materialia* 192 (June): 67–77. https://doi.org/10.1016/j.actamat.2020.03.047.

Dursun, Tolga, and Costas Soutis. 2014. 'Recent Developments in Advanced Aircraft Aluminium Alloys'. *Materials & Design (1980-2015)* 56 (April): 862–71. https://doi.org/10.1016/j.matdes.2013.12.002.

El-Shennawy, M, Kh Abdel-Aziz, and A A Omar. 2017. 'Metallurgical and Mechanical Properties of Heat Treatable Aluminum Alloy AA6082 Welds' 12 (11): 8.

Ericsson, M. 2003. 'Influence of Welding Speed on the Fatigue of Friction Stir Welds, and Comparison with MIG and TIG'. *International Journal of Fatigue* 25 (12): 1379–87. https://doi.org/10.1016/S0142-1123(03)00059-8.

European Environment Agency. 2020. 'Final Energy Consumption by Sector and Fuel in Europe'. Indicator assessment IND-16-en. European Environment Agency. https://www.eea.europa.eu/data-and-maps/indicators/final-energy-consumption-by-sector-10/assessment.

Fan, Xigang, Daming Jiang, Qingchang Meng, and Li Zhong. 2006. 'The Microstructural Evolution of an Al–Zn–Mg–Cu Alloy during Homogenization'. *Materials Letters*, 5.

Fonda, R. W., and J. F. Bingert. 2004. 'Microstructural Evolution in the Heat-Affected Zone of a Friction Stir Weld'. *Metallurgical and Materials Transactions A* 35 (5): 1487–99. https://doi.org/10.1007/s11661-004-0257-7.

Forth Engineering. n.d. 'FSWBOT'. Forth. Accessed 16 March 2021. https://forth.pinksquaremediadev.co.uk/case-study/fswbot-friction-stir-welding-crawler/.

'Friction Stir Welding – Joining the Future of Industry | Cambridge Network'. n.d. Accessed 2 June 2020. https://www.cambridgenetwork.co.uk/news/friction-stir-welding-joining-the-future-of-industry/.

Frigaard, Ø., Ø. Grong, and O. T. Midling. 2001. 'A Process Model for Friction Stir Welding of Age Hardening Aluminum Alloys'. *Metallurgical and Materials Transactions A* 32 (5): 1189–1200. https://doi.org/10.1007/s11661-001-0128-4.

Fuller, Christian B., Murray W. Mahoney, Mike Calabrese, and Leanna Micona. 2010a. 'Evolution of Microstructure and Mechanical Properties in Naturally Aged 7050 and 7075 Al Friction Stir Welds'. *Materials Science and Engineering: A* 527 (9): 2233–40. https://doi.org/10.1016/j.msea.2009.11.057.

———. 2010b. 'Evolution of Microstructure and Mechanical Properties in Naturally Aged 7050 and 7075 Al Friction Stir Welds'. *Materials Science and Engineering: A* 527 (9): 2233–40. https://doi.org/10.1016/j.msea.2009.11.057.

Gandra, João. 2020. 'CoreFlow - Technology Launch Webinar'. June 5. https://www.youtube.com/watch?v=zvjVkNxKSd4.

Gao, Y K. 2011. 'Experimental Investigation and Fatigue Life Prediction for 7475-T7351 Aluminum Alloy with and without Shot Peening-Induced Residual Stresses'. *Acta Materialia*, 11.

Gite, Rishikesh Arun, Praveen Kumar Loharkar, and Rajendra Shimpi. 2019. 'Friction Stir Welding Parameters and Application: A Review'. *Materials Today: Proceedings* 19: 361–65. https://doi.org/10.1016/j.matpr.2019.07.613.

Goswami, R., G. Spanos, P.S. Pao, and R.L. Holtz. 2010. 'Precipitation Behavior of the ß Phase in Al-5083'. *Materials Science and Engineering: A* 527 (4–5): 1089–95. https://doi.org/10.1016/j.msea.2009.10.007.

Hahn, G. T., and A. R. Rosenfield. 1975. 'Metallurgical Factors Affecting Fracture Toughness of Aluminum Alloys'. *Metallurgical Transactions A* 6 (4): 653–68. https://doi.org/10.1007/BF02672285.

Hahn, Th., ed. 2006. *International Tables for Crystallography: Space-Group Symmetry*. 1st ed. Vol. A. International Tables for Crystallography. Chester, England: International Union of Crystallography. https://doi.org/10.1107/97809553602060000100.

Halahan, Ron. 1997. 'Modes of Fracture'. 25 April 1997. http://www.sv.rkriz.net/classes/MSE2094_NoteBook/97ClassProj/exper/halahan/www/halahan.html.

Hasting, Håkon S., Anders G. Frøseth, Sigmund J. Andersen, Rene Vissers, John C. Walmsley, Calin D. Marioara, Frédéric Danoix, Williams Lefebvre, and Randi Holmestad. 2009. 'Composition of B" Precipitates in Al–Mg–Si Alloys by Atom Probe Tomography and First Principles Calculations'. *Journal of Applied Physics* 106 (12): 123527. https://doi.org/10.1063/1.3269714.

Hatch, John E., Aluminum Association, and American Society for Metals, eds. 1984. *Aluminum: Properties and Physical Metallurgy*. Metals Park, Ohio: American Society for Metals.

Hertzberg, Richard W. 1996. *Deformation and Fracture Mechanics of Engineering Materials*. 4th ed. New York: J. Wiley & Sons.

Hovanski, Yuri, Rajiv Mishra, Yutaka Sato, Piyush Upadhyay, David Yan, TMS Annual Meeting & Exhibition, and Minerals, Metals and Materials Society. 2017. *Friction Stir Welding and Processing IX*. The Minerals, Metals & Materials Series. Cham: Springer.

Hoyos, Elizabeth, and María Camila Serna. 2021. 'Basic Tool Design Guidelines for Friction Stir Welding of Aluminum Alloys'. *Metals* 11 (12): 2042. https://doi.org/10.3390/met11122042.

Hu, Jianguo, Keisuke Ikeda, and Tadasu Murakami. 1996. 'Effect of Heat Treatment after Hot-Rolling on Texture and Formability for 5083 Alloy Sheet.' *Journal of*

Japan Institute of Light Metals 46 (3): 126–31. https://doi.org/10.2464/jilm.46.126.

Huang, Xiaomin, and A. P. Reynolds. 2018. 'Effects of the Friction Stir Welding Process Variants on Residual Stress'. *Science and Technology of Welding and Joining* 23 (4): 279–86. https://doi.org/10.1080/13621718.2017.1377335.

Imam, Murshid, Yufeng Sun, Hidetoshi Fujii, Ninshu Ma, Seiichiro Tsutsumi, and Hidekazu Murakawa. 2017. 'Microstructural Characteristics and Mechanical Properties of Friction Stir Welded Thick 5083 Aluminum Alloy'. *Metallurgical and Materials Transactions A* 48 (1): 208–29. https://doi.org/10.1007/s11661-016-3819-6.

Institute of British Standards. 2012. 'BS EN ISO 25239-3:2011 Friction Stir Welding - Aluminium. Part 3: Qualification of Welding Operators'. https://bsol-bsigroup-com.hallam.idm.oclc.org/PdfViewer/Viewer?pid=000000000030171116.

Jacquin, Dimitri, and Gildas Guillemot. 2021. 'A Review of Microstructural Changes Occurring during FSW in Aluminium Alloys and Their Modelling'. *Journal of Materials Processing Technology* 288 (February): 116706. https://doi.org/10.1016/j.jmatprotec.2020.116706.

Jata, K. V., K. K. Sankaran, and J. J. Ruschau. 2000. 'Friction-Stir Welding Effects on Microstructure and Fatigue of Aluminum Alloy 7050-T7451'. *Metallurgical and Materials Transactions A* 31 (9): 2181–92.

Jata, Kumar V., M. W. Mahoney, Symposium on Friction Stir Welding and Processing, and Minerals, Metals and Materials Society, eds. 2003. *Friction Stir Welding and Processing II: Proceedings of a Symposium Sponsored by the Shaping and Forming Committee of the Materials Processing and Manufacturing Division (MPMD) of TMS (The Minerals, Metals & Materials Society) [Held in San Diego, March 4 - 6, 2003 at] 2003 TMS Annual Meeting, San Diego, California, March 2 - 6, 2003*. Warrendale, Pa: TMS (The Minerals, Metals & Materials Society).

Kah, Paul, Richard Rajan, Jukka Martikainen, and Raimo Suoranta. 2015. 'Investigation of Weld Defects in Friction-Stir Welding and Fusion Welding of Aluminium Alloys'. *International Journal of Mechanical and Materials Engineering* 10 (1): 26. https://doi.org/10.1186/s40712-015-0053-8.

Kalemba, I., M. Kopyściański, C. Hamilton, and S. Dymek. 2015. 'Natural Aging Behavior Of Friction Stir Welded Al-Zn-Mg-Cu Aluminum Alloys'. *Archives of Metallurgy and Materials* 60 (2): 875–79. https://doi.org/10.1515/amm-2015-0222.

Kallee, Stephen, Wayne Thomas, and E. David Nicholas. 2001. 'Industrialisation of Friction Stir Welding for Aerospace Structures'. In . Strasbourg, France: TWI. https://www.twi-global.com/technical-knowledge/published-papers/industrialisation-of-friction-stir-welding-for-aerospace-structures-december-2001/.

Kallee, S.W. 2010. 'Industrial Applications of Friction Stir Welding'. In *Friction Stir Welding*, 118–63. Elsevier. https://doi.org/10.1533/9781845697716.1.118.

Kalpakjian, Serope, and Steven R. Schmid. 2001a. *Manufacturing Engineering and Technology*. 4. ed. Upper Saddle River, NJ: Prentice Hall.

———. 2001b. *Manufacturing Engineering and Technology*. 4. ed. Upper Saddle River, NJ: Prentice Hall.

Kamp, N, N Gao, M Starink, and I Sinclair. 2007. 'Influence of Grain Structure and Slip Planarity on Fatigue Crack Growth in Low Alloying Artificially Aged 2xxx

Aluminium Alloys'. *International Journal of Fatigue* 29 (5): 869–78. https://doi.org/10.1016/j.ijfatigue.2006.08.005.
Kamp, N., A. P. Reynolds, and J. D. Robson. 2009. 'Modelling of 7050 Aluminium Alloy Friction Stir Welding'. *Science and Technology of Welding and Joining* 14 (7): 589–96. https://doi.org/10.1179/136217109X12538726589987.
Kerins, John C. n.d. '(74) Attorney, Agent, or Firm Miles & Stockbridge P.C.';, 7.
Kim, Chung-Youb. 2013. 'Fatigue Crack Growth and Closure Behavior under Random Loadings in 7475-T7351 Aluminum Alloy'. *International Journal of Fatigue*, 9.
Krasnowski, K, C. Hamilton, and S. Dymek. 2015. 'Influence of the Tool Shape and Weld Configuration on Microstructure and Mechanical Properties of the Al 6082 Alloy FSW Joints | Elsevier Enhanced Reader'. *Archives of Civil and Mechanical Engineering* 15 (1): 133–41. https://doi.org/10.1016/j.acme.2014.02.001.
Krishnan, K.N. 2002. 'On the Formation of Onion Rings in Friction Stir Welds'. *Materials Science and Engineering: A* 327 (2): 246–51. https://doi.org/10.1016/S0921-5093(01)01474-5.
Kumar, Nilesh, Rajiv S. Mishra, and John A. Baumann. 2014. *Residual Stresses in Friction Stir Welding*. Friction Stir Welding and Processing Book Series. Amsterdam: Elsevier/Butterworth-Heinemann.
Liang, Zhimin, Xue Wang, Congwei Cai, and Dianlong Wang. 2019. 'Microstructure and Mechanical Properties of Thick Plate Friction Stir Welds for 6082-T6 Aluminum Alloy'. *High Temperature Materials and Processes* 38 (2019): 525–32. https://doi.org/10.1515/htmp-2018-0074.
Lienert, T., T. Siewert, S. Babu, and V. Acoff, eds. 2011. 'Friction Stir Welding Tool Designs'. In *Welding Fundamentals and Processes*, 664–77. ASM International. https://doi.org/10.31399/asm.hb.v06a.a0005629.
Lin, Sen, Jianguo Tang, Shengdan Liu, Yunlai Deng, Huaqiang Lin, Hua Ji, Lingying Ye, and Xinming Zhang. 2019. 'Effect of Travel Speed on Microstructure and Mechanical Properties of FSW Joints for Al–Zn–Mg Alloy'. *Materials* 12 (24): 4178. https://doi.org/10.3390/ma12244178.
Lin, Ying-Kai, Shing-Hai Wang, Ren-Yu Chen, Tso-Sheng Hsieh, Liren Tsai, and Chia-Chin Chiang. 2017. 'The Effect of Heat Treatment on the Sensitized Corrosion of the 5383-H116 Al-Mg Alloy'. *Materials* 10 (3): 275. https://doi.org/10.3390/ma10030275.
Liu, Huihong, and Hidetoshi Fujii. 2018. 'Microstructural and Mechanical Properties of a Beta-Type Titanium Alloy Joint Fabricated by Friction Stir Welding'. *Materials Science and Engineering: A* 711 (January): 140–48. https://doi.org/10.1016/j.msea.2017.11.006.
Liu, Jun-Tao, Yong-An Zhang, Xi-Wu Li, Zhi-Hui Li, Bai-Qing Xiong, and Ji-Shan Zhang. 2016. 'Phases and Microstructures of High Zn-Containing Al–Zn–Mg–Cu Alloys'. *Rare Metals* 35 (5): 380–84. https://doi.org/10.1007/s12598-014-0222-6.
Lombard, H., D.G. Hattingh, A. Steuwer, and M.N. James. 2009. 'Effect of Process Parameters on the Residual Stresses in AA5083-H321 Friction Stir Welds'. *Materials Science and Engineering: A* 501 (1–2): 119–24. https://doi.org/10.1016/j.msea.2008.09.078.
Lucadamo, G., N.Y.C. Yang, C. San Marchi, and E.J. Lavernia. 2006. 'Microstructure Characterization in Cryomilled Al 5083'. *Materials Science and Engineering: A* 430 (1–2): 230–41. https://doi.org/10.1016/j.msea.2006.05.039.

Lumley, Roger. 2018. *Fundamentals of Aluminium Metallurgy: Recent Advances.* Kent: Elsevier Science & Technology. https://public.ebookcentral.proquest.com/choice/publicfullrecord.aspx?p=5400802.

Lyman, Taylor. 1973. *Metallography, Structures, and Phase Diagrams*. Vol. 8. Metals Handbook. Metals Park, Ohio: American Society for metals.

Madhu. 2018. 'Difference between Edge and Screw Dislocation'. Difference Between.Com. 2018. https://www.differencebetween.com/difference-between-edge-and-screw-dislocation/.

Magalhães, Danielle Cristina Camilo, Marcio Ferreira Hupalo, and Osvaldo Mitsuyuki Cintho. 2014. 'Natural Aging Behavior of AA7050 Al Alloy after Cryogenic Rolling'. *Materials Science and Engineering: A* 593 (January): 1–7. https://doi.org/10.1016/j.msea.2013.11.017.

Magalhães, V. M., C. Leitão, and D. M. Rodrigues. 2018. 'Friction Stir Welding Industrialisation and Research Status'. *Science and Technology of Welding and Joining* 23 (5): 400–409. https://doi.org/10.1080/13621718.2017.1403110.

Mahoney, M. W., C. G. Rhodes, J. G. Flintoff, W. H. Bingel, and R. A. Spurling. 1998. 'Properties of Friction-Stir-Welded 7075 T651 Aluminum'. *Metallurgical and Materials Transactions A* 29 (7): 1955–64. https://doi.org/10.1007/s11661-998-0021-5.

Martin, Jonathan Peter. 2017. 'Friction Stir Welding of Thick Section Aluminium Alloys—New Techniques'. In *Friction Stir Welding and Processing IX*, edited by Yuri Hovanski, Rajiv Mishra, Yutaka Sato, Piyush Upadhyay, and David Yan, 99–108. The Minerals, Metals & Materials Series. Springer International Publishing.

Maślak, Mariusz, and Ryszard Skiba. 2015. 'Fire Resistance Increase of Structural Steel through the Modification of Its Chemical Composition'. *Procedia Engineering* 108: 277–84. https://doi.org/10.1016/j.proeng.2015.06.148.

Massalski, T. B., H. Okamoto, and ASM International, eds. 1990. *Binary Alloy Phase Diagrams*. 2nd ed. Materials Park, Ohio: ASM International.

'Master Welders Renewal'. n.d. Accessed 28 May 2020. https://www.cswip.com/microsites/cswip/master-welders-thermal-cutting-operators-certificate-renewal.aspx.

Matsuda, K, Y Sakaguchi, Y Miyata, Y Uetani, T Sato, A Kamio, and S Ikeno. 2000. 'Precipitation Sequence of Various Kinds of Metastable Phases in Al-1.0mass% Mg2Si-0.4mass% Si Alloy'. *Journal of Materials Science* 35 (1): 179–89.

Mazak MegaStir. n.d. 'Aerospace'. *Mazak MegaStir* (blog). Accessed 1 June 2020. https://megastir.com/aerospace/.

Melton, Geoff. 2019. 'Comparison of FSW and MIG Welding', 2019.

'Metallographic Etchants for Aluminum Alloys'. n.d. Accessed 19 March 2020. https://www.metallographic.com/Metallographic-Etchants/Metallography-Aluminum-etchants.htm.

'Mineral Commodity Summaries 2012'. 2012, 201.

'Mineral Commodity Summaries 2017'. 2017.

'Mineral Commodity Summaries 2021'. 2021.

Mishra, R. S., and Z. Y. Ma. 2005. 'Friction Stir Welding and Processing'. *Materials Science and Engineering: R: Reports* 50 (1): 1–78. https://doi.org/10.1016/j.mser.2005.07.001.

Mondolfo, L. F. 1943. *Metallography of Aluminum Alloys*. New York, NY: J. Wiley & Sons.

Mondolfo, L. F. 1976. *Aluminum Alloys: Structure and Properties*. London ; Boston: Butterworths.

Monteiro, Waldemar Alfredo, and Waldemar Alfredo Monteiro. 2014. *Light Metal Alloys Applications*.

Mouritz, Adrian P., ed. 2012a. 'Aluminium Alloys for Aircraft Structures'. In *Introduction to Aerospace Materials*, 173–201. Elsevier. https://doi.org/10.1533/9780857095152.173.

———. 2012b. *Introduction to Aerospace Materials*. AIAA Education Series. Reston, Va: AIAA, American Inst. of Aeronautics and Astronautics.

Murayama, M, K Hono, M Saga, and M Kikuchi. 1998. 'Atom Probe Studies on the Early Stages of Precipitation in Al–Mg–Si Alloys'. *Materials Science and Engineering: A* 250 (1): 127–32. https://doi.org/10.1016/S0921-5093(98)00548-6.

Murr, L.E., E.V. Esquivel, S.A. Quinones, S.M. Gaytan, M.I. Lopez, E.Y. Martinez, F. Medina, et al. 2009. 'Microstructures and Mechanical Properties of Electron Beam-Rapid Manufactured Ti–6Al–4V Biomedical Prototypes Compared to Wrought Ti–6Al–4V'. *Materials Characterization* 60 (2): 96–105. https://doi.org/10.1016/j.matchar.2008.07.006.

Nandan, R, T Debroy, and H Bhadeshia. 2008. 'Recent Advances in Friction-Stir Welding – Process, Weldment Structure and Properties'. *Progress in Materials Science* 53 (6): 980–1023. https://doi.org/10.1016/j.pmatsci.2008.05.001.

National Aeronautics and Space Administration. 2005. 'Super Lightweight External Tank'. FS-2005-04-025-MSFC. Marshall Space Flight Center - Huntsville, Alabama 35812: NASA. https://www.nasa.gov/centers/marshall/pdf/113020main_shuttle_lightweight.pdf.

Ninive, Per Harald, Are Strandlie, Sverre Gulbrandsen-Dahl, Williams Lefebvre, Calin D. Marioara, Sigmund J. Andersen, Jesper Friis, Randi Holmestad, and Ole Martin Løvvik. 2014. 'Detailed Atomistic Insight into the B" Phase in Al–Mg–Si Alloys'. *Acta Materialia* 69 (May): 126–34. https://doi.org/10.1016/j.actamat.2014.01.052.

Okamoto, H. 2002. *Phase Diagrams of Dilute Binary Alloys*. Materials Park, OH: ASM International.

Okamoto, H., M.E. Schlesinger, and E.M. Mueller, eds. 2016. 'Al (Aluminum) Binary Alloy Phase Diagrams'. In *Alloy Phase Diagrams*, 113–39. ASM International. https://doi.org/10.31399/asm.hb.v03.a0006144.

Olea, C. A. W., L. Roldo, T. R. Strohaecker, and J. F. dos Santos. 2006. 'Friction Stir Welding of Precipitate Hardenable Aluminium Alloys: A Review'. *Welding in the World* 50 (11–12): 78–87. https://doi.org/10.1007/BF03263464.

Oosterkamp, A, L Djapic Oosterkamp, and A Nordeide. 2004. '"Kissing Bond" Phenomena in Solid-State Welds of Aluminum Alloys', 7.

'Opinions on Cubic Crystal System'. n.d. Accessed 4 November 2018. http://www.writeopinions.com/face-centered-cubic.

Ou, Bin-Lung, Ji-Gang Yang, and Mon-Yu Wei. 2007. 'Effect of Homogenization and Aging Treatment on Mechanical Properties and Stress-Corrosion Cracking of 7050 Alloys'. *Metallurgical and Materials Transactions A* 38 (8): 1760–73. https://doi.org/10.1007/s11661-007-9200-z.

Perrett, J G, J. Martin, P L Threadgill, and M M Z Ahmed. 2007. 'Recent Developments in Friction Stir Welding of Thick Section Aluminium Alloys'. In . Florence, Italy. https://www.twi-global.com/technical-knowledge/published-papers/recent-developments-in-friction-stir-welding-of-thick-section-aluminium-alloys-march-2007.

Polmear, I. J., Jian-Feng Nie, Ma Qian, and David StJohn. 2017. *Light Alloys: Metallurgy of the Light Metals*. Fifth edition. Oxford: Butterworth-Heinemann, an imprint of Elsevier.

Porter, David A., and Kenneth E. Easterling. 1997. *Phase Transformations in Metals and Alloys*. 2. ed., Reprint. London: Chapman & Hall.

Prangnell, P.B., and C.P. Heason. 2005. 'Grain Structure Formation during Friction Stir Welding Observed by the "Stop Action Technique"'. *Acta Materialia* 53 (11): 3179–92. https://doi.org/10.1016/j.actamat.2005.03.044.

Prime, Michael B. 1999. 'Residual Stress Measurement by Successive Extension of a Slot: The Crack Compliance Method'. *Applied Mechanics Reviews* 52 (2): 75. https://doi.org/10.1115/1.3098926.

Princeton University. n.d. 'Dislocations and Slip'. Educational. Materials and Structure. https://www.princeton.edu/~maelabs/hpt/materials/dislocations.htm.

Radmilovic, V., R. Kilaas, U. Dahmen, and G.J. Shiflet. 1999. 'Structure and Morphology of S-Phase Precipitates in Aluminum'. *Acta Materialia* 47 (15–16): 3987–97. https://doi.org/10.1016/S1359-6454(99)00259-1.

Rahmatian, B., S. E. Mirsalehi, and K. Dehghani. 2019. 'Metallurgical and Mechanical Characterization of Double-Sided Friction Stir Welded Thick AA5083 Aluminum Alloy Joints'. *Transactions of the Indian Institute of Metals* 72 (10): 2739–51. https://doi.org/10.1007/s12666-019-01751-8.

Rai, R, A De, H K D H Bhadeshia, and T DebRoy. 2011. 'Review: Friction Stir Welding Tools'. *Science and Technology of Welding and Joining* 16 (4): 325–42. https://doi.org/10.1179/1362171811Y.0000000023.

Reza-E-Rabby, Md., Wei Tang, and Anthony P. Reynolds. 2018. 'Effects of Thread Interruptions on Tool Pins in Friction Stir Welding of AA6061'. *Science and Technology of Welding and Joining* 23 (2): 114–24. https://doi.org/10.1080/13621718.2017.1341363.

Rohrer, Gregory S. 2001. *Structure and Bonding in Crystalline Materials*. Cambridge New York: Cambridge University Press.

Roldo, Liane, and Nenad Vulić. 2019. 'Friction Stir Welding for Marine Applications: Mechanical Behaviour and Microstructural Characteristics of Al-Mg-Si-Cu Plates'. *Transactions on Maritime Science* 8 (1): 75–83. https://doi.org/10.7225/toms.v08.n01.008.

Rosefort, M, C Matthies, H Buck, and H Koch. n.d. 'Determination of α- and β-AlFeSiPhases in Wrought Aluminium Alloys'. Essen, Germany: Trimet Aluminium AG.

Sahu, Mrinal. 2021. 'Optimization of Process Parameters of Friction Stir Welded Joints of Marine Grade AA 5083'. *Materials Today*, 6.

Salih, Omar S., Hengan Ou, W. Sun, and D.G. McCartney. 2015. 'A Review of Friction Stir Welding of Aluminium Matrix Composites'. *Materials & Design* 86 (December): 61–71. https://doi.org/10.1016/j.matdes.2015.07.071.

Sanders, R.E., S.F. Baumann, and H.C. Stumpf. 1989. 'Wrought Non–Heat-Treatable Aluminum Alloys'. In *Treatise on Materials Science & Technology*, 31:65–105. Elsevier. https://doi.org/10.1016/B978-0-12-341831-9.50008-5.

Sanders, Robert, and James Staley. 2019. 'A History of Wrought Aluminum Alloys and Applications'. In *Properties and Selection of Aluminum Alloys*, edited by Kevin Anderson, 157–201. ASM International. https://doi.org/10.31399/asm.hb.v02b.a0006516.

Sato, Yutaka S., Hiroyuki Kokawa, Masatoshi Enomoto, and Shigetoshi Jogan. 1999. 'Microstructural Evolution of 6063 Aluminum during Friction-Stir Welding'. *Metallurgical and Materials Transactions A* 30 (9): 2429–37. https://doi.org/10.1007/s11661-999-0251-1.

Sato, Yutaka S., Seung Hwan C. Park, and Hiroyuki Kokawa. 2001. 'Microstructural Factors Governing Hardness in Friction-Stir Welds of Solid-Solution-Hardened Al Alloys'. *Metallurgical and Materials Transactions A* 32 (12): 3033–42. https://doi.org/10.1007/s11661-001-0178-7.

Sauvage, X., A. Dédé, A. Cabello Muñoz, and B. Huneau. 2008. 'Precipitate Stability and Recrystallisation in the Weld Nuggets of Friction Stir Welded Al–Mg–Si and Al–Mg–Sc Alloys'. *Materials Science and Engineering: A* 491 (1–2): 364–71. https://doi.org/10.1016/j.msea.2008.02.006.

'Save the SS United States | PropTalk'. n.d. Accessed 29 April 2020. https://www.proptalk.com/save-ss-united-states.

Scamans, G.M., N.J.H. Holroyd, and C.D.S. Tuck. 1987. 'The Role of Magnesium Segregation in the Intergranular Stress Corrosion Cracking of Aluminium Alloys'. *Corrosion Science* 27 (4): 329–47. https://doi.org/10.1016/0010-938X(87)90076-X.

Schindler, H. -J., W. Cheng, and I. Finnie. 1997. 'Experimental Determination of Stress Intensity Factors Due to Residual Stresses'. *Experimental Mechanics* 37 (3): 272–77. https://doi.org/10.1007/BF02317418.

Segal, Vladimir, Svetlana V. Reznikov, Nagendra Murching, Vincent H. Hammond, and Laszlo J. Kecskes. 2019. 'Semi-Continuous Equal-Channel Angular Extrusion and Rolling of AA5083 and AZ31 Alloys'. *Metals* 9 (10): 1035. https://doi.org/10.3390/met9101035.

Serizawa, Ai, Tatsuo Sato, and Warren J. Poole. 2010. 'The Characterization of Dislocation–Nanocluster Interactions in Al–Mg–Si(–Cu/Ag) Alloys'. *Philosophical Magazine Letters* 90 (4): 279–87. https://doi.org/10.1080/09500831003633231.

Sha, Gang, and Alfred Cerezo. 2004. 'Early-Stage Precipitation in Al–Zn–Mg–Cu Alloy (7050)'. *Acta Materialia* 52 (15): 4503–16. https://doi.org/10.1016/j.actamat.2004.06.025.

Shahzad, M., M. Chaussumier, R. Chieragatti, C. Mabru, and F. Rezai-Aria. 2010. 'Influence of Anodizing Process on Fatigue Life of Machined Aluminium Alloy'. *Procedia Engineering* 2 (1): 1015–24. https://doi.org/10.1016/j.proeng.2010.03.110.

Shrivastava, Amber, Manuela Krones, and Frank E. Pfefferkorn. 2015. 'Comparison of Energy Consumption and Environmental Impact of Friction Stir Welding and Gas Metal Arc Welding for Aluminum'. *CIRP Journal of Manufacturing Science and Technology* 9 (May): 159–68. https://doi.org/10.1016/j.cirpj.2014.10.001.

Sielski, Robert A. 2008. 'Research Needs in Aluminum Structure∗'. *Ships and Offshore Structures* 3 (1): 57–65. https://doi.org/10.1080/17445300701797111.
Silva-Magalhães, A., J. De Backer, J. Martin, and G. Bolmsjö. 2019. 'In-Situ Temperature Measurement in Friction Stir Welding of Thick Section Aluminium Alloys'. *Journal of Manufacturing Processes* 39 (March): 12–17. https://doi.org/10.1016/j.jmapro.2019.02.001.
Singh, Gurmeet, Amardeep S. Kang, Kulwant Singh, and Jagtar Singh. 2017. 'Experimental Comparison of Friction Stir Welding Process and TIG Welding Process for 6082-T6 Aluminium Alloy'. *Materials Today: Proceedings* 4 (2): 3590–3600. https://doi.org/10.1016/j.matpr.2017.02.251.
Smilauerova, Jana. n.d. 'Deformation of Alloys: Precipitation Hardening'. Lecture presented at the NFPL135: Physics of Materials I, Faculty of Mathematics and Physics, Charles University Prague, Czech Republic. https://material.karlov.mff.cuni.cz/people/smilauerova/vyuka/FyzMat_I/FyzMat_I_7_precipitates.pdf.
Soboyejo, W. O. 2003. *Mechanical Properties of Engineered Materials*. Mechanical Engineering 152. New York: Marcel Dekker.
'Space Exploration Technologies Corporation - Falcon 9'. 2010. 22 December 2010. https://web.archive.org/web/20101222155322/http://www.spacex.com/falcon9.php.
'SPECTROMAXx Metal Analyzer | SPECTRO Analytical'. n.d. Accessed 11 May 2020. www.spectro.com/products/optical-emission-spectroscopy/spectromaxx-metal-analyzer.
Staines, D J, and E R Watts. 2005. 'THE SIMULTANEOUS USE OF TWO OR MORE FRICTION STIR WELDING TOOLS'. TWI.Global. 2005.
Styles, M.J., C.R. Hutchinson, Y. Chen, A. Deschamps, and T.J. Bastow. 2012. 'The Coexistence of Two S (Al2CuMg) Phases in Al–Cu–Mg Alloys'. *Acta Materialia* 60 (20): 6940–51. https://doi.org/10.1016/j.actamat.2012.08.044.
Su, J.-Q, T.W Nelson, R Mishra, and M Mahoney. 2003. 'Microstructural Investigation of Friction Stir Welded 7050-T651 Aluminium'. *Acta Materialia* 51 (3): 713–29. https://doi.org/10.1016/S1359-6454(02)00449-4.
Svensson, L.-E., L. Karlsson, H. Larsson, B. Karlsson, M. Fazzini, and J. Karlsson. 2000. 'Microstructure and Mechanical Properties of Friction Stir Welded Aluminium Alloys with Special Reference to AA 5083 and AA 6082'. *Science and Technology of Welding and Joining* 5 (5): 285–96. https://doi.org/10.1179/136217100101538335.
Tamadon, Abbas, Dirk Pons, Kamil Sued, and Don Clucas. 2017. 'Development of Metallographic Etchants for the Microstructure Evolution of A6082-T6 BFSW Welds'. *Metals* 7 (10): 423. https://doi.org/10.3390/met7100423.
Taylor, John A. 2012. 'Iron-Containing Intermetallic Phases in Al-Si Based Casting Alloys'. *Procedia Materials Science* 1: 19–33. https://doi.org/10.1016/j.mspro.2012.06.004.
tec-science. 2018. 'Influence of the Lattice Structure on Ductility'. 28 May 2018. https://www.tec-science.com/material-science/ductility-of-metals/influence-of-the-lattice-structure-on-the-ductility/.
'Temperature of Ocean Water'. 2001. Windows to the Universe. 2001. https://web.archive.org/web/20100327205743/http://www.windows.ucar.edu/tour/link=/earth/Water/temp.html.

Texier, D., F. Atmani, P. Bocher, F. Nadeau, J. Chen, Y. Zedan, N. Vanderesse, and V. Demers. 2018. 'Fatigue Performances of FSW and GMAW Aluminum Alloys Welded Joints: Competition between Microstructural and Structural-Contact-Fretting Crack Initiation'. *International Journal of Fatigue* 116 (November): 220–33. https://doi.org/10.1016/j.ijfatigue.2018.06.020.

Thomas, W M. 1998. 'Friction Stir Welding and Related Friction Process Characteristics'. In . Cambridge, United Kingdom.

Thomas, W M, D J Staines, E R Watts, and I M Norris. n.d. 'The Simultaneous Use of Two or More Friction Stir Welding Tools', 6.

Threadgill, P L, A J Leonard, H R Shercliff, and P J Withers. 2009. 'Friction Stir Welding of Aluminium Alloys'. *International Materials Reviews* 54 (2): 49–93. https://doi.org/10.1179/174328009X411136.

Totten, George E., ed. 2016a. 'Age Hardening of Aluminum Alloys'. In *Heat Treating of Nonferrous Alloys*, 214–39. ASM International. https://doi.org/10.31399/asm.hb.v04e.a0006268.

———, ed. 2016b. 'Age Hardening of Aluminum Alloys'. In *Heat Treating of Nonferrous Alloys*, 214–39. ASM International. https://doi.org/10.31399/asm.hb.v04e.a0006268.

———, ed. 2016c. 'Annealing of Aluminum and Its Alloys'. In *Heat Treating of Nonferrous Alloys*, 137–47. ASM International. https://doi.org/10.31399/asm.hb.v04e.a0006285.

Totten, George E., and D. Scott MacKenzie, eds. 2016. 'Quenching of Aluminum Alloys'. In *Heat Treating of Nonferrous Alloys*, 148–78. ASM International. https://doi.org/10.31399/asm.hb.v04e.a0006260.

Tsemekidi-Tzeiranaki, S, P Bertoldi, N Labanca, L Castellazzi, T Serrenho, M Economidou, and P Zangheri. 2018. 'Energy Consumption and Energy Efficiency Trends in the EU-28 for the Period 2000-2016'. EUR 29473 EN. Luxenbourg: Publications Office of the European Union. https://doi.org/10.2760/574824.

TWI Ltd. 2018a. *An Overview of Friction Stir Welding (Internal Use Only)*. 2nd ed.

———. 2018b. 'TWI Core Research Project #30146'. Sheffield: TWI Ltd.

———. 2021a. 'What Is Friction Welding?' TWI Global. 2021. https://www.twi-global.com/technical-knowledge/faqs/faq-what-is-friction-welding.

———. 2021b. 'What Is Fusion Welding?' TWI Ltd. 2021. https://www.twi-global.com/technical-knowledge/faqs/what-is-fusion-welding.

———. 2021c. 'What Is Welding?' TWI Ltd Global. 2021. https://www.twi-global.com/technical-knowledge/faqs/what-is-welding.

———. n.d. 'FUNCTIONS, DESIGNS AND MATERIALS OF FRICTION STIR WELDING TOOLS'. TWI Technical Knowledge. https://www.twi-global.com/technical-knowledge/faqs/friction-stir-welding-tools.

'TWI Technology Used for Ground-Breaking SpaceX Flight'. n.d. Accessed 2 June 2020. https://www.twi-global.com/media-and-events/press-releases/2018-02-twi-technology-used-for-ground-breaking-spacex-flight.aspx.

'Understanding the Aluminum Alloy Designation System'. n.d. Accessed 8 May 2020. https://www.esabna.com/us/en/education/blog/understanding-the-aluminum-alloy-designation-system.cfm.

Ungar, T, J Lendvai, I Kovacs, and G Groma. 1979. 'The Decomposition Ofthe Solid Solution State in the Temperature Range 20 to 200~ in an AI-Zn-Mg Alloy'. *Journal of Materials Science* 14 (3): 671–79.

Vander Voort, George F., ed. 2004. 'Metallographic Techniques for Aluminum and Its Alloys'. In *Metallography and Microstructures*, 711–51. ASM International. https://doi.org/10.31399/asm.hb.v09.a0003769.

Wang, Guoqing, Yanhua Zhao, and Yunfei Hao. 2018. 'Friction Stir Welding of High-Strength Aerospace Aluminum Alloy and Application in Rocket Tank Manufacturing'. *Journal of Materials Science & Technology* 34 (1): 73–91. https://doi.org/10.1016/j.jmst.2017.11.041.

Wang, Guo-Qing, Yan-Hua Zhao, and Ying-Ying Tang. 2020. 'Research Progress of Bobbin Tool Friction Stir Welding of Aluminum Alloys: A Review'. *Acta Metallurgica Sinica (English Letters)* 33 (1): 13–29. https://doi.org/10.1007/s40195-019-00946-8.

Wang, Junsheng. 2020. 'Physical Metallurgy of Aluminum Alloys', 37.

Wang, S. C., and M. J. Starink. 2005. 'Precipitates and Intermetallic Phases in Precipitation Hardening Al–Cu–Mg–(Li) Based Alloys'. *International Materials Reviews* 50 (4): 193–215. https://doi.org/10.1179/174328005X14357.

World Nuclear Association. 2017. 'Treatment and Conditioning of Nuclear Waste'. World Nuclear Association. June 2017. https://www.world-nuclear.org/information-library/nuclear-fuel-cycle/nuclear-wastes/treatment-and-conditioning-of-nuclear-wastes.aspx.

Xu, Daofen, Changjun Zhu, Chengfu Xu, and Kanghua Chen. 2021. 'Microstructures and Tensile Fracture Behavior of 2219 Wrought Al–Cu Alloys with Different Impurity of Fe'. *Metals* 11 (1): 174. https://doi.org/10.3390/met11010174.

Xu, Weifeng, Huan Wang, Yuxuan Luo, Wenjun Li, and M.W. Fu. 2018. 'Mechanical Behavior of 7085-T7452 Aluminum Alloy Thick Plate Joint Produced by Double-Sided Friction Stir Welding: Effect of Welding Parameters and Strain Rates'. *Journal of Manufacturing Processes* 35 (October): 261–70. https://doi.org/10.1016/j.jmapro.2018.07.028.

Xu, W.F., Y.X. Luo, and M.W. Fu. 2018. 'Microstructure Evolution in the Conventional Single Side and Bobbin Tool Friction Stir Welding of Thick Rolled 7085-T7452 Aluminum Alloy'. *Materials Characterization* 138 (April): 48–55. https://doi.org/10.1016/j.matchar.2018.01.051.

Yan, J. H., M. A. Sutton, and A. P. Reynolds. 2007. 'Processing and Banding in AA2524 and AA2024 Friction Stir Welding'. *Science and Technology of Welding and Joining* 12 (5): 390–401. https://doi.org/10.1179/174329307X213639.

Yan, Jianfeng, and Andrea M. Hodge. 2017. 'Study of β Precipitation and Layer Structure Formation in Al 5083: The Role of Dispersoids and Grain Boundaries'. *Journal of Alloys and Compounds* 703 (May): 242–50. https://doi.org/10.1016/j.jallcom.2017.01.360.

Yi, Gaosong, Binhan Sun, Jonathan D Poplawsky, Yakun Zhu, and Michael L Free. n.d. 'Investigation of Pre-Existing Particles in Al 5083 Alloys', 22.

Yuqing, Mao, Ke Liming, Liu Fencheng, Chen Yuhua, and Xing Li. 2016. 'Investigations on Temperature Distribution, Microstructure Evolution, and Property Variations along Thickness in Friction Stir Welded Joints for Thick AA7075-T6 Plates'. *The International Journal of Advanced Manufacturing Technology* 86 (1–4): 141–54. https://doi.org/10.1007/s00170-015-8182-z.

Zeng, X. H., P. Xue, D. Wang, D. R. Ni, B. L. Xiao, K. S. Wang, and Z. Y. Ma. 2018. 'Material Flow and Void Defect Formation in Friction Stir Welding of Aluminium

Alloys'. *Science and Technology of Welding and Joining* 23 (8): 677–86. https://doi.org/10.1080/13621718.2018.1471844.

Zhou, L., T. Wang, W. L. Zhou, Z. Y. Li, Y. X. Huang, and J. C. Feng. 2016. 'Microstructural Characteristics and Mechanical Properties of 7050-T7451 Aluminum Alloy Friction Stir-Welded Joints'. *Journal of Materials Engineering and Performance* 25 (6): 2542–50. https://doi.org/10.1007/s11665-016-2106-4.

8 Appendix

Appendix 1 - Tensile test piece drawing for 20 mm thick AA6082-T651.

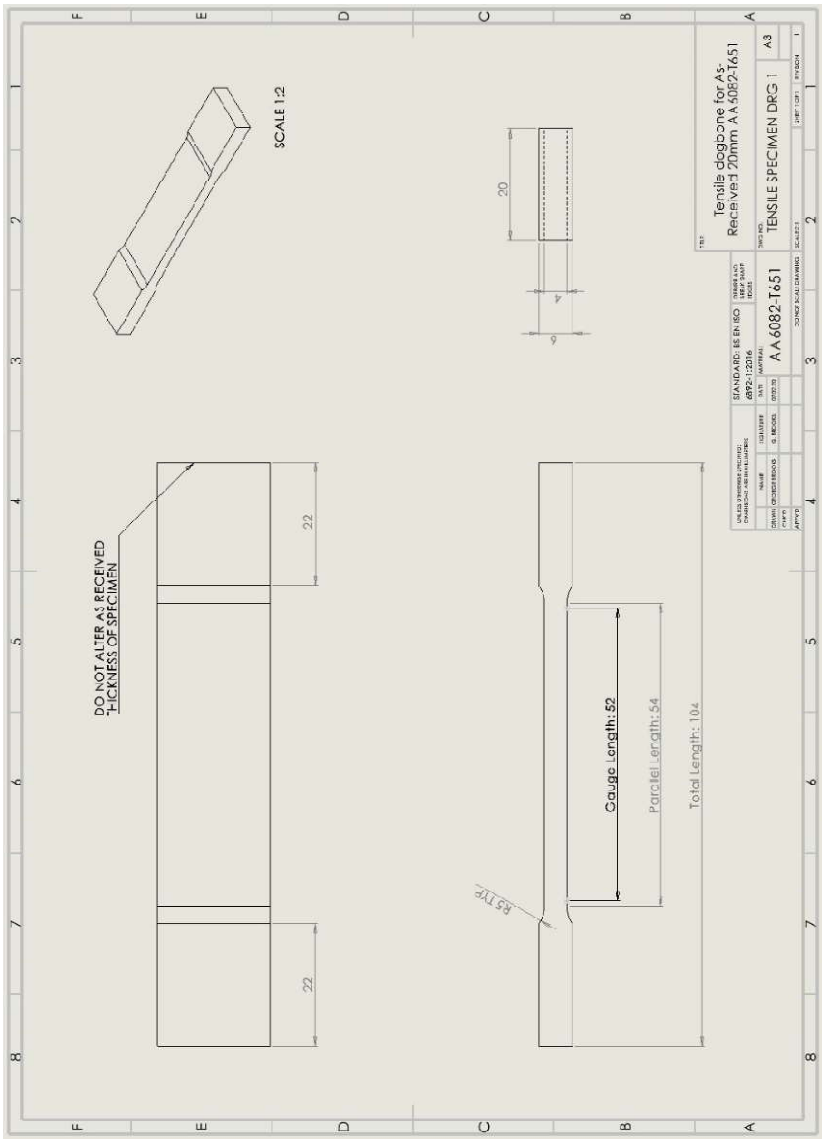

Appendix 2 - Triflat™ tool 30146-E011, used during WFW.

Appendix 3 - Second Triflat™ tool 30146-E011, used in conjunction with the tool used to produce the WFW-FSW, to produce SDS-FSW.

Appendix 4 - Tool D030, using 4 flats and fine thread pitch to weld using SSS-FSW technique.

Appendix 5 - Tool D070, using 4 flats and coarse thread pitch to weld using SSS-FSW technique.

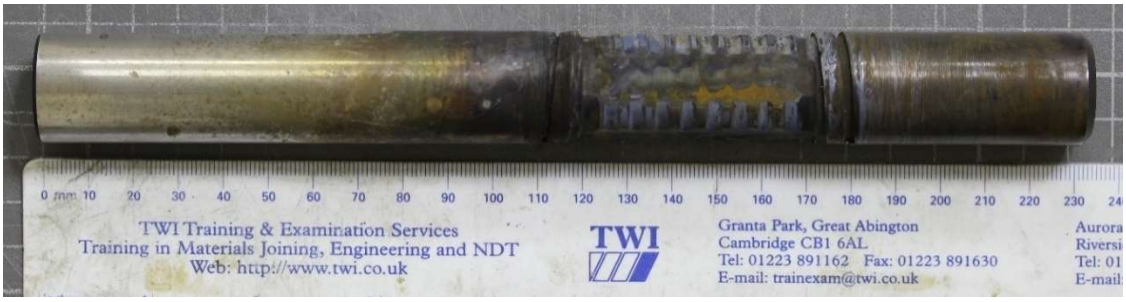

Appendix 6 - Tool D080, using 3 flats and coarse thread pitch to weld using SSS-FSW technique

SPECTRO

Sample Results

Sample Result Name	Type	Measure Date Time	Recalculation Date Time	Origin	Method Name	Operator Name
5083/Paul Allender	Unknown	28/08/2019 10:05	23/08/2019 10:07	Measured	Al-40-M	Paul Allender

Check Type	Check Status	Correction Type	Outlier Test Type	Status
None	Not Used	None	None	Not Used

Sample Name	Operator	Grade ID
5083	Paul Allender	

	Si Conc %	Fe Conc %	Cu Conc %	Mn Conc %	Mg Conc %	Cr Conc %	Ni Conc %	Zn Conc %	Ti Conc %	Be Conc %	Bi Conc %	Ca Conc %	Cd Conc %	Ga Conc %	Li Conc %	Na Conc %	Pb Conc %
1	0.23	0.37	0.071	0.48	4.42	0.11	0.002	0.074	0.017	0.0006	0.001	0.001	A 0.006!	0.016	0.0002	0.002	0.005
2	0.26	0.34	0.070	0.48	4.42	0.11	0.002	0.076	0.017	0.0006	0.001	0.003	A 0.005!	0.016	0.0002	0.0007	0.005
3	0.23	0.35	0.069	0.48	4.45	0.11	0.002	0.074	0.017	0.0006	0.001	0.002	A 0.004!	0.016	0.0002	<0.0001	0.006
Mean	**0.24**	**0.35**	**0.070**	**0.48**	**4.43**	**0.11**	**0.002**	**0.075**	**0.017**	**0.0006**	**0.001**	**0.002**	A 0.005!	**0.016**	**0.0002**	**0.0008**	**0.005**

	Sn Conc %	V Conc %	Zr Conc %	Al Conc %	Bg %
1	A 0.005!	0.010	<0.0003	94.2	--
2	A 0.005!	0.010	<0.0003	94.2	--
3	A 0.001!	0.010	<0.0003	94.2	--
Mean	A 0.004!	**0.010**	<-0.0006	**94.2**	--

Appendix 8 - Microstructure of G07/08. Etched in Kellers.

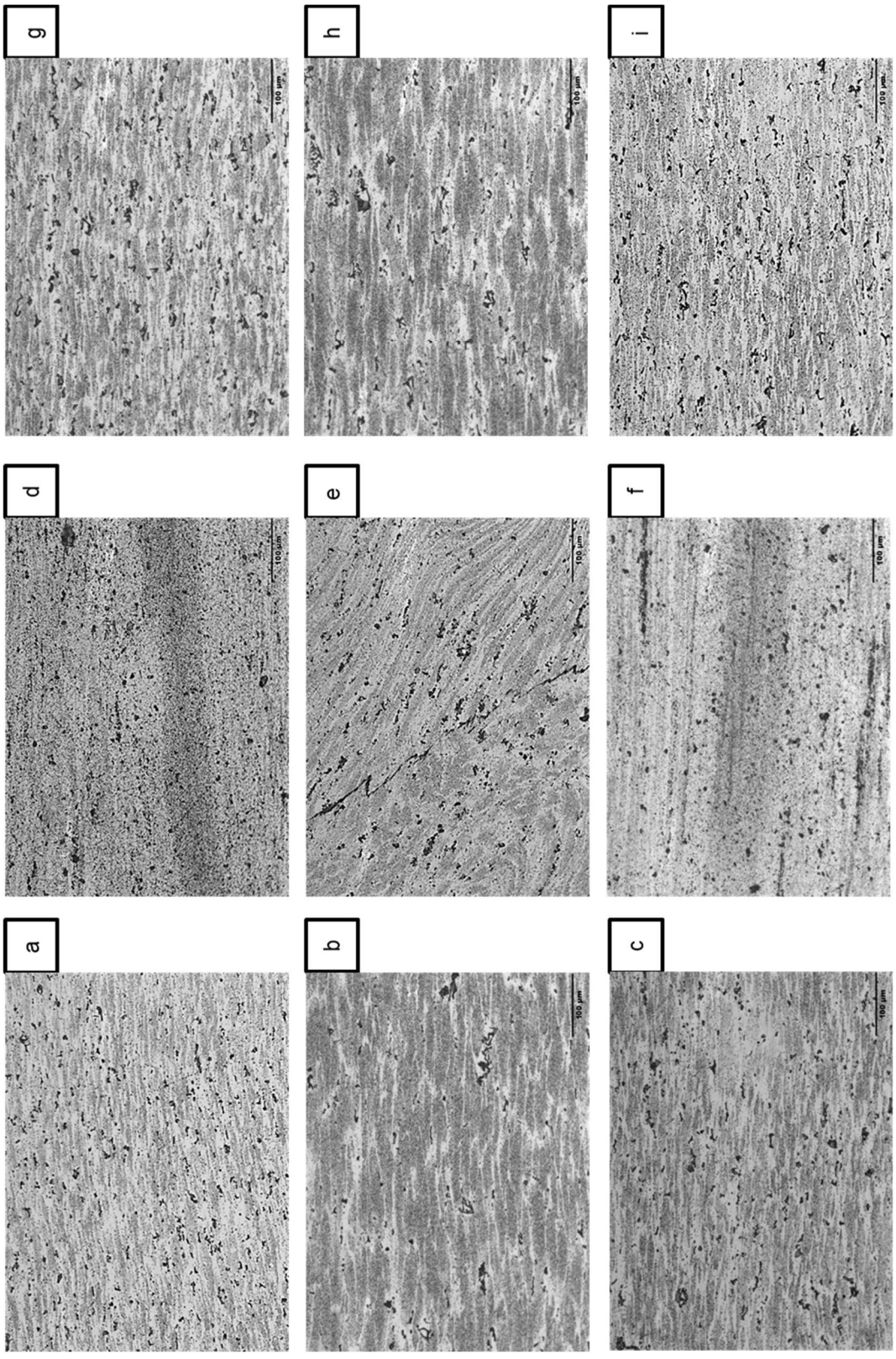

Appendix 9 – Microstructure of G13. Etched in Kellers.

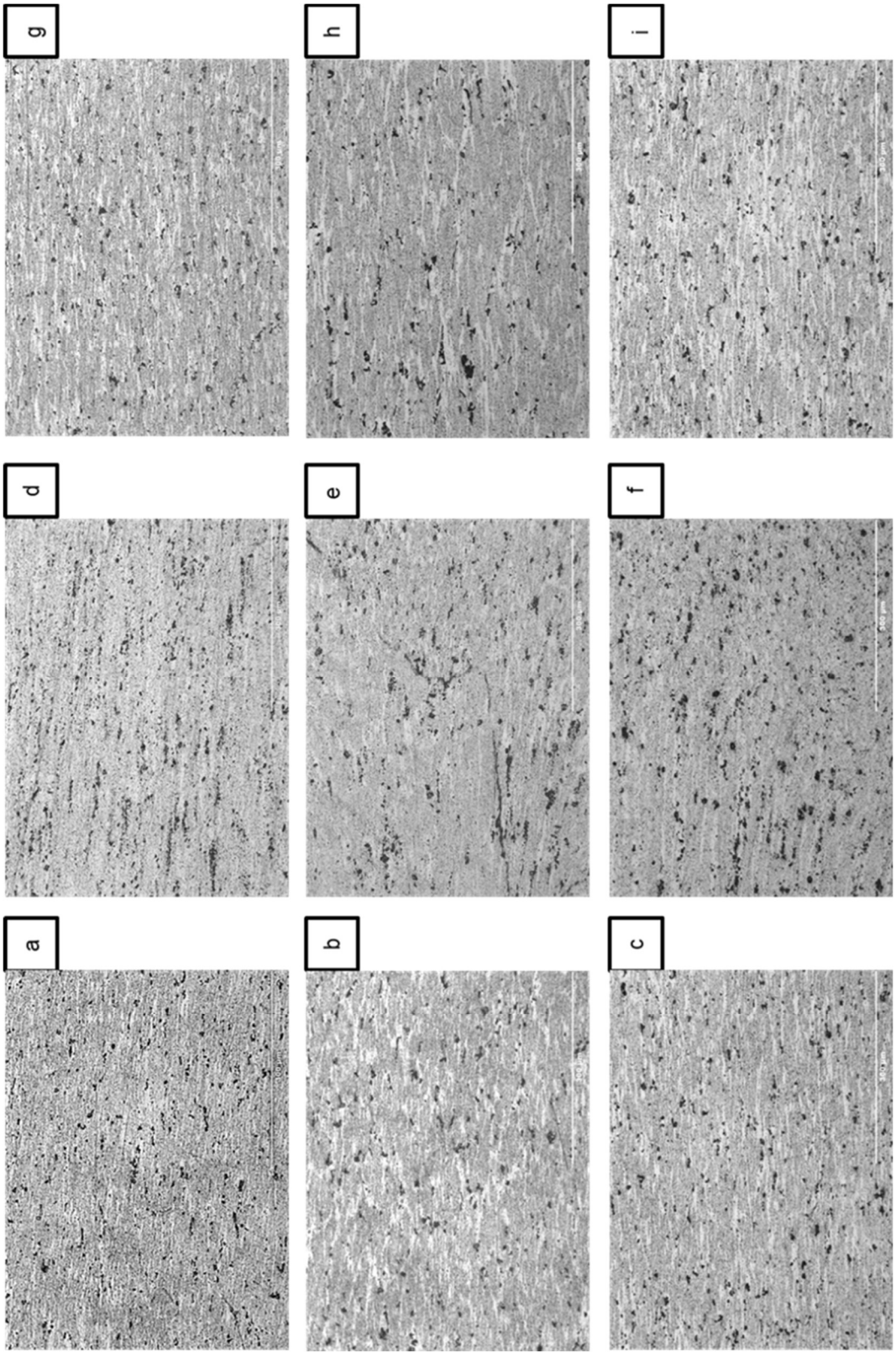

Appendix 10 – Microstructure of G34. Etched in Kellers.

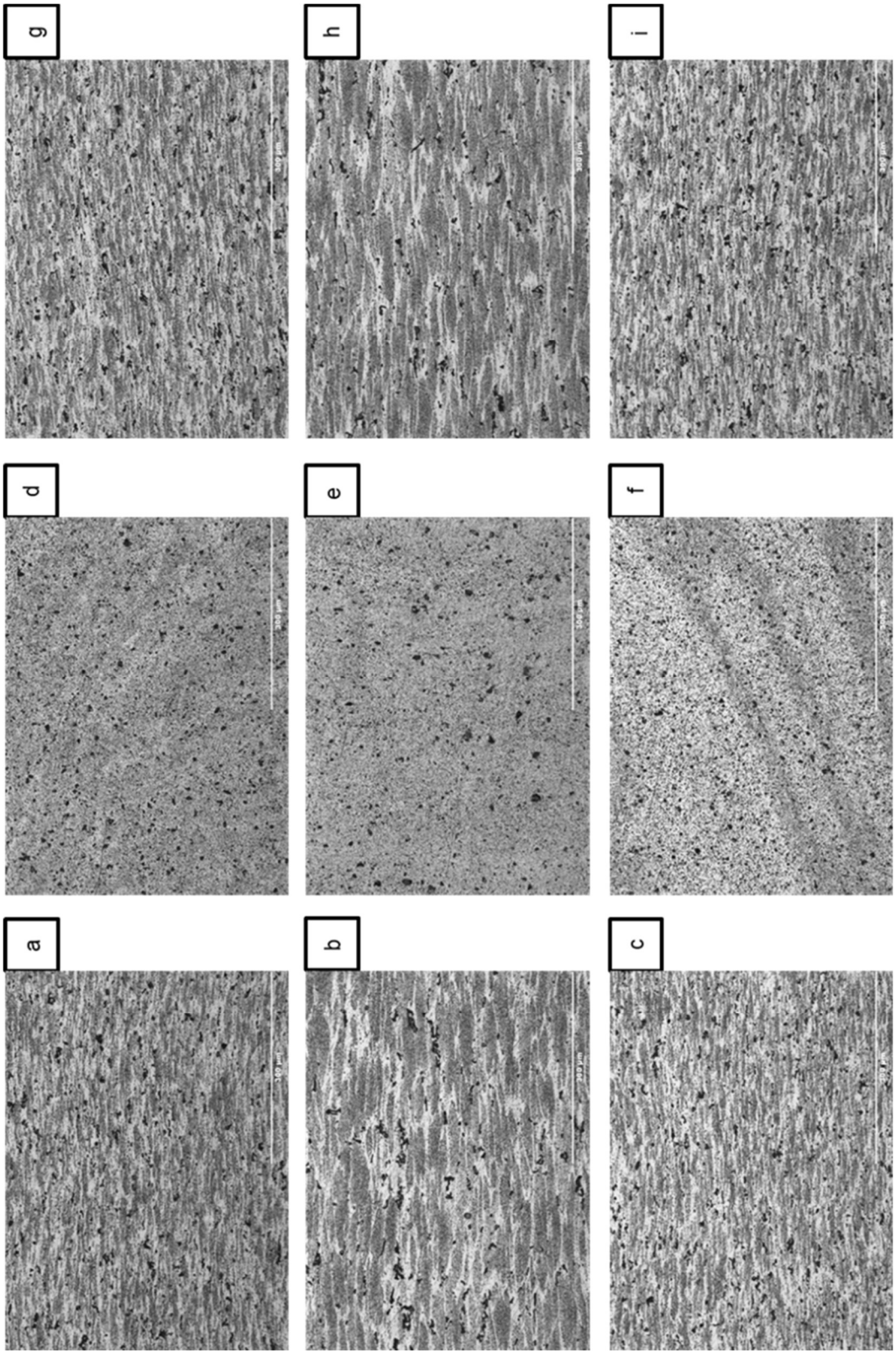

Appendix 11 – Microstructure of as-received AA5083-H111 after heat treatment to reveal grains. Etched in Kellers. Images taken at 20x objective.

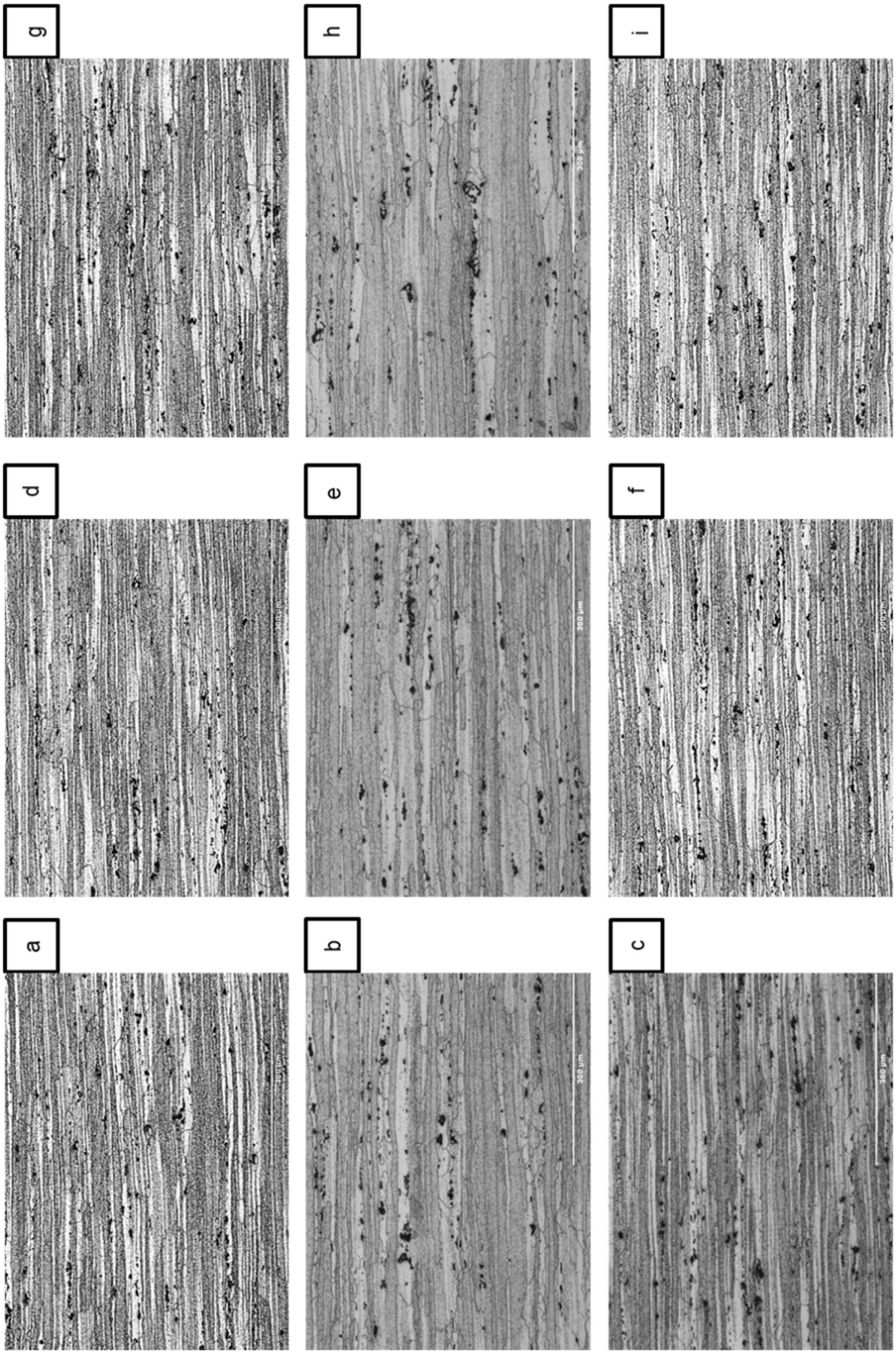

Appendix 12 – Microstructure of G07/08 after heat treatment to reveal grains. Etched in Kellers. Images taken at 20x objective.

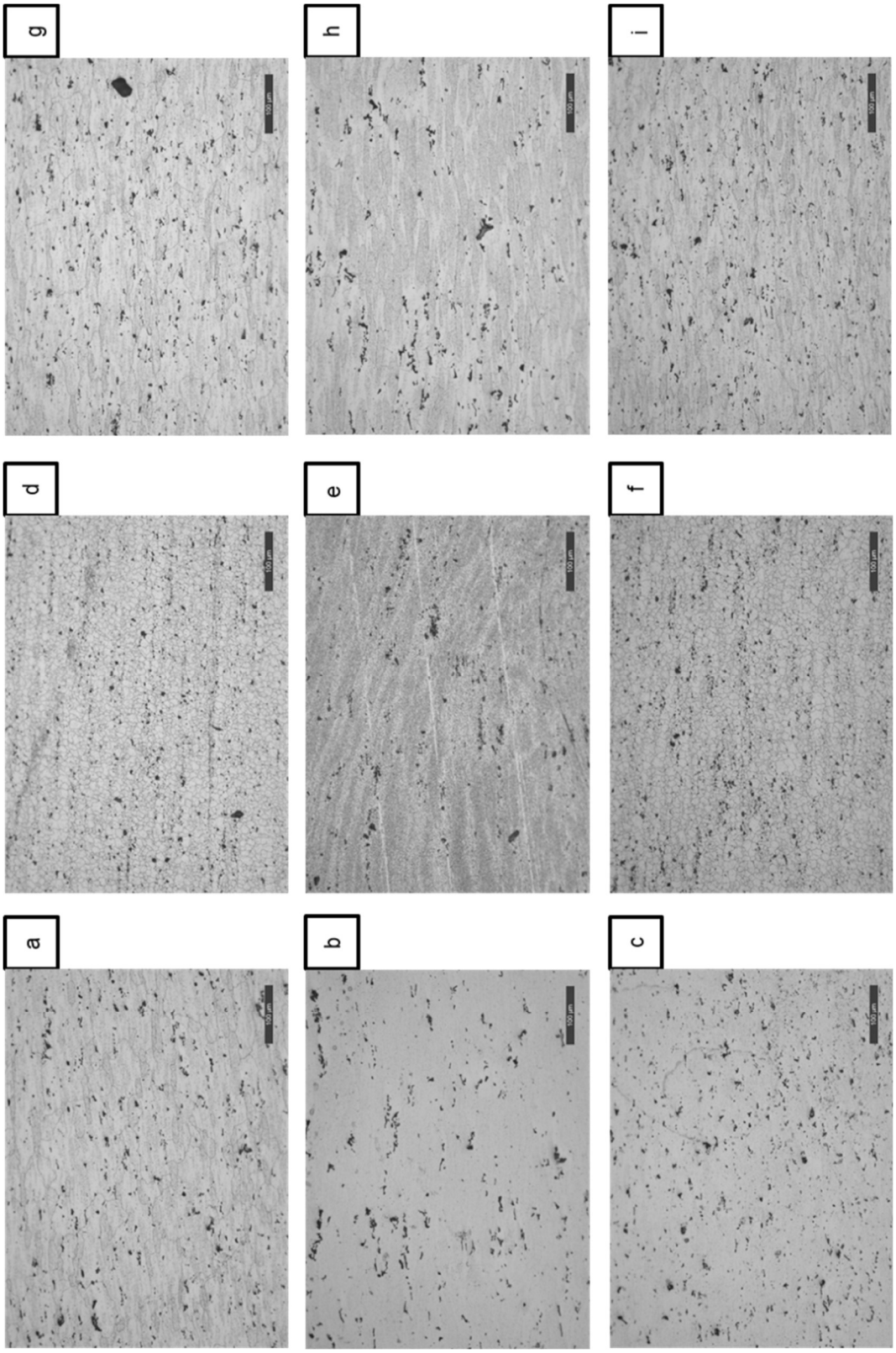

Appendix 13 – Microstructure of G13 after heat treatment to reveal grains. Etched in Kellers. Images taken at 20x objective.

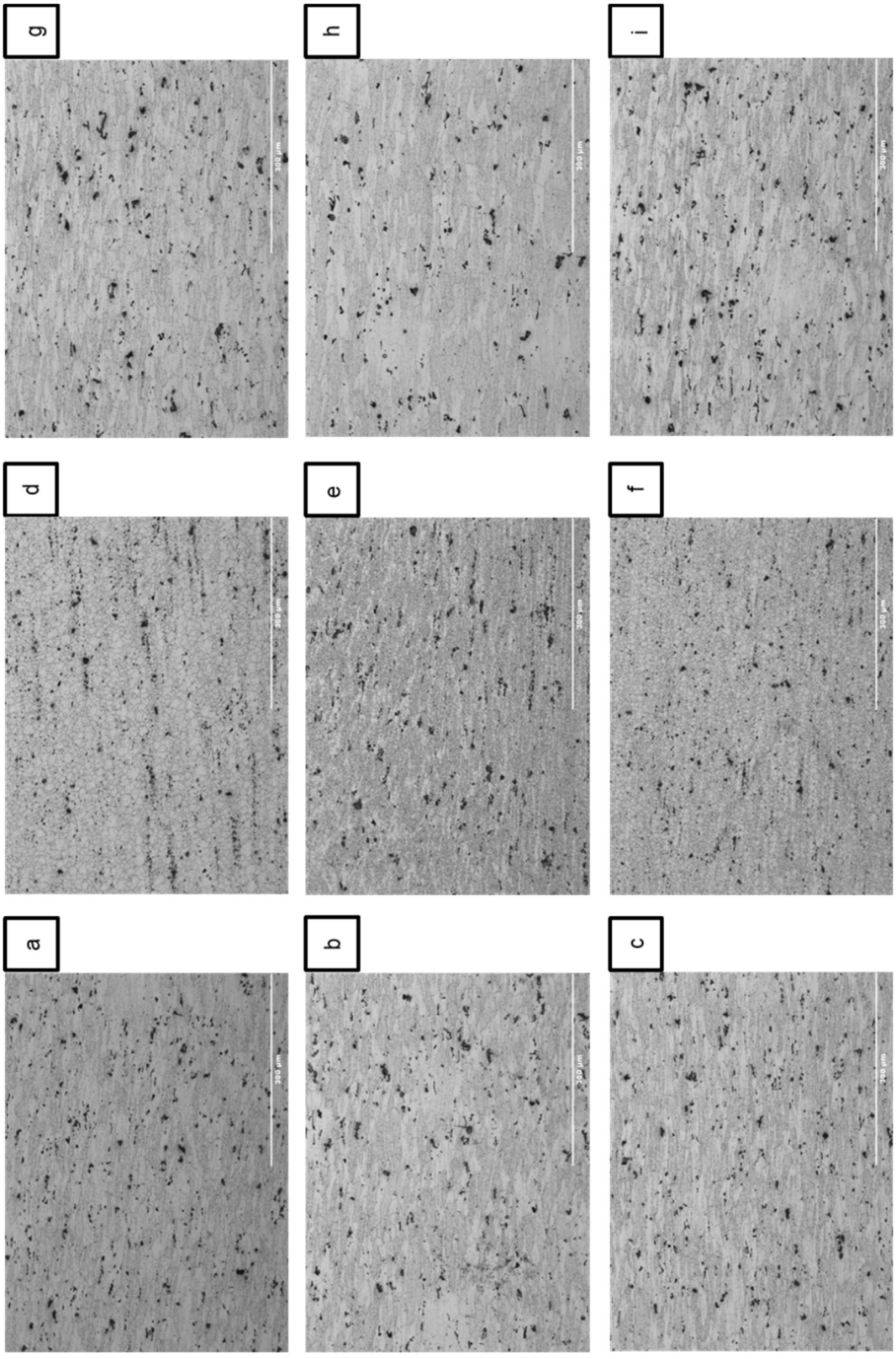

Appendix 14 – Microstructure of G34 after heat treatment to reveal grains. Etched in Kellers. Images taken at 20x objective.

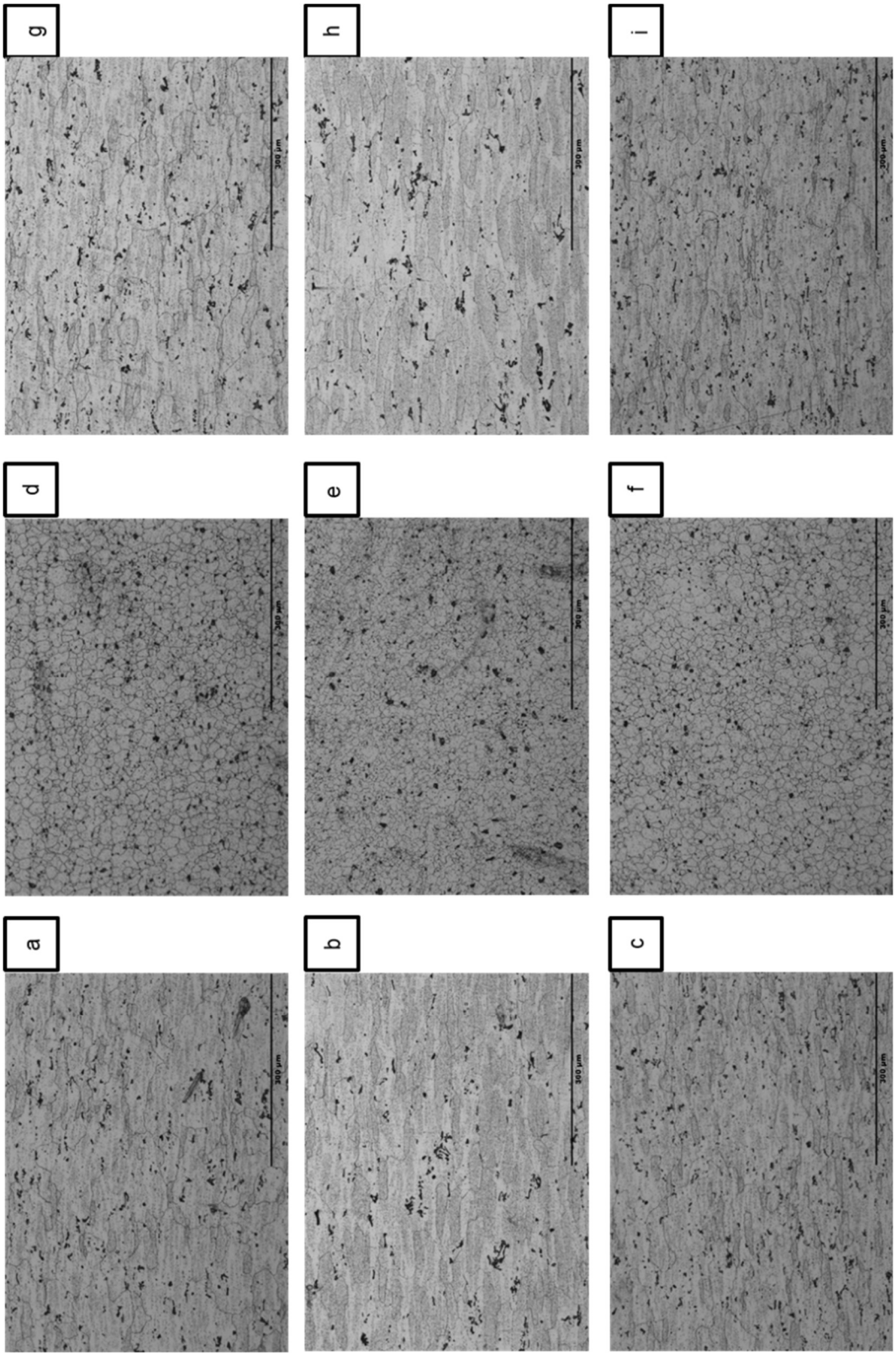

Appendix 15 – Advancing side transition region between SZ and HAZ of G07 taken near the shoulder. Image captured at 5x objective.

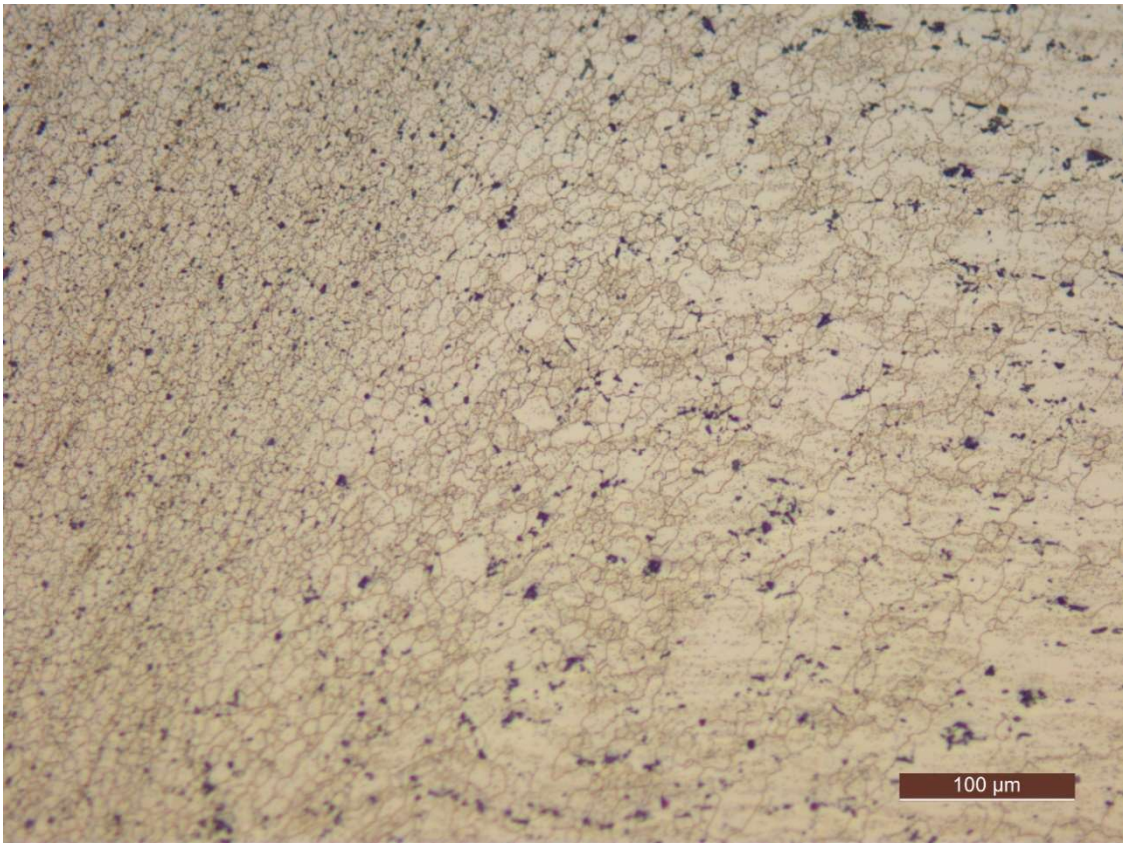

Appendix 16 – Retreating side transition region between SZ and HAZ of G07 taken near the shoulder. Image captured at 20x objective.

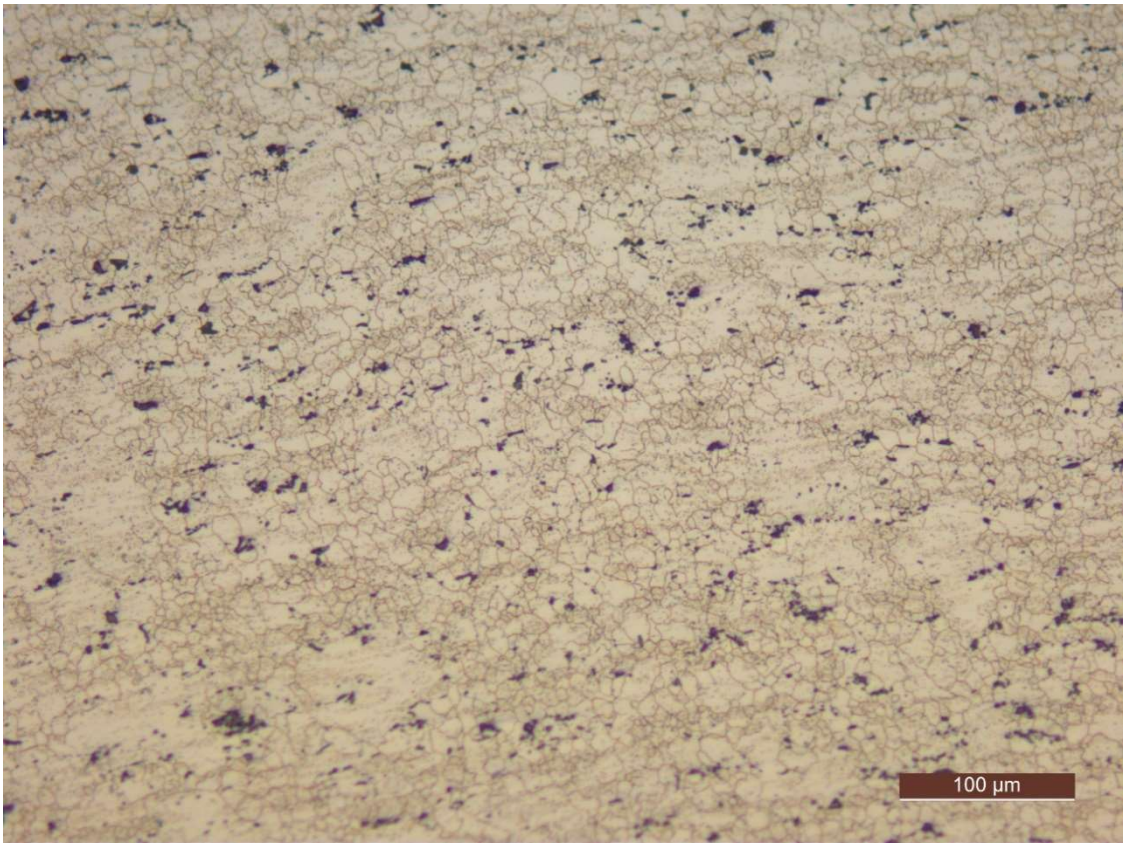

Appendix 17 - Failed tensile specimens of as-received AA5083-H111 parent material.

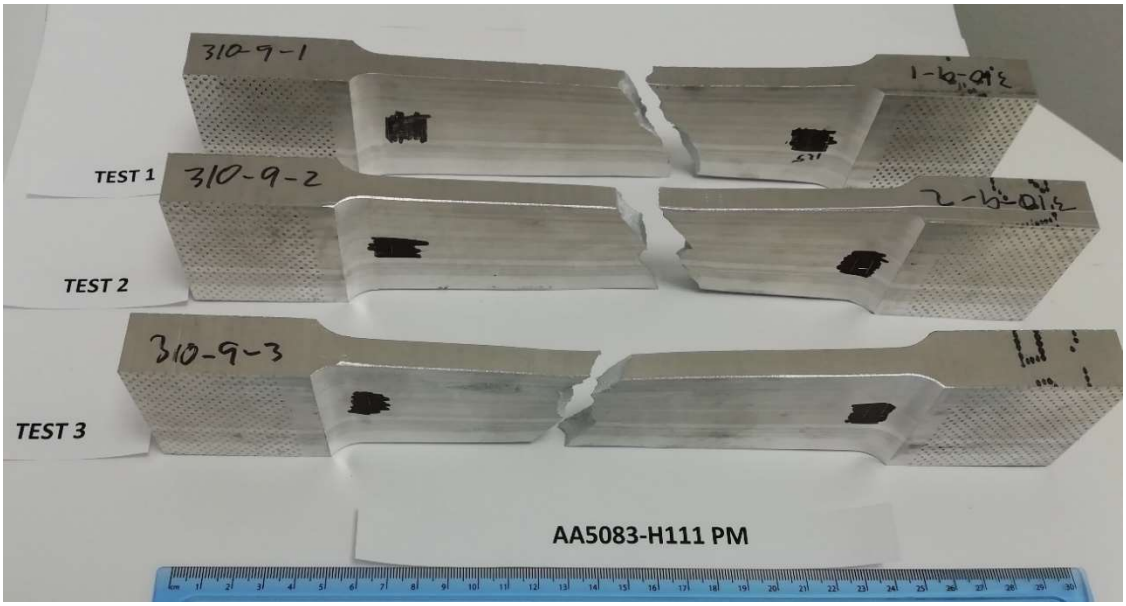

Appendix 18 - Failed tensile specimens of WFW-FSW, G07/08.

Appendix 19 - Failed tensile specimens of SDS-FSW, G13.

Appendix 20 - Failed tensile specimens of SSS-FSW, G34.

SPECTRO

Sample Results

Sample Result Name	Type	Measure Date Time	Recalculation Date Time	Origin	Method Name	Operator Name
6082/Paul Allender	Unknown	09/10/2019 08:54	09/10/2019 08:56	Measured	Al-40-M	Paul Allender

Check Type	Check Status	Correction Type	Outlier Test Type	Status
None	Not Used	None	None	Not Used

Sample Name	Operator	Grade ID
6082	Paul Allender	

	Si Conc %	Fe Conc %	Cu Conc %	Mn Conc %	Mg Conc %	Cr Conc %	Ni Conc %	Zn Conc %	Ti Conc %	Be Conc %	Bi Conc %	Ca Conc %	Cd Conc %	Ga Conc %	Li Conc %	Na Conc %	Pb Conc %
1	0.95	0.20	0.017	0.53	0.74	0.012	0.005	<0.0010	0.012	0.0003	<0.0010	0.0009	A 0.021!	0.006	<0.0001	0.0005	0.004
2	0.90	0.17	0.016	0.53	0.72	0.011	0.003	<0.0010	0.010	0.0003	<0.0010	0.0008	A 0.014!	0.005	<0.0001	0.0004	0.0009
3	0.92	0.19	0.016	0.54	0.76	0.011	0.003	<0.0010	0.009	0.0003	<0.0010	0.0006	A 0.011!	0.005	<0.0001	0.0003	0.001
Mean	**0.92**	**0.19**	**0.016**	**0.53**	**0.74**	**0.011**	**0.004**	<-0.007	**0.010**	**0.0003**	<-0.0004	**0.0008**	A 0.015!	**0.006**	<0.0000	**0.0004**	**0.002**

	Sn Conc %	V Conc %	Zr Conc %	Al Conc %	Bg %
1	A 0.010!	0.014	0.002	97.5	--
2	A 0.003!	0.013	0.0003	97.6	--
3	A 0.005!	0.012	<0.0003	97.5	--
Mean	A 0.006!	**0.013**	**0.0008**	**97.5**	--

Appendix 22 - Microstructure of G20/21. Etched in Kellers.

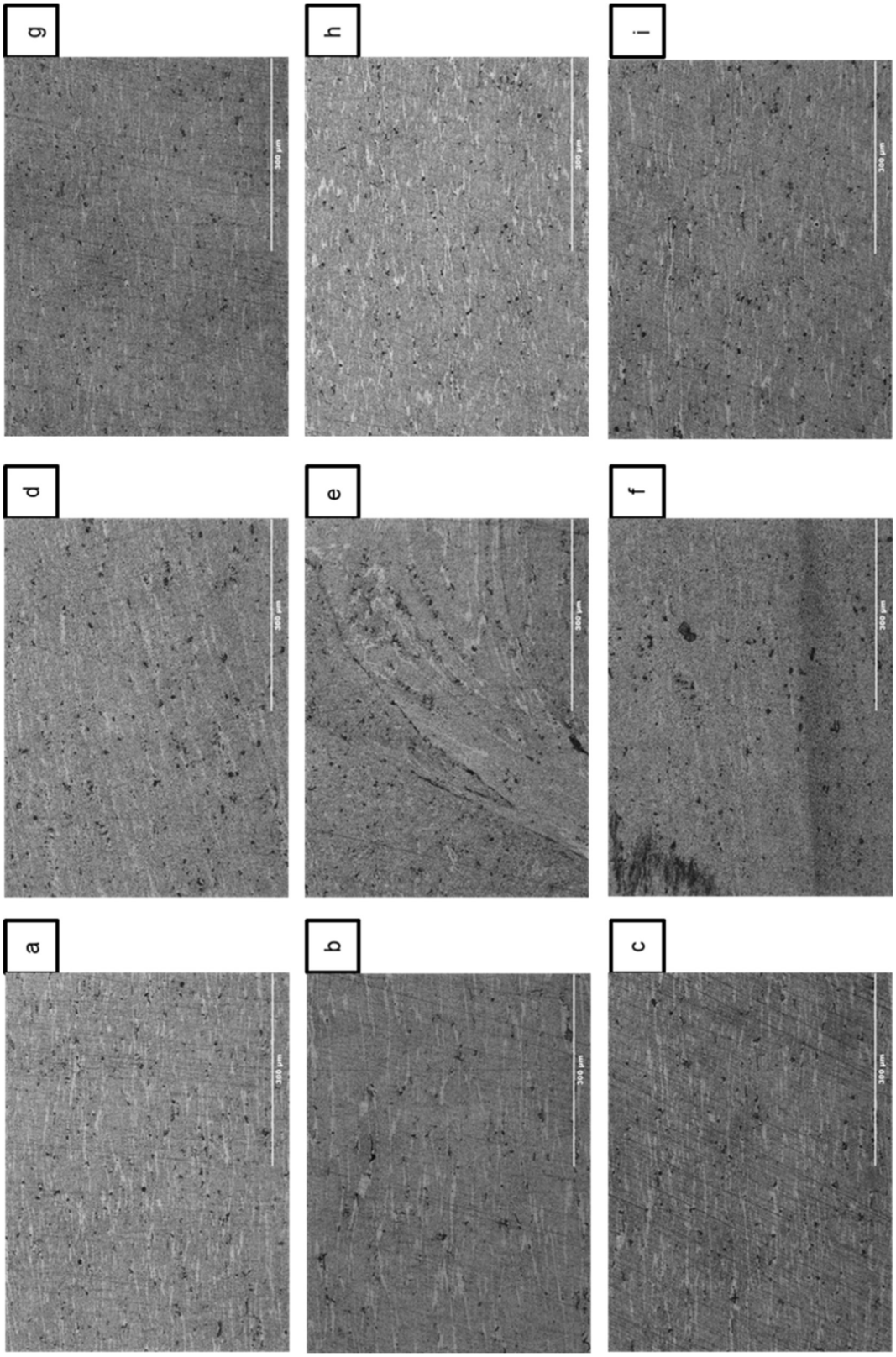

Appendix 23 - Microstructure of G22. Etched in Kellers.

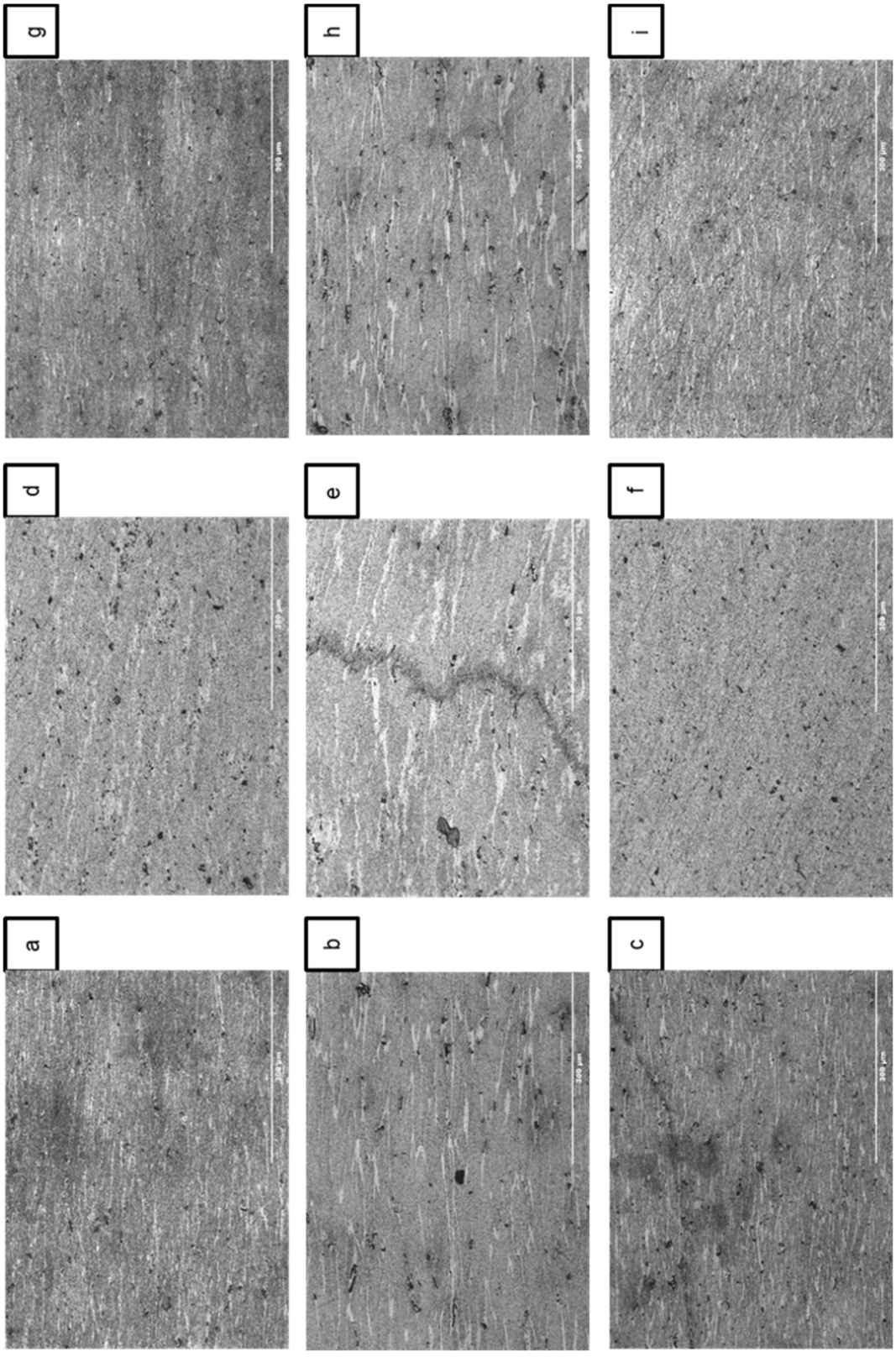

Appendix 24 - Microstructure of G14. Etched in Kellers.

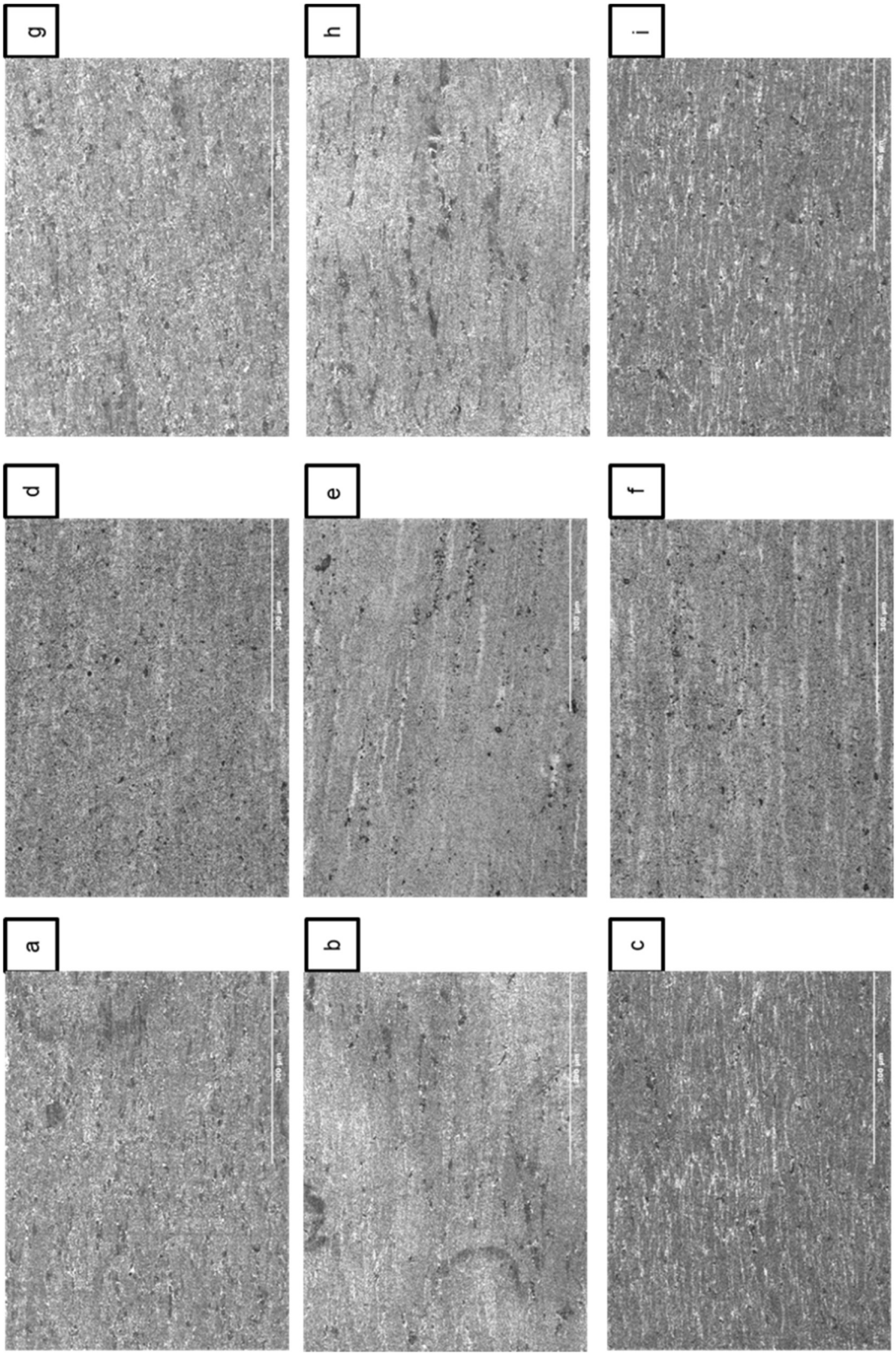

Appendix 25 - Microstructure of G16. Etched in Kellers.

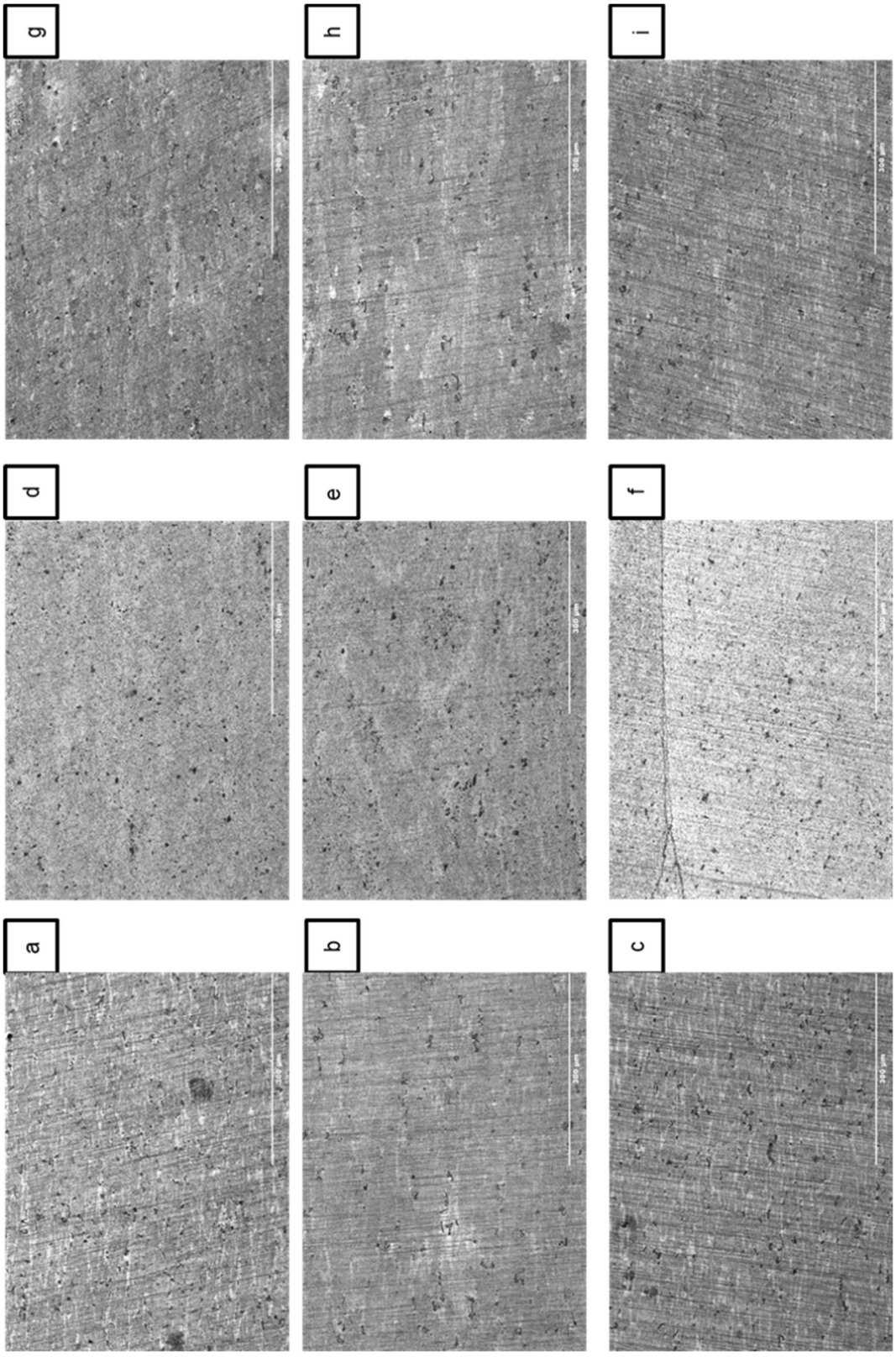

Appendix 26 - Microstructure of G17. Etched in Kellers.

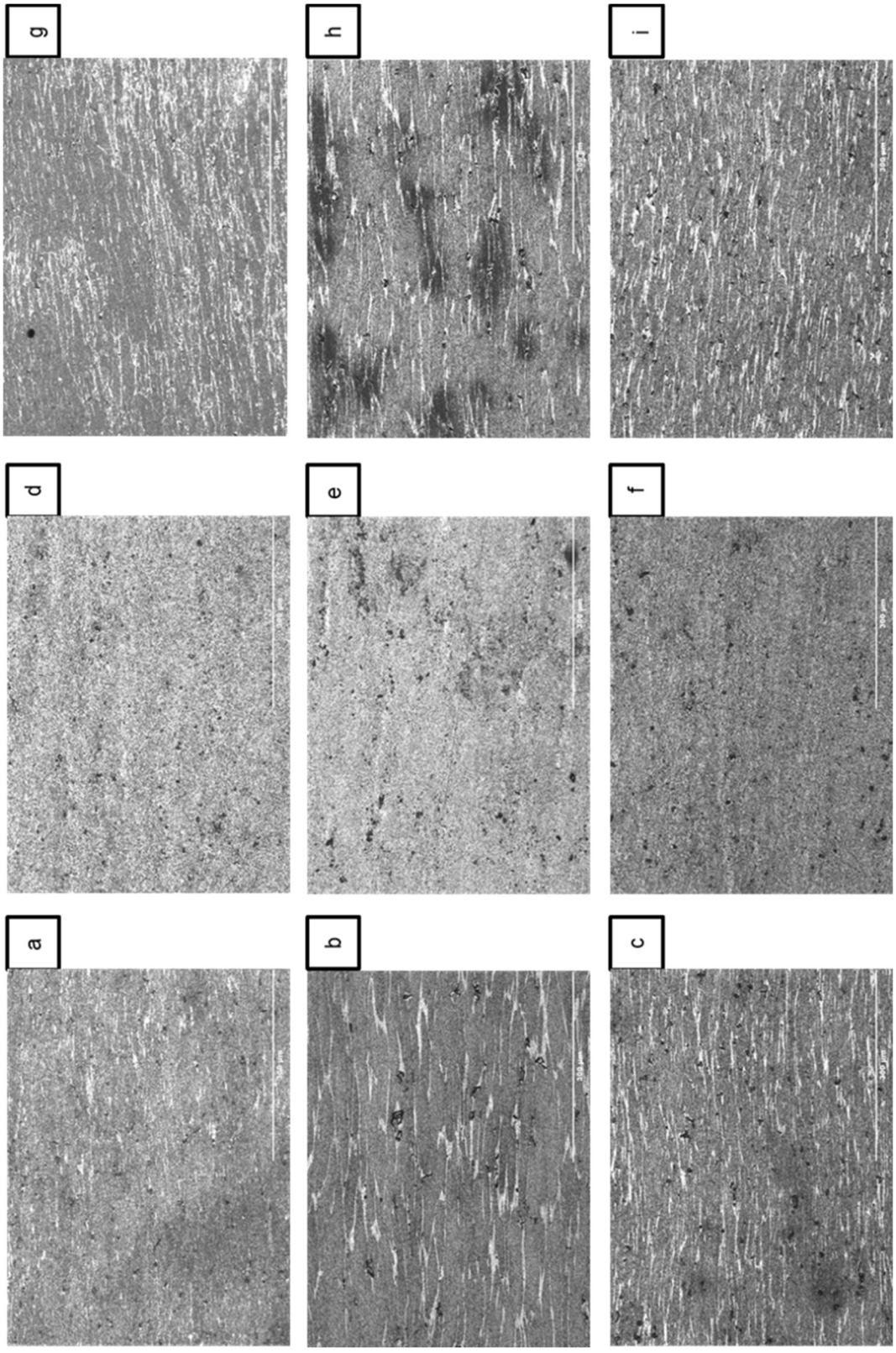

Appendix 27 - Microstructure of G19. Etched in Kellers.

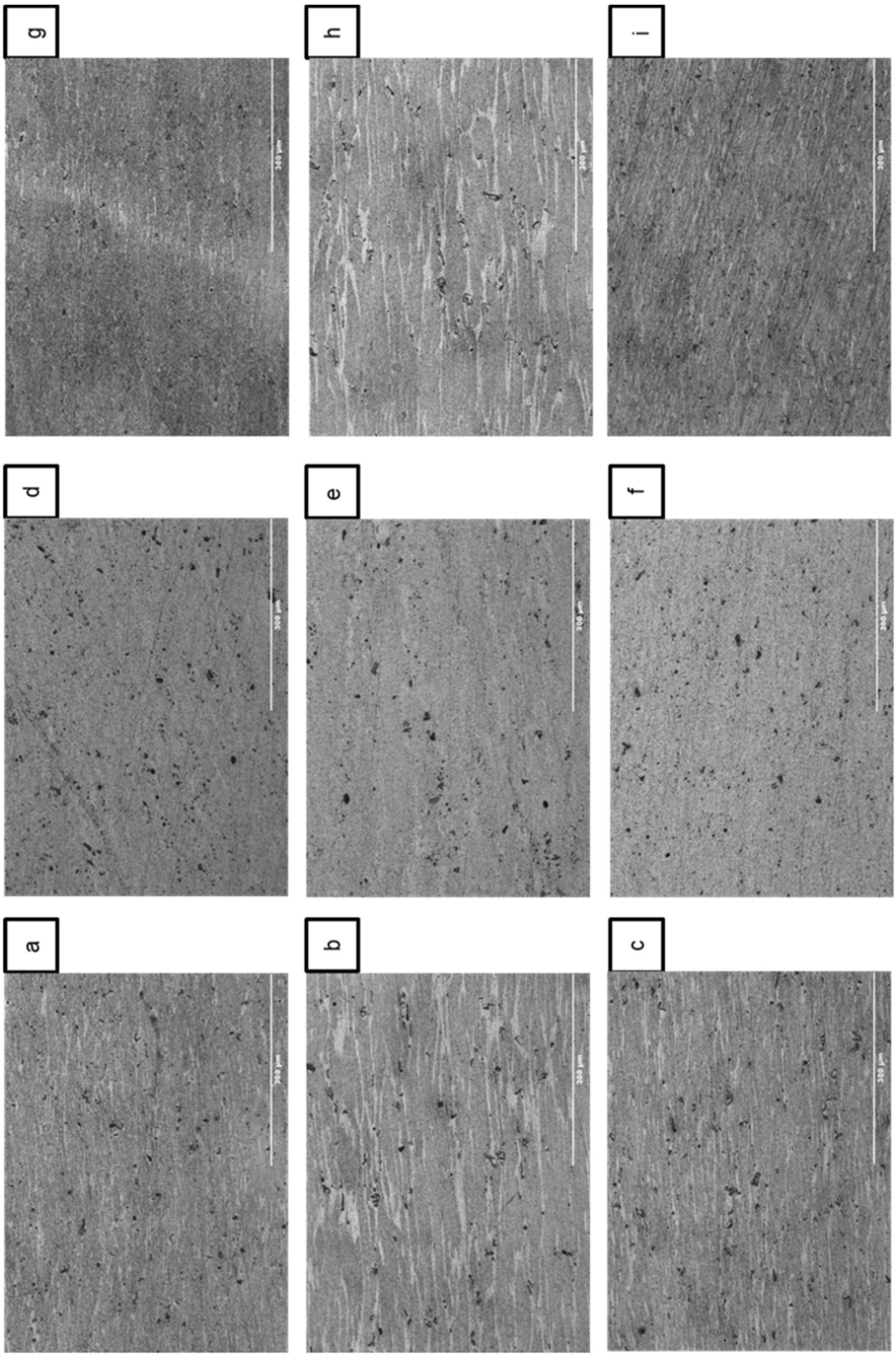

Appendix 28 - Failed tensile specimens of WFW-FSW, G20/21.

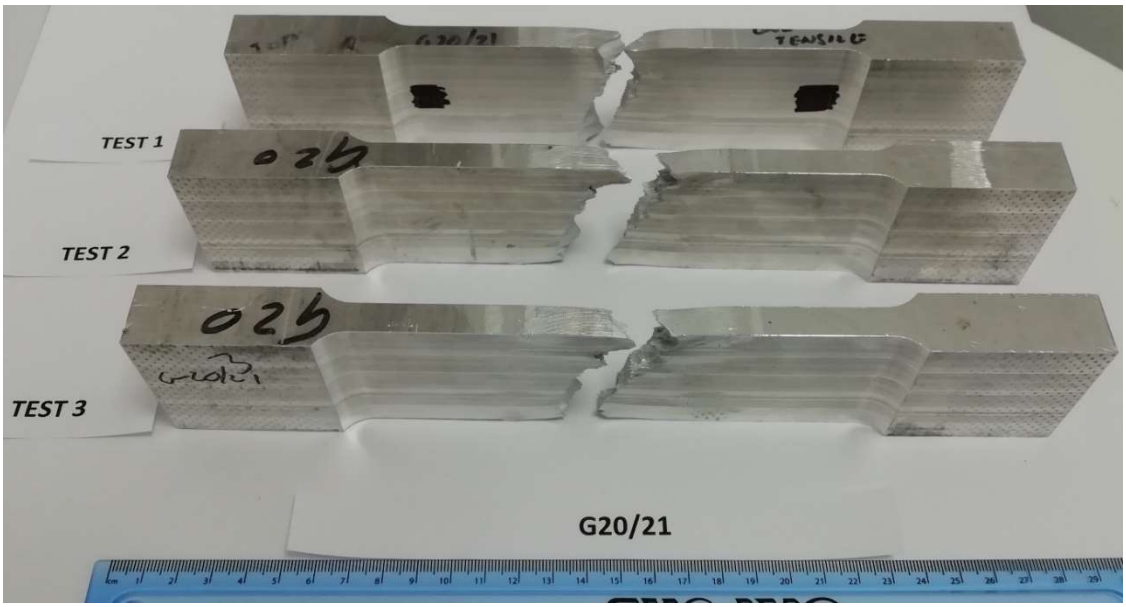

Appendix 29 - Failed tensile specimens of WFW-FSW, G22.

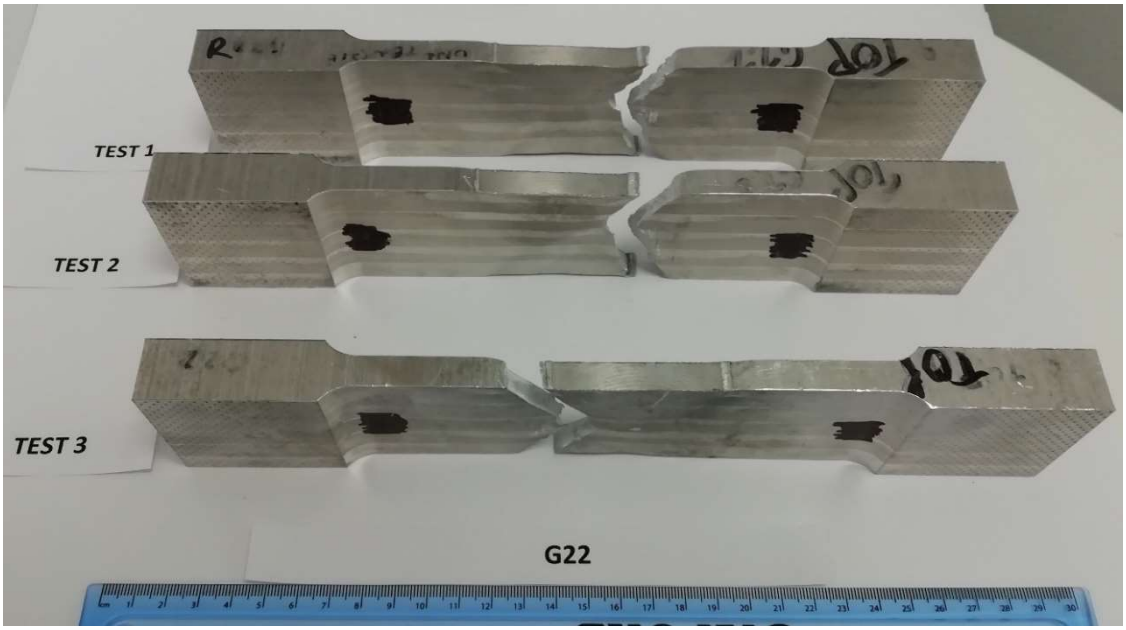

Appendix 30 - Failed tensile specimens of SSS-FSW, G14.

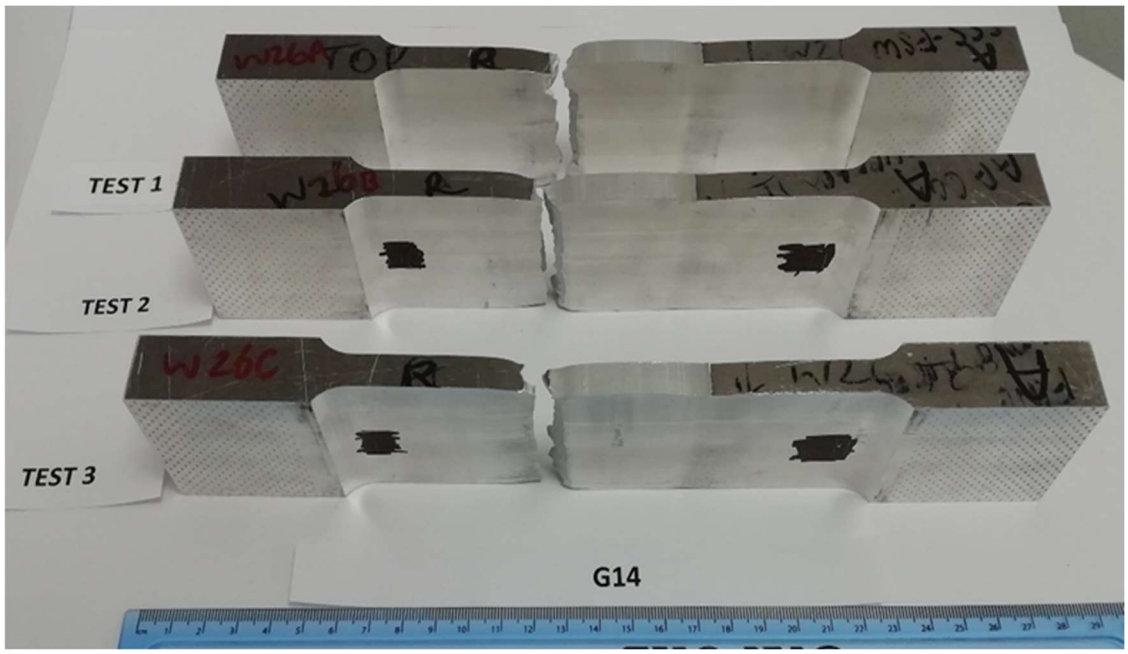

Appendix 31 - Failed tensile specimens of SSS-FSW, G16.

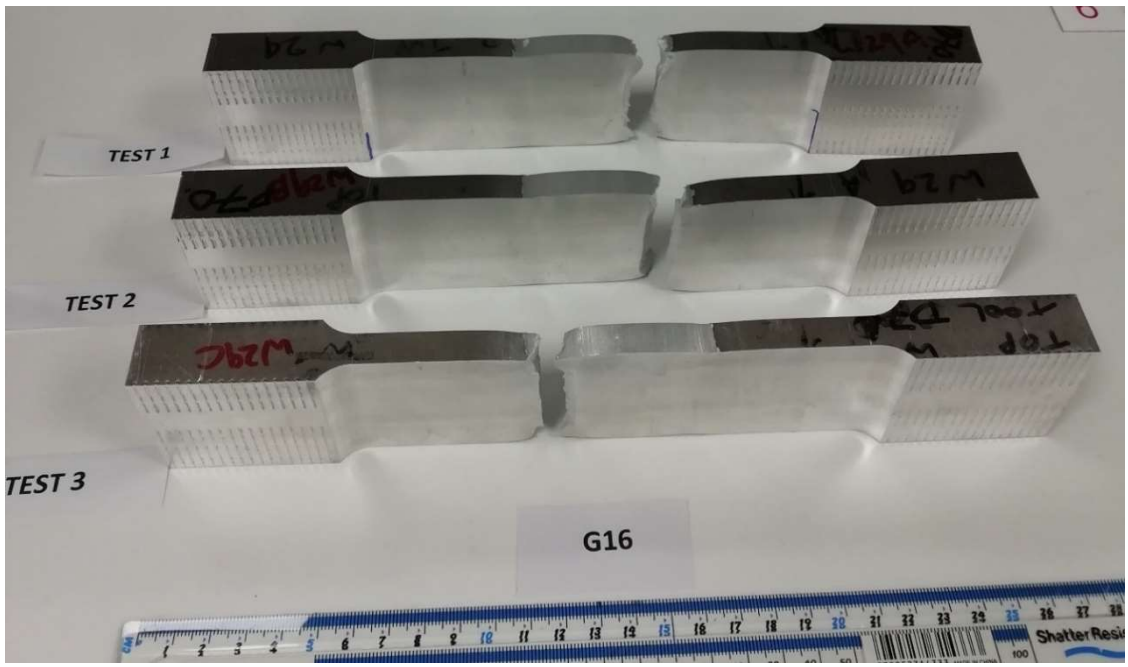

Appendix 32 - Failed tensile specimens of SSS-FSW, G17.

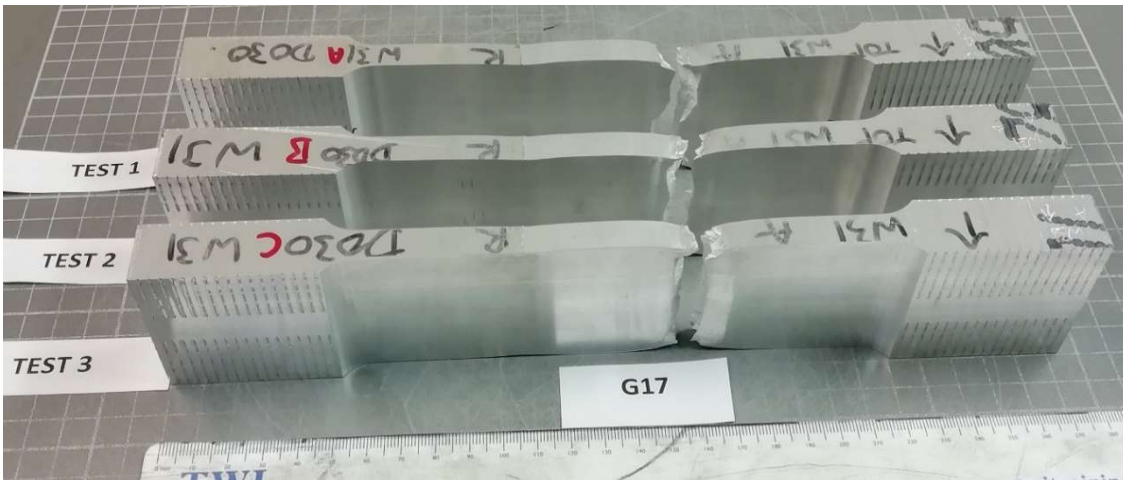

Appendix 33 - Failed tensile specimens of SSS-FSW, G19.

Appendix 34 - OES analysis of AA7050-T7451 parent material.

SPECTRO

Sample Results

Sample Result Name	Type	Measure Date Time	Recalculation Date Time	Origin	Method Name	Operator Name
7050/Paul Allender	Unknown	28/08/2019 09:40	28/08/2019 09:47	Measured	AI-50-M	Paul Allender

Check Type	Check Status	Correction Type	Outlier Test Type	Status
None	Not Used	None	None	Not Used

Sample Name	Operator	Grade ID
7050	Paul Allender	

	Si	Fe	Cu	Mn	Mg	Cr	Ni	Zn	Ti	Be	Pb	Sn	Sr	V	Zr	Al	Bg
	Conc %	Conc %	Conc %	Conc %	Conc %	Conc %	Conc %	Conc %	Conc %	Conc %	Conc %	Conc %	Conc %	Conc %	Conc %	Conc %	%
1	2.96	0.56	3.00	0.059	0.68	0.031	0.11	4.05	0.12	0.0008	0.14	0.12	0.012	0.013	0.20	87.9	--
2	2.42	0.62	2.93	0.043	0.62	0.026	0.091	6.91	0.078	0.0009	0.068	0.23	0.008	0.013	0.20	85.7	--
3	0.047	0.14	1.90	0.010	1.80	0.009	0.005	5.21	0.062	0.0002	0.003	A 0.009!	<0.0001	>0.013	0.15	90.6	--
4	0.058	0.11	1.76	0.011	1.79	0.008	0.004	5.24	0.064	0.0002	0.003	A 0.002!	<0.0001	>0.013	0.14	90.8	--
5	0.059	0.12	1.89	0.010	1.90	0.007	0.006	5.43	0.048	0.0002	0.002	A 0.005!	<0.0001	0.012	0.12	90.4	--
Mean	**0.054**	**0.12**	**1.85**	**0.010**	**1.83**	**0.008**	**0.005**	**5.29**	**0.058**	**0.0002**	**0.003**	A 0.005!	<-0.0003	>0.014	**0.14**	**90.6**	**--**

Appendix 35 - Microstructure of G03/04. Etched in Krolls reagent.

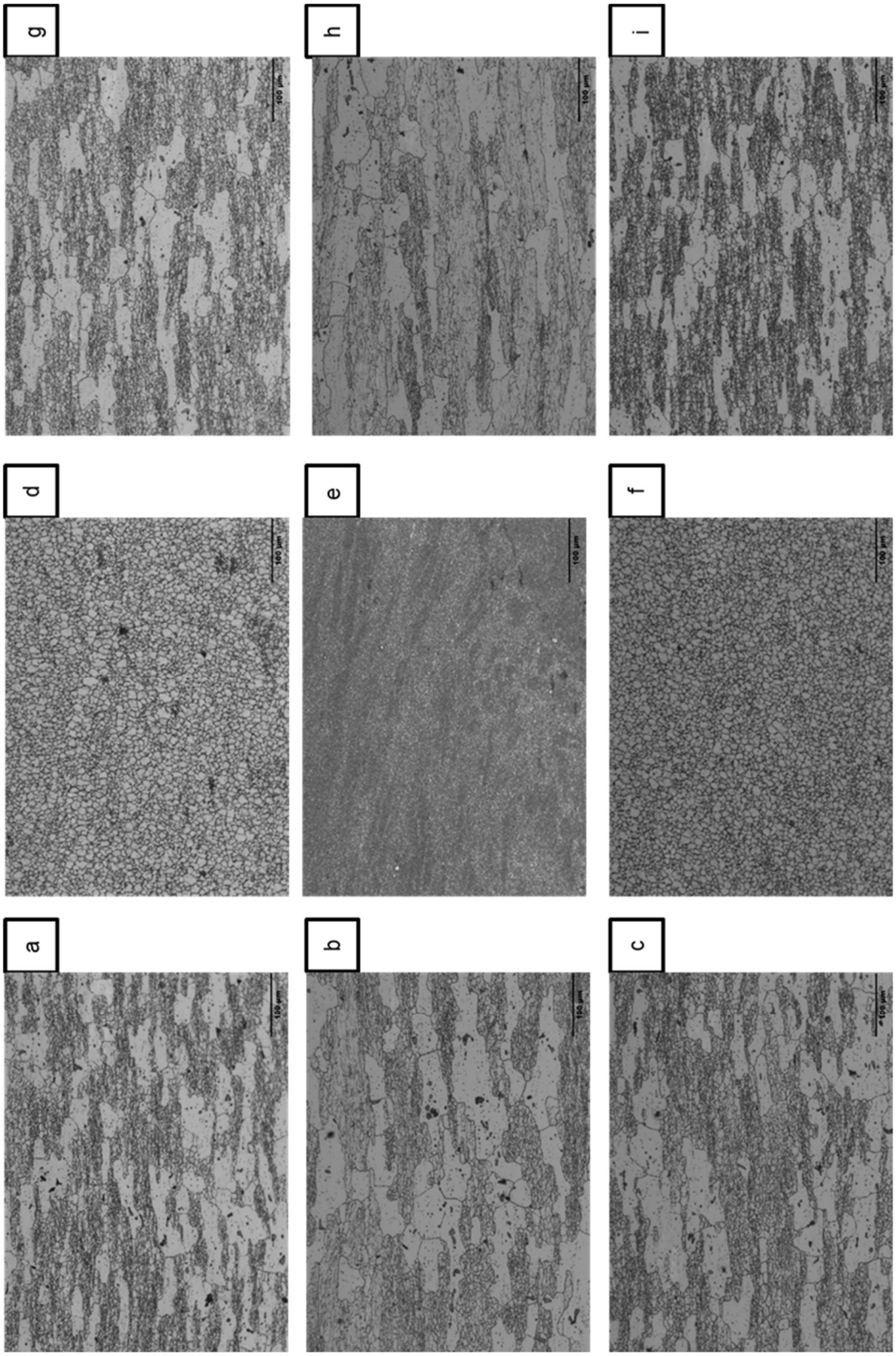

Appendix 36 - Microstructure of G12. Etched in Krolls reagent.

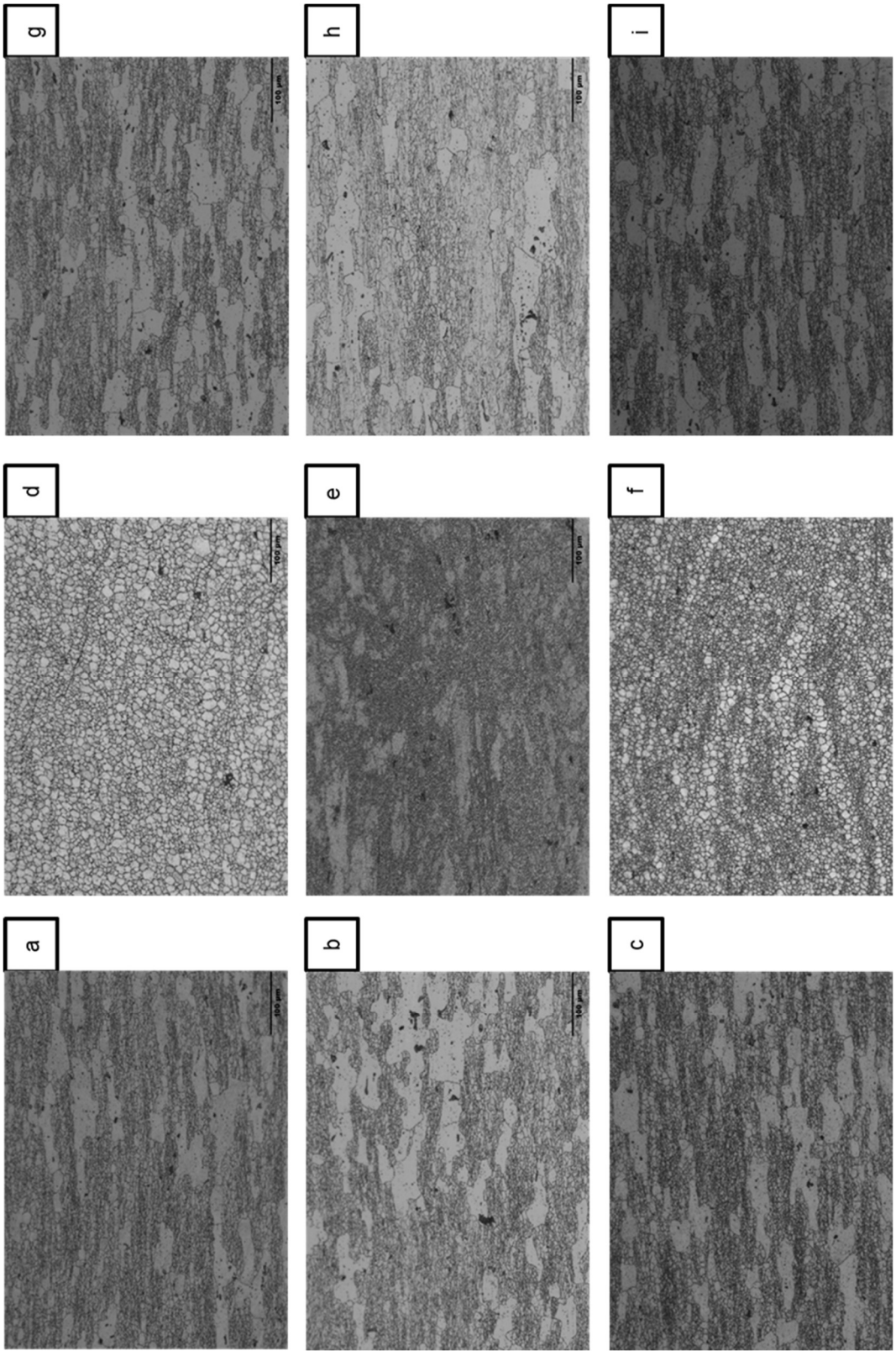

Appendix 37 - Microstructure of G18. Etched in Krolls reagent.

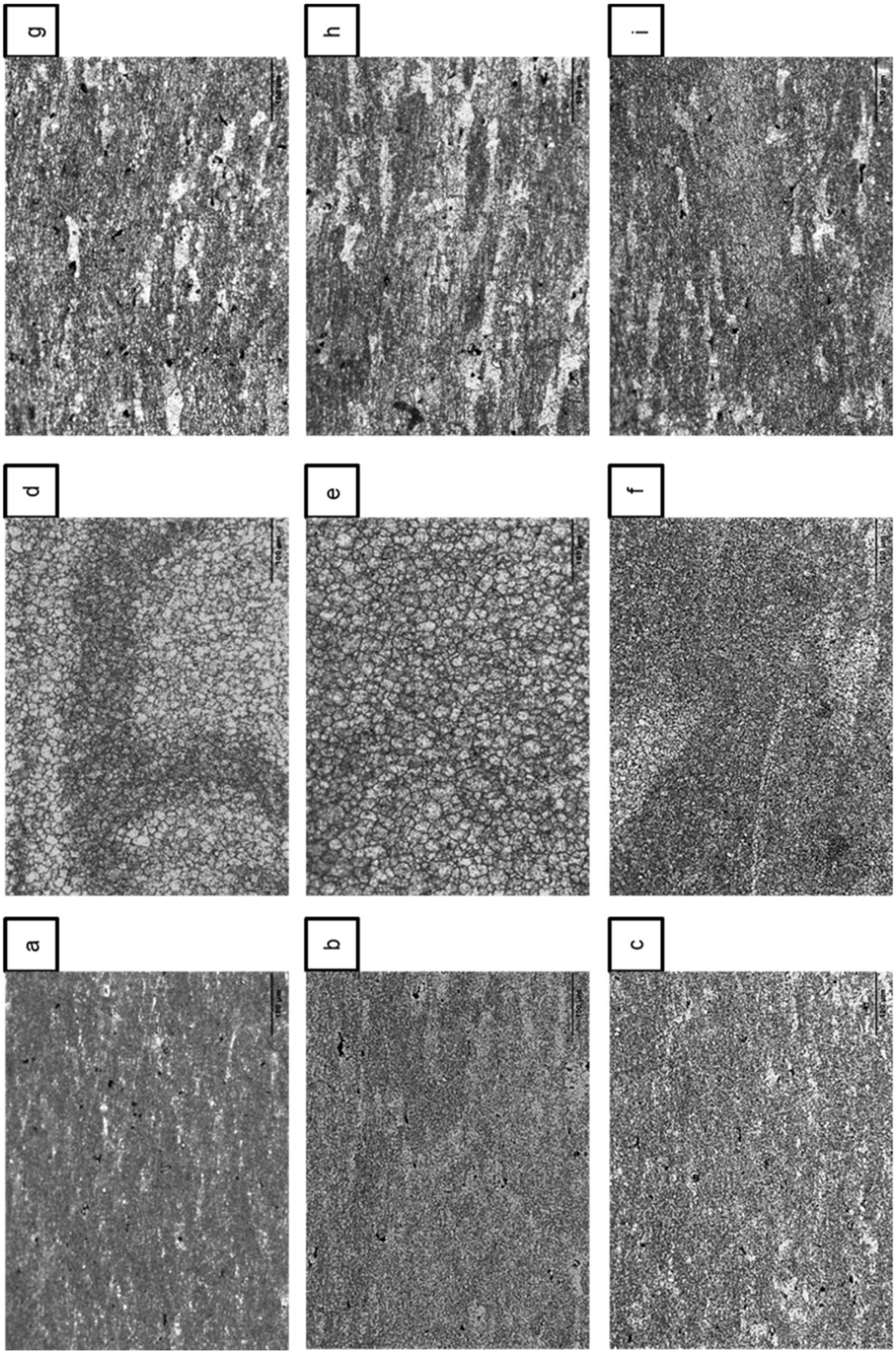

Appendix 38 - Failed tensile specimens of as-received AA7050-T7451 parent material.

Appendix 39 - Failed tensile specimens of as-welded G03/04.

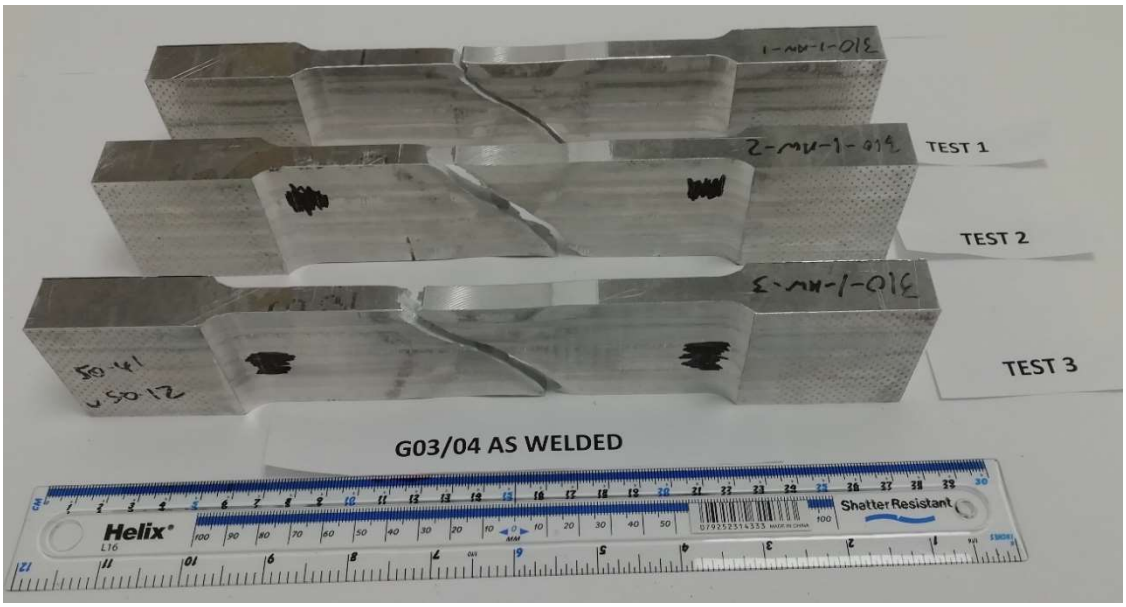

Appendix 40 - Failed tensile specimens of as-welded G12.

Appendix 41 - Failed tensile specimens of 6 month naturally aged G03/04.

Appendix 42 – Failed tensile specimens of 12 month naturally aged G03/04.

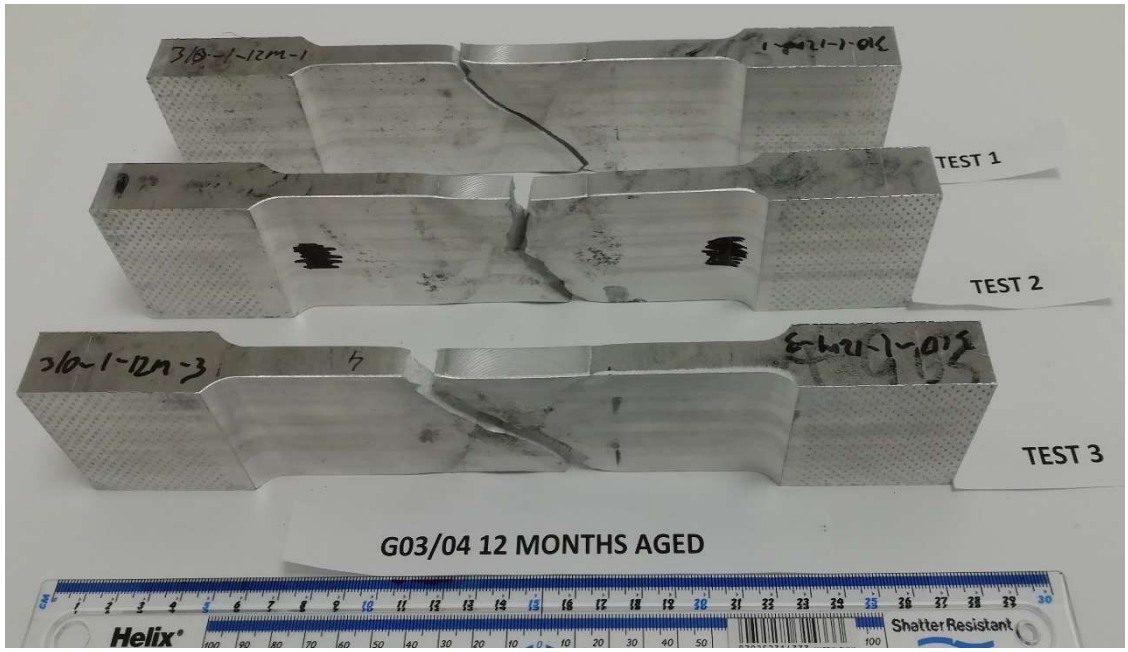

Appendix 43 – Failed tensile specimens of 18 month naturally aged G03/04.

Appendix 44 - Failed tensile specimens of 6 month naturally aged G12.

Appendix 45 – Failed tensile specimens of 12 month naturally aged G12.

Appendix 46 – Failed tensile specimens of 18 month naturally aged G12.

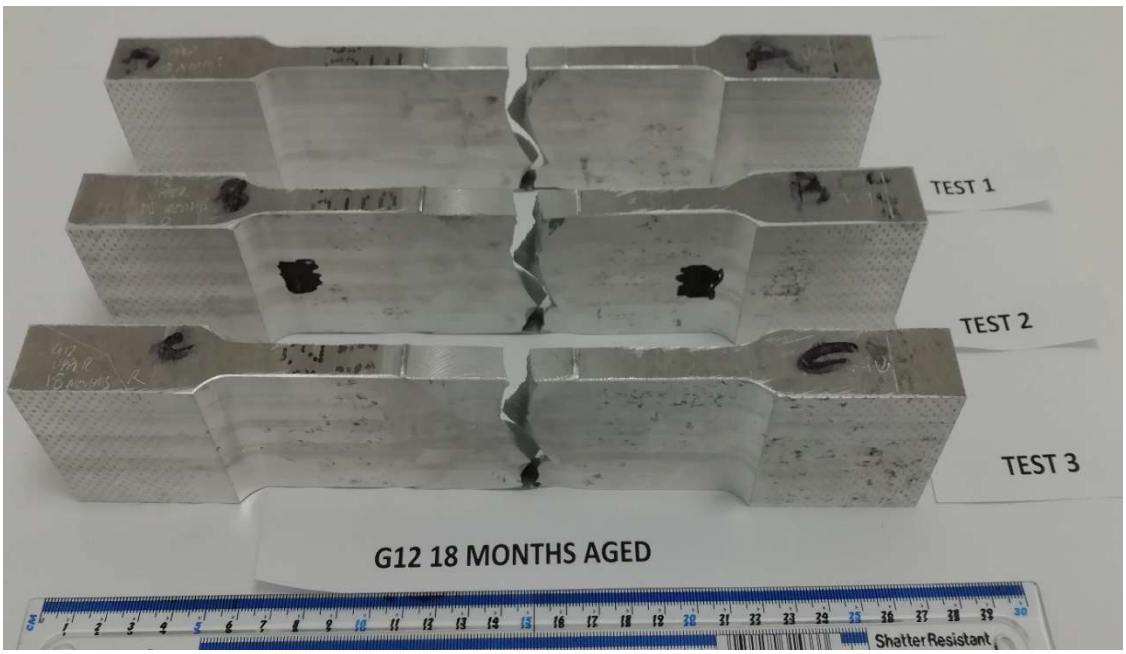

Appendix 47 – Micro-hardness contour map of 6-month aged weld G03/04 - WFW-FSW in AA7050-T7451.

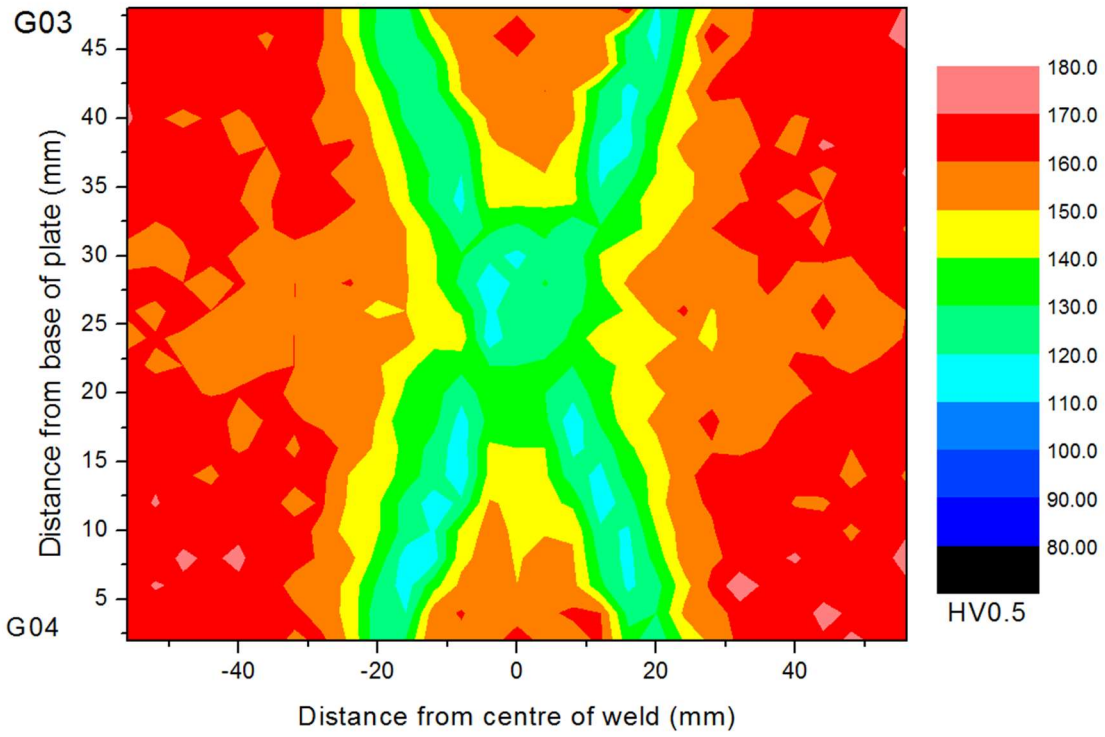

Appendix 48 - Micro-hardness contour map of 12-month aged weld G03/04 - WFW-FSW in AA7050-T7451.

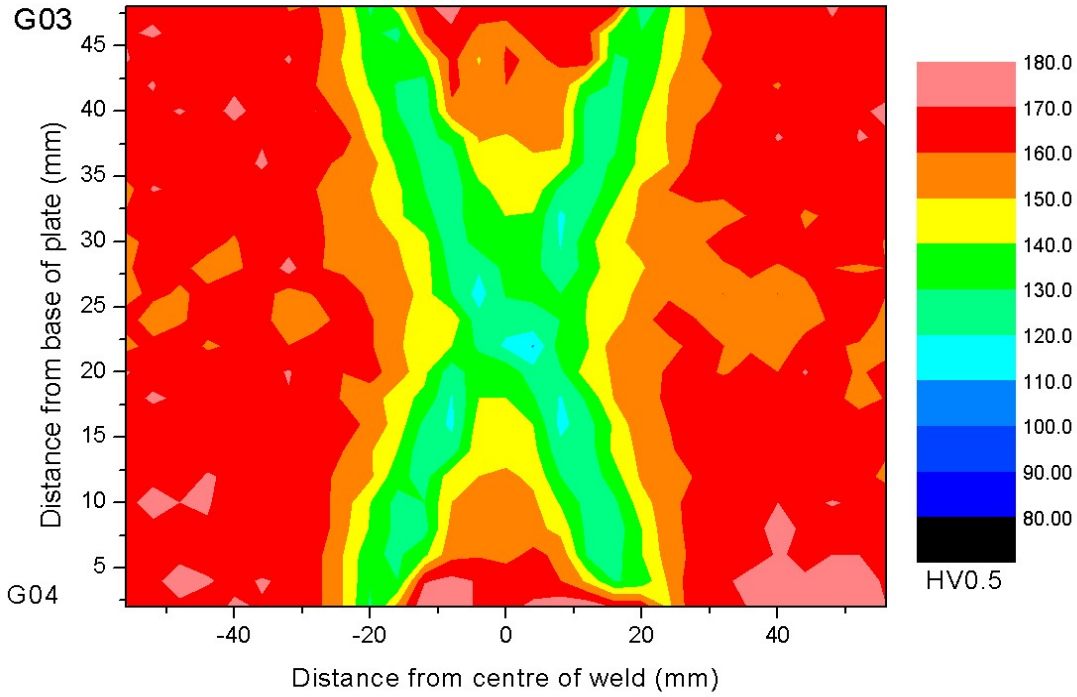

Appendix 49 - Micro-hardness contour map of 18-month aged weld G03/04 - WFW-FSW in AA7050-T7451.

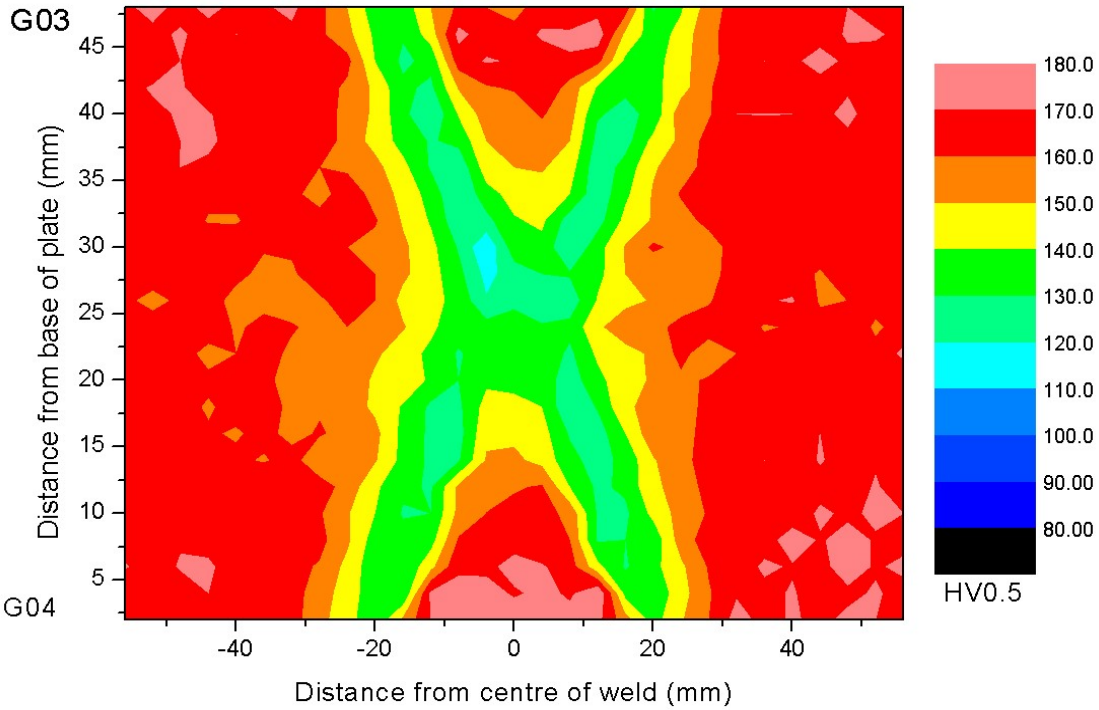

Appendix 50 - Micro-hardness contour map of 6-month aged weld G12 - WFW-FSW in AA7050-T7451.

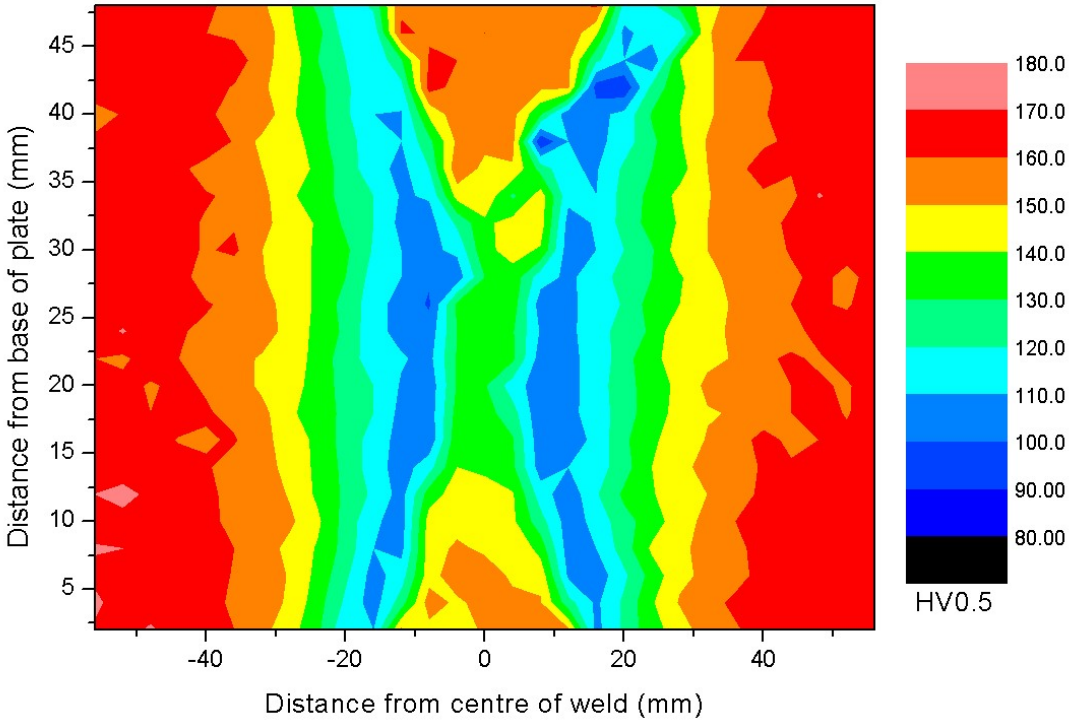

Appendix 51 - Micro-hardness contour map of 12-month aged weld G12 - WFW-FSW in AA7050-T7451.

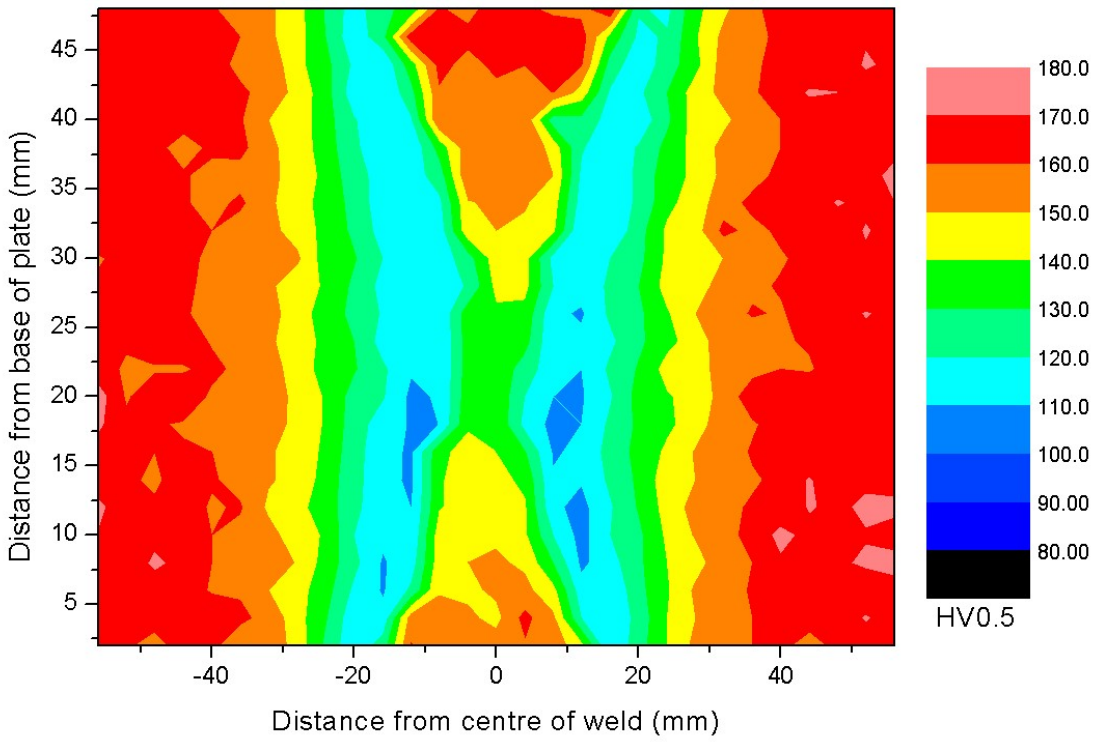

Appendix 52 - Micro-hardness contour map of 18-month aged weld G12 - WFW-FSW in AA7050-T7451.

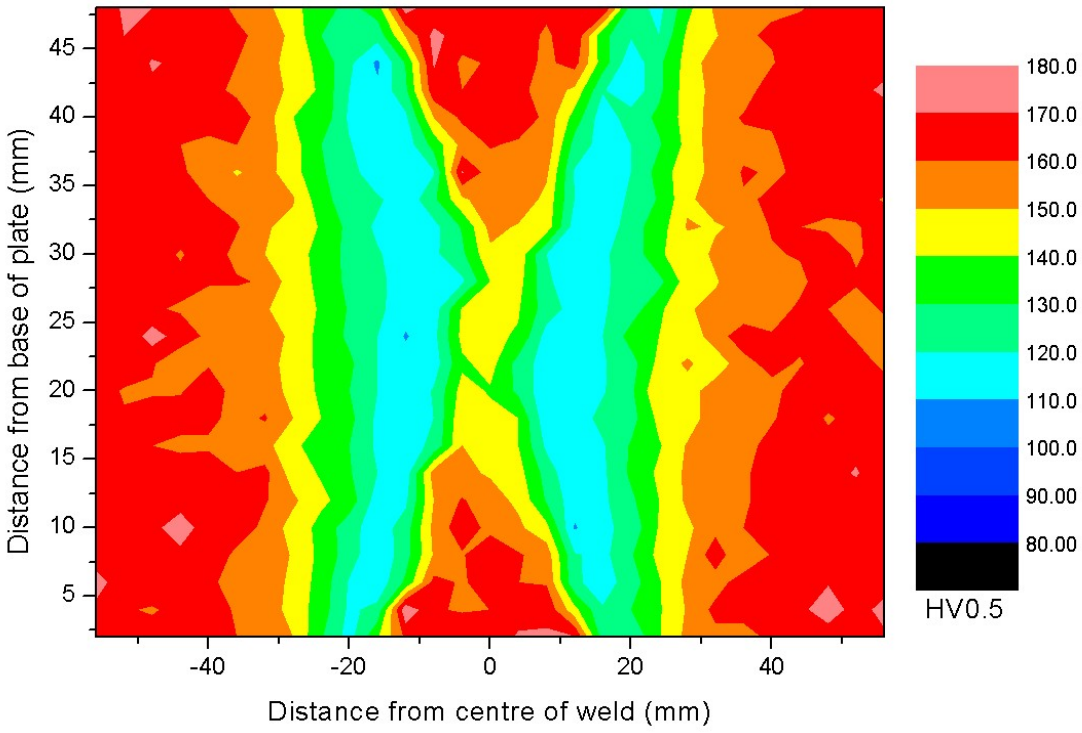

Appendix 53 – Thermocouple data from the weld G03.

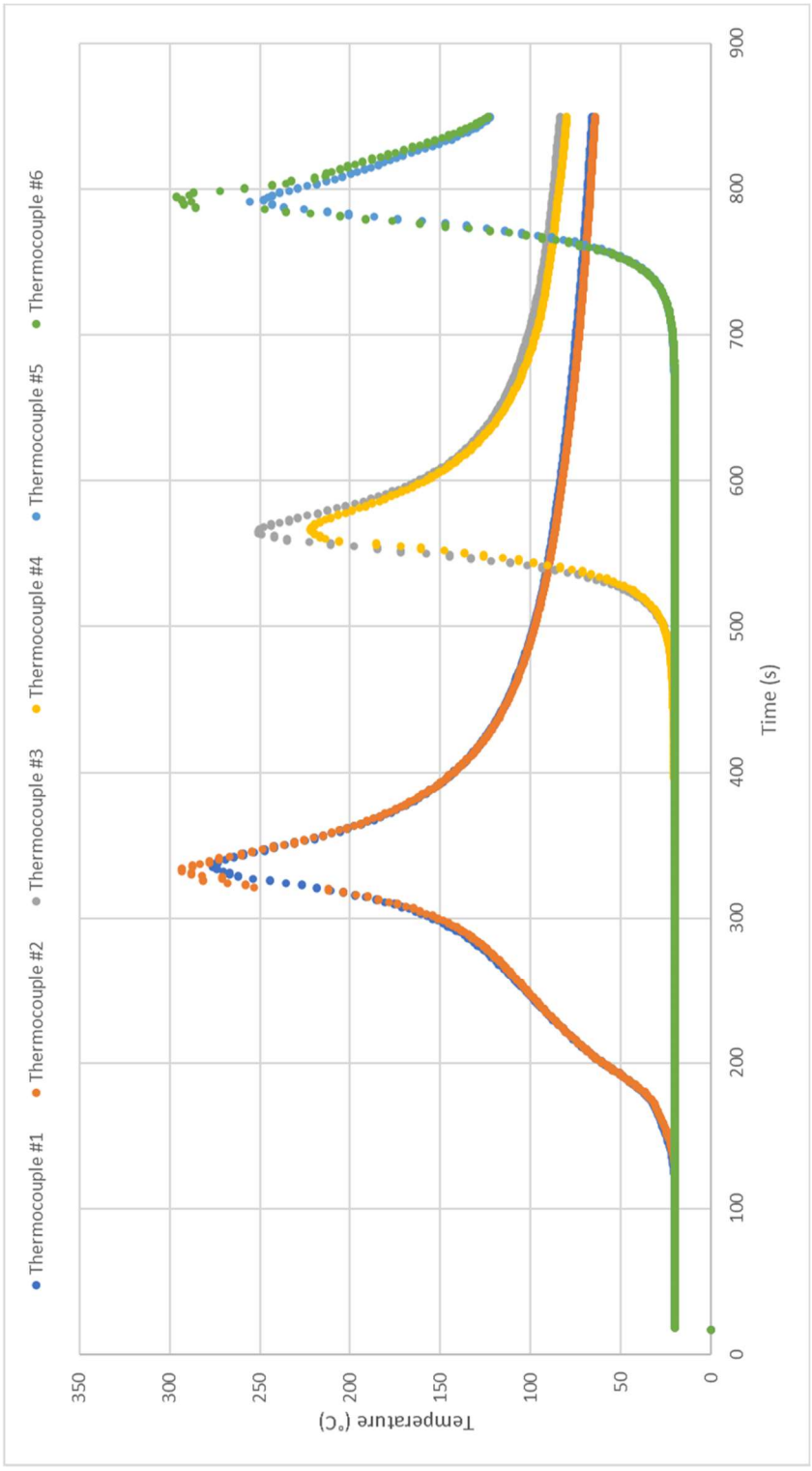

Appendix 54 – Thermocouple data from the weld G04.

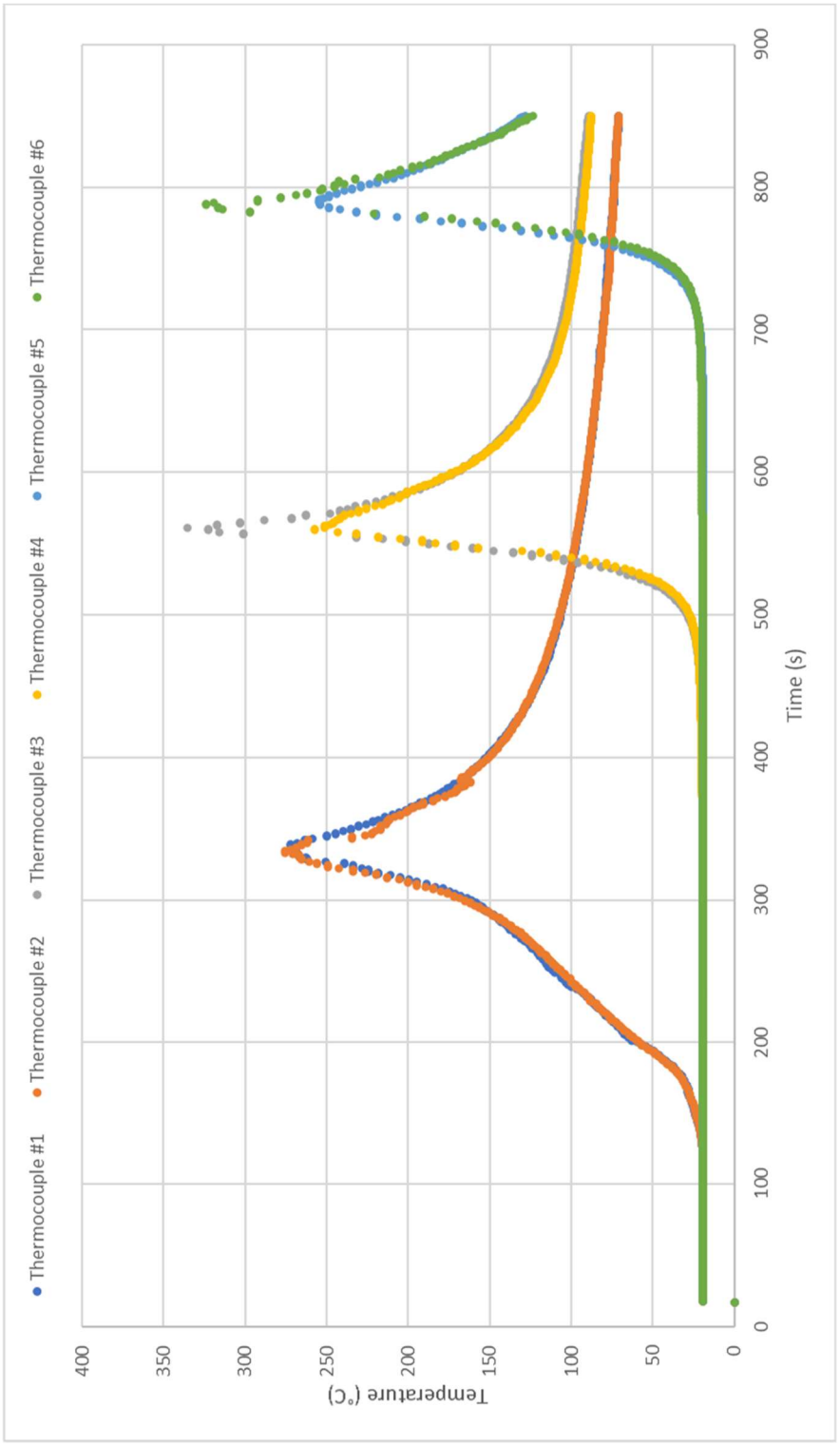

Appendix 55 – Thermocouple data from the upper pass of weld G12.

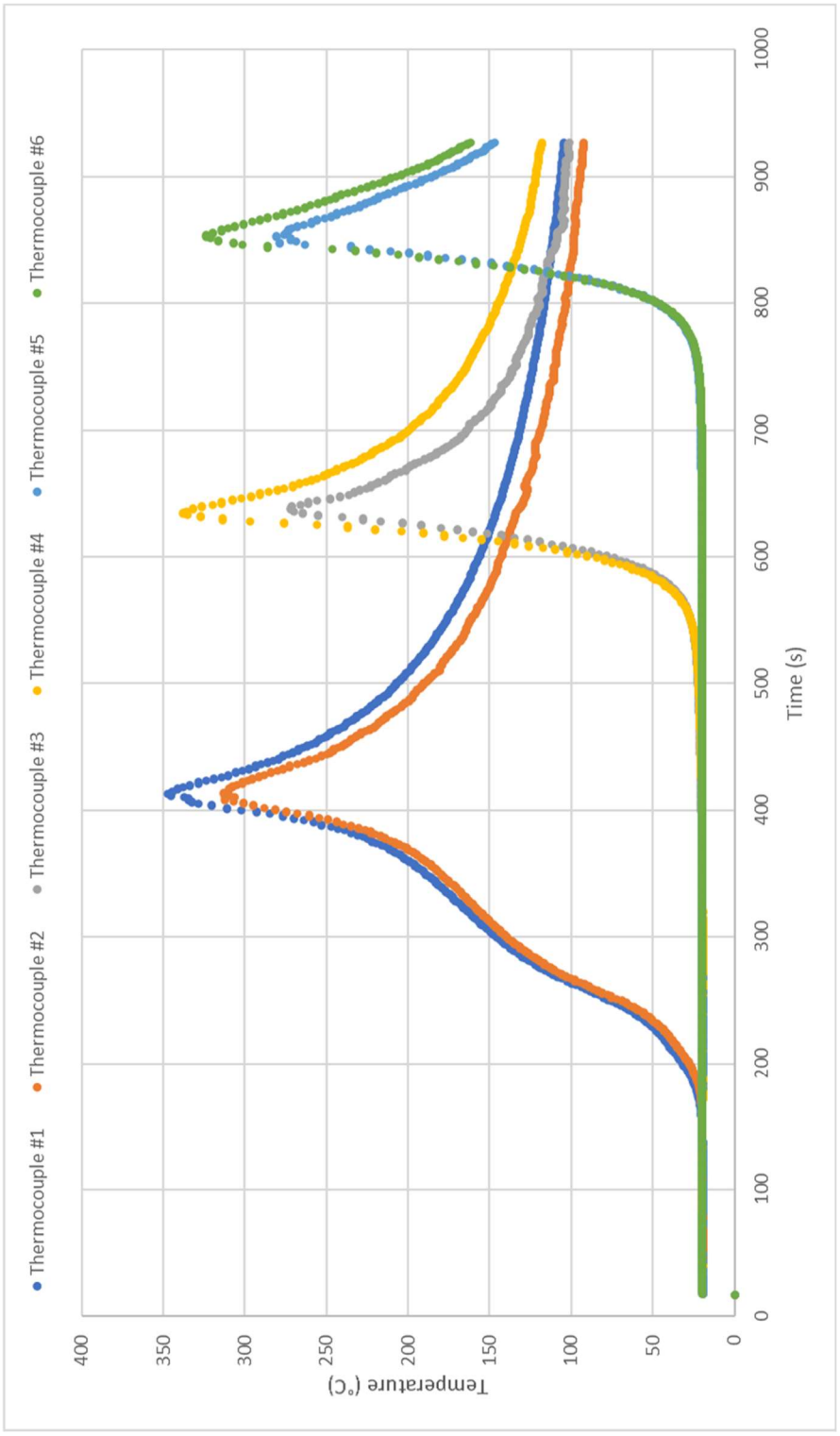

Appendix 56 – Hardness plot identifying the ‘W’ shape apparent at 14 mm from the base of the plate in the transverse plane in the AA6082 FS welds.

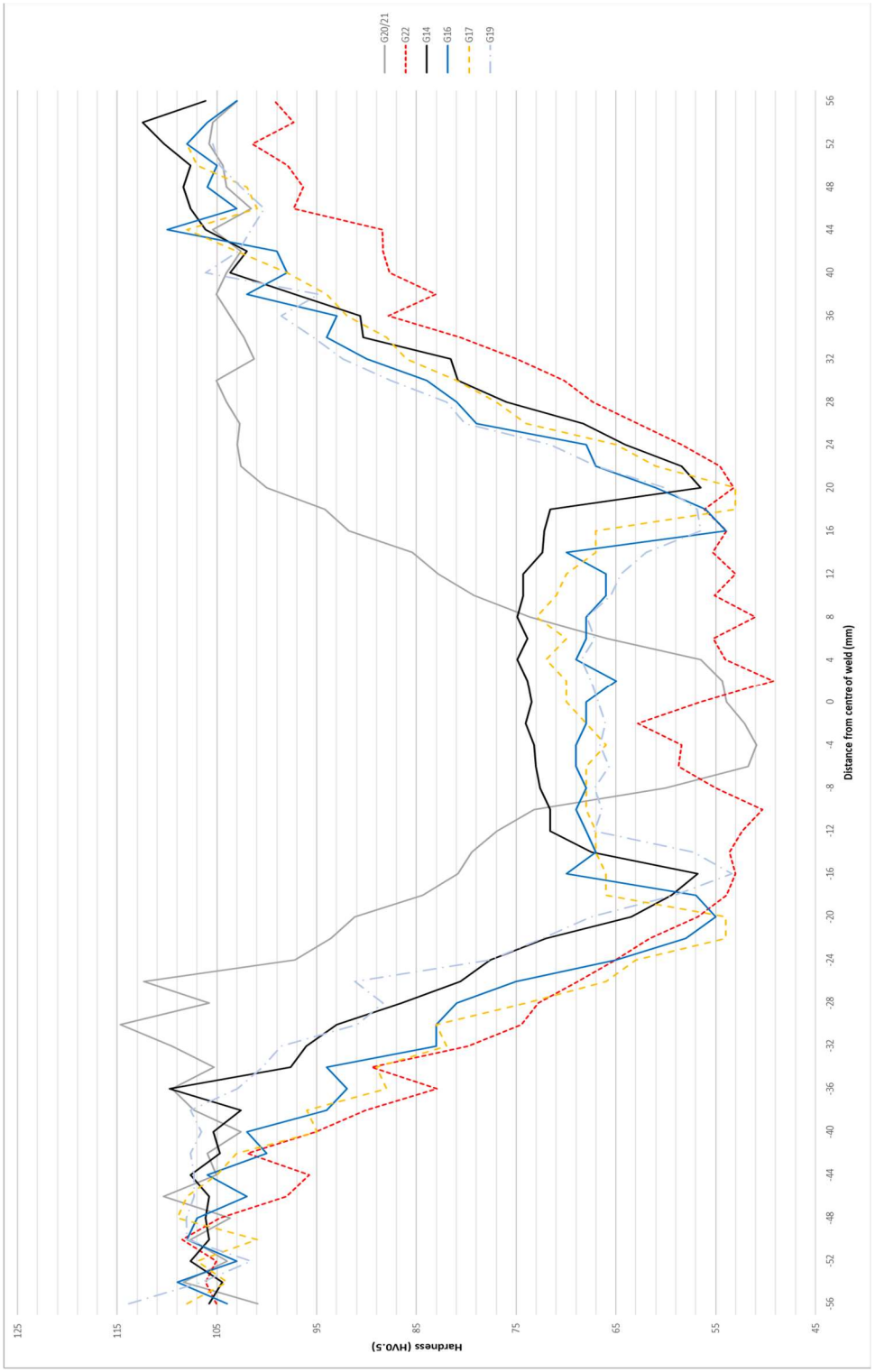

Appendix 57 – Hardness plot identifying the ‘W’ shape apparent at 14 mm from the base of the plate in the transverse plane in the AA7050 FS welds.

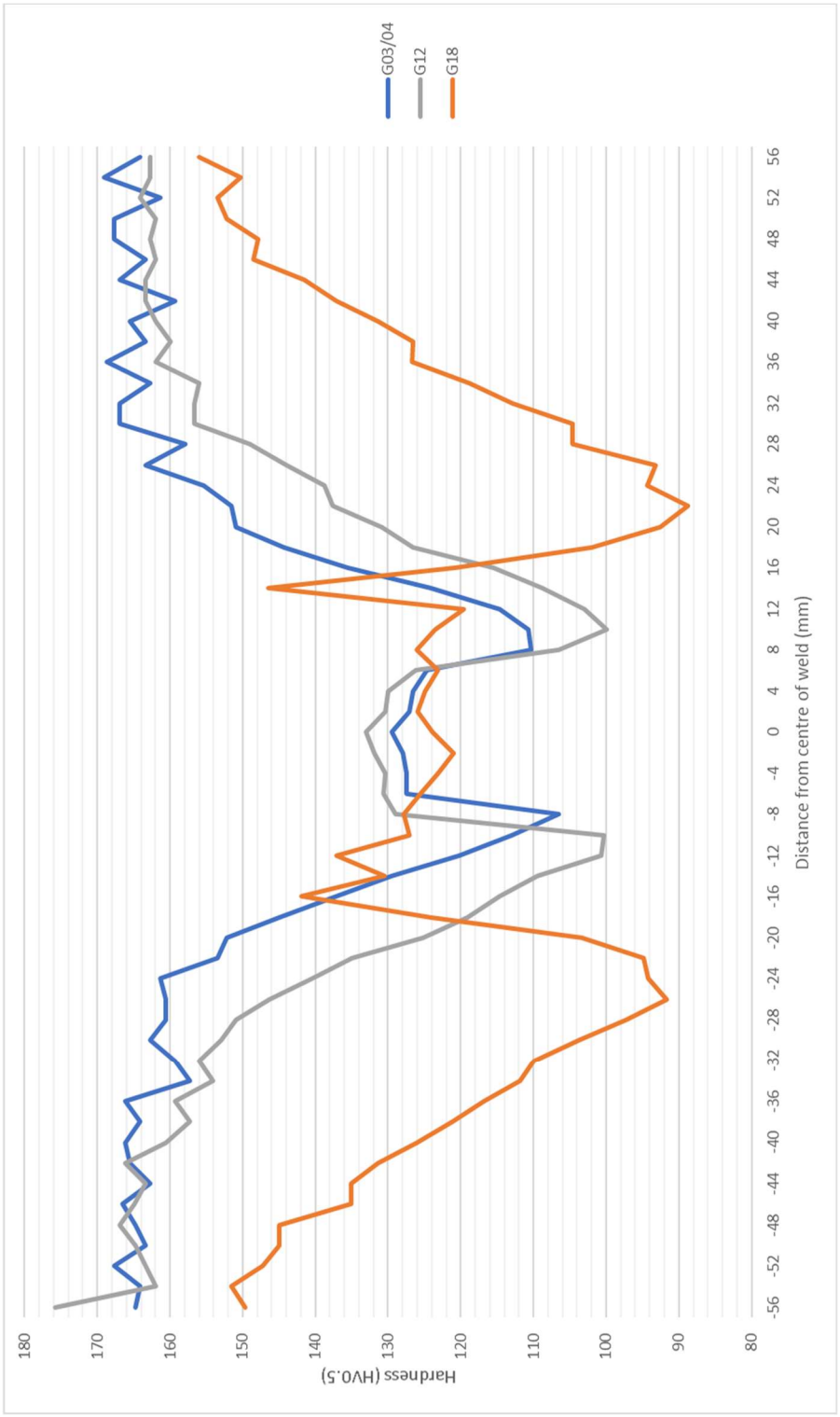

Appendix 58 – Surface blistering defect present in the back up material.